

CONFERENCE IN MEMORY OF PROFESSOR JERZY WRÓBEL

CAD in Machinery Design

Implementation and Educational Issues

XXXI International Conference

COLLECTIVE MONOGRAPH

EDITORS

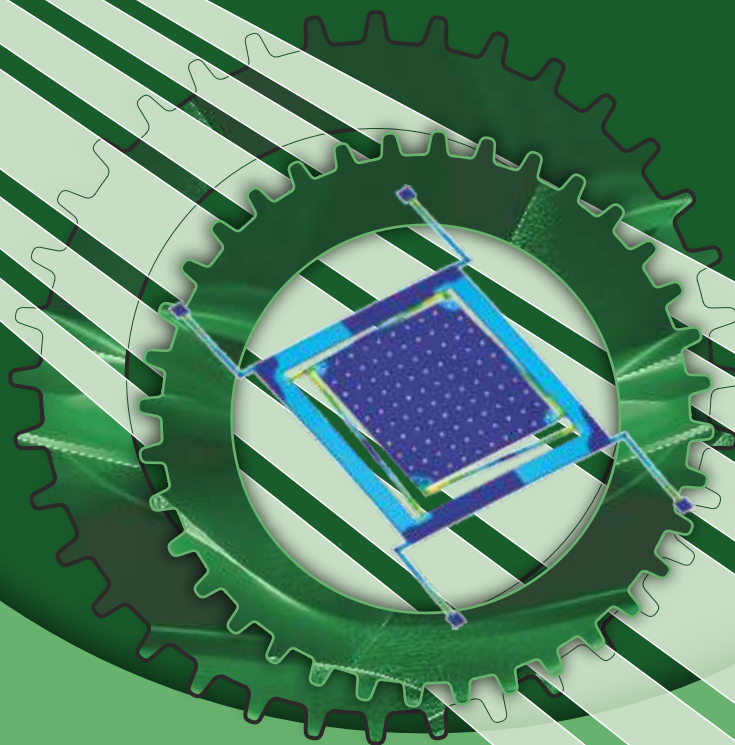
Andrzej Łukaszewicz

Andriy Zdobytskyi

Grzegorz Mieczkowski

Roman Kaczyński

Mykhaylo Lobur



Politechnika
Białostocka



COLLECTIVE MONOGRAPH

**CAD IN MACHINERY DESIGN
IMPLEMENTATION
AND EDUCATIONAL ISSUES
XXXI INTERNATIONAL CONFERENCE**

Editors

Andrzej Łukaszewicz (Białystok University of Technology)
Andriy Zdobytskyi (Lviv Polytechnic National University)
Grzegorz Mieczkowski (Białystok University of Technology)
Roman Kaczyński (Białystok University of Technology)
Mykhaylo Lobur (Lviv Polytechnic National University)

CONFERENCE IN MEMORY OF PROFESSOR JERZY WRÓBEL



OFICyna WYDAWNICZA POLITECHNIKI BIAŁOSTOCKIEJ
BIAŁYSTOK 2024

Reviewers:

Prof. Józef Jonak, PhD, DSc, Eng.
Prof. Yaroslav Sokolovskyi, PhD, DSc
Assoc. Prof. Jakub Gajewski, PhD, DSc, Eng.
Prof. Mykhaylo Andriychuk, PhD, DSc
Prof. Tomasz Węgrzyn, PhD, DSc, Eng.
Prof. Petro Kosobytskyy, PhD, DSc
Assoc. Prof. Zbigniew Oksiuta, PhD, DSc, Eng.
Prof. Olena Stankevych, PhD, DSc

Science editor in the discipline of mechanical engineering:
Prof. Oleksandr Jewtuszenko, PhD, DSc

Copy editor:

Aniela Staszewska, Edyta Chrzanowska

DTP & cover of a book:

Marcin Dominów

© Copyright by Politechnika Białostocka, Białystok 2024

ISBN 978-83-68077-19-3 (e-Book)

DOI: 10.24427/978-83-68077-19-3



The publication is available on license Creative Commons Recognition of authorship
– Non-commercial use – Without dependent works 4.0 (CC BY-NC-ND 4.0)

Full license content available

on the site creativecommons.org/licenses/by-nc-nd/4.0/legalcode.pl.

The publication is available on the Internet
on the site of the Publishing House of Białystok University of Technology.

Publishing House of Białystok University of Technology

Wiejska 45C, 15-351 Białystok

e-mail: oficina.wydawnicza@pb.edu.pl

www.pb.edu.pl

Table of contents

Preface.....	5
CHAPTER 1.....	9
1.1. Measurement of EM Field Characteristics in Laboratory Buildings	10
1.2. Development of HDL Models of Heterogeneous Microsystems for Behavioral Level of Computer-Aided Design	18
1.3. Behavioral Modelling and Simulation of Microelectromechanical Gyroscopes	28
1.4. Hardware and Software Development for Vibration Monitoring System	38
1.5. Mathematical modelling of the root crops separation and cleaning machine's parameters influence on the intensity of its functioning	47
1.6. Axisymmetric contact problem for a space with a spherical cavity	56
1.7. Study of the technical characteristics of modern LED lamps	65
1.8. Modeling and optimization of 3D object recognition using neural networks	76
CHAPTER 2.....	86
2.1. Modelling multi-bolted connections at the preloading state in a systemic approach	87
2.2. Designing and strength analysis of a screw-type press for sunflower oil production	98
2.3. Investigation of orthopedic constructions fracture using CAE technologies and the acoustic emission method	106
2.4. Automated design of fire detection devices body components	114
2.5. Recycling product model and its usage in selected aspects of eco-design	123
2.6. Fastening elements by blind rivets – research on the strength aspects	134
2.7. Numerical Simulation of the Axial Compression Test of the “Crash-Box” Energy Absorber	141
2.8. Design and numerical simulations of a modular mine explosion protection vehicle seat	147
CHAPTER 3.....	158
3.1. Leveraging smart measurement technologies for enhanced food and beverage servicing: a case study of the kypsys system	159
3.2. Synthesis of the car speed regulator using the method of pole placement	170

3.3. CAD tools for vtol propulsion unit design.....	178
3.4. Automation of the process of oil pressing using the LabVIEW system	183
3.5. CAD modeling and generative manufacturing in orthopedics on the example of a personalized targeter to support osteotomy	190
3.6. Software and methodological complex for researching the use of graph models.....	197
CHAPTER 4.....	203
4.1. Evaluation of the impact of a three-axis milling plotter accuracy on the surface quality after machining an aluminum alloy	204
4.2. Design and material selection optimization for additively manufactured modular components of a bioprosthetic hand.....	215
4.3. The role and development of CAx methods and tools in reverse engineering.....	222
4.4. Applying software development black-box, grey-box and white box reverse engineering frameworks to the mechanical industry	231
4.5. The use of artificial intelligence in teaching and learning CAx: perspectives and approaches.....	239
4.6. Application of 3-D simulation in the educational process for designing the manipulator of a robotic mobile platform	248
4.7. Educational aspects of designing a low-energy electromagnetic field generating system	257
List of Tables.....	266
List of Figures.....	268

Preface

The CADMD conference series started in Warsaw in 1994 and has been organized annually since then in Poland and Ukraine.

In 2023 the XXXI CADMD conference took place in Supraśl and has been dedicated to the memory of Professor Jerzy Wróbel.

A short history of the conference can be found on its website (<http://cadmd.lpnu.ua/>).

The organizers are as follows:

- Faculty of Mechanical Engineering, Białystok University of Technology, Białystok, Poland;
- Department of Automated Design Systems, Lviv Polytechnic National University, Lviv, Ukraine;
- Faculty of Mechanical Engineering and Robotics, AGH University of Science and Technology, Krakow, Poland;
- Institute of Fundamentals of Mechanical Engineering, Warsaw University of Technology, Warsaw, Poland.

The aim of the conference is to exchange experiences between scientists in modern information technology, the development of CAx systems, teaching methods and the implementation of automated systems in the educational process, and establishing closer ties between researchers.

The conference papers are presented on problems in the field of MCAD and ECAD techniques and CAx tools in automation of machine and mechanism design, identification, modelling of processes and systems, UAV, UGV, robotics, automation, electromechanical systems, application of information technologies in engineering, software, programming and algorithms, additive technologies, reverse engineering, databases, CAx engineering education, educational methods and Internet technologies in education.

The XXXI International Conference CAD in Machinery Design – Implementation and Educational Issues occurred under the patronage of:

- Rector of Białystok University of Technology
- Rector of L'viv Polytechnic National University
- Rector of AGH University of Science and Technology
- Rector of Warsaw University of Technology
- Main Board of SIMP (Polish Society of Mechanical Engineers and Technicians)
- President of ProCAx Association

The conference took place in Supraśl, Poland, on October 26–28, 2023.

Conference CADMD_2023 was co-financed from the state budget under the programme of the Ministry of Education and Science of Poland called “Doskonała Nauka” project no. DNK/SP/548614/2022.



MEMORIES OF PROFESSOR JERZY WRÓBEL (1948–2012)

Jerzy Pokojski
Warsaw University of Technology in Warsaw
jerzy.pokojski@pw.edu.pl,

All his professional life was closely associated with the Faculty of Automotive and Construction Machinery Engineering at the Warsaw University of Technology. The first phase was his studies at the aforementioned faculty in 1966–1972. The next stage was the doctoral studies in the years 1972–1975 – also at the Warsaw University of Technology. In 1975, Jerzy Wróbel began working at the Institute of Machine Design Fundamentals of the Warsaw University of Technology. At the beginning he worked there as an assistant professor and then as a professor. Jerzy Wróbel received his habilitation degree in 1987 and the title of professor in 1994. From 1987 to 1996, he was deputy director of the Institute of Machine Design Fundamentals, then its director until 2003.

At the beginning of his career, Jerzy Wróbel dealt with issues of numerical computation in machine dynamics. Later he broadened his field of interests in the direction of computer-aided engineering, primarily design and applications of optimization methods in both areas.

In the second half of the 1970s, Jerzy Wróbel was one of the initiators of the establishment and launch of a computer laboratory at the Institute of Machine Design Fundamentals. In the following years he made efforts to ensure its systematic

development. At the same time, he strongly encouraged many people to join projects based on computer techniques applications. Over time, a large number of colleagues, doctoral students and undergraduates appeared around him, who became deeply and intensively involved, with apparent fascination, in the work aimed at the expansion of computer methods in supporting engineering activities. Another result of those activities was that quite a large group among the scientific staff of the Faculty of Automotive and Construction Machinery Engineering started to take interest in these issues. The potential of computer methods in both mechanics, and mechanical engineering and operation began to be recognized.

Jerzy Wróbel gradually became not only an effective organizer, but also a widely known promoter of approaches based on computer techniques. At the same time, he remained a person willing to share his knowledge and experience.

In the second half of the 1980s, he completed a long-term internship in West Germany at a company developing software to support engineering processes in industry. As a direct result of his internship, Jerzy Wróbel continued to focus on the expansion of computer methods in mechanical engineering. Gradually, his research interests evolved into combination of computer methods and computer decision support. Jerzy Wróbel's achievements found applications in many areas typical for industry. Other elements such as database implementations and the integration of engineering information (specially design information), into processes carried out directly in industry also appeared in them.

During the same period, Jerzy Wróbel co-founded postgraduate studies devoted to computer-aided engineering. Later, those studies became the beginning of a new specialization at the Faculty of Automotive and Construction Machinery Engineering: Computer Aided Engineering. This specialization functioned very intensively in the 1990s and early 2000s.

The scientific output of Prof. Jerzy Wróbel constitutes about 200 papers. It includes 4 monographs, 5 textbooks and 8 coursebooks. Prof. Jerzy Wróbel has lectured on theory of design, computer techniques and engineering applications of databases. He cooperated with several foreign universities. He was the promoter of 10 doctors of technical sciences. He intensively participated in the work of various institutions related to the organization of scientific life.

Jerzy Wróbel was a member of a several scientific organizations and associations. He was also a member of scientific councils of institutes and participated in numerous scientific conferences. Some of the conferences were organized on his initiative and he promoted interdisciplinary contacts and cooperation.

Jerzy Wróbel was a great nature lover and fond of hiking. As soon as he had the chance, he undertook – often quite demanding tours in the mountains or by the sea.

IN REMEMBRANCE OF PROFESSOR JERZY WRÓBEL (1948–2012)

*dr inż. Andriy Kernytskyy
Lviv Polytechnic National University
andriy.b.kernytskyy@lpnu.ua*

It is with sincere respect and warmth that I reflect upon the memory of my mentor, Professor Jerzy Wróbel. He was an unparalleled master of his craft and a beacon of inspiration for the upcoming generation of mechanical scientists and practitioners. He was not just a skilled educator who imparted solid knowledge to his pupils, but he also demonstrated through his own practice that the profession of mechanics was amongst the best.

Jerzy Wróbel lived a fulfilling life dedicated to creation and service of others. He wrote scholarly works, articles, and instructed students and doctoral candidates. His pedagogical innovation, tenacity, energy, hard work, patriotism, benevolence, and altruism are defining traits of this eminent scientist, educator, and leader. His sharp intellect, strong character, love for his homeland, and his songs originating from his native Podlasie amidst pleasant nature and hardworking folk left me profoundly impressed. His unique thinking, excellent memory, and a formidable combination of kindness, sternness, and concern for his students dominated every aspect of his personality.

Jerzy Wróbel was exceptionally skillful in piquing the interest in his subject, simplifying complex concepts and inducing meaningful discussion which made people naturally drawn to him for advice. He had an incredible ability to recognize the potential in individuals and was quick to acknowledge their achievements - big or small, constantly encouraging them to strive for more, especially so with the youth. He deeply admired the younger generation and stressed that our aim should not just be to train specialists but the future intellectual pillars of our societies - in Poland and Ukraine. His perception of his students and doctoral candidates garnered him their deep respect and affection.

In 1998, I had the good fortune of meeting Jerzy Wróbel and his cherished wife Maria Wróbel. In 1999, he invited me to the Institute of Machine Design Fundamentals for Postgraduate studies, under his leadership. I successfully defended my dissertation in 2003, which was a triumph shared with my mentor who nurtured me as his own. Through him, I entered the scientific world of automation an experience for which I remain eternally grateful. He introduced me to the scientific elite of Poland: Professor Jerzy Bajkowski, Professor Piotr Krawiec, Professor Wojciech Batko, Professor Zbigniew Dąbrowski, and the teaching staff of Faculty of Automotive and Construction Machinery Engineering.

Jerzy Wróbel was among those rare individuals whose spiritual and creative energy perpetually flourish even as time passes by. Even today, we draw sustenance from this

energy. A testament to this continuing legacy is the XXXI CAD in Machinery Design Conference, which was initiated by him. My heartfelt thanks go to dr inż Andrzej Łukaszewicz current secretary of the Conference for the splendid idea of dedicating this XXXI Conference to the memory of the professor on his 10th death anniversary. The fact that the conference was held in Podlasie is fittingly symbolic. I am especially grateful to have served as the Secretary of this conference for over a decade. As I browse through the pages of the Conference's records, I can still sense the lingering warmth and energy of our esteemed Professor between the lines.

Chapter 1

1.1. Measurement of EM Field Characteristics in Laboratory Buildings

Mykhaylo Andriychuk¹, Taras Nazarovets², Ihor Farmaha³

¹*Lviv Polytechnic National University, CADS Department, Pidstryhach Institute for Applied Problems of Mechanics and Mathematics, e-mail: mykhaylo.i.andriychuk@lpnu.ua*

²*Lviv Polytechnic National University, CADS Department, taras.b.nazarovets@lpnu.ua, ³ihor.v.farmaha@lpnu.ua*

Summary: This chapter is devoted to measurement of electromagnetic (EM) field characteristics in laboratories in order to estimate its impact on laboratory staff. The analytical estimation uses the concept of the equivalent cylindrical monopole antenna, which models a grounded standing human. Analytical derivations provide the EM field strength values of the environment. A set of experimental tools is used for measurements. It is supplemented with the spectrum analyzer USB-SA44B and respective software, a notebook for analysis of signals, a transmitting-receiving antenna array, the transmitting antenna operating in the specific frequencies, and a SA6 signal generator. The setup allows the measurement of spectral characteristics of 4G radiation, which will be compared with the modelling data. It is substantiated that the strength of radiation depends on the antenna setup, which is examined.

Keywords: EM field radiation; 4G/5G range; monopole antenna model; strength of radiation; spectrum analyzer; signal generator; computational and experimental data.

Introduction

The increasing use of electromagnetic (EM) fields for a wide spectrum of applications is one of many significant technological achievements nowadays. But the occurrence of possible harmful effects of EM fields are also increasing in human life. Exceeding total-body exposure to radio-frequency (RF) EM fields results in the increase of the internal temperature of the human body. To handle this issue, international standards [1] and guidelines [2] have been substantiated, which use the total-body averaged specific absorption rate (SAR) as a representative metric to quantify the temperature rise in the human body. The SAR is the quantity of the RF power absorbed by the human body averaged over the total body. Since it is not suitable to evaluate the SAR inside a human, the computational results are often used to associate the SAR with the quantities externally measurable, such as the characteristics of the incident EM field.

One such technological application is the mobile telephone. Mobile phones are the most frequently used electronic devices that humans interact with. Despite the valuable impact they continue to have, scientists have expressed a possible health risk. The estimation shows that this impact is now increasing exponentially. The above requires the comprehensive study of their impact on the users.

The proximity of mobile phones to the heads of users results in a high SAR of the EM fields of radiofrequency range comparable to other sources of radiation of such kind [1].

The EM fields of the 4G/5G mobile phone can evoke effects on human organisms due to both thermal and non-thermal effects. The definitive effects of the first type on the human body and the brain tissue have been extensively studied, and the impact limits were estimated [2]–[4], but the effects of the second type are studied to a lesser extent [5]–[7].

The effects of EM field impact have been evaluated on the basis of different experimental models in the laboratory environment [8], [9], and by modelling for humans [10], [11]. Such effects invoke alterations in the intracellular signal pathways, likely in ionic density and changes in the calcium ionic permeability [12], growing cell excitability or evoking a cell response to the stresses [13]. The EM fields radiated by mobile phones cause influence on the usual brain physiology by changes of cortical excitability that modulates the activity of the neural networks regarding the EM field instability in humans [14]. The above confirms that measuring the rate of the EM Field in the indoor environment, where the users of mobile phones spend much of their time, and the study of the EM radiation impact on the human body is an actual problem.

In this chapter, we analyze the different kinds of the equipment that can be used for measuring EM field intensity and using the extracted data to evaluate the strength of EM radiation, including the SAR values.

The aim of this chapter is to extend the approach based on the cylindrical antenna theory for studying the impact of EM field exposure in the frequency range of 1–150 MHz [22] to the range of 4G frequencies, to build the experimental setup to explore the impact of the EM field radiation in the above frequencies, as well as to compare the computational and experimental data.

The Currents Acting on the Human Body

In order to model the impact of the EM field on the human body, we use a model of the cylindrical antenna (Fig. 1). This model represents a standing posture with arms in contact with the sides. The dielectric properties of biological tissues are dependent on dielectric dispersion at the cellular and molecular levels [15]. The dielectric properties of muscle are approximated by Cole-Cole dispersions, which is defined by relation of [16].

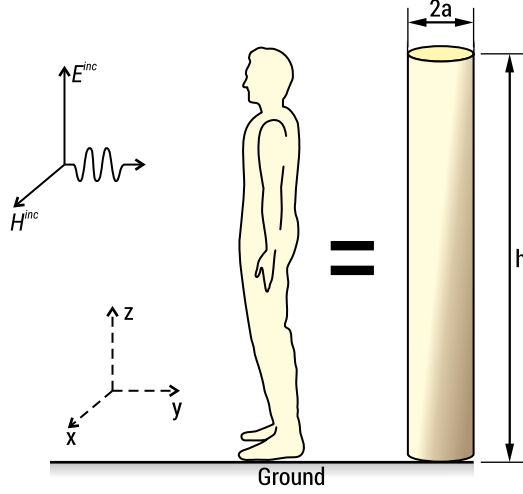


FIG. 1. Cylindrical model of the human body and a vertically polarized plane wave

We should estimate the currents, which are induced on the human body by the action of EM field radiation to estimate the EM field exposure. We consider here the action of a vertically polarized plane wave. The induced axial currents and total dissipated power inside the body (cylinder) supplementing this power are important to evaluate the respective SAR.

We assume a symmetric current density inside the equivalent cylindrical monopole antenna representing a grounded standing human induced by a time-harmonic vertically polarized plane wave. Let the high of the antenna be equal to l , its radius is equal to a , and the body is characterized by complex conductivity σ_b . The total induced axial current inside the equivalent antenna is [17]

$$I_z = V_0^\varepsilon v(z) + U_0 u(z), \quad (1)$$

where

$$V_0^\varepsilon = -I_{sc}(0) \frac{2Z_A Z_L}{2Z_A + Z_L}, \quad U_0 = \frac{E_0}{k_2} \quad (2)$$

$$v(z) = \frac{2i\pi k_0}{\xi_0 \gamma \Phi_{dR} \cos(\gamma h)} \sin \gamma(h - |z|) + \quad (3)$$

$$T_U (\cos(\gamma z) - \cos(\gamma h)) + T_D (\cos(\frac{1}{2} k_0 z) - \cos(\frac{1}{2} k_0 h)),$$

$$u(z) = \frac{4i\pi}{\xi_0} \left[H_U (\cos(\gamma z) - \cos(\gamma h)) + H_D (\cos(\frac{1}{2} k_0 z) - \cos(k_0 h)) \right], \quad (4)$$

where E_0 (measured in Vm^{-1}) is the electric incident field at the surface of the body (antenna), k_0 is the wave number of free space, $Z_A = 1/(2\nu(0))$ (measured in Ω)

is the driving point impedance of the same cylinder if driven into the ground. $Z_L(\Omega)$ is the load impedance at the ground of cylinder, $I_{sc} = U_0 u(0)$ is the current at the ground if there no load, and ζ_0 is the impedance of free space. The specification of the coefficients T_U, T_D, H_U, H_D , and Ψ_{dR} one can find in [21]; they present some integral formula, which can be calculated numerically. The imperfectly conducting characteristic of the equivalent cylindrical antenna is described by the complex propagation constant γ [22]

$$\gamma = k_0 \sqrt{1 - i \frac{4\pi z_i}{k_0 \zeta_0 \Psi_{dR}}}, \quad (5)$$

where z_i (measured in Ωm^{-1}) is the surface impedance situated to the unit length of a cylinder, which is defined as [18]

$$z_i = \frac{\kappa}{2\pi a \sigma_\omega^*} \frac{J_0(ka)}{J_1(ka)} = r_i + ix_i, \quad (6)$$

where $J_0(ka)$ and $J_1(ka)$ are the zeroth and first-order function of Bessel, respectively. The coefficient κ has form

$$\kappa = \sqrt{-i\omega \varepsilon_0 \mu_0 \left(\frac{\sigma_\omega^*}{\varepsilon_0} - i\omega - \frac{4\pi z_i}{\mu_0 \Psi_{dR}} \right)}, \quad (7)$$

where ω is the angular frequency, ε_0 and μ_0 are the permittivity and permeability of a free space, respectively.

We should have the value of the total average dissipated power P_{dis} inside the cylinder, in our case, it has the form [19]

$$P_{dis} \simeq \frac{1}{2} \int_0^l r_i |I_z(z)|^2 dz, \quad (8)$$

where r_i is real part of z_i in (6). WBA SAR is characterized as the total average RF power, which is absorbed by the antenna (human body), divided by its total mass [20, 23]. Following this rule, the total averaged absorbed power per unit mass is

$$WBA - SAR_{cyl} = \frac{P_{dis}}{W_c} = \frac{r_i}{2\pi \rho a^2 l} \int_0^l |I_z(z)|^2 dz, \quad (9)$$

where ρ is density of body, weight $W_c = \pi \rho a^2 l$.

An equivalent cylindrical dipole antenna approaching the isolated human body is characterized by the parameters [22]

$$a = L_1 \sqrt{\frac{W}{\pi \rho H}}, \quad h = H, \quad (10)$$

$$\sigma_{\omega}^* = L_2 \frac{2x}{3-t} \sigma_{mus}^*, \quad (11)$$

$$\rho = L_3 \frac{\rho_m}{t}, \quad (12)$$

where L_1, L_2 and L_3 are known constant, σ_{mus}^* is defined in accordance with [23], $\rho_m \approx 1050 \text{ kg/m}^3$ [24], variable t is the function defining the lean-body-mass of the body [22]. The function t is given as

$$t = 0.321 + \frac{1}{W} (33.92H - 29.53) \quad (13)$$

for males, and

$$t = 0.295 + \frac{1}{W} (41.81H - 43.29) \quad (14)$$

for females.

Eqs. (13) and (14) testify that parameter x depends on the weight and height of the human. If we consider the fixed frequency and parameters of the body, one can conclude that the value of $WBA - SAR_{cyl}$ in Eq. (9) depends on three parameters L_1, L_2, L_3 [22]. These parameters can be used either as optimization ones or they can be used for the validation of the model when compared with other approaches, for example, the FDTD-method, proposed in [24]. The other important role of these parameters is the application towards the determination of the resonant frequencies providing the extrema of SAR [22, 25–28].

Equipment for Measurement of EM Field Strength

The equipment for measurement of EM field characteristics consists of a receiving-transmitting antenna of pin type, allowing operation in the range of frequencies 900 GHz, 1800 GHz, and 2450 GHz. The spectrum analyzer SA6 with the standard input impedance of 50 Ohm, operating in a range up to 6GHz is considered as a source of high-frequency radiation. The frequency range of a built-in tracking generator from 35 MHz up to 6.2 GHz allows the evaluation of the 4G/5G working frequency range. The noise floor is not less than -90 dBm , this provides the visible difference between active signals and noise, and the value of error attenuation is not greater than 8 dB . The attractive frequency characteristics of the device are the following: frequency

range: from 1 Hz to 4.4 GHz (RF Preamp Off); 500 kHz to 4.4 GHz (RF Preamp On); internal frequency reference accuracy: ± 1 ppm; counter accuracy: $\pm (1 \text{ Hz} + \text{time base error})$; resolution bandwidth: 0.1 Hz to 250 kHz and 5 MHz. The above parameters allow the carrying out of measurements with an accuracy sufficient for many practical applications. The receiving-transmitting antenna with the connected generator is shown in Fig. 2.



FIG. 2. The receiving-transmitting antenna with the generator SA6

The receiving antenna array consisting of four microstrip antennas is used for reception of signals. It is connected to the spectrum analyzer by the standard 50 Ohm SMA RG316 RF cable, and the spectrum analyzer is connected to a PC by a USB 2.0 port. The setup for fixing the input radiation is shown in Fig. 3.

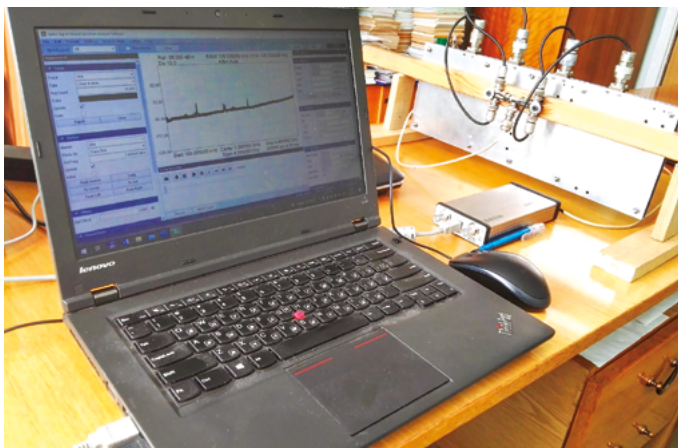


FIG. 3. The setup for measurement of the spectral EM field characteristics

Conclusions

The analytical formulas for calculation of the SAR absorbed by the human body are derived in the framework of the equivalent cylindrical monopole antenna model. The simple analytical formula for the SAR is derived that allows for a simplification of the procedure compared with experimental data. The experimental setup to extract the spectral frequency radiation and getting the SAR values in the range of 4G operators is elaborated. It consists of the spectrum analyzer USB-SA44B supplemented by the respective software, a notebook for analysis of signals, a transmitting-receiving antenna array, a transmitting antenna, and a SA6 signal generator that is used for measurements. The setup was calibrated using the signal generator, and it demonstrates the possibility to extract the spectral characteristics of radiation in a range from GPS to 4G operator frequencies. The perspective of approach is the determination of the resonance frequencies supplemented by the maximal values of the SAR and the verification of the obtained values using the developed experimental setup.

References

1. Kuster N., Balzano Q., Lin J.C., 1997, *Mobile Communications Safety (Telecommunications Technology & Applications Series)*, London: Springer.
2. Hyland G.J., 2000, *Physics and biology of mobile telephony*, Lancet, 356(9244), 1833–1836. DOI: 10.1016/s0140-6736(00)03243-8.
3. Ishihara T., Yamazaki K., Araki A. et al., 2020, *Exposure to Radiofrequency Electromagnetic Field in the High-Frequency Band and Cognitive Function in Children and Adolescents: A Literature Review*, International Journal of Environmental Research and Public Health, 17(24), # 9179. DOI: 10.3390/ijerph17249179.
4. Liang P., Li Z., Li J. et al., 2023, *Impacts of complex electromagnetic radiation and low-frequency noise exposure conditions on the cognitive function of operators*, Frontiers in Public Health, 11, # 1138118. DOI: 10.3389/fpubh.2023.1138118.
5. International Commission on Non-Ionizing Radiation Protection, 1998, *Guidelines for limiting exposure to time-varying electric, magnetic, and electromagnetic fields (up to 300 GHz)*, Health Physics, 74, 494–522.
6. Zhu Y., Gao F., Yang X. et al., 2008, *The effect of microwave emission from mobile phones on neuron survival in rat central nervous system*, Progress In Electromagnetic Research, 82, 287–298.
7. Repacholi R.M., 1998, *Low-level exposure to radiofrequency electromagnetic fields: health effects and research needs*, Bioelectromagnetics, 19, 1–19.
8. Nylund R., Leszczynski D., 2004, *Proteomics analysis of human endothelial cell line EA.hy926 after exposure to GS M900 radiation*, Proteomics, 4(5), 1359–1365. DOI: 10.1002/pmic.200300773.
9. Sarimov R., Malmgren L.O.G., Marková E. et al., 2004, *Nonthermal GSM microwaves affect chromatin conformation in human lymphocytes similar to heat shock*, IEEE Transactions on Plasma Science, 32(4), 1600–1608. DOI: 10.1109/TPS.2004.832613.
10. Buttiglione M., Roca L., Montemurno E. et al., 2007, *Radiofrequency radiation (900 MHz) induces Egr-1 gene expression and affects cell-cycle control in human neuroblastoma cells*, Journal of Cellular Physiology, 213(3), 759–767. DOI: 10.1002/jcp.21146.

11. Moustafa Y.M., Moustafa R.M., Belacy A. et al., 2001, *Effects of acute exposure to the radiofrequency fields of cellular phones on plasma lipid peroxide and antioxidant activities in human erythrocytes*, Journal of Pharmaceutical and Biomedical Analysis, 26(4), 605–608. DOI: 10.1016/S0731-7085(01)00492-7.
12. Hossmann K.A., Hermann D.M., 2003, *Effects of Electromagnetic Radiation of Mobile Phones on the Central Nervous System*, Bioelectromagnetics, 24, 49–62. DOI: 10.1002/bem.10068.
13. Tattersall J.E., Scott I.R., Wood S.J. et al., 2001, *Effects of low intensity radiofrequency electromagnetic fields on electrical activity in rat hippocampal slices*, Brain Research Journal, 904(1), 43–53. DOI: 10.1016/S0006-8993(01)02434-9.
14. Beason R.C., Semm P., 2002, *Responses of neurons to an amplitude modulated microwave stimulus*, Neuroscience Letters, 333(3), 175–178. DOI: 10.1016/S0304-3940(02)00903-5.
15. Foster K.R., Schwan H.P., 1989, *Dielectric properties of tissues and biological materials. A critical review*, Critical Reviews in Biomedical Engineering, 17(1), 25–104.
16. Gabriel S., Lau R., Gabriel G., 1996, *The dielectric properties of biological tissues: III. Parametric models for the dielectric spectrum of tissues*, Physics in Medicine and Biology, 41(11), 2271–2293.
17. King R.W.P., Wu T.T., 1966, *The imperfectly conducting cylindrical transmitting antenna*, IEEE Transactions on Antennas and Propagation, 14(5), 524–534.
18. Taylor C.D., Charles W.H., Eugene A.A., 1967, *Resistive receiving and scattering antenna*, IEEE Transactions on Antennas and Propagation, 15(3), 371–376.
19. Hirata A., K. Yanase, I. Laakso et al., 2012, *Estimation of the whole-body averaged SAR of grounded human models for plane wave exposure at respective resonance frequencies*, Physics in Medicine and Biology, 57(24), 8427–8436.
20. Hirata A., Fujiwara O., Nagaoka T. et al., 2010, *Estimation of whole-body average SAR in human models due to plane-wave exposure at resonance frequency*, IEEE Transactions on Electromagnetic Compatibility, 52(1), 41–48.
21. Yanase K., Hirata A., 2011, *Effective resistance of grounded humans for whole-body averaged SAR estimation at resonance frequencies*, Progress In Electromagnetics Research B, 35, 15–27.
22. Kibret B., Teshome A.K., Lai D.T.H., 2015, *Cylindrical antenna theory for the analysis of whole-body averaged specific absorption rate*, IEEE Transactions Antennas on Propagation, 63(11), 5234–5229.
23. Dimbylow P.J., 1997, *FDTD calculations of the whole-body averaged SAR in an anatomically realistic voxel model of the human body from 1 MHz to 1 GHz*, Physics in Medicine and Biology, 42(3), 479–490.
24. Dimbylow P., 2005, *Resonance behaviour of whole-body averaged specific energy absorption rate (SAR) in the female voxel model*, NAOMI, Physics in Medicine and Biology, 50(17), 4053–4068.
25. 5G, 4G, 3G Small Cell Tower Radiation Health Effects Science, <https://ehtrust.org/5g-4g-3g-small-cell-tower-radiation-health-effects-science/> [accessed 7.01.2023].
26. Betta G., Capriglione D., Cerro G. et al., 2022, *Measurements of Human Exposure to EMF from 4G systems: some experimental issues in urban environments*, IOP Conference Series: Materials Science and Engineering, 1254, # 012014. DOI: 10.1088/1757-899X/1254/1/012014.
27. Levitt B., Lai H., Manville A., 2021, *Effects of non-ionizing electromagnetic fields on flora and fauna, part 1. Rising ambient EMF levels in the environment*, Reviews on Environmental Health, 37(1), 81–122. DOI: 10.1515/reveh-2021-0026.
28. Deaconescu D.B., Buda A.M., Vatamanu D. et al. 2022, *The Dynamics of the Radiated Field Near a Mobile Phone Connected to a 4G or 5G Network*, Engineering, Technology & Applied Science Research, 12(1), 8101–8106. DOI: DOI: 10.48084/etasr.4670.

1.2. Development of HDL Models of Heterogeneous Microsystems for Behavioral Level of Computer-Aided Design

*Andriy Holovatyy¹, Mykhaylo Lobur², Kostyantyn Kolesnyk³,
Andriy Kernyskyy⁴, Vladyslav Vichkovskyy⁵, Andriy Yazh⁶*

*Lviv Polytechnic National University, Institute of Computer Sciences and Information Technologies,
Department of Computer-Aided Design Systems,*

¹andrii.i.holovatiy@lpnu.ua, ²mykhaylo.v.lobur@lpnu.ua,

³kostyantyn.k.kolesnyk@lpnu.ua, ⁴andriy.b.kernyskyy@lpnu.ua,

⁵vladyslavvichkovskyy@gmail.com, ⁶andrii.yazh.knm.2018@lpnu.ua

Summary: In this paper, HDL models of heterogeneous sensor microsystems are developed. The developed models make it possible to perform the behavioral simulation of MEMS comb-drive capacitive and piezoresistive accelerometers, MEMS accelerometer with delta-sigma ADC and also to conduct the analysis of such heterogeneous microsystems as MEMS at the functional design level.

Keywords: Micro-Electro-Mechanical Systems (MEMS); heterogeneous microsystems; MEMS crab-leg resonator; comb-drive capacitive microaccelerometer; piezoresistive MEMS accelerometer; sigma-delta control; VHDL-AMS; Verilog-AMS; hAMSter; SMASH; computer-aided design

Introduction

The development of microelectronics and micromechanics technologies made it possible to create a qualitatively new class of devices called microelectromechanical systems (MEMS). The MEMS feature is the combination of both electronic control and signal processing circuits (microprocessor part) and mechanical elements (microsensors, microactuators, micromotors, etc.) in one integrated microcircuit. Among MEMS, a separate group of inertial sensors. Such inertial sensors include integral accelerometers. MEMS accelerometers can be classified according to the physical effect used in the sensing mechanism: capacitive, piezoresistive, piezoelectric, electrochemical, optical, thermal, etc. [1–4]. In Fig. 1–2, sensitive elements of MEMS comb-drive capacitive and piezoresistive accelerometers are shown.

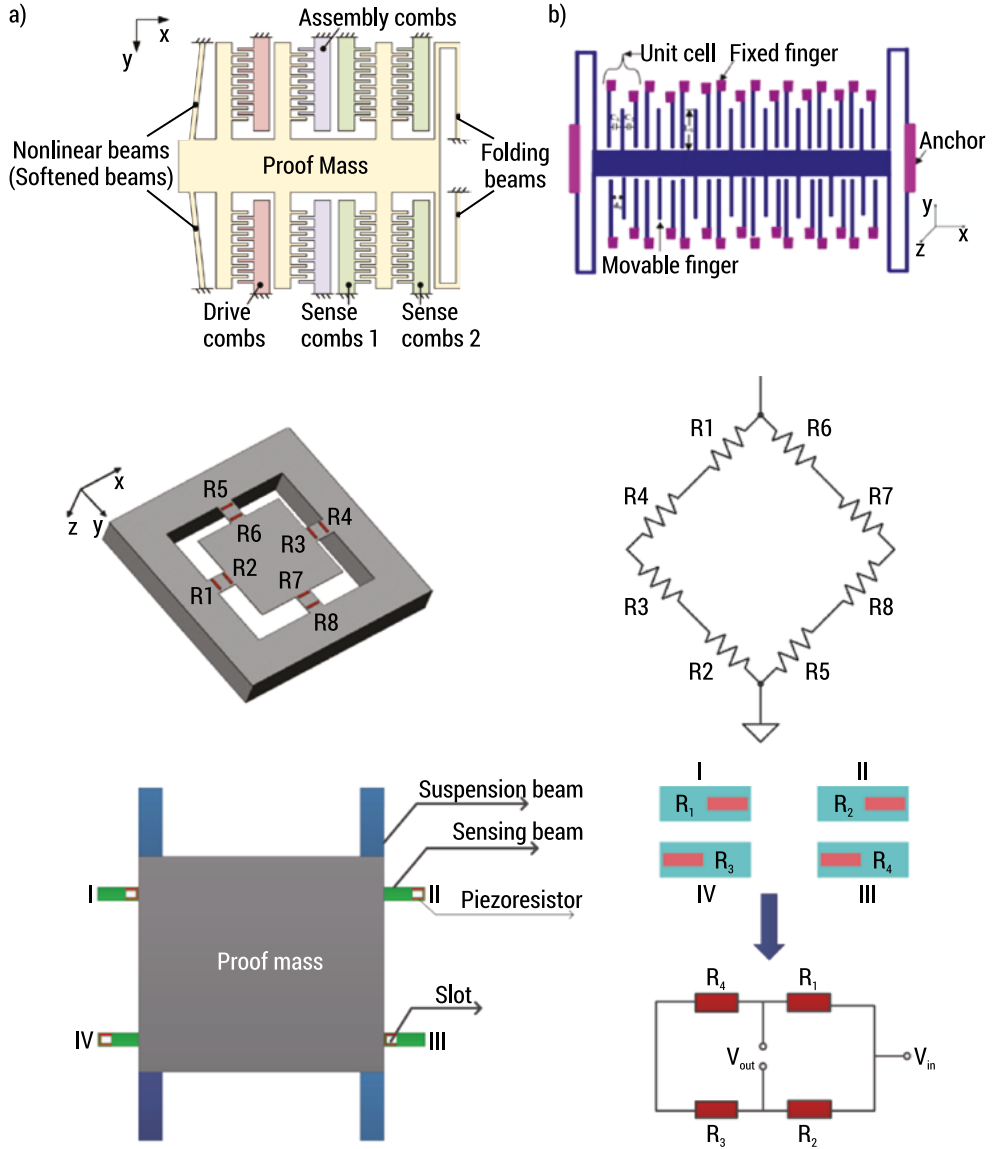


FIG. 1. Sensitive element of MEMS comb-drive capacitive accelerometer (a) and MEMS piezoresistive accelerometer (b). Piezoresistors are connected to the Wheatstone bridge to measure acceleration

The motion microsensors play an important role in modern technology and are widely used in cars (anti-lock ABS systems, anti-skid systems, active suspension systems, anti-theft systems); in consumer electronics (inertial navigation, smartphones, tablets, laptops, video game consoles, stabilization systems in photo and video cameras, hard disk protection systems against possible damage in the event of sudden accelerations atypical for their normal operation); sports equipment (trainers, pedometers);

geophysical application (earthquake monitoring systems); monitoring systems of engineering structures (machines, bridges), military industry (high-tech weapons, airplanes, helicopters, unmanned aerial vehicles, ground robotic complexes and systems), etc.

The MEMS production, improvement of their technical and operational characteristics, reduction of the full cycle of introduction of new products is determined by the automation of both the design of integrated devices and the technological process of their production.

The design process of MEMS when using modern technologies requires the simultaneous optimization of the technological process, the design of the integrated device and the functional circuit, therefore the optimization of MEMS is an integral part of the modern production process of integrated devices. Works related to the development of mathematical and behavioral models in the languages VHDL-AMS, Verilog-AMS intended for the description of such complex heterogeneous systems as MEMS, is an urgent issue today for the automation of their design.

Development of HDL MODELS of Heterogeneous Microsystems

The MEMS design involves the construction of behavioral models. The peculiarity of such models is that they contain data from various fields of science and technology. In particular, models of the MEMS sensors have values from mechanics, electricity and electronics. The hardware description languages such as VHDL-AMS (Very High-Speed Integrated Circuits Hardware Description Language Analog-Mixed Signals) and Verilog-AMS make it possible to create digital, analog and mixed behavioral models that use not only electrical signals, but also, in particular, mechanical ones [5–8]. In Fig. 2, listing of the behavioral model of the MEMS crab-leg resonator is shown.

```

module crableg1D (dy);
inout dy; kinematic_translational dy; velocity vy;
parameter real La = 1e-5; parameter real Lb = 1e-4; real density = 2330, E = 165e9, viscosity = 1.79e-5,
deff = 2e-6;
real h = 2e-6, w = 2e-6, Lp = 1e5; real m, b, k;
analog begin
m = density*h*(Lp^2+4*w*La); b = viscosity*Lp^2/deff; k = E*h*(w/Lb)^3*(4*Lb+La)/(Lb+La);
Vel(vy) <+ ddt(Disp(dy)); F(dy) <+ m*ddt(Vel(vy)) + b*Vel(vy) + k*Disp(dy);
end endmodule

```

FIG. 2. Verilog-AMS behavioral model of the MEMS crab-leg resonator

In Fig. 3 the fragment of the VHDL-AMS code of the behavioral model of MEMS piezoresistive accelerometer is shown.

```

`include "disciplines.vams" `include "constants.vams"

module sensitive_element (tmass, tmref, tetop, temid, tebot);

inout tmass, tmref, tetop, temid, tebot; kinematic tmass, tmref; electrical tetop, temid, tebot; velocity
cd_vel; acceleration cd_accel; electrical vdiff_tm, vdiff_bm, vdiff_dtm, vdiff_dbm; ecurrent i1, i2;

parameter real Wpm = 120u from (0:inf); parameter real Lpm = 450u from (0:inf); parameter real
T = 2u from (0:inf);

parameter real Ls = 176u from (0:inf); parameter real Ws = 2u from (0:inf); parameter real Lsf = 150u
from (0:inf);

parameter real Wsf = 2u from (0:inf); parameter real G = 1.5u from (0:inf); parameter integer Ns = 54
from (0:inf);

parameter real Vm = 300.0m from (0:inf); parameter PHYS_RHO_POLY = 2330.0; parameter PHYS_E_
POLY = 170.0e9; real M, Kmechanical, Ke, K, D, A; real cd_pos; real dtm, dbm, ctm, cbm;

analog begin

M = PHYS_RHO_POLY*(Wpm*Lpm*T+Ns*Lsf*Wsf*T); Kmechanical = 4.0*PHYS_E_
POLY*Ws*Ws*Ws*T/(Ls*Ls*Ls); Ke = -1.0*Ns*(2.0*P_EPS0*Lsf*T*Vm*Vm)/(G*G*G); K =
Kmechanical*Ke; D = 14.4*Ns*1.85e-5*T*Lsf*Lsf*Lsf/(G*G*G); A = Lsf*T; cd_pos = Pos(tmass);
Vel(cd_vel) <+ ddt(Pos(tmass)); Acc(cd_accel) <+ ddt(Vel(cd_vel)); F(tmass, tmref) <+ K*cd_pos
+ D*Vel(cd_vel) + M*Acc(cd_accel); dtm = G + cd_pos; dbm = G - cd_pos; ctm = A*P_EPS0/dtm;
cbm = A*P_EPS0/dbm; V(vdiff_tm) <+ V(tetop, temid); V(vdiff_bm) <+ V(tebot, temid);

V(vdiff_dtm) <+ ddt(V(tetop, temid)); V(vdiff_dbm) <+ ddt(V(tebot, temid)); I(tetop, temid) <+
ctm*V(vdiff_dtm); I(i1) <+ I(tetop, temid); I(tebot, temid) <+ cbm*V(vdiff_dbm); I(i2) <+ I(tebot, temid);

end endmodule // sensitive_element

module applied_force(tmass, tref);

input tmass, tref; kinematic tmass, tref; parameter real Wpm = 120u from (0:inf); parameter real
Lpm = 450u from (0:inf); parameter real T = 2u from (0:inf); parameter real Lsf = 150u from (0:inf);
parameter real Wsf = 2u from (0:inf); parameter integer Ns = 54 from (0:inf); parameter PHYS_
RHO_POLY = 2330.0; parameter real accel = 5.0; parameter real freq = 100.0; real M;

analog begin

M = PHYS_RHO_POLY*(Wpm*Lpm*T+Ns*Lsf*Wsf*T); F(tmass, tref) <+
M*accel*9.81*sin(2*M_PI*freq*$abstime);

$bound_step(0.05/freq);

end endmodule

```

FIG. 3. Verilog-AMS behavioral model of the sensitive element of the comb-drive microaccelerometer

In Fig. 4 the fragment of the behavioral model of the MEMS piezoresistive accelerometer is shown, developed in the VHDL-AMS language.

```

library ieee, disciplines;
use disciplines.kinematic_system.all;
use disciplines.electromagnetic_system.all;
use ieee.math_real.all;
entity mems_piezoresistive_accelerometer is
end entity mems_piezoresistive_accelerometer;

architecture top_level of mems_piezoresistive_accelerometer is

    constant Lpm: real := 3500.0e-6; constant Wpm: real := 3500.0e-6; constant Tpm:
real := 300.0e-6; constant Lb: real := 1200.0e-6; constant Wb: real := 250.0e-6; constant Tb:
real := 35.0e-6; constant Lr: real := 100.0e-6; constant Wr: real := 20.0e-6; constant Tr: real := 2.0e-6;
constant D: real := 20.0e-6; constant RHO : real := 640.0; --2.0e-5;    constant PHYS_RHO: real
:= 2330.0;    constant PHYS_E: real := 160.0e9; constant PHYS_EPS0: real := 8.85e-12;
constant MU: real := 18.75e-6; constant BETA: real := 0.42; constant G: real := 120.6; constant GRAV:
real := 9.81; constant FREQ: real := 100.0; quantity m, k, c, aext: real; quantity z: displacement; quantity
vel: velocity; quantity eps_max, S: real; quantity R, deltaR, deltaLr, R1, R2, R3, R4: real; quantity I, I1, I2:
current; quantity Vad, Vac, Vcd, Vab, Vbd, Vcb, Vout: emf;

begin

m == PHYS_RHO*Wpm*Lpm*Tpm; k == (PHYS_E*Wb*Tb*Tb)/(Lb*Lb*Lb);
c == (MU*BETA*Lpm*Wpm*Wpm*Wpm)/(D*D*D); aext == 5.0 * GRAV * sin(2.0 * 3.14 * FREQ * now);
break z => 0.0, vel => 0.0; (z'dot) == vel; (vel'dot) == -k/m*z - c/m*vel + aext;

R == RHO*Lr/(Wr*Tr); eps_max == 1.5*m/(PHYS_E*Wb*Tb*Tb)*(Lb+Lpm/2.0)*vel'dot;
deltaR == R*G*eps_max; deltaLr == deltaR*Lr/(R*G); S == deltaR/(R*vel'dot); R1 == R-deltaR; R2 ==
R+deltaR; R3 == R-deltaR; R4 == R+deltaR; Vad == 5.0; I == Vad*(R1+R2)*(R3+R4)/(R1+R2+R3+R4); I1
== Vad/(R1+R2); I2 == Vad/(R3+R4); Vac == I1*R1; Vab == I2*R4; Vcd == I1*R2; Vbd == I2*R3; Vcb ==
Vcd - Vbd; Vout == Vcb;

end architecture top_level;

```

FIG. 4. VHDL-AMS behavioral model of MEMS piezoresistive acceleration sensor (accelerometer)

In Fig. 5. the fragment of the behavioral model of the integrated microaccelerometer with sigma-delta control developed in VHDL-AMS is presented.

```

library ieee, disciplines;

use disciplines.kinematic_system.all; use disciplines.electromagnetic_system.all; use ieee.math_real.all;

architecture behav of sensing_element is

quantity M: real; quantity K: real; quantity Kmechanical: real; quantity Ke: real; quantity D: real;
quantity Ff: real;

constant PHYS_RHO_POLY: real := 2330.0; constant PHYS_E_POLY: real := 170.0e9; constant PHYS_EPS0: real := 8.85e-12;

begin

M == PHYS_RHO_POLY*(Wpm*Lpm*T+(Ns+Nf)*Lsf*Wsf*T); Kmechanical == 4.0*PHYS_E_POLY*Ws*Ws*Ws*T/(Ls*Ls*Ls); Ke == -1.0*Ns*(2.0*PHYS_EPS0*Lsf*T*Vm*Vm)/(G*G*G);
K == Kmechanical*Ke; D == 14.4*(Ns+Nf)*1.85e-5*T*Lsf*Lsf*Lsf/(G*G*G); Ff == 0.5*Nf*PHYS_EPS0*Lff*T*(Vf1*Vf1-Vf2*Vf2)/(G2*G2); M*pos'DOT'DOT+D*pos'DOT+K*pos == M*ain+Ff;

end architecture behav;

architecture behavioral of compensator is

quantity vin across ip to electrical_ground; quantity vout across op to electrical_ground;

constant num : real_vector (1 to 2) := (Fz, 1.0); constant den : real_vector (1 to 2) := (Fp, 1.0);

begin vout == K * vin'ltf(num, den); end architecture behavioral;

architecture bhv of quantizer is

quantity vip across ip;

begin process(clk) begin

if(rising_edge(clk)) then

if vip > Fs then op <= '1'; else op <= '0'; end if; end if; end process;

end architecture bhv;

architecture bhv of DAC is

signal Fe : force := 0.0; quantity F through op1;

begin Fe <= 35.0E-6 when ip <= '0' else -35.0E-6; F == -Fe; end architecture bhv;

architecture sine of a_source is

```

```

begin op == MAG * sin(MATH_2_PI*FREQ*NOW); end architecture sine;

architecture testbench of test_ACCELEROMETER is
quantity a: acceleration; quantity d: displacement; quantity V1, V2, vp, vb, como: real; signal output:
std_logic;
begin

Acceleration: entity a_source(sine) generic map (MAG=>1.0*PHYS_GRAVITY, FREQ=>1000.0) port
map (op=>a);

Sensing: entity sensing_element generic map (Wpm=>120.0e-6, Lpm=>450.0e-6, T=>2.0e-6,
Ls=>176.0e-6, Ws=>2.0e-6, Lsf=>150.0e-6, Wsf=>2.0e-6, Lff=>150.0e-6, Wff=>2.0e-6, G=>1.3e-6,
G2=>1.3e-6, Ns=>54.0, Nf=>4.0, Vm=>1.0) port map (ain=>a, Vf1=>V1, Vf2=>V2, pos=>d);
Compensation: entity compensator_generic map (Fz=>5000.0, Fp=>250000.0) port map (ip=>vb,
op=>como); Q: entity quantizer generic map (Fs=>2048.0*256.0*2.0) port map (ip=>como,
op=>output);

DAC: entity DAC(bhv) port map (ip=>output, op1=>V1, op2=>V2);
end architecture testbench;

```

FIG. 5. VHDL-AMS model of the integrated microaccelerometer with sigma-delta control

Simulation of HDL Models

The results of the simulation of capacitive comb drive microaccelerometer carried out using the SMASH software of the Dolphin Integration company [9] are graphically presented in Fig. 6 with a sinusoidal change in the external acceleration of 5g. From the obtained results, it can be seen that the change in the output voltages on the plates of capacitors C1 and C2 lies in the range from –300 mV to 300 mV. The currents flowing through capacitors C1 and C2 change in antiphase with a frequency of 1 MHz and an amplitude of 2.5 pA. Therefore, with such design parameters of the sensitive element of the integrated capacitive microaccelerometer, precision amplifiers and highly sensitive circuits for processing such signals are necessary.

The developed Verilog-AMS model of a micromechanical sensing element of a comb design for an integrated capacitive microaccelerometer allows the simulation of the response of a micromechanical sensing element to an applied acceleration. Namely, changing the capacities of its comb drive, output voltages and currents for given input design parameters, as well as analyzing the mechanical component of the integrated device at the behavioral level of automated design.

The simulation of piezoresistive microaccelerometer is performed using hAM-Ster software [10] and are graphically presented in Fig. 7–8 with a sinusoidal change in external acceleration of 5g. From the obtained results, it can be seen that the change in the output voltage of the Wheatstone measuring bridge lies in the range from –67 μ V

to 67 μV . Therefore, with such design parameters of the sensitive element of MEMS piezoresistive accelerometer, precision amplifiers and highly sensitive circuits for processing such signals are necessary.

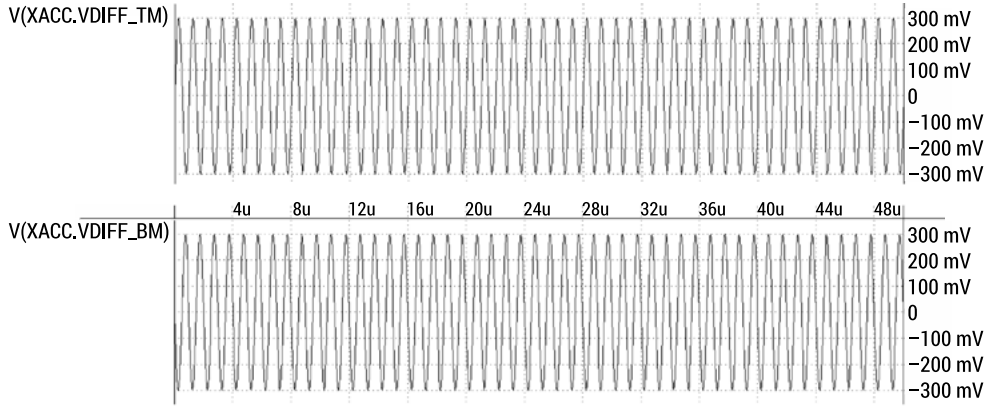


FIG. 6. Change in the output voltages on the plates of the upper capacitor C1 and the lower capacitor C2

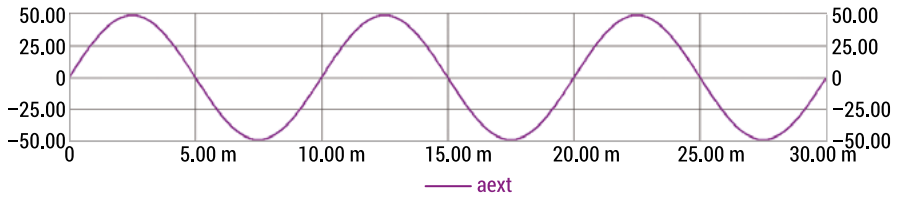


FIG. 7. External acceleration change a_{ext}

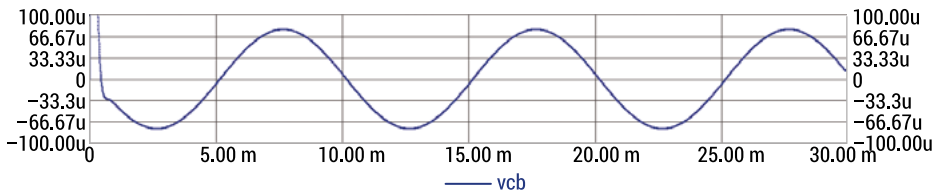


FIG. 8. Output voltage change V_{out}

The developed VHDL-AMS model makes possible to simulate dynamic characteristics of the integrated capacitive microaccelerometer, signal processing and digitizing, simulation of force feedback control using sigma-delta technique on the applied force of acceleration. The simulation results at the applied sinusoidal acceleration 1 g are graphically illustrated in Fig. 9.

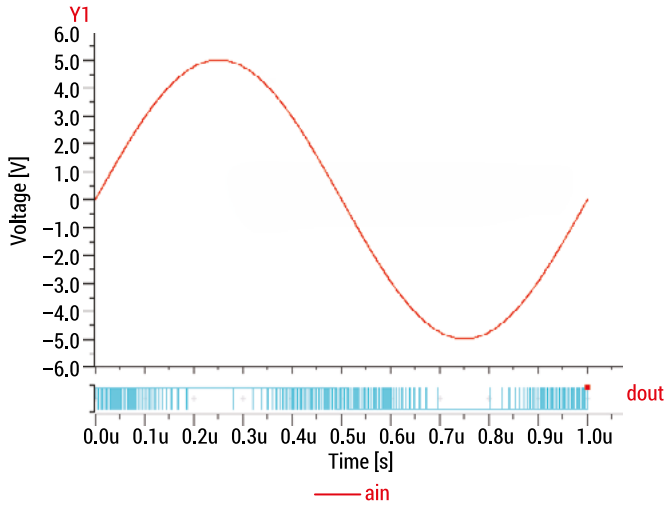


FIG. 9. Simulation results of microaccelerometer with sigma-delta control

A VHDL-AMS model of a microaccelerometer with sigma-delta control for computer-aided design has been developed. The created model has made possible the simulation of dynamic characteristics of the integrated capacitive microaccelerometer, signal processing and digitizing, simulation of force feedback control using sigma-delta technique on the applied force of acceleration and also the performance of analysis of the device at the behavioral level of computer-aided design.

Conclusions

On the basis of the performed research, the scientific problem of developing HDL – models of heterogeneous sensor microsystems for the behavioral level of automated design has been solved. The behavioral models of the sensitive element of MEMS comb-drive capacitive acceleration sensor, piezoresistive accelerometer, MEMS – accelerometer with sigma-delta control have been developed, and on their base the behavioral simulation and analysis of the operation of microsensors are carried out. The developed behavioral models can be used to implement the automated design subsystem of heterogeneous sensor microsystems.

References

1. Khir M.H., Qu P., Qu H., 2011, *A Low-Cost CMOS-MEMS Piezoresistive Accelerometer with Large Proof Mass*, Sensors, 11, 7892–7907. DOI:10.3390/s110807892.
2. Ranjith Kumar V., Bhaskar Y.B.N.V., Rajesh Kumar B. et al., 2014, *Design and Simulation of Piezoresistive MEMS Accelerometer*, International Journal of Education and Applied Research, 4(Spl 1), 126–131.

3. Sharma K., Macwan I.G., Zhang L. et al., 2008, *Design Optimization of MEMS Comb Accelerometer*, Proceedings of 2008 Zone, Conference of the American Society for Engineering Education.
4. Kaya T., Shiari B., Petsch K. et al., 2012, *Design of a MEMS Capacitive Comb-drive Accelerometer*, Proceedings of the 2011 COMSOL.
5. Ashenden P.J., 2004, *VHDL Tutorial*, Elsevier Science, USA.
6. IEEE Standard for VHDL Analog and Mixed-Signal Extensions – Packages for Multiple Energy Domain Support, in: IEEE Std 1076.1.1-2011 (Revision of IEEE Std 1076.1.1-2004), 2011, 1–30. DOI: 10.1109/IEEESTD.2011.5752649.
7. *Verilog-AMS Language Reference Manual. Analog & Mixed-Signal Extensions to Verilog-HDL, Version 2.1*, 2003, Accelera, Napa.
8. Verilog-AMS Language Reference Manual: <https://www.accellera.org/downloads/standards/v-ams>, <https://www.accellera.org/images/downloads/standards/v-ams/VAMS-LRM-2023.pdf>
9. SMASH Mixed-Signal Simulator: https://support.dolphin-design.fr/index.php/eda_solutions/products/smash/evolution_over_time.
10. hAMSter Software, http://www.theoinf.tu-ilmenau.de/~twangl/VHDL-AMS_online_en/download.html.

1.3. Behavioral Modelling and Simulation of Microelectromechanical Gyroscopes

*Andriy Holovaty¹, Andrzej Łukaszewicz², Wojciech Giernacki³,
Kostyantyn Kolesnyk⁴, Artur Pitsyshyn⁵, Andriy Yazh⁶*

Lviv Polytechnic National University, Department of Computer-Aided Design Systems:

¹andrii.i.holovaty@lpnu.ua, ⁴kostyantyn.k.kolesnyk@lpnu.ua,

⁵artur.pitsyshyn.mknit.2022@lpnu.ua, ⁶andrii.yazh.mknsp.2022@lpnu.ua,

Bialystok University of Technology, Department of Machinery Design and Operation,

Faculty of Mechanical Engineering, ²a.lukaszewicz@pb.edu.pl

Poznan University of Technology, Institute of Robotics and Machine Intelligence, Faculty of Control,

Robotics and Electrical Engineering, ³wojciech.giernacki@put.poznan.pl

Summary: In this paper, behavioral modelling and simulation of the microelectromechanical tuning fork and comb-drive gyroscopes (MEMS angular velocity sensors) have been performed. The models of MEMS angular velocity sensors are developed that make it possible to simulate capacitance changes, output voltages and currents depending on the applied angular velocity and also to perform the behavioral analysis of integrated devices.

Keywords: Micro-Electro-Mechanical Systems (MEMS); integrated angular velocity microsensor; angular velocity; Coriolis force; computer-aided design; VHDL-AMS, hAMster

Introduction

Integrated devices for measuring angular velocity are called gyroscopes. The development of microelectronics technologies makes it possible to create qualitatively new gyroscopes – micromechanical. Such devices include the control and measurement circuits and mechanical moving elements in one chip.

The Microelectromechanical (MEMS) gyroscope is one of the most complex devices manufactured using modern MEMS technologies. Depending on the field of application, manufacturers design MEMS gyroscopes with various sufficient technical characteristics [1–4].

In order to effectively design MEMS devices, increase their variety, quality and reliability, and obtain the specified technical characteristics, various computer models are created by means of application software such as ANSYS, CoventorWare, NODAS, Cadence, MATLAB, hAMster (VHDL-AMS) [5] and others.

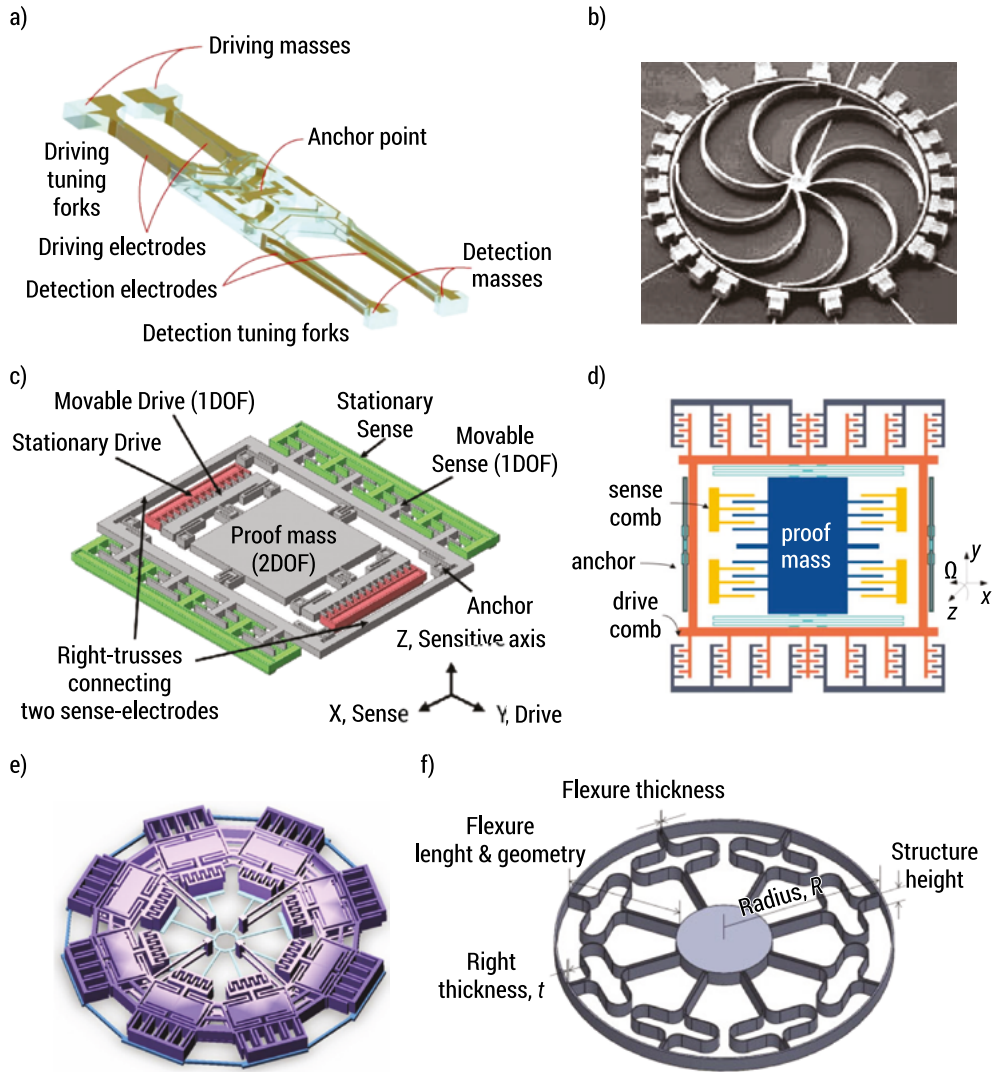


FIG. 1. Different constructions of MEMS gyroscopes

Development of Behavioral Models of Microelectromechanical Gyroscopes (MEMS Angular Velocity Sensors)

The movement of the sensitive element of the MEMS gyroscope can be described by the system of the second order differential equations:

$$m \frac{d^2 x}{dt^2} + c_x \frac{dx}{dt} + k_x x = F_0 \sin(\omega t) \quad (1)$$

$$m \frac{d^2 z}{dt^2} + c_z \frac{dz}{dt} - 2m\Omega \frac{dx}{dt} + k_z z = 0 \quad (2)$$

where m – sensitive element mass; c_x and c_z – damping coefficients on x - and z – directions, respectively; k_x and k_z – spring constants of the beams on x - and z – directions, respectively (Fig. 2).

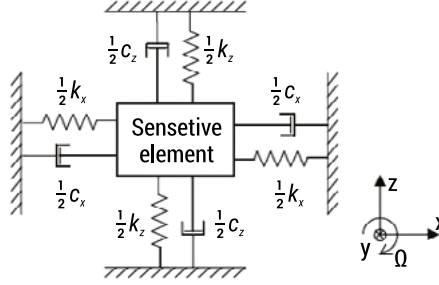


FIG. 2. Schematic view of the model “sensitive element-spring-damper” (where c_x, c_z – damping coefficients, k_x, k_z – spring constants of the spring elements on x - and z -direction respectively)

The sensitive element (rotor), substrate and cover (stators) of the sensor have deposited electrodes. The electrodes form a differential capacitor (Fig. 3). Capacitances of the differential capacitor C_1 and C_2 change when the sensitive element vibrates in the direction of z -axis.

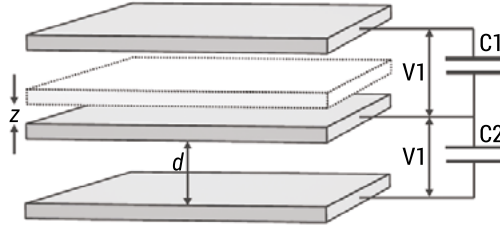


FIG. 3. Differential capacitor formed by the electrodes deposited on the mechanical sensitive element (rotor), substrate and cover (stators) of the sensor

$$C_1 = C_2 \text{ at } \Omega = 0 \text{ and } C_2 - C_1 \neq 0 \text{ at } \Omega \neq 0$$

Capacitances of the differential capacitor C_1 and C_2 can be calculated by the formulas:

$$C_1 = \epsilon_0 \epsilon_r S \frac{1}{d+z} = C_0 - \Delta C \quad (3)$$

$$C_2 = \epsilon_0 \epsilon_r S \frac{1}{d-z} = C_0 + \Delta C \quad (4)$$

where S – area of the capacitor electrode plate; ε_r – environment dielectric permeability between capacitor plates; ε_0 – vacuum dielectric permeability; d – distance between capacitor plates at $\Omega = 0$; z – sense vibrations of the sensitive element.

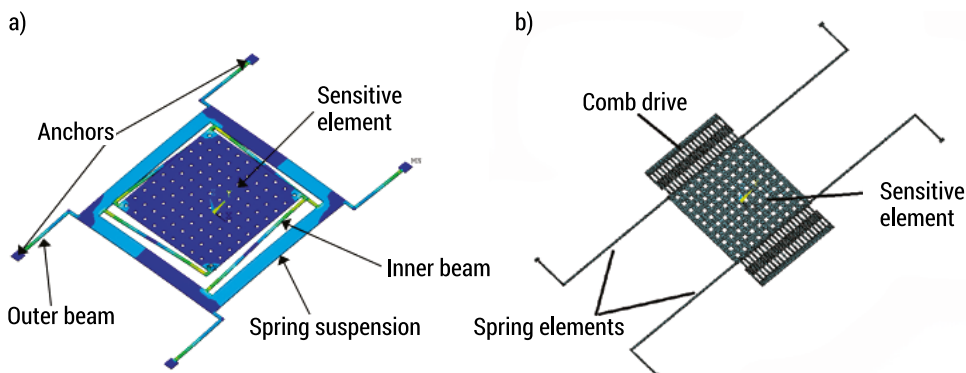


FIG. 4. CAD models of MEMS tuning fork (a) and comb-drive (b) gyroscopes

The MEMS device design at the computer-aided design involves creation of behavioral model. The peculiarity of the behavioral model is that it contains data from various fields of science and technology. In particular, the behavioral model of the MEMS gyroscope model (behavioral model of angular velocity sensor) has mechanical and electrical parts. To develop such models, special hardware description languages are used. One such HDL is VHDL-AMS which is used to develop mixed-signal behavioral models [6–8]. The fragment of the VHDL-AMS model of MEMS tuning fork gyroscope sensitive element is shown in Fig. 5.

```
library ieee;
```

```
library disciplines;
```

```
use disciplines.kinematic_system.all;
```

```
use disciplines.electromagnetic_system.all;
```

```
use disciplines.rotational_system.all;
```

```
use ieee.math_real.all;
```

```
entity sensitive_mass is
```

```
generic (m : real := 0.29e-9;
```

```
cx : real := 4.95e-5;
```

```
cy : real := 4.95e-5;
```

```
kx : real := 1.8786; --2.6455;
```

```

ky : real := 1.8786;
A : real := 320.0e-6*400.0e-6;
d0 : real := 1.5e-6; -- 7.0e-6
port (terminal proof_mass, ref : kinematic;
terminal top_el, bot_el : electrical);
end entity sensitive_mass;

architecture behav of sensitive_mass is
quantity vel_x : velocity;
quantity q : charge;
quantity disp : displacement;
quantity C : real; -- capacitance
quantity pos_x across force through proof_mass to ref;
quantity omega : angular_velocity; -- rad/s
quantity acor : acceleration;
quantity pos_y : displacement;
quantity v across i through top_el to bot_el;
constant eps : real := 1.0;
constant eps0 : real := 8.85419e-12;
begin
vel_x == pos_x'dot;
force == kx*pos_x + cx*pos_x'dot + m*vel_x'dot;
omega == 1.0*MATH_PI/180.0; --* cos(MATH_2_PI*100.0*NOW); -- omega in degree/sec is converted
into radian/second
pos_y == (- cy*pos_y'dot - m*pos_y'dot'dot - 2.0*m*vel_x*omega)/ky;
acor == - 2.0*vel_x*omega;
disp == d0 - pos_y;
C == eps*eps0*A/disp;
q == C*v;
i == q'dot;
end architecture behav;

```

FIG. 5. VHDL-AMS model of microelectromechanical tuning fork gyroscope

The fragment of the developed VHDL-AMS model of MEMS comb drive gyroscope is shown in Fig. 6. Using it the displacement, changes in Coriolis acceleration, capacitance and current depending on the applied angular velocity can be simulated.

----- Behaviour of sensitive mass of MEMS Comb Drive Gyroscope -----

```
library ieee;
library disciplines;

use disciplines.kinematic_system.all;
use disciplines.electromagnetic_system.all;
use disciplines.rotational_system.all;
use ieee.math_real.all;

entity sensitive_mass is
generic (m : real := 0.29e-9; -- SE mass
dy : real := 4.95e-6; -- damping coefficient along y
dz : real := 4.95e-5; -- damping coefficient along z
ky : real := 1.8786; --2.6455; -- spring coefficient along y
kz : real := 1.8786; -- spring coefficient along z
A : real := 320.0e-6*400.0e-6; -- area of electrode
d0 : real := 1.5e-6; -- 7.0e-6 -- distance between electrodes
port (terminal proof_mass, ref : kinematic;
terminal top_el, mid_el, bot_el : electrical);
end entity sensitive_mass;

architecture behav of sensitive_mass is
quantity pos_y across force through proof_mass to ref;
quantity vel_y : velocity;
quantity omega : angular_velocity; -- rad/s
quantity pos_z : displacement;
--quantity coriolis_force : force;
quantity dtm, dbm : displacement;
quantity ctm, cbm : real; -- capacitance
quantity vtm across itm through top_el to mid_el;
```



```

quantity vbm across ibm through bot_el to mid_el;
quantity qtm, qbm : charge;
constant eps : real := 1.0;
constant eps0 : real := 8.85419e-12;
begin
vel_y == pos_y'dot;
force == ky*pos_y + dy*pos_y'dot + m*vel_y'dot;
omega == 150.0*MATH_PI/180.0;-- * cos(MATH_2_PI*100.0*NOW); -- omega in degree/sec
is converted into radian/second
pos_z == (- dz*pos_z'dot - m*pos_z'dot'dot - 2.0*m*vel_y*omega)/kz;
--coriolis_force == 2.0*m*vel_y*omega;
dtm == d0 + pos_z; dbm == d0 - pos_z;
ctm == eps*eps0*A/dtm; cbm == eps*eps0*A/dbm;
qtm == ctm*vtm; qbm == cbm*vbm;
itm == qtm'dot; ibm == qbm'dot;
end architecture behav;

-- gyroscope
library disciplines;
use disciplines.kinematic_system.all;
use disciplines.electromagnetic_system.all;

entity gyroscope is
end;

architecture behav of gyroscope is
terminal smass : kinematic;
terminal top, mid, bot : electrical;
begin
f1: entity exciting_force (sine) generic map (n => 20.0, volt => 15.0, t => 3.5e-6, gap => 1.5e-6, freq =>
10000.0) port map (smass, kinematic_ground);
--v1: entity vsorce (dc) generic map (mag_dc => 300.0e-6) port map (p => top, m =>
electrical_ground);
--v2: entity vsorce (dc) generic map (mag_dc => -300.0e-6) port map (p => bot, m =>
electrical_ground);

```

```

v1: entity vsource (sine) generic map (mag_ac => 300.0e-3, freq => 1000.0, mag_dc => 0.0) port map
(p => top, m => electrical_ground);

v2: entity vsource (sine) generic map (mag_ac => -300.0e-3, freq => 1000.0, mag_dc => 0.0) port map
(p => bot, m => electrical_ground);

a1: entity sensitive_mass (behav) generic map (m => 10.0*0.16e-9, ky => 2.6455, kz => 2.6455, dy
=> 4.0e-6, dz => 4.0e-6, A => 2.0e-6*110.0e-6, d0 => 1.0e-9) port map (proof_mass => smass, ref =>
kinematic_ground, top_el => top, mid_el => mid, bot_el => bot);

r1: entity resistor (behav) generic map (r_r => 300000.0) port map (p=> mid, m=>electrical_ground);

end;

```

FIG. 6. VHDL-AMS model of microelectromechanical comb-drive gyroscope

Simulation of Microelectromechanical Gyroscopes (MEMS Angular Velocity Sensors)

The obtained results of simulation of MEMS tuning fork gyroscope are shown in Fig. 7–13.

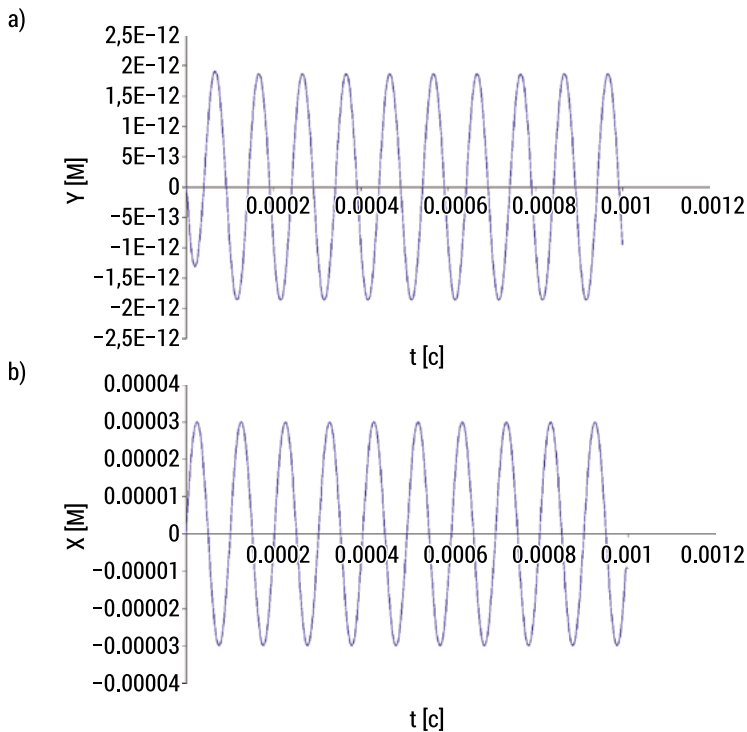


FIG. 7. Drive and sense oscillations of the sensitive element of MEMS tuning fork gyroscope caused by Coriolis force at $\Omega = 1^\circ/\text{s}$.

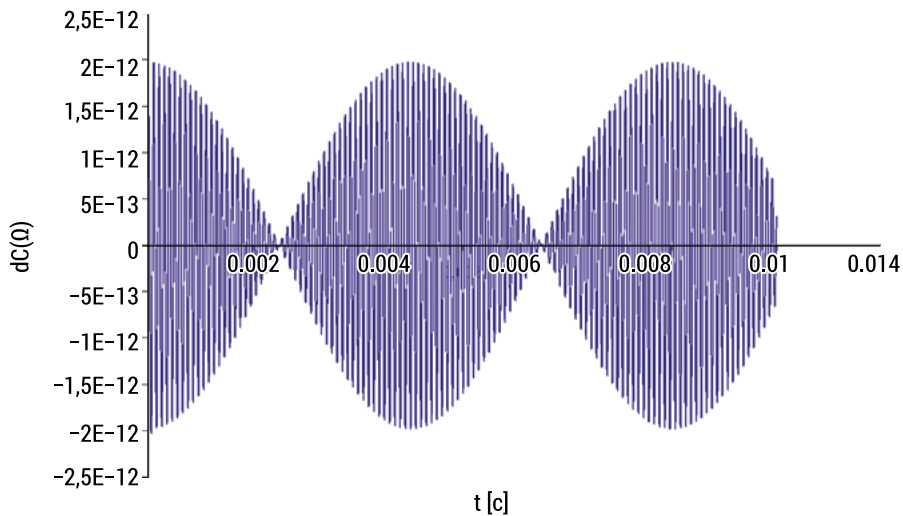


FIG. 8. Capacitance change at an angular velocity oscillations of $1^\circ/\text{s}$ and frequency of 100 Hz

The simulation results of MEMS comb-drive gyroscope are graphically presented in Fig. 9–10 at the applied angular velocity 10 degrees/sec.

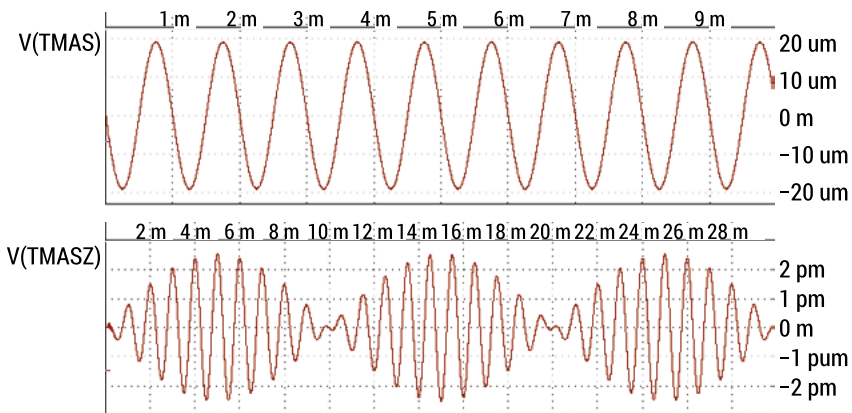


FIG. 9. Drive oscillations on x-direction and sense oscillations on z-direction of the sensitive element

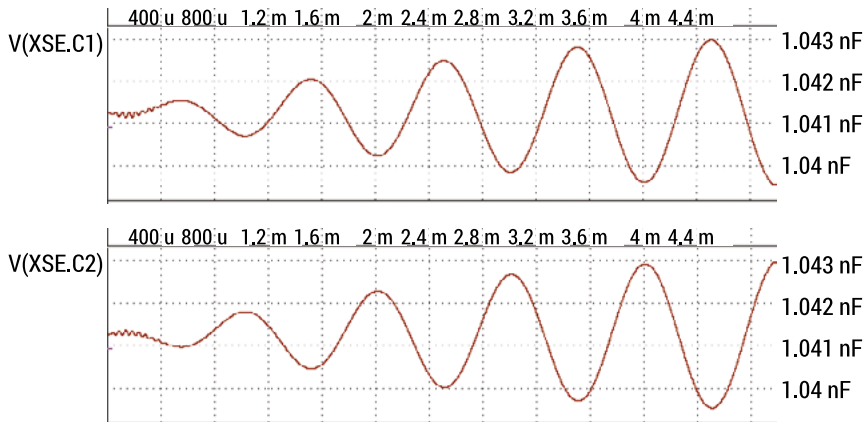


FIG. 10. Capacitance changes C_1 and C_2

Conclusions

VHDL-AMS models of MEMS tuning fork and comb-drive gyroscopes (MEMS angular velocity sensors) for computer-aided design have been developed. By using the developed models, the drive and sense oscillations of the sensitive element, capacitance changes, changes of output voltages and currents, and sensitivity of the mechanical module of the MEMS gyroscope depending on the applied angular velocity can be performed and also the behavioral analysis of the sensors can be conducted.

References

1. Nasiri S., 2000, *A Critical Review of MEMS Gyroscopes Technology and Commercialization Status*, 1–8.
2. Bernstein J., Cho S., King A.T. et. al., 1993, *A Micromachined Comb-Drive Tuning Fork Rate Gyroscope*, Proceedings IEEE Micro Electro Mechanical Systems, 143–148.
3. Geen J., Krakauer D., 2003, *New iMEMS Angular-Rate-Sensing Gyroscope*, Analog Dialogue, 37(3).
4. Lee Y., 2007, *A Study Of Parametric Excitation Applied To A MEMS Tuning Fork Gyroscope*, dissertation, University of Missouri-Columbia, 4–8.
5. ANSYS Simplorer and ANSYS Twin Builder multi-domain, multi-technology simulation programs: <https://simplorer.software.informer.com/7.0/>, <https://www.ansys.com/products/digital-twin/ansys-twin-builder>
6. Ashenden P.J., 2004, *VHDL Tutorial*, Elsevier Science, USA.
7. IEEE Standard for VHDL Analog and Mixed-Signal Extensions -- Packages for Multiple Energy Domain Support, in: IEEE Std 1076.1.1-2011 (Revision of IEEE Std 1076.1.1-2004), 2011, 1–30. DOI: 10.1109/IEEESTD.2011.5752649.
8. Christen E., Bakalar K., 1997, *VHDL 1076.1: Analog and Mixed-Signal Extensions to VHDL*, in: *Analog and mixed-signal hardware description languages*, eds. A. Vachoux, J.M. Bergé, O. Levia et al., Norwell, MA, Kluwer Academic Publishers, 19–41.

1.4. Hardware and Software Development for Vibration Monitoring System

Andriy Holovatyy¹, Vasyl Teslyuk², Sofia Holovata³, Marko Odynak⁴

Lviv Polytechnic National University, Institute of Computer Science and Information Technologies,

Department of Computer-Aided Design Systems, ¹andrii.i.holovati@lpnu.ua,

Department of Automated Control Systems, ²vasyl.m.teslyuk@lpnu.ua

Ukrainian National Forestry University, Institute of Woodworking, Computer Technology and Design,

Department of Information Technologies, ³sofi.pobereyko@nltu.edu.ua.

Lviv Polytechnic National University, Institute of Computer Science and Information Technologies,

Department of Computer-Aided Design Systems, ⁴marko.odynak.mknsp.2022@lpnu.ua.

Summary: The structure of the vibration acceleration spectrum monitoring system is developed which is based on the modular principle. Algorithms of the vibration acceleration spectrum monitoring system are developed, including the accelerometer calibration algorithm, the dynamic acceleration measurement algorithm, and the FFT algorithm. The software for processing the input information from accelerometers connected to a Raspberry Pi is developed, which enables multi-channel measurements and their analysis. The results of testing the built system are given, which make it possible to assert the correctness of the functioning of the developed system.

Keywords: vibration acceleration spectrum; monitoring system; vibration acceleration; spectral analysis; hardware and software; discrete Fourier transform; ADXL345 accelerometer, Raspberry Pi

Introduction

One of the most important parameters of any designed technical system is its reliability of functioning in adverse conditions. The source of such adverse conditions can be vibrations and shocks. Among all types of mechanical influences, vibration is the most dangerous for technical objects. Alternating stresses caused by vibration contribute to the accumulation of damage in materials, system design, and failure. The destruction of the object occurs quite quickly under vibrational influences under the conditions of resonance, at the same time, vibration causes a violation of the physiological and functional states of a person. The impact of vibration on a person depends on its spectral composition, direction of action, duration of exposure, as well as individual characteristics of the person [1].

Accordingly, vibration monitoring systems make it possible to solve numerous problems associated with vibrations that arise during the operation of various systems of technological equipment (mechanisms, machines, machines with CNC) [2, 3] and to minimize their impact on the human body [4]. Therefore, the development of systems designed for monitoring and analyzing vibrations of technical objects is an urgent issue today.

The purpose of this work is to develop a system for monitoring vibration accelerations, which is based on the modular principle, low cost of the technical solution and cross-platform software.

To achieve the specified goal, the following main tasks of the research have been defined:

- development of the structure of the vibration acceleration spectrum monitoring system, which is based on the modular principle and includes a microcontroller, accelerometer, liquid crystal graphic color display, flash memory, minicomputer monitor;
- development of operation algorithms for the vibration acceleration spectrum monitoring system, which includes an accelerometer calibration algorithm, a dynamic acceleration measurement algorithm, and a fast Fourier transform algorithm;
- software development for processing input information from several accelerometers connected to the Raspberry Pi, which will enable multi-channel measurements and their analysis;
- communication interface definition for data exchange between the ADXL345 accelerometer and the Raspberry Pi 3 Model B microcomputer;
- testing conduction of the developed vibration acceleration spectrum monitoring system.

The various scientific and technical articles are devoted to the development of vibration monitoring and analysis systems [5–8].

Structure and Information Support of the System for Vibration Acceleration Spectrum Monitoring

In Fig. 1 the developed structure of the vibration acceleration spectrum monitoring system is shown. It includes the following main components:

- Raspberry Pi 3 Model B single-board mini-computer, which is used for collecting and processing data from vibration sensors (accelerometers);
- three-axis digital accelerometer ADXL345 from Analog Devices, which is used as a vibration sensor;
- flash memory for installing the OS, drivers, software and saving data;
- 7" TFT display for outputting information from Raspberry Pi;
- wireless communication interfaces for remote information exchange with a PC.

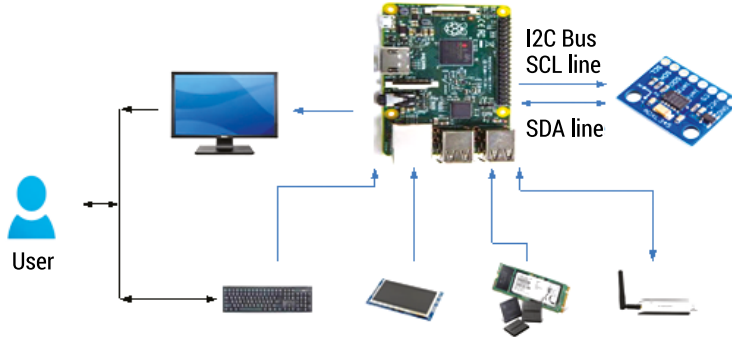


FIG. 1. Structure of the system for monitoring the vibration acceleration spectrum

The structure of the system can be formalized using a chart:

$$\text{System_structure} = \langle S_{IC}, S_{DPS}, S_{ID} \rangle \quad (1)$$

where S_{IC} is a set of components that refer to information collection means; S_{DPS} is a set of information collection, processing and saving means and S_{ID} is a set of information displaying means.

The set of means for collecting information about vibration acceleration includes an accelerometer.

The set of means of collecting, processing and saving data directly includes a minicomputer, flash memory, wireless communication interfaces, and other components. A method of displaying information is a minicomputer monitor. The developed structure is based on the modular principle, which ensures rapid modernization of the developed device. In the structure of the system shown in Fig. 1, the accelerometer is used for measuring vibration accelerations. The received values of vibration accelerations from the accelerometer are transmitted to a single-board minicomputer Raspberry Pi 3 Model B, which processes the received data using the developed software and transmits the processing results to the minicomputer monitor and graphic liquid crystal display.

Data exchange between the components of the structure must be implemented using standardized interfaces (buses), which makes it possible not to develop your own interface, avoid errors and save development time. Nowadays, there are several standard interfaces that are used for data exchange between equipment components. In particular, the I²C interface is one of the standardized and widely used for data exchange in embedded systems.

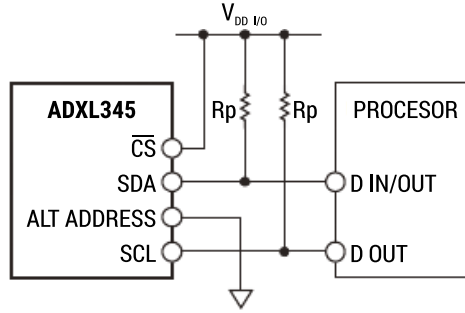


FIG. 2. Typical I²C connection diagram of the ADXL345 accelerometer to the Raspberry Pi mini-computer

Therefore, it is proposed to use the I²C bus to implement data exchange between the components of the vibration acceleration spectrum monitoring system. The use of the ADXL345 accelerometer and the Raspberry Pi 3 Model B microcomputer in the hardware implementation of the vibration acceleration spectrum monitoring system ensures a low price of the designed system.

Algorithms and Software of the System for Vibration Acceleration Spectrum Monitoring

The developed algorithm of the vibration acceleration monitoring system includes the following steps:

- Step 1. Initialization of the ADXL345 accelerometer on the I2C bus.
- Step 2. Reading the acceleration value from the ADXL345_DEVID register at address 0x00 and check the accelerometer number, which should be equal to ADXL345_ID 0xE5.
- Step 3. Setting up the ADXL345 accelerometer.
- Step 4. Transferring the acceleration sensor to the operating mode (write byte 0x00), set the bandwidth to 100 Hz (write byte 0x0A) using the function ADXL345_SetRegisterValue (ADXL345_BW_RATE, (0x00|ADXL345_RATE (0x0A))).
- Step 5. Defining the input data format, measurement range 16, interrupt, alignment of measured values using the function ADXL345_SetRegisterValue (ADXL345_DATA_FORMAT, (0x00|ADXL345_RANGE (ADXL345_RANGE_PM_16G)|ADXL345_FULL_RES))
- Step 6. Carrying out ADXL_NO_SAMPLES acceleration measurements (samples) along all three axes x, y, z with a step of $t_s = 1e6/F_s$ (where F_s is the sampling frequency) and their values in two-byte integer arrays of size 1024.
- Step 7. Calculation of the real values of accelerations a_x , a_y , a_z in the time interval from 0 to $1e6/F_s$ according to the formula $axx[i] \times g/LSB \times 9.80665$, xx is the measurement axis x, y or z. The g/LSB ratio when the FULL_RES bit is set = 1 in the mode with the maximum resolution is equal to 0.0039. Recording of the received values in defined arrays.

- Step 8. Writing the calculated acceleration values to the files `fp_samples_ax`, `fp_samples_ay`, `fp_samples_az`, `fp_samples_a`.
- Step 9. Call the function `adxl345_spectrum_analysis` (`ADXL_NO_SAMPLES`, `FS`) to calculate the Discrete Fourier Transform (DFT).
- Step 10. Recording of the received spectrum data in files and plotting graphs of the functions of the dependence of acceleration on time and spectra of vibration accelerations.
- Step 11. Completion of the algorithm. Otherwise, go to step 6.

The system uses the FFTW library to perform a fast Fourier transform [9]. The FFTW library is a set of modules in the C and Fortran for computing the Fast Fourier Transform (FFT). FFTW allows us to work with both real and complex numbers, with an arbitrary size of input data, that is, with a data length that is not necessarily a multiple of $2n$.

The driver and special software have been developed to communicate with the ADXL345 acceleration sensor (accelerometer). The driver reads the data from the accelerometer, processes it and adjusts the sensor according to the user's needs. The obtained values of accelerations for each axis are recorded respectively in `ax.dat`, `ay.dat` and `az.dat` files. The accelerometer driver was created in C using the wiring-Pi2C library and the gcc compiler [10].

Shell scripts `accel_plot.sh`, `spectrum_plot.sh`, `spectrum_plot_all.sh` have been written, which perform plotting. The software is developed under Raspbian Jessie OS. Raspbian is a free OS that is built on the Unix-like Debian OS optimized for the technical support of the Raspberry Pi mini-computer. The developed software provides the following operations: system user interface; data collection and analysis; saving data to files on a microSD memory card; visual presentation of data; network connection with a PC. The structural diagram of the software system is shown in Fig. 3.

In addition, the developed software enables a direct comparison of the relative intensity of each frequency component. The developed software processes input information from several accelerometers connected to the Raspberry Pi, which enables multi-channel measurements and their further analysis. The software records and stores vibration data from each channel for further analysis and comparison. This function enables the user to display the intensity of vibrations in real time, as well as view the contents of previously recorded files.

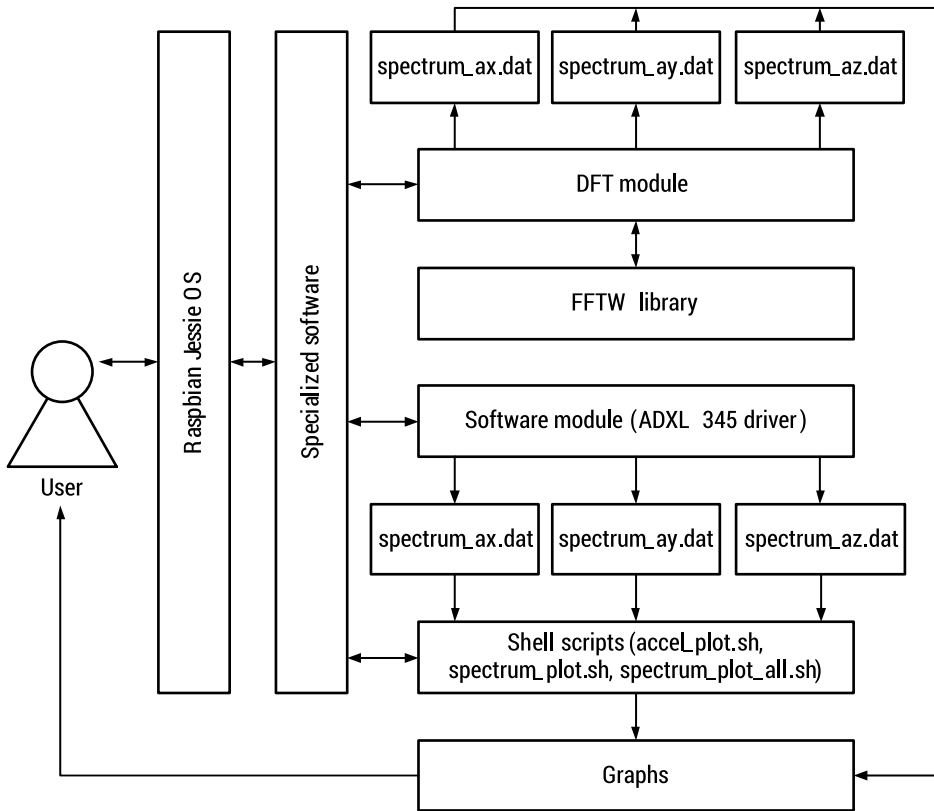


FIG. 3. Structural software diagram of the system for vibration acceleration spectrum monitoring

Research Results and Their Discussion

The research results are graphically depicted in Fig. 4–6. The analysis of the obtained results makes it possible to state that the largest peak of the vibration acceleration amplitudes. In Fig. 4 the graphs of the input vibration acceleration change along the Z-axis and all three axes are shown.

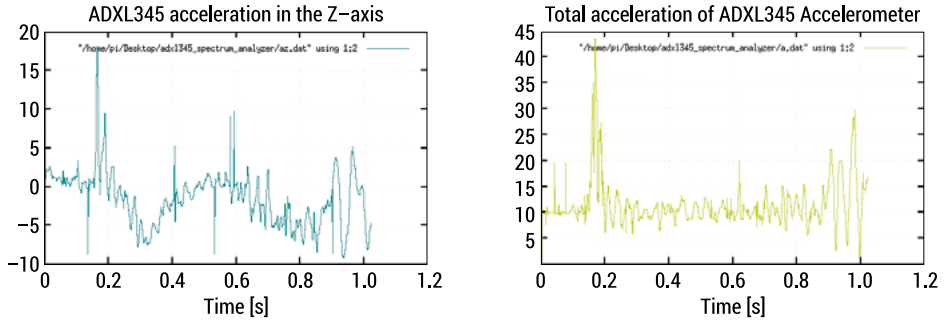


FIG. 4. Changing the output signals of the accelerometer acceleration along the Z axis and all three axes

Fig. 5 shows the spectrum of the vibration acceleration signals along the Z-axis and all three axes.

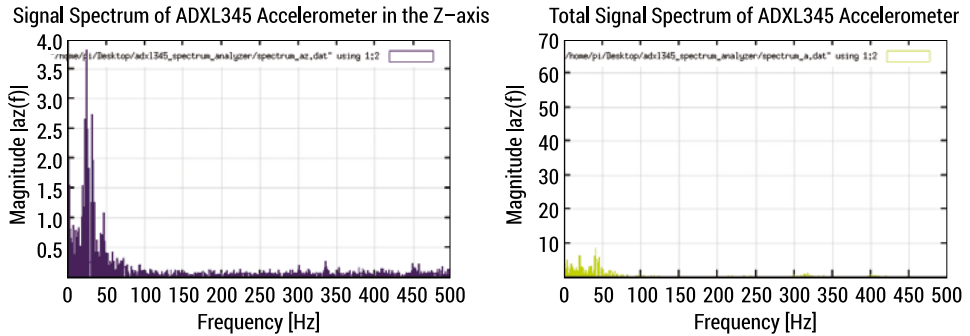


FIG. 5. Spectrum of the vibration acceleration signal along the Z-axis and all three axes

In Fig. 6 the output signals of vibration accelerations along the X-axis and all three axes during impact (shock) is shown.

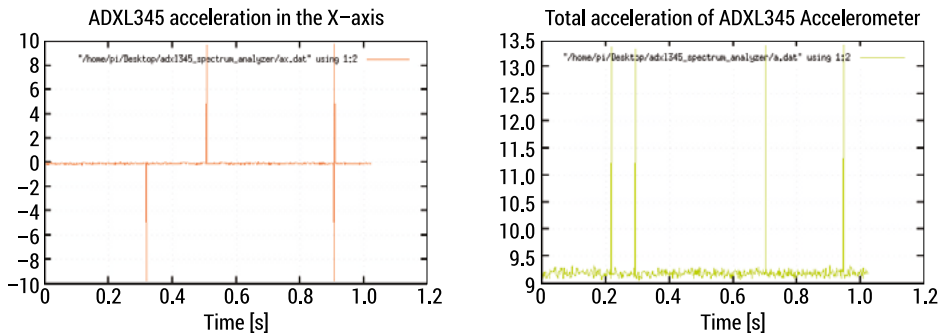


FIG. 6. Change in the output signals of the vibration acceleration along the X-axis and all three axes during impact

The obtained results make it possible to assert that the created system works correctly. The scientific novelty of the obtained research results consists in the development of a low-cost physical model of the vibration monitoring system. The practical significance of the research results lies in the development of the structural diagram of the system, the development of algorithms and software, the system for monitoring the spectrum of vibration accelerations, which ensures a low price of the technical solution.

Conclusions

1. The structure of the vibration acceleration monitoring system is developed, which is based on the modular principle and includes the Raspberry Pi 3 Model B mini-computer, ADXL345 accelerometer and graphical color LCD. The use of the ADXL345 accelerometer and Raspberry Pi mini-computer ensures a low price technical solution.
2. Algorithms for the vibration acceleration monitoring system operation have been developed, which includes the accelerometer calibration algorithm, dynamic acceleration measurement algorithm, and FFT algorithm.
3. The Raspberry Pi driver for communication with the ADXL345 accelerometers via I2C interface has been developed. Special software has been developed that processes input information from several accelerometers connected to the Raspberry Pi, which enables multi-channel measurements and their further analysis. The software records and stores vibration data from each channel for further analysis and comparison.

References

1. *Systemy monitoringu i kontroli wibracji*, <http://www.omative.com/КонтрольВибрации.html> [accessed: 15.05.2024].
2. Iwaniec M., Holovaty A., Teslyuk V. et al., 2017, *Development of vibration spectrum analyzer using the Raspberry Pi microcomputer and 3-axis digital MEMS accelerometer ADXL345*, XIIIth International Conference on Perspective Technologies and Methods in MEMS Design (MEMSTECH), 25–29.
3. Hjort A., Holmberg M., 2015, *Measuring Mechanical Vibrations using an Arduino as a slave I/O to an EPICS Control System*, FREIA Report, 4.
4. Holovaty A., Teslyuk V., Iwaniec M. et al., 2017, *Development of a system for monitoring vibration accelerations based on the raspberry pi microcomputer and the adxl345 accelerometer*, Eastern-European Journal of Enterprise Technologies, 6(9), 52–62.
5. Rață G., Rață M., 2014, *System for Monitoring and Analysis of Vibrations at Electric Motors*, International Journal of Emerging Technology and Advanced Engineering, 21(3), 97–104.
6. Milovančević M., Veg A., Makedonski A. et al., 2014, *Embedded systems for vibration monitoring*, Facta Universitatis. Mechanical Engineering, 12(2), 171–181.

7. Rocha S.M.S., Feiteira J.F.S., Mendes P.S.N. et al., 2016, *Method to Measure Displacement and Velocity from Acceleration Signals*, International Journal of Engineering Research and Applications, 6(6), 52–59.
8. Sekiya H., Kimura K., Miki C., 2016, *Technique for determining bridge displacement response using MEMS accelerometers*, Sensors, 16(2), 257.
9. FFTW library, 2023, [<http://www.fftw.org/> [accessed: 10.12.2023].
10. WiringPi C library for Raspberry Pi boards to communicate with I2C sensors: <https://github.com/WiringPi/WiringPi> [accessed 05.06.2024].

1.5. Mathematical modelling of the root crops separation and cleaning machine's parameters influence on the intensity of its functioning

*Dariia Rebot¹, Volodymyr Topilnytskyi²,
Sergiy Shcherbovskykh³, Tetiana Stefanovych⁴*

Lviv Polytechnic National University, Computer Aided Design System Department,

¹dariya.p.rebot@lpnu.ua.

²Lviv Polytechnic National University, Design and Operation of Machines Department.

³Lviv Polytechnic National University, Computer Aided Design System Department.

⁴Lviv Polytechnic National University, Computer Aided Design System Department.

Summary: A mathematical model was created to study how the root crop sorting and cleaning machine's parameters affect its performance. Using nonlinear mechanics and the Lagrange equation, the model describes the machine's operation process dynamics. Based on our mathematical model, graphical representations were created and studied of how the root vegetable sorting machine's oscillations change with different installation parameters.

Keywords: mathematical model; roots; sieve; dry method of cleaning; vibration oscillations; working chamber; transportation; pollution

Introduction

One of the promising areas of any country's development is agriculture and food processing. With a favorable climate and black soils in large areas, it is possible to be one of the world leaders in the production and supply of food products – from raw materials to semi-finished products and finished products from them. Manufacturers can provide all links of food production and create a complete closed cycle of production, which will certainly affect the growth of the country's economy. However, such a production process consists of many elements, each of which has high requirements. The process “from the field to the table” consists not only in the cultivation of “raw materials” for food production, but also in their preparation for processing, transportation, storage, actual processing, production of products, again their storage, transportation and sale, including export.

This article is devoted to one of the important stages of collected agricultural product's preparation for further processing and storage. This is the stage

of cleaning and separation from impurities, in particular, dry cleaning of root vegetables (carrots, beets, radishes, radishes, potatoes, etc.). Root crops are harvested automatically on farms under different weather conditions. Due to this, a lot of dirt can accumulate on their surfaces. To transport root crops to processing plants or to the consumer, they must be cleaned, sorted and packed. Of course, root crops can usually be washed with the water [1], [2]. However, with this method of cleaning, the following three tasks should be solved: supply and drainage of the water, water consumption, and subsequent high-quality drying of washed vegetables. Solving these problems is quite expensive, which will definitely be reflected in the price of the final product made from this raw material or in the sale price of the vegetables. A significantly cheaper alternative to washing with water is dry cleaning of root crops and their separation from contamination, when there are no costly operations with water and their subsequent drying. The equipment for such cleaning ensures the relative movement of root crops in bulk volume and the removal of impurities from their surfaces due to friction between themselves. Therefore, the development of new universal designs of equipment for cleaning vegetables by dry method is an urgent applied problem.

Analysis of the latest research

The range of machine designs for vegetable and fruit cleaning is quite wide [1]. Dry cleaning has a number of advantages over “wet” mean washing [4]. Accordingly, root crops should be cleaned and separated in a dry method before their storage, and washing can be done immediately before processing (the production of food products at processing enterprises). If the raw materials will be processed without storage, then the cleaning process can be directly divided into two stages – dry cleaning, which will help remove a large percentage of dirt from the surfaces of the raw materials, and then – washing. At the same time, money for water use (cost of the water, water supply, its filtering, drainage), and time and money for drying wet vegetables and fruits will be saved.

The disadvantage of modern equipment of the dry method of cleaning is its narrow focus – that is, it is intended for cleaning raw materials of a certain type or a certain size [2], [3]. The urgent task of today is the development of universal equipment for the dry method of cleaning root crops of various types, the optimal designs of which can be obtained with the help of a preliminary theoretical study of both the cleaning process itself and the equipment for its implementation by means of mathematical modelling of its work. Previous studies of this type either solved these problems in a linear formulation [5], or were again narrowly focused. It is the development of mathematical models in a non-linear formulation of the description of the dynamics of the equipment of the dry method of cleaning root crops that will allow quickly and economically obtaining its optimal design and modes of its optimal functioning.

Main material presentation

It is proposed the construction of a machine for cleaning and separating root crops in a dry way, in which the cleaning of their surfaces occurs due to the mutual friction of root crops among themselves. The machine is of the vibration type with adjustable amplitude of oscillations. The relative movement of root crops in their bulk volume is ensured by the energy of the oscillating movement of the machine's working container in which they are placed. The machine is versatile in terms of cleaning various root crops, both in type and size. The level of vibration energy of the machine can be varied, thus choosing the cleaning mode of one or another type of root crops. Also, the machine is characterized by high productivity. It can provide simultaneous dry cleaning and movement in space of raw materials to be cleaned.

In figure 1 we show the scheme of the machine's proposed design for cleaning root crops from contamination by a dry method. The machine includes a working container (1) in the form of a cylinder, in the middle of which is placed a cylindrical grid that has small meshes (within a few millimetres). The grid consists of three main parts: a) internal grid (2) (it limits the space of the working container of the machine, where the cleaning intensity is the lowest); b) outer grid (3), which is placed with a gap to the inner wall of the working container; c) systems of connectors (4), which divide the volume of root crops between the nets for better cleaning and form a single frame from two grids (2) and (3). The main purpose of the grids is: a) cleaning the surfaces of root crops that are in direct contact with it; b) passing through the grid's holes removed impurities and foreign inclusions in the space of the gap between the grid (3) and the lower inner part of the working container. Contaminated root crops are loaded in bulk through the feed port (5). Accumulated at the bottom of the working container, the dirt removed from the surfaces of the root crops, which have passed through the grid, are discharged through the out port (6). Unloading of cleaned root crops takes place through the out port (12), located in the lower part of the end wall of the working container. The oscillating movement of the machine's working container, which is placed on a system of springs (8), is provided by four unbalanced rotating masses (7) through elastic couplings (10) from electric motors (11). The whole machine is mounted on a welded frame (9) from a metal profile. Due to the different magnitude of the rotating masses (7) or the magnitude of the displacement of their center of mass from the axis of rotation, it is possible to achieve a different amplitude of oscillations of the parts of the working container of the machine and the internal grid. This will ensure the directional movement of root crops from the loading zone (5) to the unloading zone (12). At the same time, the root crops will intensively mix among themselves, rub against each other with their surfaces and against the surface of the grid and will be cleaned. That is, we will have an overlap of three technological operations – dry cleaning, separating and movement (transportation). Depending on the required transportation distance, the working chamber can have

different lengths. It should be emphasized that the directed vibration energy will parallelly move the removed impurities through the bottom of the working container to the out port (6).

The study of the influence of the parameters of the developed design of the machine for cleaning and separating root crops from impurities in a dry way on the intensity of its operation was carried out on the mathematical model of this machine, which describes its dynamics. The model was built using asymptotic methods of nonlinear mechanics and the Lagrange equation [5]. All parameters of the machine, and they are of three types – geometric, force and kinematic, are displayed in the model in symbolic format. That is, their numerical values in the real range of change can be substituted directly into a model that will describe the oscillating movement of an arbitrary point of the machine, build the trajectory of its movement and determine the amplitude of its oscillations.

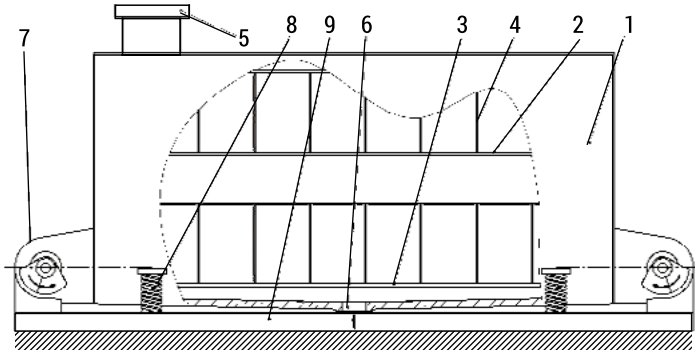


FIG. 1. Schematic of a machine for separation and cleaning root crops from contamination using a dry method

The last value will be one of the key factors that will determine the intensity of the dry cleaning process of root crops and the speed of their movement along the working container of the machine, that is, the intensity of the machine's functioning. From a mathematical point of view, the model will be displayed in the system of analytical dependencies of generalized coordinates describing the movement of the working container of the machine for dry cleaning of root crops from contamination x_{o3} , y_{o3} and ϕ from machine parameters of type (1), (2) and (3):

$$x_0 \sin\left(\sqrt{\frac{c}{M}}t + \alpha_x\right) +$$

$$+ \frac{\varepsilon}{\sqrt{\frac{c}{M}}} \int_0^t -\ddot{\phi} \left(\begin{array}{l} |M_K S \cos \phi + M_{D1} \left(|r_1 \cos(\omega_1 t + \phi + \alpha_0) \right) + \\ | + l_1 \sin \phi - k_1 \cos \phi \end{array} \right) + \left(\begin{array}{l} | + M_{D2} \left(r_2 \cos(\omega_2 t + \phi + \psi_0) - l_2 \sin \phi - k_2 \cos \phi \right) \end{array} \right) \right) -$$

$$\begin{aligned}
& -(\dot{\phi})^2 \left(\begin{aligned} & | -M_K S \sin \phi + M_{D1} (-r_1 \sin(\omega_1 t + \phi + \alpha_0) + l_1 \cos \phi + k_1 \sin \phi) + \\ & | + M_{D2} (-r_2 \sin(\omega_2 t + \phi + \psi_0) - l_2 \cos \phi + k_2 \sin \phi) \end{aligned} \right) + \\
& + M_{D1} r_1 \sin(\omega_1 t + \phi + \alpha_0) (\omega_1^2 + 2\omega_1 \dot{\phi}) + M_{D2} r_2 \sin(\omega_2 t + \phi + \psi_0) (\omega_2^2 + 2\omega_2 \dot{\phi}) - \\
& - C_1 \left(\sqrt{(x_{o3} - b \cos \phi + f \sin \phi + b)^2 + \left(y_{o3} - b \sin \phi - f \cos \phi + f + L_{spr} - \frac{Mg}{c} \right)^2} - L_{spr} \right) \times \\
& \times \left(- \frac{x_{o3} - b \cos \phi + f \sin \phi + b}{\sqrt{(x_{o3} - b \cos \phi + f \sin \phi + b)^2 + \left(y_{o3} - b \sin \phi - f \cos \phi + f + L_{spr} - \frac{Mg}{c} \right)^2}} - \right. \\
& - C_2 \left(\sqrt{(x_{o3} + q \cos \phi + f \sin \phi - q)^2 + \left(y_{o3} + q \sin \phi - f \cos \phi + f + L_{spr} - \frac{Mg}{c} \right)^2} - L_{spr} \right) \times \\
& \times \left(- \frac{x_{o3} + q \cos \phi + f \sin \phi - q}{\sqrt{(x_{o3} + q \cos \phi + f \sin \phi - q)^2 + \left(y_{o3} + q \sin \phi - f \cos \phi + f + L_{spr} - \frac{Mg}{c} \right)^2}} \right) \times \\
& \left. \times \sin \left(\sqrt{\frac{c}{M}} (t - u) \right) du \right) \quad (1)
\end{aligned}$$

$$\begin{aligned}
& y_{o3} = y_0 \sin \left(\sqrt{\frac{c}{M}} t + \alpha_y \right) + \\
& + \frac{\varepsilon}{\sqrt{\frac{c}{M}}} \int_0^t \left(-\ddot{\phi} \left(\begin{aligned} & | M_K S \sin \phi + M_{D1} \left(| r_1 \sin(\omega_1 t + \phi + \alpha_0) - \right. \right. \\ & | + l_1 \cos \phi - k_1 \sin \phi \end{aligned} \right) + \left. \begin{aligned} & | + M_{D2} (r_2 \sin(\omega_2 t + \phi + \psi_0) - l_2 \cos \phi - k_2 \sin \phi) \end{aligned} \right) \right) -
\end{aligned}$$

$$\begin{aligned}
& -(\dot{\phi})^2 \left(\begin{aligned} & | -M_k S \cos \phi + M_{D1} (-r_1 \cos(\omega_1 t + \phi + \alpha_0) + l_1 \sin \phi + k_1 \cos \phi) + \\ & | + M_{D2} (-r_2 \cos(\omega_2 t + \phi + \psi_0) - l_2 \sin \phi + k_2 \cos \phi) \end{aligned} \right) + \\
& + M_{D1} r_1 \cos(\omega_1 t + \phi + \alpha_0) (\omega_1^2 + 2\omega_1 \dot{\phi}) + M_{D2} r_2 \sin(\omega_2 t + \phi + \psi_0) (\omega_2^2 + 2\omega_2 \dot{\phi}) - \\
& - \frac{C_1}{2} 2 \left(\sqrt{(x_{o3} - b \cos \phi + f \sin \phi + b)^2 + \left(y_{o3} - b \sin \phi - f \cos \phi + f + L_{spr} - \frac{Mg}{c} \right)^2} - L_{spr} \right) \times \\
& \times \left(- \frac{x_{o3} - b \sin \phi + f \cos \phi + f + L_{spr} - \frac{Mg}{c}}{\sqrt{(x_{o3} - b \cos \phi + f \sin \phi + b)^2 + \left(y_{o3} - b \sin \phi - f \cos \phi + f + L_{spr} - \frac{Mg}{c} \right)^2}} - \right. \\
& - C_2 \left(\sqrt{(x_{o3} + q \cos \phi + f \sin \phi - q)^2 + \left(y_{o3} + q \sin \phi - f \cos \phi + f + L_{spr} - \frac{Mg}{c} \right)^2} - L_{spr} \right) \times \\
& \times \left(- \frac{x_{o3} + q \sin \phi + f \cos \phi - f + L_{spr} - \frac{Mg}{c}}{\sqrt{(x_{o3} + q \cos \phi + f \sin \phi - q)^2 + \left(y_{o3} + q \sin \phi - f \cos \phi + f + L_{spr} - \frac{Mg}{c} \right)^2}} + Mg \right) \times \\
& \left. \times \sin \left(\sqrt{\frac{c}{M}} (t - u) \right) du \right), \tag{2}
\end{aligned}$$

$$\phi(t) = \phi_0 \cos(\omega_0 t + \theta(t)) \tag{3}$$

In this system of mathematical expressions, we will distinguish the following main parameters: M is a mass of the working container; M_{D_i} is the value of the corresponding unbalanced rotating mass of the drive with angular velocity ω_i ; r_i is the amount of displacement of the mass center of the unbalanced rotating mass from the axis of its rotational movement; C_i is stiffness of the work container attachment springs.

The input values for conducting studies of some parameters (the possible range of their changes) to obtain the corresponding graphical dependencies for determining their influence on the nature of the movement of the working container will be, for example, the following: a) $r_1 = r_2 = 0 - 0.095$ m is the range of changes in the amount of displacement of the mass center of an unbalanced rotating mass from the axis of its rotational motion; b) $\omega_1 = 50\text{c}^{-1} - 150\text{c}^{-1}$ is the range of angular velocities of the unbalanced rotating mass of the drive; c) $M_{Di} = 1 - 7$ kg is the range of changes in the value of the corresponding unbalanced rotating mass; d) $M = 110 - 200$ kg is the range of changes in the mass of the working container; e) $C_i = 10 - 19$ kN/m is the range of changes in the stiffness of the work container fastening springs.

As a result of the conducted research, graphical dependences of the amplitude of the oscillating movement of the dry root cleaning machine on the parameters that can be changed during the operation of the machine were obtained. After the given graphic dependencies, conclusions are drawn regarding the importance of the influence of one or another parameter on the nature and amplitude of oscillations of the machine's working container.

So, figures 2 and 3 show how the mass of the working container with loading affects the amplitude of its oscillations (when the angular velocities of the driven unbalanced masses and the value of the stiffness of the springs of the working container are changed).

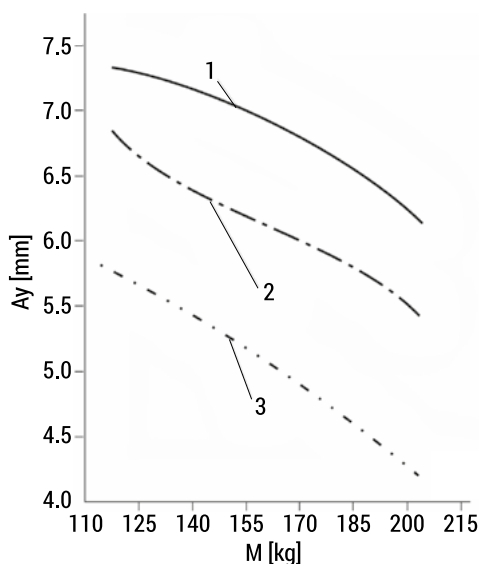


FIG. 2. Dependence of the amplitude of oscillations of the working container of the machine for cleaning and separating root crops from contamination by a dry method on the oscillating mass at the angular speed of rotation of unbalanced masses $\omega_1 = \omega_2 = 140\text{s}^{-1}$: 1 – stiffness of the work container attachment springs 12kN/m; 2 – 15kN/m; 3 – 18kN/m

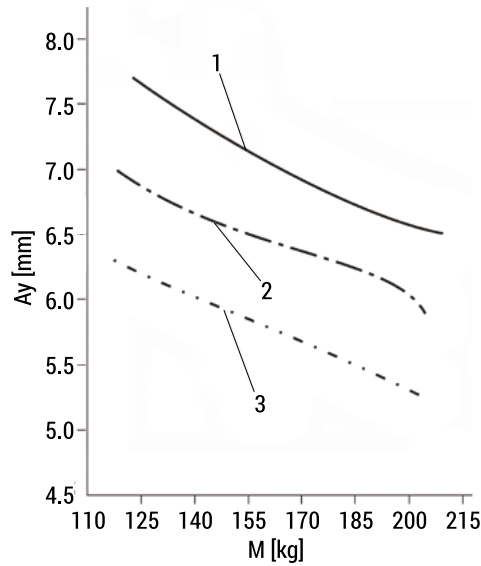


FIG. 3. Dependence of the amplitude of oscillations of the working container of the machine for cleaning root crops from contamination by the dry method on the oscillating mass at the angular speed of rotation of unbalanced masses $\omega_1 = \omega_2 = 110\text{s}^{-1}$: 1 – stiffness of the work container attachment springs 12kN/m; 2 – 15kN/m; 3 – 18kN/m

As a result of the obtained graphical dependencies, it can be asserted:

- a) a) the value of the amplitude of oscillations of the machine's working container for cleaning root crops from contamination by a dry method is nonlinearly dependent on the oscillating mass and decreases with its increase. So, for a machine with spring stiffness 15kN/m and angular speed of rotation of unbalanced masses 140s^{-1} with an increase in the oscillating mass from 125 to 200 kg (by 1.6 times), the amplitude of oscillations decreased by 1.2 times, i.e. by approximately 2 mm;
- b) b) the value of the amplitude of oscillations of the working container of the machine is nonlinearly dependent on the angular speed of rotation of the unbalanced masses and increases with a decrease in the number of revolutions of the drive motors. In particular, for example, for a machine with a spring stiffness of 18kN/m and a total oscillating mass of 170 kg with a decrease in the angular speed of the drive from 140 to 110s^{-1} (by 1.3 times), the amplitude of vertical oscillations of the working container increased by 1.16 times, or almost by 1 mm;
- c) c) the value of the amplitude of oscillations of the machine's working container for cleaning and separating root crops from contamination by a dry method nonlinearly depends on the stiffness of the springs of the working container attachment. It decreases with increasing stiffness. In particular, for example, for a machine with an oscillating mass of 155 kg and an angular speed of rotation of imbalances of 140s^{-1} with an increase in the stiffness of the springs from 12kN/m to 18kN/m (by 1.5 times), the amplitude of vertical oscillations of the working container decreased by 1.38 times, respectively by 2 mm.

Conclusions

1. The proposed design of the machine implements a highly efficient process from an economic point of view of cleaning the roots of vegetable crops from impurities in a dry way during their processing or before storage. The developed nonlinear mathematical model describing the dynamics of the machine makes it possible to determine its optimal parameters, which will ensure the best intensity of dry cleaning of root crops and their movement along the working container of the machine.
2. Theoretical studies with the use of mathematical modeling of the dynamics of the machine for cleaning root crops in a dry way make it possible to minimize the design time, to obtain a design of the machine with high cleaning productivity with low energy consumption for its operation.
3. The following are planned: a) further research into the process of cleaning the surfaces of root crops using a dry method in the aspect of studying the cleaning mechanism itself, ensuring the proper quality of the cleaned surface; b) manufacture of the developed design of the machine and its implementation for practical use.

References

1. Dorokhov A., Mosyakov M., Sazonov N., 2020, *Automated Line for Post-Harvest Processing of Root Crops and Potatoes*, Agricultural Machinery and Technologies, 14, 22–26.
2. Wang L., Ding X., 2007, *Experimental investigation washing vegetables with submerged jets of water*, Nongye Gongcheng Xuebao / Transactions of the Chinese Society of Agricultural Engineering, 23, 124–130.
3. Hevko R., Brukhanskyi R., Flonts I. et al., 2018, *Advances in methods of cleaning root crops*, Bulletin of the Transilvania University of Braşov, Series II: Forestry, Wood Industry, Agricultural Food Engineering, 11, 127–138.
4. Frolov V.J., Bychkov A.V., Sidorenko S.M. et al., 2016, *The parameters of the process of dry cleaning root crops with using screw separator*, Research Journal of Pharmaceutical, Biological and Chemical Sciences, 7, 376–382.
5. Topilnytskyy V., Rebot D., Sokil M. et al., 2017, *Modeling the dynamics of vibratory separator of the drum type with concentric arrangement of sieves*, Eastern-European Journal of Enterprise Technologies. Applied Mechanics, 2, 7(86), 26–35.

1.6. Axisymmetric contact problem for a space with a spherical cavity

Tetyana Solyar¹, Olha Soliar²

*Pidstryhach Institute for Applied Problems
of Mechanics and Mathematics, NASU:*

¹t_solyar@ukr.net, ²solyarolya@gmail.com

Summary: A numerical algorithm for solving the problem of a spherical cavity in space, under the action of a rigid stamp of axisymmetric shape, is proposed. Under the stamp action, contact occurs on separate, previously unknown areas of contact. The contact problem is formulated in the form of Signorini integral equations-inequalities, which, using quadrature formulas for singular integrals, are transformed into a system of linear algebraic equations-inequalities. Solution of the system is reduced to finding the minimum of the quadratic form under linear constraints on the unknown contact stresses. The problem of compressing axisymmetric rigid elongated and flattened spheroidal stamps into an elastic space with a spherical void has been examined utilizing the developed algorithm.

Keywords: rigid stamp; contact interaction; spherical cavity; quadratic programming

Introduction

The study of contact problems holds significant relevance within the realm of deformable body mechanics, as contact interactions represent a primary means of applying loads to structural elements and machine components. The concentration of stress within the contact zone has the potential to induce material and structural fractures. Analytical solutions have been successfully derived for a constrained set of three-dimensional contact problems [1, 9]. Consequently, there is a critical need to advance numerical and numerical-analytical methods for addressing a broader spectrum of these problems. Particularly pertinent is the contemporary challenge of developing methods and approaches that combine numerical and analytical techniques to ascertain contact stresses during interactions involving stamps and intricately shaped bodies, wherein the contact areas are not known in advance. This scenario arises when the number of contact areas and their boundaries is indeterminate, emphasizing the current relevance of this research focus.

Issues involving contact areas that are not predetermined fall under the category of non-classical contact problems and remain inadequately explored, even in the axisymmetric case. The complexity intensifies when the contact area comprises

multiple regions. Resolving such challenges typically entails employing approaches that leverage various methods for the formulation and discretization of equations and inequalities [8, 9, 11, 17–19]. In particular, in [9, 18] the finite element method was used, in [1, 8, 9, 18] – the boundary integral equations. Contact problems based on the variational method were studied in [2–5]. Other methods were considered in [17, 18].

Signorini [15, 16] introduced a comprehensive approach to address problems characterized by unknown contact areas, reducing them to the examination of problems featuring constraints expressed in the form of inequalities. The idea of using the quadratic programming method for solving contact problems is proposed in papers [10–12]. The application of quadratic programming was studied also in [5, 14].

This paper considers the problem of a spherical cavity in space, which is under the action of a rigid axisymmetric stamp. These problems have received limited attention in the literature due to the consideration of a complex form as the basis, resulting in correspondingly intricate integral equations. Additionally, the boundaries of the contact area remain unidentified. To address this challenge, we employed an algorithm that combines Signorini's approach with methods involving integral equations-inequalities and quadratic programming [7].

Formulation of the problem. Consider the problem on pressing an axisymmetric rigid stamp, the surface of which in the spherical coordinate system r, η, φ is described by the equation $r = R(1 - \rho(\eta))$, $\rho(0) = 0$, into elastic space $r \geq R$ with a spherical cavity (Fig. 1). The compressive force P acts along the stamp's axis of symmetry.

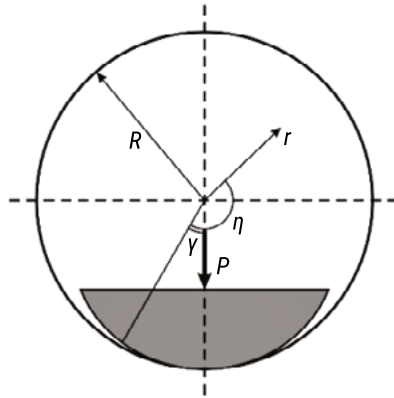


FIG. 1. Pressing an axisymmetric stamp in a half-space with a spherical cavity

Assume that the surface of the cavity $r = R$ outside the contact area is not loaded, and there is no friction in the contact area, i.e.

$$\sigma_r(R, \eta) = -p(\eta), \quad 0 \leq \eta \leq \gamma,$$

$$\sigma_r(R, \eta) = 0, \quad \gamma < \eta \leq \pi,$$

$$\tau_{r\eta}(R, \eta) = 0, \quad 0 \leq \eta \leq \pi.$$

Here $p(\eta)$ is the desired contact pressure. In the case of a stamp without sharp edges, the boundary of the contact area, i.e., the value of the contact angle γ , is also unknown in advance. The equilibrium of the stamp yields the following relationship

$$P = 2\pi R^2 \int_0^\gamma p(\eta) \sin \eta \cos \eta d\eta. \quad (1)$$

Integral equation of the contact problem

The condition of the stamp contact with the surface of the cavity in the elastic space is written as $u_r(R, \eta) = \delta \cos \eta - R\rho(\eta)$, $0 \leq \eta \leq \gamma$, and δ is the displacement of the stamp in the direction of the force P , $u_r -$ is the radial displacement of the cavity boundary.

Having used the results of study [4] to determine the displacements of the points of the cavity surface, we obtain the integral equation [1] to determine the contact pressure,

$$\int_0^\gamma p(\alpha) H(\eta, \alpha) \sin \alpha d\alpha = 2\pi G [a \cos \eta - \rho(\eta)], \quad 0 \leq \eta \leq \gamma \quad (2)$$

where

$$H(\eta, \alpha) = 4(1-\nu) \frac{K(k_1)}{h_1} + \operatorname{Re} \int_0^1 \left(\frac{A}{y^{1+w}} - y \right) U(y, \eta, \alpha) dy, \quad (3)$$

$$A = -1 + 8\nu - 8\nu^2 + i \frac{5 - 4\nu - 16\nu^2 + 16\nu^3}{\sqrt{3 - 4\nu^2}},$$

$$U(y, \eta, \alpha) = K(k_y) h_y^{-1}, \quad w = -\frac{1}{2} \left(1 - 2\nu - i\sqrt{3 - 4\nu^2} \right),$$

$$h_y^2 = 1 + y^2 - 2y \cos(\eta + \alpha), \quad h_y^2 k_y^2 = 4y \sin \eta \sin \alpha,$$

$K(k)$ is a complete elliptic integral of the first kind, $a = \delta/R$, ($a > 0$), G is the shear modulus, ν – is Poisson's ratio.

Solution of the contact problem. In the given problem, the areas of interaction are not specified in advance. For such problems, the contact conditions can be written as alternative Signorini equations-inequalities with $a < r < b$ [15]

$$\int_a^b q(\alpha) F(\eta, \alpha) d\alpha = W(\eta), \quad \text{where } q > 0, \quad a < \eta < b,$$

$$\int_a^b q(\alpha)F(\eta, \alpha)d\alpha \geq W(\eta), \text{ where } q = 0, \quad (4)$$

$$q(\rho) = \rho p(\rho), \quad p(\rho) = -\sigma_r(\rho), \quad F(\eta, \alpha) = H(\eta, \alpha) \sin \alpha / \alpha,$$

$$W(\eta) = 2\pi G[a \cos \eta - \rho(\eta)].$$

Here, a, b are the values (angles) unknown in advance, and the area $[a, b]$ must contain the contact area. The first condition (4) is valid only in the contact area. The second condition indicates that the boundary of the post-load space is below or touching the stamp.

We will solve equations-inequalities (4) numerically. To do this, we will construct a quadrature formula for the integral

$$\int_a^b q(\alpha)F(\eta, \alpha)d\alpha. \quad (5)$$

A continuous function q on the interval $a < \eta < b$ is described by linear, piece-wise continuous interpolation functions, which are presented as [6, 13]

$$q(\eta) = \sum_{n=0}^N q_n S_h(\eta - \eta_n), \quad (6)$$

$$\text{where } S_h(x) = \begin{cases} 1 - \frac{|x|}{h}, & |x| \leq h, \\ 0, & |x| > h; \end{cases} \quad q_n = q(\eta_n), \quad \eta_0 = a, \quad \eta_{j+1} = \eta_j + h, \quad j = \overline{0, N-1},$$

$N+1$ is a number of nodal points, $h = \frac{b-a}{N}$ is subinterval.

Then for the integral (5) we get

$$\int_a^b q(\alpha)F(\eta, \alpha)d\alpha = \sum_{m=0}^N C_m(\eta)q_m, \quad n = 0, \dots, N,$$

$$\text{where } C_m(\eta) = \int_{\eta_m-h}^{\eta_m+h} S_h(\tau - \eta_m)F(\eta, \tau)d\tau. \quad (7)$$

These integrals were found by standard procedures, developed in mathematical systems, which take into account the presence of integrated features in subintegral functions (the subintegral function $F(\eta, \alpha)$ has a logarithmic feature at $\eta \rightarrow \alpha$). By replacing the integrals in the system of equations-inequalities (4) with quadrature formulas (7) [6, 13], we obtain an algebraic system of equations-inequalities

$$\sum_{m=0}^N A_{nm}q_m = W_n, \text{ where } p_n \geq 0,$$

$$\sum_{m=0}^N A_{nm} q_m < W_n, \text{ where } p_n = 0, \quad n = 0, \dots, N, \quad (8)$$

where $W_n = W(\eta_n)$, $q_n = \eta_n p(\eta_n)$, $A_{nm} = C_m(\eta_n)$.

The contact pressure is determined from the minimum value condition [7]

$$J = \sum_{n=0}^N \sum_{m=0}^N A_{nm} q_m q_n - \sum_{m=0}^N W_n q_n. \quad (9)$$

when performing equations-inequalities of the form

$$\sum_{m=0}^N A_{nm} q_m < W_n, \quad q_n \geq 0, \quad n = 0, \dots, N. \quad (10)$$

The formulated problem is a quadratic programming problem. Value J under constraints (10) is a positive value, which is equal to zero on the solution of equations-inequalities (8).

Equation of the stamp base. Assume that the stamp is an ellipsoid of rotation with semi-axes a_z , $a_x = a_y$, centered at the point with coordinates $x = 0$, $y = 0$, $z = c$ and $a_z \leq R$, $a_x \leq R$. Here c is a constant, which is determined from the condition: $\rho(0) = 0$.

The equation of this ellipsoid in the Cartesian coordinate system is written as

$$z = c + a_z \cos \eta, \quad x = a_x \cos \varphi \sin \eta, \quad y = a_x \sin \varphi \sin \eta, \quad 0 < \eta < \pi, \quad 0 < \varphi < 2\pi.$$

In the spherical coordinate system we have

$$r = \sqrt{(z+c)^2 + x^2 + y^2} = \sqrt{(c + a_z \cos \eta)^2 + a_x^2 \sin^2 \eta}.$$

Write it in the form

$$r = R[1 - \rho(\eta)] = \sqrt{(c + a_z \cos \eta)^2 + a_x^2 \sin^2 \eta}.$$

From here

$$\rho(\eta) = 1 - \frac{1}{R} \sqrt{(c + a_z \cos \eta)^2 + a_x^2 \sin^2 \eta}.$$

Constant c is determined from the condition $\rho(0) = 0$. From here we have $c = R - a_z$.

Then $\rho(\eta) = 1 - \sqrt{(1 - \alpha + \alpha \cos \eta)^2 + \beta^2 \sin^2 \eta}$, where $\alpha = \frac{a_z}{R}$, $\beta = \frac{a_x}{R}$.

Calculation results

An elongated spheroidal stamp. The results of the calculations were carried out for a spheroidal stamp, elongated in the vertical direction. The major semi-axis of the spheroid is vertical and equal to the radius of the cavity, it is assumed that the displacement of the stamp is $\delta = 0.001R$. Fig. 2 shows the dependence of the relative pressure p/G on the angular coordinate η . The developed algorithm is such in which it is necessary to set (predict) the boundaries of the area containing the contact sections. When solving the contact problem by the proposed numerical method, the predicted boundaries of the contact area (angles) were set equal to $a = 0$, $b = 0.08$. Here and further, the angular coordinate η and values a, b were specified in radians. Curves 1–4 show the results of calculations performed at $\nu = 0.3$, $\alpha = 1$, $\beta = 0.6; 0.7; 0.8; 0.9$, respectively. Similar results of calculations carried out for $\delta = 0.0001R$, $a = 0$, $b = 0.03$ are shown in Fig. 3.

As we can see from the plots, the contact area occurs around the center of the lower part of the cavity, the maximum contact stresses occur in the center of the contact area. The contact area decreases when the horizontal diameter of the spheroidal stamp decreases, while the contact stresses in the center increase.

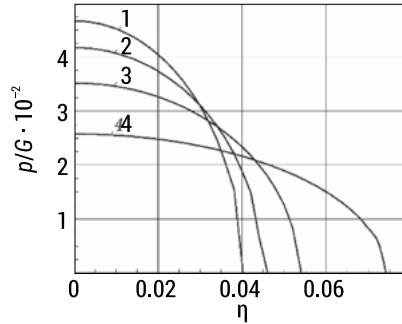


FIG. 2. Relative contact pressure at $\nu = 0.3$, $\delta = 0.001R$, $a = 0$, $b = 0.08$

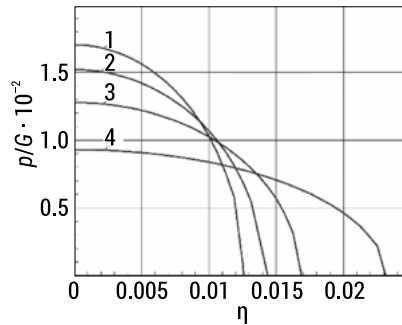


FIG. 3. Relative contact pressure at $\nu = 0.3$, $\delta = 0.0001R$, $a = 0$, $b = 0.03$

A flattened spheroidal stamp. Consider the case when the major semi-axis of the spheroid is horizontal and equal to the radius of the cavity. The relative contact pressure p/G at $\nu = 0.3$, $\delta = 0.00001R$, $\beta = 1$ and at $\alpha = 0.7; 0.8; 0.9$ is shown in Fig. 4 (curves 1–3, respectively). The predicted boundaries of the contact area were set equal to $a = 0.4$, $b = 0.5\pi + 0.2 = 1.77$.

We consider the case when the semi-axes of the stamp are smaller than the radius of the cavity. The results of the calculations are shown in Fig. 5 at $\delta = 0.0001R$, $\nu = 0.3$, $\beta = 0.8$, $\alpha = 0.9; 0.8; 0.7$ (curves 1–3, respectively).

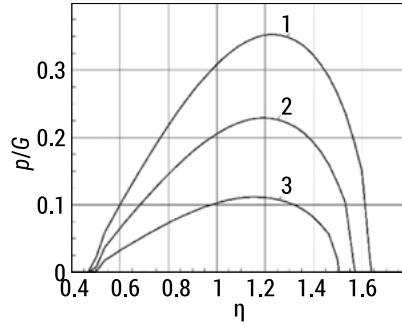


FIG. 4. Relative contact pressure at $\nu = 0.3$, $\delta = 0.00001R$, $\beta = 1$, $\alpha = 0.7; 0.8, 0.9$

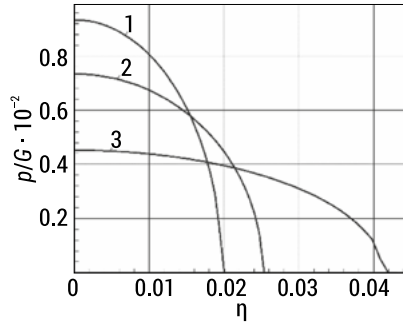


FIG. 5. Relative contact pressure at $\nu = 0.3$, $\delta = 0.0001R$, $\beta = 0.8$, $\alpha = 0.9; 0.8, 0.7$

As we can see from the graphs, for flattened stamps there is no contact in the center of the lower part of the cavity. The contact area for all cases starts at the angle $\eta = 0.43$. For $\alpha > 0.8$ the outer boundary of the contact area is smaller than $\pi/2$, that is, the contact area is located in the lower part of the cavity. At smaller α values (with more flattened stamps), the contact area becomes larger than $\pi/2$ (that is, the contact also takes place in the upper part of the cavity).

Conclusions

The method of determining contact stresses under a stamp which is pressed into a spherical cavity in space is proposed. The problems in which the contact area is not

specified in advance are considered. Their solution is reduced to the consideration of Signorini's integral equations-inequalities. The problem of solving integral equations with singular kernels is reduced to a system of linear algebraic equations-inequalities based on constructed quadrature formulas. The system of equations-inequalities was solved on the basis of the approaches developed in the quadratic programming method.

The study of contact pressure was carried out in relation to spheroidal stamps of various shapes, which are pressed into a spherical cavity. The cases are described when the contact areas are simply or doubly connected, the contact area is located in the lower part of the cavity or extends to its upper part.

References

1. Aleksandrov V.M., Pozharsky D.A., 1998, *Non-classical Spatial Problems of the Mechanics of Contact Interactions of Elastic Bodies*, Moscow.
2. Hlaváček I., Haslinger J., Nečas J. et al., 1986, *Solution of Variational Inequalities in Mechanics*, trans. from Slovak by Yu.A., Kuznetsova, A.V. Lapina, ed. N.A. Bakhvalova, Moscow.
3. Duvaut J., Lions J.L., 1980, *Inequalities in Mechanics and Physics*, Moscow.
4. Karpenko V.A., 1975, *On the closed solution of the first boundary value problem of the theory of elasticity for a space with a spherical cavity*, PMM (Journal of Applied Mathematics and Mechanics), 39(5), 951–955.
5. Kravchuk A.S., 1997, *Variational and Quasi-Variational Inequalities in Mechanics*, Moscow.
6. Maksymovych O.V., Solyar T.Ya., 2011, *Method of mechanical quadratures for solving integral equations of thermoelasticity for plates with heat exchange*, Journal of Mathematical Sciences, 174(3), 387–399. DOI: 10.1007/s10958-011-0306-x.
7. Solyar T.Ya., Solyar O.I., 2022, *Axisymmetric contact problem for a half-space with unspecified areas of interaction*, Mathematical Methods and Physico-Mechanical Fields), 65(3–4), 178–187.
8. Aleksandrov V.M., Pozharskij D.A., 2004, *Trehmernye kontaktnye zadachi pri uchete trenija i nelinejnoj sherohovatosti* [Three-dimensional contact problems taking into account friction and nonlinear roughness], Prikladnaja matematika i mehanika, 68(3), 516–527.
9. Johnson K.L., 1987, *Contact Mechanics*, Cambridge, UK: Cambridge University Press Publ.
10. Kalker J.J., 1988, *Contact mechanical algorithms*, Communications in Applied Numerical Methods, 4(1), 25–32. DOI: 10.1002/cnm.1630040105.
11. Kalker J.J., 1977, *Variational principles of contact elastostatics*, IMA Journal of Applied Mathematics, 20(2), 199–219. DOI: 10.1093/imamat/20.2.199.
12. Kalker J.J., Raden Y. van, 1972, *A minimum principle for frictionless elastic contact with application to nonHertzian half-space contact problems*, Journal of Engineering Mathematics, 6(2), 193–206.
13. Maksymovych O., Solyar T., 2021, *Determination of non-axisymmetric stresses in the bodies of revolution based on regulized integral equations*, European Journal of Mechanics A/Solids, 87, 104218. DOI: 10.1016/j.euromechsol.2021.104218.
14. Paczelt J., 1976, *Solution of elastic contact problems by the finite element displacement method*, Acta Technica Academiae Scientiarum Hungaricae, 82(3–4), 353–375.
15. Signorini A., 1933, *Sopra alcune questioni di elastostatica*, Atti della Società Italiana per il Progresso della Scienze, 513–533.

16. Signorini A., 1959, *Questioni di elasticità non linearizzata e semilinearizzata*, Rendiconti di Matematica e delle Sue Applicazioni, 18(1–2), 95–139.
17. Tkachuk N.N., 2017, *Kontaktnoe vzaimodejstvie slozhnoprofil'nyh jelementov mashinostroi-tel'nyh konstrukcij s kinematičeski soprjzhennymi poverhnostjami* [Contact interaction of complex profile elements of machine-building structures with kinematically coupled surfaces], Har'kov: FOP Panov A.N. Publ.
18. Wriggers P., 2006, *Computational Contact Mechanics*, Berlin–Heidelberg: Springer–Verlag Publ. DOI: 10.1007/978-3-540-32609-0.
19. Yastrebov V.A., 2013, *Numerical methods in contact mechanics*, ISTE–John Wiley & Sons Publ.: London–Hoboken. DOI: 10.1002/9781118647974.

1.7. Study of the technical characteristics of modern LED lamps

Markian Hoshko¹, Tetyana Hoshko²

¹*Lviv National Agrarian University, contact author via email for correspondence*

²*Lviv Polytechnic National University, ICSIT, CAD, tetiana.d.hoshko@lpnu.ua*

Summary: Each year, the importance of energy conservation and efficiency grows. Thus, the issue of conserving energy is of global significance. Electric lighting accounts for up to 20% of industrial electricity consumption. Modernizing lighting is one method to enhance energy efficiency. In the past, LED lamps were deemed costly and inefficient. Consequently, we explored various lamp types to assess their long-term economic viability. However, market dynamics have shifted, leading to decreased costs for LEDs and reduced electricity usage.

Keywords: LED lamps, energy saving lamps, LED lamps composition

Introduction

The challenge of conserving energy extends globally. Electric lighting constitutes up to 20% of industrial power consumption. Upgrading lighting systems stands as a viable strategy to boost energy efficiency.

Our tests reveal that numerous LEDs don't consistently align with manufacturers' specifications.

Currently, the impact of surrounding temperatures on LED lamp functionality and luminosity remains insufficiently researched.

Based on our review of references [1–3] and considering energy conservation challenges, it's evident that substituting incandescent lamps (IL) with compact fluorescent lamps (CFLs) – boasting 4–5 times the luminosity of IR – and light-emitting diode (LED) lamps – offering 5–8 times the luminosity of IR – is a promising approach for diminishing power consumption in both industrial settings [4–7] and public services. High-pressure sodium lamps with an output of 100–130 lm/W are viewed as more cost-effective for street lighting [8–10].

The objective of this research is to explore how ambient temperatures influence the functionality and luminosity of LED lamps.

Main material

We examined LED lamps of the brands “IEK”, “Etron”, “Ledstar”, “Lightmaster”, “Feron”, “Electro House”, “KODAK”, “Luxray”, “Jazzwau”, “Neo Max”. The characteristics of the lamps are given in Table 1.

TABLE 1. Characteristics of the lamps

Producer	Power, P, Watt	U, B	Light flux: F, Lm	Light temperature: K	Ra	Term of service: hour	Lighting angle: degree
IEK	11	230	990	4000	70	30000	200
Etron	10	165–265	900	4200	80	25000	200
Ledstar	10	160–230	850	3000	80	30000	270
Lightmaster	11	230	1100	4000	80	30000	200
Feron	10	230	850	4000	80	30000	200
Electro House	10	160–230	900	4100	90	50000	220
KODAK	10	220–240	890	4100	80	25000	270
Luxray	11	165–265	880	4200	80	30000	180
Jazzway	11	220–240	880	3000	75	25000	230
Neo Max	10	175–250	1000	4200	80	50000	360



FIG. 1. LED lamps under investigation



FIG. 2. LED lamp "IEK" 11 Watt

TABLE 2. Measurement results of the "IEK" 11 watt

U, B	E. Lx	F, Lx/ Watt	t, °C
200	1215	71.5	19
210	1200	67.2	20
220	1198	68.1	21
230	1188	64.6	23
240	1183	61.6	26

The temperature of the environment during the study of the light source was 15°C, the illumination of the room was 15 Lux, and the distance to the luxmeter was 30 cm.



FIG. 3. LED lamp "Etron" 10 Watt

TABLE 3. Measurement results of the "Etron" 10 watt

U, B	E. Lx	F, Lx/ Watt	t, °C
200	1385	72.9	22
210	1346	71.2	25
220	1309	70.0	26
230	1285	65.7	27
240	1275	62.5	27



FIG. 4. LED lamp "Ledstar" 10 Watt

TABLE 4. Measurement results of the "Ledstar" 10 watt

U, B	E. Lx	F, Lx/ Watt	t, °C
200	730	66.4	17.8
210	1016	64.5	19
220	1025	62.1	19.4
230	1012	58.7	20
240	988	54.9	22.2



FIG. 5. LED lamp "Lightmaster" 11 Watt

TABLE 5. Measurement results of the "Lightmaster" 11 watt

U, B	E. Lx	F, Lx/ Watt	t, °C
200	1830	91.5	22.2
210	1772	87.0	23
220	1748	83.6	25
230	1708	78.2	26.5
240	1700	74.6	27



FIG. 6. LED lamp "Feron" 10 Watt

TABLE 6. Measurement results of the "Feron" 10 watt

U, B	E. Lx	F, Lx/ Watt	t, °C
200	1080	67.5	21.5
210	1055	65.2	22.5
220	1030	60.8	23
230	1000	58.0	25
240	1000	55.6	25.6



FIG. 7. LED lamp "Electro House" 10 Watt

TABLE 7. Measurement results of the "Electro house" 10 watt

U, B	E. Lx	F, Lx/ Watt	t, °C
200	1075	76.8	24.1
210	1051	71.5	26.3
220	1040	72.7	30
230	1028	68.8	32
240	1029	66.0	32.8



FIG. 8. LED lamp “KODAK” 10 Watt

TABLE 8. Measurement results of the “Kodak” 10 watt

U, B	E. Lx	F, Lx/ Watt	t, °C
200	460	85.2	16.8
210	680	101.2	18
220	1020	74.8	20
230	1330	68.0	22.3
240	1460	64.0	24



FIG. 9. LED lamp “Luxray” 11 Watt

TABLE 9. Measurement results of the “Luxray” 11 Watt

U, B	E. Lx	F, Lx/ Watt	t, °C
200	1493	74.7	21
210	1463	69.7	22.5
220	1465	121.1	22.5
230	1421	112.3	23.7
240	1405	65.0	25



FIG. 10. LED lamp "Jazzwau" 11 Watt

TABLE 10. Measurement results of the "Jazzwau" 11 watt

U, B	E. Lx	F, Lx/ Watt	t, °C
200	720	62.1	18.8
210	865	57.2	20
220	880	53.3	21
230	870	50.4	23
240	850	47.2	25



FIG. 11. LED lamp "Neo Max" 10 Watt

TABLE 11. Measurement results of the "Neo Max" 10 watt

U, B	E. Lx	F, Lx/ Watt	t, °C
200	720	62.1	18.8
210	865	57.2	20
220	880	53.3	21
230	870	50.4	23
240	850	47.2	25

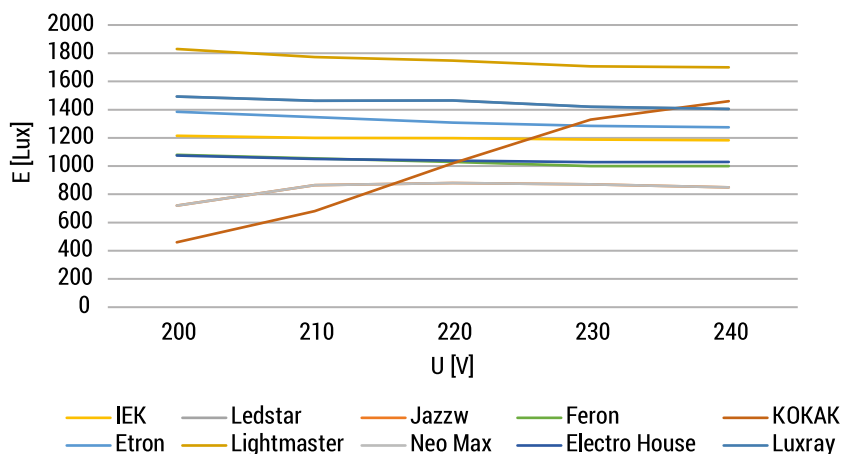


FIG. 12. Generalized research characteristics of modern lamps. Graphical dependence of light emission on the voltage of light sources of the brands “IEK”, “Etron”, “Ledstar”, “Lightmaster”, “Feron”, “Electro House”, “KODAK”, “Luxray”, “Jazzwau”, “Neo Max”

Analyzing the graphical dependence of light emission on voltage, we see that for some lamps the control scheme provides a constant level of light emission when the voltage changes in this range and is from 870 Lux to 1708 Lux at the nominal voltage (“IEK”, “Etron”, “Ledstar”, “Lightmaster”, “Feron”, “Electro House”, “Luxray”, “Jazzwau”), and for others, the light emission depends on the voltage and is from 850 Lux to 1330 Lux at the nominal voltage (“KODAK”, “Neo Max”).

The highest value of light emission at the nominal voltage was obtained for the “Lightmaster” lamp and it is 1700 Lux.

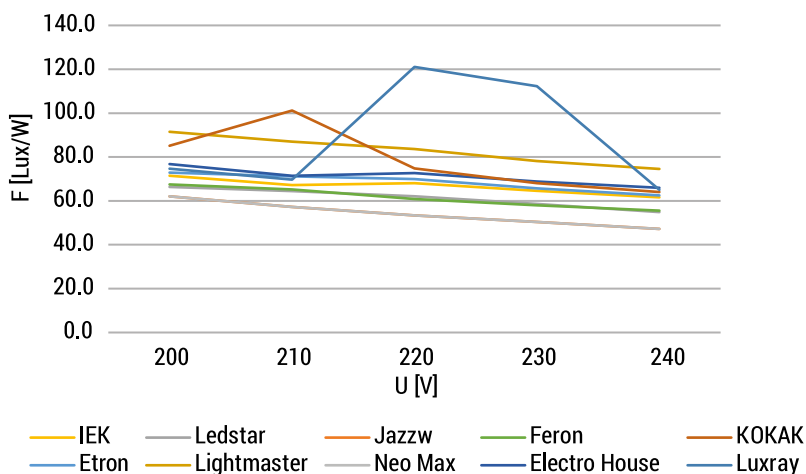


FIG. 13. Graphic dependences of light output on the voltage of light sources of the brands “IEK”, “Etron”, “Ledstar”, “Lightmaster”, “Feron”, “Electro House”, “KODAK”, “Luxray”, “Jazzwau”, “Neo Max”

Analyzing the graphical dependence of light output on voltage, we see that for some lamps the control scheme provides a constant level of light output when the voltage changes in this range and is from 50 to 78 Lux/W at the nominal voltage (“Neo Max”, “Feron”, “IEK”, “Etron”, “Ledstar”, “Lightmaster”, “Electro House”, “Jazzwau”), and for others, the light output depends on the voltage from 68 to 112 Lux/W at the nominal voltage (“Luxray”, “KODAK”).

The highest value of the dependence of light output on voltage at the nominal voltage was obtained for the Luxray lamp and it is 112 Lux/W.

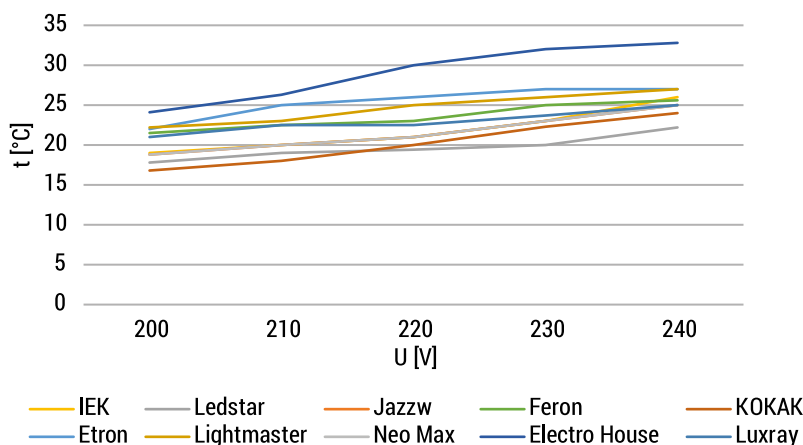


FIG. 14. Graphical dependences of the lamp heating temperature on the voltage of light sources of the brands “IEK”, “Etron”, “Ledstar”, “Lightmaster”, “Feron”, “Electro House”, “KODAK”, “Luxray”, “Jazzwau”, “Neo Max”

Analyzing the graphical dependence of the heating temperature of the lamps on the voltage, we see that for all lamps the heating temperature of the lamps depends on the voltage and increases smoothly from 16.8°C to 32°C (“IEK”, “Etron”, “Ledstar”, “Lightmaster”, “Feron”, “Electro House”, “KODAK”, “Luxray”, “Jazzwa”, “Neo Max”).

We obtained the highest value of the heating temperature of the lamps at the nominal voltage for the „Electro House” lamp, and it is 32°C.

Conclusions

Having conducted the analysis of the available modern light sources, it is possible to draw some conclusions.

Analyzing the graphical dependence of light emission on voltage, we see that for some lamps the control scheme provides a constant level of light emission when the voltage changes in this range and is from 870 Lux to 1708 Lux at the nominal voltage (“IEK”, “Etron”, “Ledstar”, “Lightmaster”, “Feron”, “Electro House”, “KODAK”, “Luxray”, “Jazzwa”, “Neo Max”) and for others, the light emission depends on the voltage and is from 850 Lux to 1330 Lux at the nominal voltage (“KODAK”, “Neo Max”).

Analyzing the graphical dependence of the heating temperature of the lamps on the voltage, we see that for all lamps the heating temperature of the lamps depends on the voltage and increases smoothly from 16.80C to 320C (“IEK”, “Etron”, “Ledstar”, “Lightmaster”, “Feron”, “Electro House”, “KODAK”, “Luxray”, “Jazzwa”, “Neo Max”).

Analyzing the graphical dependence of light output on voltage, we see that for some lamps the control scheme provides a constant level of light output when the voltage changes in this range and is from 50 to 78 Lux/W at the nominal voltage (“Neo Max”, “Feron”, “IEK”, “Etron”, “Ledstar”, “Lightmaster”, “Electro House”, “Jazzwau”), and for others, the light output depends on the voltage from 68 to 112 Lux/W at the nominal voltage (“Luxray”, “KODAK”).

We obtained the highest value of the heating temperature of the lamps at the nominal voltage for the “Electro House” lamp, and it is 32°C.

The highest value of light emission at the nominal voltage was obtained for the “Lightmaster” lamp and it is 1700 Lux.

The highest value of light output dependence on voltage at nominal voltage was obtained for the Luxray lamp and it is 112 Lux/W.

Based on the results of the experiments, we recommend the use of Luxray lamps, which have the highest indicators in this class (light output at nominal voltage is 112 Lux/W, $\cos\phi$ is 0.79).

References

1. Hoshko T.D., Hoshko M.O., Khimka S.M. et al., 2013, *Choosing a financial strategy as a direction of enterprise development*, Bulletin of the Kamianets-Podilskyi National Ivan Ohienko University, 8, 123–125 (in Ukraine).
2. Hoshko T.D., Hoshko M.O., Drobot I.M. et al., 2013, *Migration Policy in the Agrarian Sector of Economy*, Visnyk of Lviv National Agrarian University Agroengineering Research: Economics of AIC, 20(1), 420–423 (in Ukraine).
3. Hoshko M.O., Vasiliev K.M., Herman A.F. et al., 2013, *Mathematical model of the three-phase single-phase voltage modulator of the contactless excitation system of an asynchronous generator*, Visnyk of Lviv National Agrarian University Agroengineering Research, 17, 10 (in Ukraine).
4. Andrushko A., Hoshko M., 2014, *The quality characteristics of electric illuminants*, IOSR Journal of Humanities and Social Science, 19(1), 105–114.
5. Hoshko M.O., Khimka S.M., Syrotyuk V.M., 2015, *Results of experimental study of energy-saving dispenser of loose feed*, MOTROL. Motoryzacja i Energetyka Rolnictwa, 16D, 148–156 (in Polish).
6. Hoshko M.O., Khimka S.M., 2015, *Investigation of the characteristics of modern electric light sources by the example of CLL*, MOTROL. Motoryzacja i Energetyka Rolnictwa, 17(4), 61–66.
7. Goshko M., 2015, *Investigation of contemporary illuminants characteristics the led lamps example*, ECONTECHMOD. An International Quarterly Journal on Economics of Technology and Modelling Processes, 4(4), 63–70.
8. Goshko M., 2016, *Investigation of contemporary illuminants characteristics the led lamps example*, ECONTECHMOD. An International Quarterly Journal on Economics of Technology and Modelling Processes, 5(3), 205–210.

9. Hoshko M., Levonyuk V., Drobot I., 2016, *Investigation of the characteristics of modern electric light sources on the example of lamps for external illumination*, MOTROL. Motoryzacja i Energetyka Rolnictwa, 18(4), 17–20.
10. Hoshko M., 2017, *Energy supply under conditions of energy deficiency – use of the security electric LED lamps*, ECONTECHMOD. An International Quarterly Journal on Economics of Technology and Modelling Processes, 6(3), 205–210.

1.8. Modeling and optimization of 3D object recognition using neural networks

*Volodymyr Mykhailiuk¹, Andrii Zdobytskyi²,
Uliana Marikutsa³, Roman Trochimczuk⁴*

¹*Lviv Polytechnic National University, CAD Department, volodymyr.mykhailiuk.mknit.2022@lpnu.ua*

²*Lviv Polytechnic National University, CAD Department*

³*Lviv Polytechnic National University, CAD Department*

⁴*Bialystok University of Technology, Faculty of Electrical Engineering.*

Summary: The paper considers the existing means of scanning and optimization of the scanned models of 3D objects and the application of a neural network built on the latest PointNet architecture for optimization and further recognition of scanned 3D objects. The relevance of the research consists in the need to provide visual recognition of ground objects from unmanned aerial vehicles under the conditions of radar and thermal masking.

Keywords: 3D scanner, 3D object, optimization, object recognition, neural network, machine learning, PointNet

Introduction

In this research we will take a look at and compare 3D object scanning technologies and the application of neural networks for further optimization and recognition of scanned 3D objects. As we know, a 3D object scanner measures the distance to a target and stores collected data in the form of a point cloud. For recognition, the point cloud is usually converted into some other representation like voxel before it's fed into the neural networks. Such transformations, however, result in data that is excessively voluminous, and adding quantization to the 3D structure can also cause variation from natural artifacts. The PointNet method is based on direct consumption of point clouds and the output is the relevant classification of the image or segmentation.

The problem of 3D object shape recognition

Despite the constant development of unmanned vehicles, 3D objects shape recognition by them remains an urgent task. It is most necessary for unmanned aerial vehicles, which, due to the specifics of their work, must perform tasks in autonomous mode, without the participation of a human operator.

In September 2023, satellite images obtained from the Maxar company (Fig. 1) showed the placement of car tires on Tu-95 bombers located at the Engels-2 Russian military base [1].

Based on this information, SATIM conducted a SAR scan of the bombers, during which changes in the reflected signal were detected. The recorded characteristics of the reflected signal do not correspond to the geometry and material composition of the bombers.

In addition to masking using car tires, it was also noticed that images of airplanes were painted on the runway to mislead when observing the terrain from a satellite (Fig. 2) [2].



FIG. 1. Satellite image of the Tu-95 bomber at the Engels-2 air base



FIG. 2. Satellite image of the Tu-95 bomber decoy copies at the Engels-2 air base

Under the condition of the hypothetical usage of unmanned aerial vehicles to a depth similar to the location of this air base (>600 km) with the constant use of electronic warfare, the participation of a human operator in the process of objects recognition is impossible.

It is obvious that for effective use an unmanned vehicle must be autonomous. A key feature to ensure the autonomy of a unmanned vehicle is its ability to recognize a 3D object's shape without the intervention of a human operator. In addition, the recognition method must retain the ability to recognize when visual detection of 3D objects is countered by masking similar to the mentioned above.

Overview of technologies used in research

In the course of research, the following stages of optimization of the methodology of 3D object shape recognition using neural networks were determined:

1. Obtaining the geometry of the 3D object.
2. Comparison of the obtained geometry.
3. Initial optimization of the 3D object point cloud by scanning tools and further optimization by neural network.
4. 3D objects shape recognition using neural network.

For the implementation of optimization of the methodology of 3D object shape recognition using neural networks were used following technologies:

Polycam – one of the most popular 3D scanning apps for iOS, web, and Android. This program allows the scanning of the surrounding world using a mobile device, DSLR camera or drone to get sufficiently accurate 3D models.

Autodesk ReCap Photo – an Autodesk product for capturing 3D reality using photogrammetry.

EinScan-SE – a new generation 3D scanner. It uses structured light technology to create an accurate 3D image of an object.

A neural network built on PointNet architecture using the Python programming language used to optimize the methodology for 3D objects shape recognition.

PointNet neural network will take sets of points from a point cloud as input. A point cloud will be represented by a set of 3D points, where each point is represented by coordinates in 3 dimensions.

Let's take a closer look at the architecture (Fig. 3) of a neural network for classification and segmentation of 3D object shape. For the object classification task, the input point cloud directly selected from the figure or pre-segmented from the scene's point cloud. For the classification task, each of the n points in the classification neural network is mapped from three dimensions to 64 dimensions using a shared multi-layer perceptron. It is crucial that each of the n points share a single multi-layer perceptron. Similar to this, in the following layer, every n point is mapped from 64 dimensions to 1024 dimensions. Next we use max-pooling to create a global 1024 dimensional feature vector. After that, the global feature vector is mapped to k output classification scores using a three-layer fully connected neural network (FCNs) [3].

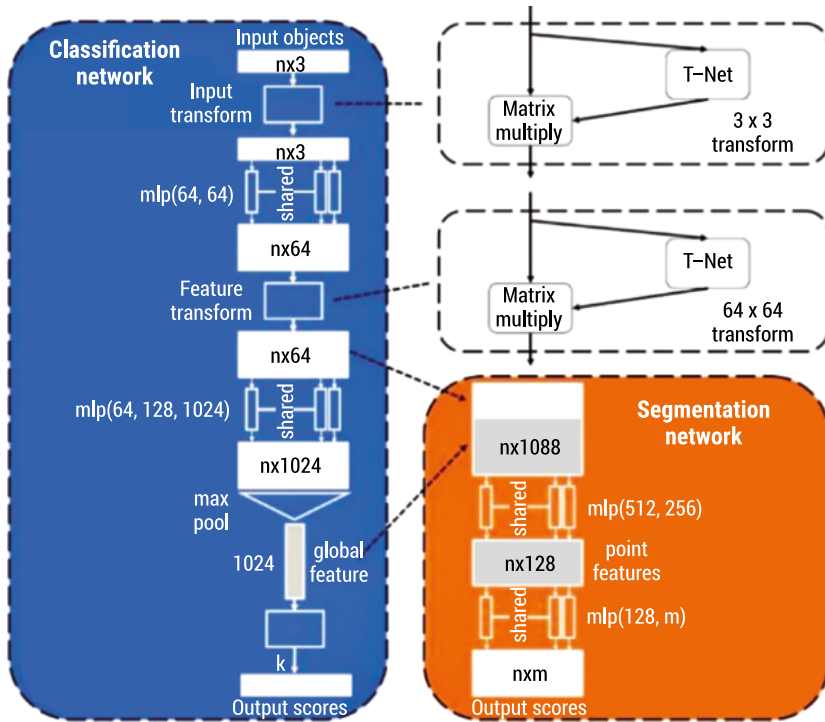


FIG. 3. Typical PointNet architecture

Implementation of the developed solution

A computer mouse was chosen as a 3D object for optimization of the methodology for 3D objects shape recognition using neural networks (Fig. 4).



FIG. 4. 3D Object used in research

The first scan was performed using the Polycam scanner program. Despite the fact that this program is not aimed at accurate scanning, the geometry of the object was preserved.

Polycam provides a wide range of formats for exporting the obtained model, including point cloud format (Fig. 5).

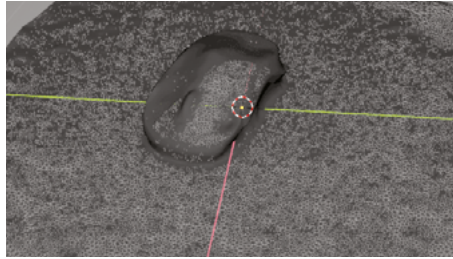


FIG. 5. Visualization of point cloud obtained using Polycam software

To obtain a 3D model of an object using photogrammetry in the Autodesk ReCap Photo environment, first must be taken detailed photographs after that they must be uploaded into the system. While using the same camera, in this case, the photogrammetry will be clearer due to the more advanced Autodesk ReCap Photo algorithms (Fig. 6).

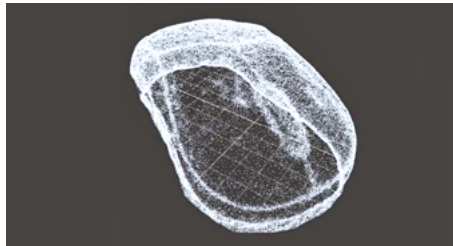


FIG. 6. Visualization of point cloud obtained using Autodesk ReCap Photo software

To obtain a 3D model of an object using a 3D scanner EinScan-SE, the object must be placed on the rotating platform of the scanner. After that the number of scans and the level of illumination must be adjusted. As a result, obtained model of a 3D object has a higher quality than obtained by previous methods (Fig. 7).

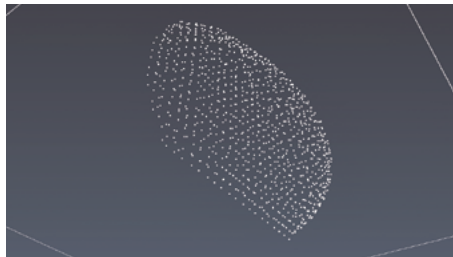


FIG. 7. Visualization of point cloud obtained using EinScan-SE scanner

On following graphs we can see the number of points in the point cloud obtained by various scanning environments (Fig. 8) and change of 3d object model quality based on the number of points in the point cloud (Fig. 9). Comparing the obtained results by such characteristics as the preservation of the shape, size and clarity of the image (which are represented on x-axis by numerical characteristic), we see that the quality of the model and the number of points is related by exponential distribution with the coefficient 0.99.

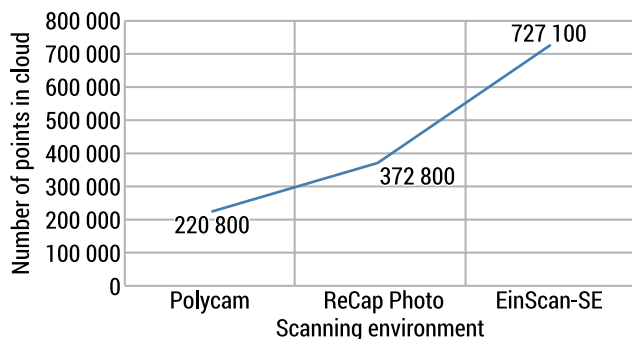


FIG. 8. Dependence of the number of points to scanning environment

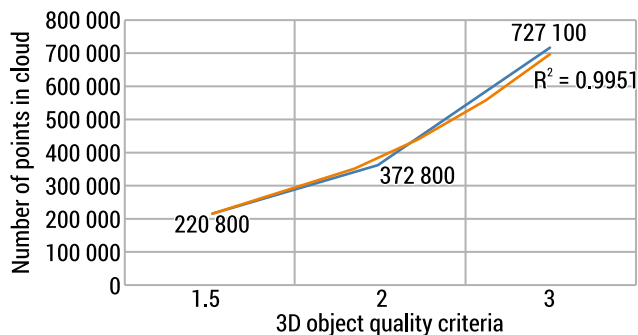


FIG. 9. Dependence of the number of points to model quality criteria

To optimize the obtained point clouds and provide 3D objects shape recognition a PointNet neural network was built. To train the neural network a dataset was used with scanned 3D objects – ModelNet10 [4], with the addition of the geometry of the computer mouse, obtained during the first part of the research.

The next step was to train PointNet neural network on this dataset for 20 epochs. As a result, after completing the training, the percentage of losses was reduced to 1.56% and the accuracy level of 3D object shape recognition was 85% (Fig. 10).


```

Epoch 1/20
98/98 [=====] - 386s 4s/step - loss: 3.3646 - sparse_categorical_accuracy: 0.3525
Epoch 2/20
98/98 [=====] - 361s 4s/step - loss: 2.7710 - sparse_categorical_accuracy: 0.4658
Epoch 3/20
98/98 [=====] - 423s 4s/step - loss: 2.6263 - sparse_categorical_accuracy: 0.5243
Epoch 4/20
98/98 [=====] - 419s 4s/step - loss: 2.4583 - sparse_categorical_accuracy: 0.5669
Epoch 5/20
98/98 [=====] - 344s 4s/step - loss: 2.4801 - sparse_categorical_accuracy: 0.4927
Epoch 6/20
98/98 [=====] - 381s 4s/step - loss: 2.2026 - sparse_categorical_accuracy: 0.6513
Epoch 7/20
98/98 [=====] - 357s 4s/step - loss: 2.1115 - sparse_categorical_accuracy: 0.6804
Epoch 8/20
98/98 [=====] - 409s 4s/step - loss: 2.0798 - sparse_categorical_accuracy: 0.6811
Epoch 9/20
98/98 [=====] - 372s 4s/step - loss: 2.1176 - sparse_categorical_accuracy: 0.6942
Epoch 10/20
98/98 [=====] - 404s 4s/step - loss: 2.0184 - sparse_categorical_accuracy: 0.7028
Epoch 11/20
98/98 [=====] - 382s 4s/step - loss: 1.9433 - sparse_categorical_accuracy: 0.7258
Epoch 12/20
98/98 [=====] - 348s 3s/step - loss: 1.9450 - sparse_categorical_accuracy: 0.7434
Epoch 13/20
98/98 [=====] - 335s 3s/step - loss: 1.8467 - sparse_categorical_accuracy: 0.7431
Epoch 14/20
98/98 [=====] - 350s 4s/step - loss: 2.2594 - sparse_categorical_accuracy: 0.7163
Epoch 15/20
98/98 [=====] - 339s 3s/step - loss: 1.8426 - sparse_categorical_accuracy: 0.7713
Epoch 16/20
98/98 [=====] - 340s 3s/step - loss: 1.7747 - sparse_categorical_accuracy: 0.7796
Epoch 17/20
98/98 [=====] - 340s 3s/step - loss: 1.7405 - sparse_categorical_accuracy: 0.7991
Epoch 18/20
98/98 [=====] - 361s 4s/step - loss: 1.7072 - sparse_categorical_accuracy: 0.8128
Epoch 19/20
98/98 [=====] - 345s 4s/step - loss: 1.6304 - sparse_categorical_accuracy: 0.8354
Epoch 20/20
98/98 [=====] - 355s 4s/step - loss: 1.5607 - sparse_categorical_accuracy: 0.8512

```

FIG. 10. Training of the neural network

To visualize the learning efficiency of the PointNet neural network, a graph of the reduction in the percentage of data loss (Fig. 11) and a graph of the increase in the accuracy of 3D objects shape recognition during 20 learning epochs (Fig. 12) are plotted.

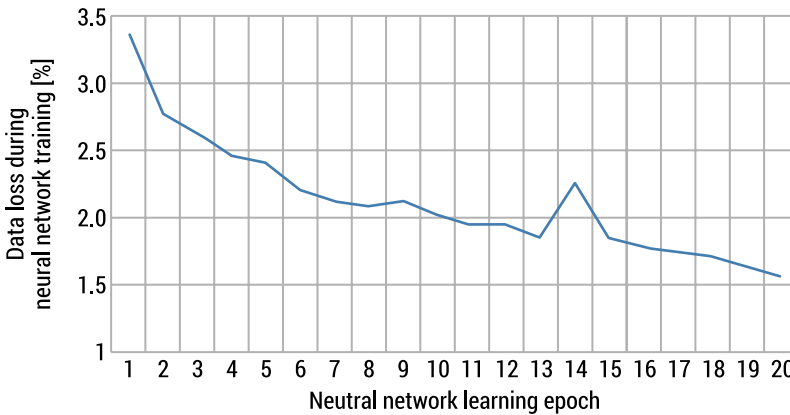


FIG. 11. Dependence of the data loss to neural network learning epoch

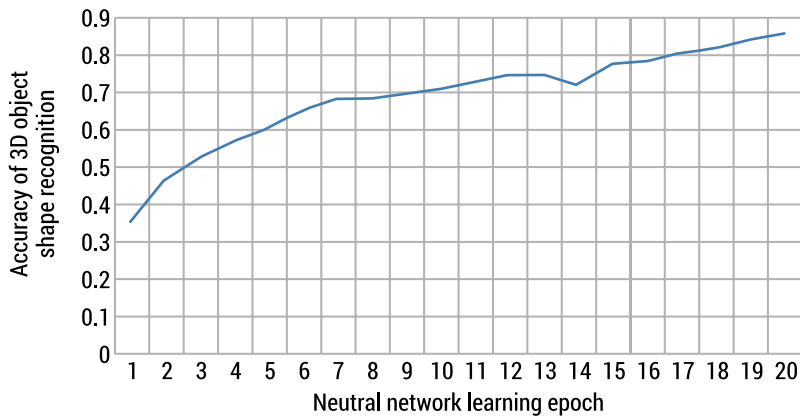


FIG. 12. Dependence of the recognition accuracy to neural network learning epoch

During the neural network testing, the point cloud was optimized: due to the selection of critical points, their number decreased from 727100 to 1000 (Fig. 13, Fig. 14)



FIG. 13. Point cloud before optimization



FIG. 14. Point cloud after optimization

As a result of 3D objects shape recognition, 7 out of 8 objects were successfully recognized, which confirms the recognition accuracy level of 85%, obtained during training (Fig. 15).

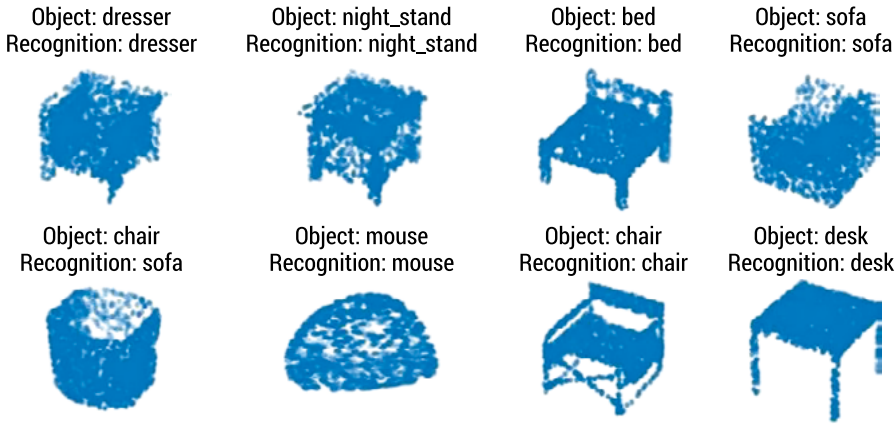


FIG. 15. Result of 3D objects shape recognition

Conclusions

In the course of the research, modeling and optimization of 3D object shape recognition processes using neural networks was carried out.

The current problem of recognizing the shape of 3D objects has been studied.

At the stage of obtaining the geometry of a 3D object, three different environments for the formation of point cloud of 3D object model were used. After comparing the obtained results, it was determined that the environments that use the photogrammetry method to obtain the geometry of the object provide a better optimized result with a deterioration in the quality of preserving the geometry of the 3D object. Despite this, all obtained results are characterized by a large number of points in the cloud, which is a confirmation of the need to use the neural network for further optimization of the obtained geometry.

The advantage of the PointNet neural network is the direct processing of the cloud of points as input data, due to which the use of computing resources is significantly optimized.

After training the neural network on a data set, its performance was tested. During testing, the neural network optimized the input point cloud by selecting the critical points of the object (in the case of the computer mouse point cloud, the number of points decreased from 727100 to 1000) and recognized the shapes of 3D objects with an accuracy of 85%.

As a result, during the research, optimization of the methodology for 3D objects shape recognition using neural networks was performed. Obtained solution, when implemented in unmanned systems, can provide the autonomy (which they need to work in difficult conditions) due to the use of publicly available means of obtaining 3D objects geometry and the PointNet neural network for optimization and recognition of their shape.

References

1. Cotovio V., Mezzofiore G., 2023, *Russia is covering aircraft with car tires, potentially to protect them from Ukrainian drones*, CNN, <https://edition.cnn.com/2023/09/06/europe/russia-aircraft-car-tires-ukraine-drones-intl-hnk/index.html> [accessed: 6.09.2023].
2. Payne S., 2023, *Tu-95 Decoys Are Being Painted On Russian Air Base's Apron*, The Warzone, <https://www.thedrive.com/the-war-zone/tu-95-decoys-are-being-painted-on-russian-air-bases-apron> [accessed: 30.09.2023].
3. Qi C.R., Su H., Mo K. et al., 2017, *PointNet: deep learning on point sets for 3D classification and segmentation*, CVPR Papers, https://openaccess.thecvf.com/content_cvpr_2017/papers/Qi_PointNet_Deep_Learning_CVPR_2017_paper.pdf [accessed: 10.12.2023].
4. Wu Z., Song S., Khosla A. et al., 2014, *3D ShapeNets for 2.5D Object Recognition and Next-Best-View Prediction*, <http://3dvision.princeton.edu/projects/2014/3DShapeNets/ModelNet10.zip> [accessed: 10.12.2023].

Chapter 2

2.1. Modelling multi-bolted connections at the preloading state in a systemic approach

Rafał Grzejda¹

¹*West Pomeranian University of Technology in Szczecin,
Faculty of Mechanical Engineering and Mechatronics, Department of Mechanics,
rafal.grzejda@zut.edu.pl*

Summary: The paper deals with the modelling of multi-bolted connections under preload conditions in a systemic approach. A modelling procedure based on the finite element method is presented. According to it, the connection was treated as a combination of four subsystems: a bolt-nut set, a pair of joined components and a contact layer between them. The contact layer model used allows the actual mechanical properties of the contact joint to be taken into account. The application of the method is illustrated using the example of an asymmetric connection. First, its solid model was built, followed by a discrete model in which the bolt-nut set was replaced by a hybrid model with a non-deformable bolt head and nut and a deformable bolt shank. Finally, selected results of connection calculations are also provided. The utilitarian relevance of a systemic approach to modelling multi-bolted connections and the opportunities it delivers for connection assessment is presented.

Keywords: multi-bolted connection; systemic approach; contact joint; preloading state; finite element method

Introduction

Multi-bolted connections are used to mechanically fasten components in all fields of engineering, particularly in mechanical or civil engineering [1–4]. Nowadays, they are increasingly being applied to join not only steel, but also composite [5–7] or additively manufactured [8–10] components. Sometimes even polylactic acid bolts produced using the fused deposition modelling method are used [11]. Multi-bolted connections are therefore among the most popular detachable connections used in engineering practice.

The appropriate operation of multi-bolted connections depends on the correct stiffness of the contact joints present in them. Machine components forming multi-bolted structures are most often joined on machined surfaces. Their joining takes place not on the whole contact surface, but on a small part of it, depending on the texture of the surfaces, i.e. their roughness or waviness [12–14].

Any irregularities on the contact surface affect the stiffness of the contact joint and the stiffness of the entire assembled structure. As a result of the phenomena occurring at the interface of the components to be joined, multi-bolted connections by which component surfaces are joined must be regarded as non-linear systems. In the general case where a multi-bolted connection is preloaded and then loaded with an arbitrarily directed external load [15, 16], the stiffness is affected by physical phenomena occurring between the joined components in the normal and tangential directions [17]. In engineering calculations, the description of these phenomena is usually limited to considering only the constant coefficients of normal and tangential stiffness and friction in the contact model [6]. These values then remain constant over time across the contact area of the joined components. In fact, experimental validation of contact models shows that this simplified modelling approach leads to the need to estimate the stiffness of the contact model in order to converge the results of calculations and experimental tests [18].

The phenomena occurring at the contact of joined components for small values of pressures and deformations, for which the contact layer is highly ductile, can be described by non-linear relations between the normal displacements of the points of this layer and the normal pressure, and between the tangential displacements and the shear pressure. To formalise the description of these phenomena, it is necessary to adopt an appropriate model of the rough surface of the interacting bodies and their contact. For this purpose, both analytical [19, 20] and experimental [21, 22] approaches are used.

As analytical studies usually result in very sophisticated formulas characterising the mechanical properties of the contact, in this study it was decided to use experimental relationships for this purpose. The scope of the paper includes the preloading of the selected multi-bolted connection, i.e. the normal contact loading direction of the joined components. In this case, the contact features can be expressed by an exponential function, as in [21, 23, 24]. This function can then be incorporated into the modelling of the contact according to the concept of the so-called conventional third-body thin layer [25].

The use of the third-body concept is easy to implement in finite element modelling (FE-modelling). By knowing the actual characteristic of the normal stiffness of a given contact, it can be taken into consideration independently for each of the finite elements in the contact layer. In other words, each of these elements, depending on the given loading situation, can have a different value of the normal stiffness coefficient, which is not possible with traditional contact modelling using commercial finite element method (FEM) software.

Authors modelling contact joints usually use finite elements with conventional settings, according to which it is only possible to introduce constant values of the normal and tangential contact stiffness into the model. Jaszak [26] and Jaszak et al. [27] conducted numerical analyses to determine the contact pressure at the interface between a serrated or flat gasket and a flange in a pipe connection. They used TARGET 170 and CONTA 174 contact elements available in ANSYS software with standard

settings. The same type of finite elements and the same method for modelling contact joints were used in [28–31], among others. Authors using another popular commercial FEM software, ABAQUS, often assume contact properties as ‘hard’ contact in the normal direction without friction [32] or with friction [33]. The same is true for another FEM software, Midas NFX. In this case also, constant normal and tangential stiffness coefficients and a friction coefficient are inserted [34, 35]. In some works, the stiffness of the contact layer is not mentioned in detail in the modelling. It is then stated that the contact has been modelled in a standard way in the relevant software [36, 37, 38].

Compared to the literature review above, the idea of autonomously attributing a stiffness coefficient to each contact layer element depending on a given contact joint load is new. As mentioned above, to exploit this idea, it is necessary to examine the actual characteristic of a given contact joint. This paper presents a modelling process for multi-bolted connections based on the characteristic of a contact joint separated from the connection, the experimental study of which is described in [17]. The finite element method (using Midas NFX 2023 R1 software supplemented with additional calculation routines) was used to present a systemic approach to the modelling of multi-bolted connections.

System Modelling Procedure

Multi-bolted connections are connections consisting of several structural components. There are some elastic couplings between these components, which can be represented by the relation among the subsystems of the multi-bolted system. An example of a multi-bolted system is shown in Figure 1. It can be subdivided into the following subsystems: a pair of elastically coupled elements (component 1 and component 2), a contact layer between them and a bolt-nut set.

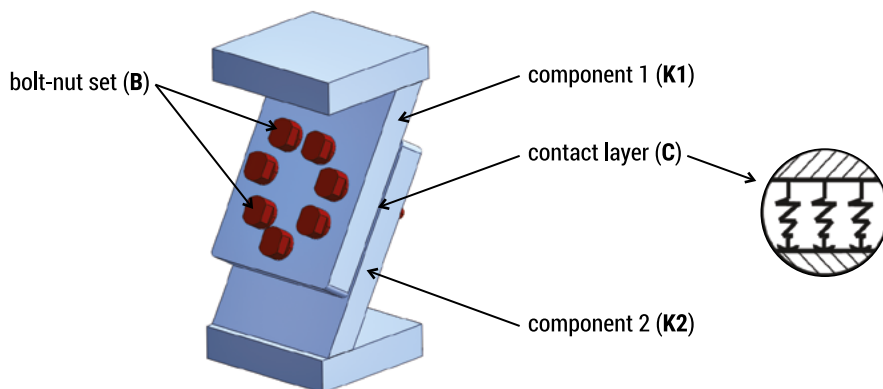


FIG. 1. Multi-bolted system and its subsystems

The following designations are assigned to the various subsystems of the multi-bolted system:

- B – bolt-nut set,
- $K1$ – component 1,
- C – j -element contact layer (for $j = 1, 2, 3, \dots, n$),
- $K2$ – component 2.

The joined components in multi-bolted connections are most often modelled using solid finite elements [26, 27, 39]. Such elements are also used in this paper.

A specific subsystem of the multi-bolted system is the bolt-nut set. This is because individual bolt connectors can be modelled in many different ways [40]. In this paper, a hybrid model has been chosen to simulate a single connector, consisting of a non-deformable head and nut connected by a deformable beam replacing the bolt shank (Fig. 2).

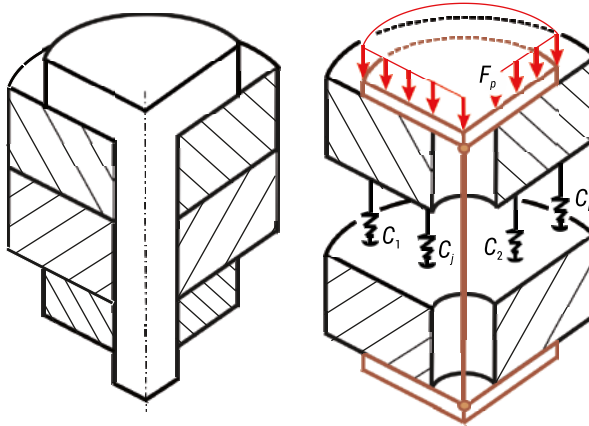


FIG. 2. Hybrid model of a single bolt connector

The contact layer can also be replaced by different finite models. If the multi-bolted connection is loaded only with preload forces F_p and therefore forces normal to the contact surface of the joined components, this layer can be treated as a non-linear Winkler model [41]. An example of such a model is shown in Figure 2, in which the stiffness of a single spring, i.e. an element of the Winkler model, is denoted by c_j .

The equilibrium equation for the multi-bolted connection model can be written as

$$K \cdot q = p, \quad (1)$$

where: K is the stiffness matrix, q is the displacements vector and p is the loads vector.

Once the division of the multi-bolted system into subsystems has been taken into account, Eq. (1) can be transformed into the form

$$\begin{bmatrix} K_{BB} & K_{BK1} & 0 & K_{BK2} \\ K_{K1B} & K_{K1K1} & K_{K1C} & 0 \\ 0 & K_{CK1} & K_{CC} & K_{CK2} \\ K_{K2B} & 0 & K_{K2C} & K_{K2K2} \end{bmatrix} \cdot \begin{bmatrix} q_B \\ q_{K1} \\ q_C \\ q_{K2} \end{bmatrix} = \begin{bmatrix} p_B \\ p_{K1} \\ p_C \\ p_{K2} \end{bmatrix}, \quad (2)$$

where: K_{xx} is the stiffness matrix of the X -th subsystem, K_{xz} is the matrix of elastic couplings between X -th and Z -th subsystems, q_x is the vector of displacements of the X -th subsystem and p_x is the vector of loads of the X -th subsystem, (X and Z are the symbols of the subsystems, $X = Z = \{B, K1, C, K2\}$).

The process of preloading the connection can be carried out according to the following principles:

- simultaneous tightening of all bolts,
- tightening of the bolts in a specific sequence in a single pass,
- tightening of the bolts in a specific sequence in several passes.

During preloading, the multi-bolted connection is loaded only with normal forces. Then, as a result of solving Eq. (2), the normal displacements of the non-linear springs are determined. Multiplying these by the stiffness of the springs yields the reactions in the springs R_{nj} . The linearisation of the characteristic of the non-linear springs is carried out using the secant method [24]. The calculation is performed in an iterative process involving the condition

$$\left| \frac{R'_{nj} - R_{nj}}{R_{nj}} \right| \leq e, \quad (3)$$

where: R_{nj} is the reaction in the j -th non-linear spring, R'_{nj} is the reaction in the j -th non-linear spring after the linearisation and e is the relative error.

Practical Implementation of the Method

The procedure for systemic modelling of multi-bolted connections and the benefits of such an approach are presented in the following subsections.

Selected Multi-Bolted Connection

A connection was modelled, the solid model of which is shown in Figure 3a. The thickness of the joined components is 28 mm and the height of the connection after assembly is 266 mm. The connection is made by means of seven M10×1.25 connectors preloaded simultaneously with a preload force F_p of 22 kN.

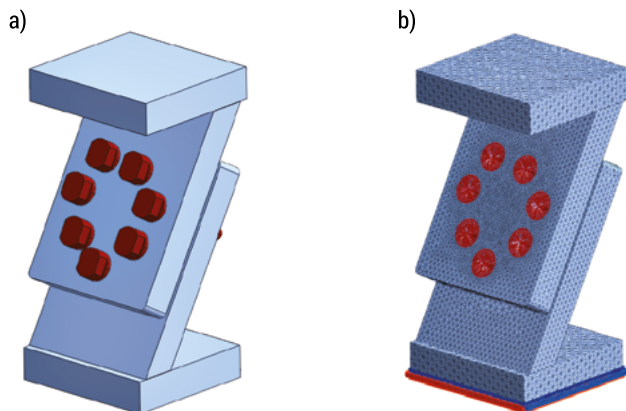


FIG. 3. Multi-bolted connection analysed as an example: a) solid model, b) discrete model

The connection is inclined from the horizontal by 60 degrees, so that in a later stage of the calculation (which will be presented in a separate paper) it is possible to load the connection with forces not perpendicular to the contact surface of the joined components. Selected experimental studies of this connection have been shown in [18, 42].

Characteristic of a Contact Joint Between the Connected Components

The contact joint of the connected components was tested on the INSTRON 8850 testing machine. Before starting the tests, the contact surfaces were machined on a grinding machine. The joint loading was carried out in the direction normal to the contact surface, and the relative displacements of the joined components were measured in two ways: by measuring the displacement of the testing machine heads using the machine software and separately using an INSTRON extensometer.

The tested joint was loaded and unloaded over several cycles. Finally, the characteristic of the tested component contact joint was determined for the last of the cycles of unloading. It can be assumed that then the final matching of the connected surfaces has taken place, and when evaluating the stiffness characteristic from the unloading curve alone, the influence of the contribution of plastic deformation between the connected components is neglected [43].

Investigation of the component connection on the testing machine is shown in Figure 4. In contrast, the course of the normal characteristic of a contact joint between the connected components is illustrated in Figure 5. The characteristic was prepared for a range of force variation from 0 to 160 kN, which did not lead to joint failure.

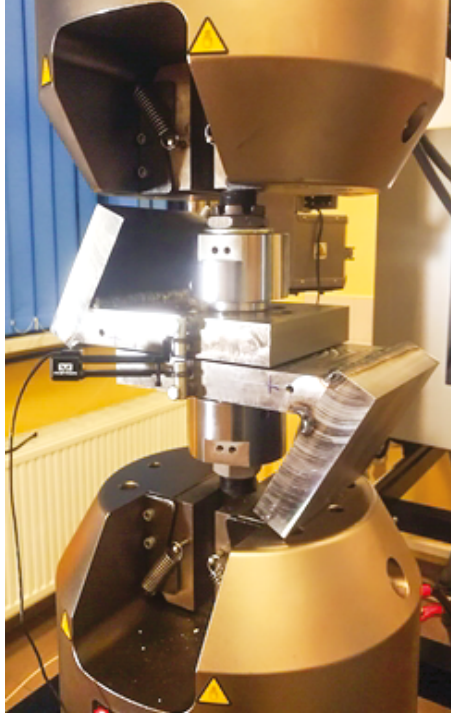


FIG. 4. Component joint investigation on the testing machine

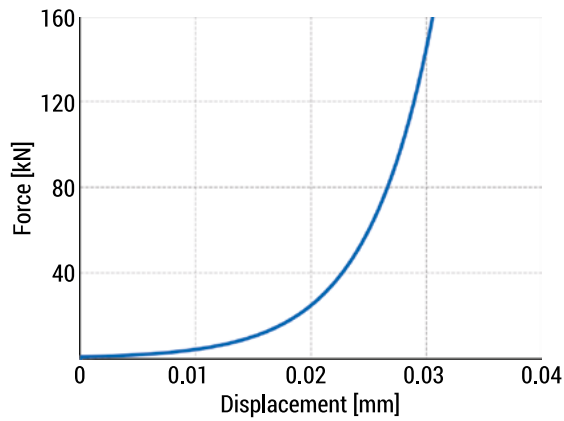


FIG. 5. Normal characteristic of a contact joint between the connected components

The waveform of the characteristic shown in Figure 5 was approximated by the following exponential function

$$F = 0.7257 \cdot e^{176,45 \cdot u}, \quad (4)$$

where: F is the loading force and u is the relative displacement of the components.

The coefficient of determination for the study variables R^2 was 0.873, which was at an acceptable level. The full process of determining the characteristic is placed in [17].

Selected Calculation Results

As examples of the calculation results, Figure 6 shows the reduced stress map in the components of the multi-bolted connection and the final distribution of forces in the bolts.

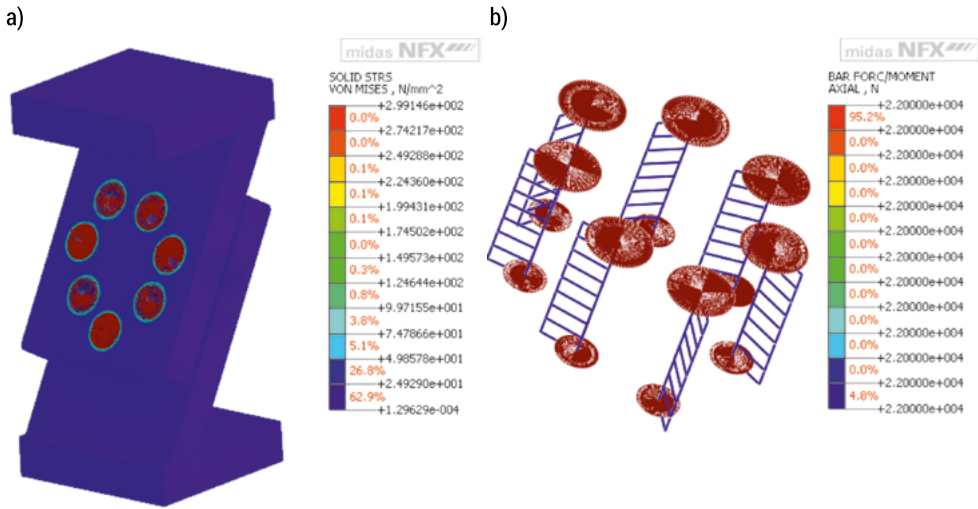


FIG. 6. Selected calculation results: a) reduced stress map in the components of the multi-bolted connection, b) final distribution of forces in the bolts

The maximum reduced stresses are less than the allowable values for the materials used to construct the multi-bolted connection [42]. The forces in the bolts at the end of the preloading process are equal, because all bolts in the connection have been tightened simultaneously.

Conclusions

In the paper, a systemic method for calculating multi-bolted connections with the use of experimental normal characteristic of the contact between the joined components is presented. The method is related to the preloading state of the multi-bolted connection, and the calculations were prepared taking into account the variability of the stiffness coefficients for each element of the contact layer. As a practical implementation of the method, calculations of a selected connection are shown, in the modelling of which previously published real contact characteristic was used.

The subsystems of a multi-bolted connection can be modelled using a variety of methods and models, in particular this applies to the bolt-nut set and the contact layer subsystem between the joined components.

The method also allows for preloading of the connection according to different methods, which include simultaneous tightening of the bolts and tightening of the bolts according to an assumed sequence in one or more passes.

The most important possible results that this method can lead to include the distribution of forces in the bolts and the distribution of pressures between the joined components during and at the end of the preloading process.

References

1. Gutowski P., Leus M., 2020, *Computational model of friction force reduction at arbitrary direction of tangential vibrations and its experimental verification*, Tribology International, 143, 106065.
2. Nowakowski M., Kurylo J., 2023, *Usability of perception sensors to determine the obstacles of unmanned ground vehicles operating in off-road environments*, Applied Sciences, 13(8), 4892.
3. Leus M., Gutowski P., Rybkiewicz M., 2023, *Effectiveness of friction force reduction in sliding motion depending on the frequency of longitudinal tangential vibrations, sliding velocity and normal pressure*, Acta Mechanica et Automatica, 17(4), 490–498.
4. Nowakowski M., 2023, *Perception technology for conversion of off-road vehicles for the purposes of unmanned missions*, Journal of Civil Engineering and Transport, 5(4), 15–27.
5. Prusinowski A., Kaczyński R., 2020, *Investigation of tribological and strength properties of ABS/CF fibrous composites formed in fused deposition modeling*, Journal of Friction and Wear, 41(4), 318–325.
6. Wysmulski P., 2022, *The effect of load eccentricity on the compressed CFRP Z-shaped columns in the weak post-critical state*, Composite Structures, 301, 116184.
7. Wysmulski P., 2023, *Numerical and experimental study of crack propagation in the tensile composite plate with the open hole*, Advances in Science and Technology Research Journal, 17(4), 249–261.
8. Śniezek L., Grzelak K., Torzewski J. et al., 2016, *Study of the mechanical properties components made by SLM additive technology*, in: *Proceedings of the 11th International Conference on Intelligent Technologies in Logistics and Mechatronics Systems*, 28–29 April 2016, eds. L. Koczy, D. Susnienė, D. Žostautienė, Panevėžys, Lithuania, 145–153.
9. Zdobytskyi A., Lobur M., Klymkovych T. et al., 2021, *Use of methods and technologies of additive production for optimization of parameters of designs*, IOP Conference Series: Materials Science and Engineering, 1016, 012019.
10. Šančić T., Brčić M., Kotarski D. et al., 2023, *Experimental characterization of composite-printed materials for the production of multirotor UAV airframe parts*, Materials, 16(14), 5060.
11. Kukla M., Sieracki I., Maliga W. et al., 2022, *Compression strength of PLA bolts produced via FDM*, Materials, 15(24), 8740.
12. Kostek R., 2013, *Analysis of the primary and superharmonic contact resonances – Part 1*, Journal of Theoretical and Applied Mechanics, 51(2), 475–486.

13. Zmarzły P., 2020, *Influence of bearing raceway surface topography on the level of generated vibration as an example of operational heredity*, Indian Journal of Engineering & Materials Sciences, 27, 356–364.
14. Zmarzły P., 2020, *Technological heredity of the turning process*, Tehnicki Vjesnik – Technical Gazette, 27(4), 1194–1203.
15. Smolnicki T., Derlukiewicz D., Stańco M., 2008, *Evaluation of load distribution in the super-structure rotation joint of single-bucket caterpillar excavators*, Automation in Construction, 17(3), 218–223.
16. Walczak R., Pawlicki J., Zagórski A., 2016, *Tightness and material aspects of bolted flange connections with gaskets of nonlinear properties exposed to variable loads*, Archives of Metallurgy and Materials, 61(3), 1409–1416.
17. Grzejda R., Kwiatkowski K., 2024, *Modelling of multi-bolted systems at the pretension stage – Part 1: Mechanical characteristics of the contact between the joined elements*, Archives of Metallurgy and Materials, 69(2), in press.
18. Grzejda R., Kwiatkowski K., Parus A., 2023, *Experimental and numerical investigations of an asymmetric multi-bolted connection preloaded and subjected to monotonic loads*, International Applied Mechanics, 59(3), 363–369.
19. Buczkowski R., Kleiber M., 2006, *Elasto-plastic statistical model of strongly anisotropic rough surfaces for finite element 3D-contact analysis*, Computer Methods in Applied Mechanics and Engineering, 195(37–40), 5141–5161.
20. Stupkiewicz S., Lewandowski M.J., Lengiewicz J., 2014, *Micromechanical analysis of friction anisotropy in rough elastic contacts*, International Journal of Solids and Structures, 51(23–24), 3931–3943.
21. Grzejda R., 2014, *Designation of a normal stiffness characteristic for a contact joint between elements fastened in a multi-bolted connection*, Diagnostyka, 15(2), 61–64.
22. Kucharski S., Starzyński G., 2019, *Contact of rough surfaces under normal and tangential loading*, Wear, 440–441, 203075.
23. Grudziński K., Kostek R., 2007, *An analysis of nonlinear normal contact microvibrations excited by a harmonic force*, Nonlinear Dynamics, 50(4), 809–815.
24. Grzejda R., 2021, *Finite element modeling of the contact of elements preloaded with a bolt and externally loaded with any force*, Journal of Computational and Applied Mathematics, 393, 113534.
25. Xiao H., Sun Y., 2018, *An improved virtual material based acoustic model for contact stiffness measurement of rough interface using ultrasound technique*, International Journal of Solids and Structures, 155, 240–247.
26. Jaszak P., 2019, *The elastic serrated gasket of the flange bolted joints*, International Journal of Pressure Vessels and Piping, 176, 103954.
27. Jaszak P., Skrzypacz J., Borawski A. et al., 2022, *Methodology of leakage prediction in gasketed flange joints at pipeline deformations*, Materials, 15(12), 4354.
28. Shi G., Shi Y., Wang Y. et al., 2008, *Numerical simulation of steel pretensioned bolted end-plate connections of different types and details*, Engineering Structures, 30(10), 2677–2686.
29. Cao J., Zhang Z., 2019, *Finite element analysis and mathematical characterization of contact pressure distribution in bolted joints*, Journal of Mechanical Science and Technology, 33(10), 4715–4725.
30. Wang H., Wu Q., Qian H. et al., 2019, *Buckling behavior of a circular steel tube with a bolt-ball joint under installation eccentricity*, Engineering Structures, 197, 109407.
31. Nia M.M., Moradi S., 2021, *Surrogate models for endplate beam-column connections with shape memory alloy bolts*, Journal of Constructional Steel Research, 187, 106929.

32. Sadowski T., Kneć M., Golewski P., 2010, *Experimental investigations and numerical modelling of steel adhesive joints reinforced by rivets*, International Journal of Adhesion and Adhesives, 30(5), 338–346.
33. Chybiński M., Polus Ł., 2021, *Experimental and numerical investigations of aluminium-timber composite beams with bolted connections*, Structures, 34, 1942–1960.
34. Grzejda R., 2022, *Thermal strength analysis of a steel bolted connection under bolt loss conditions*, Eksploatacja i Niezawodność – Maintenance and Reliability, 24(2), 269–274.
35. Grzejda R., Warzecha M., Urbanowicz K., 2022, *Determination of pretension in bolts for structural health monitoring of multi-bolted connection: FEM approach*, Lubricants, 10(5), 75.
36. Drygala I.J., Polak M.A., Dulinska J.M., 2019, *Vibration serviceability assessment of GFRP pedestrian bridges*, Engineering Structures, 184, 176–185.
37. Wymulski P., 2022, *Load eccentricity of compressed composite Z-columns in non-linear state*, Materials, 15(21), 7631.
38. Wymulski P., 2023, *Non-linear analysis of the postbuckling behaviour of eccentrically compressed composite channel-section columns*, Composite Structures, 305, 116446.
39. Bernatowska E., Ślęczka L., 2021, *Experimental and numerical investigation into failure modes of tension angle members connected by one leg*, Materials, 14(18), 5141.
40. Grzejda R., 2016, *New method of modelling nonlinear multi-bolted systems*, in: *Advances in Mechanics: Theoretical, Computational and Interdisciplinary Issues, Proceedings of the 3rd Polish Congress of Mechanics (PCM) and 21st International Conference on Computer Methods in Mechanics (CMM)*, Gdansk, Poland, 8–11 September 2015, eds. M. Kleiber, T. Burczyński, K. Wilde et al., Leiden, CRC Press, 213–216.
41. Kouretzis G., Wu J., 2021, *Recommendations for determining nonlinear Winkler spring parameters for buried steel pipe stress analysis applications*, Computers and Geotechnics, 135, 104196.
42. Grzejda R., Parus A., 2021, *Experimental studies of the process of tightening an asymmetric multi-bolted connection*, IEEE Access, 9, 47372–47379.
43. Oliver W.C., Pharr G.M., 2004, *Measurement of hardness and elastic modulus by instrumented indentation: Advances in understanding and refinements to methodology*, Journal of Materials Research, 19(1), 3–20.

2.2. Designing and strength analysis of a screw-type press for sunflower oil production

Vitaliy Korendiy¹, Oleksandr Kachur², Volodymyr Havran³

*¹Lviv Polytechnic National University, Institute of Mechanical Engineering and Transport,
Department of Technical Mechanics and Engineering Graphics,
contact author via email for correspondence vitalii.m.korendii@lpnu.ua*

*²Lviv Polytechnic National University, Institute of Mechanical Engineering and Transport,
Department of Technical Mechanics and Engineering Graphics*

*³Lviv Polytechnic National University, Institute of Computer Science and Information Technologies,
Department of Computer-Aided Design*

Summary: Sunflower oil is extremely important and widely used in the food industry, pharmaceuticals, cosmetology, and numerous technical fields. The main purpose of this research is to propose a novel design of a crew-type press for sunflower oil extraction and to analyze the stress-strain conditions of its certain components, particularly, connecting shaft and screw. Simulation results obtained in SolidWorks software show the distribution of equivalent stresses and deformations in the corresponding element.

Keywords: oil extraction; stress-strain state; simulation; SolidWorks software; deformation

Introduction

Currently, agriculture and, in particular, the production of oilseeds are relevant industries that play a key role in the world economy and food industry. Among various plants used to produce oil, sunflower (*Helianthus Annuus*) occupies one of the leading places. Sunflower is considered as one of the most affordable and important oilseeds in the world. Studies on sunflower oil are of great importance because these products are used not only in the food industry [1], but also in pharmaceuticals [2], cosmetology [3], and technical fields [4, 5]. It is a source of fats needed for human health, as well as a component of many other products. Sunflower oil has numerous beneficial properties and is used in various areas of life. The use of this oil in the diet helps to provide the body with the necessary fatty acids and promotes the health of the heart and skin [1, 6]. Sunflower oil is widely used in cooking while frying, salad dressing, sauce preparation, etc. [7]. It is used in cosmetics, and pharmaceuticals, as well as in the production of soaps and detergents [2, 3]. Sunflower oil can also be used for biodiesel

production [8]. This is important from an environmental point of view since biodiesel is less harmful to the environment than traditional fuel types. Sunflower oil is used for medical purposes, such as massage and treatment procedures [9]. It can also be used to make some medicines and drugs [10, 11].

Oil production presses are key equipment in the production of oil from different seeds, including sunflower, soybean, rapeseed, and others [12]. These presses provide the extraction of oil from the seeds by compression and separation of oil from the plant mass. The main components of the oil production presses include the following parts: squeeze shaft (screw, auger, worm) and compression chamber [13]. The screw (auger, worm) or squeeze shaft is the main part of the press that separates the oil from the seeds. It works at a large torque used for compression of the plant mass and separation of oil. The compression chamber is the place where the seeds are immersed, destructed, and compressed. In this chamber, the process of oil extraction is performed. Some presses are additionally equipped with built-in heating elements that help raise the temperature during compression. This can improve the output and quality of oil, especially from cold seeds [14]. As well, some presses are additionally equipped with filtration systems that help clean the oil from seeds and other particles [15].

Designing a screw-type press is a complex and multidisciplinary process that requires attention to details, experiments, and constant improvement to achieve optimal results in the production of quality oil from sunflower seeds. Here are the main tasks and stages that form the basis of designing a screw-type press to extract oil from sunflower seeds. The first stage is a thorough analysis of the requirements and needs for sunflower oil production [16, 17]. This may include production volume, oil quality, extraction efficiency (productivity), etc. The second stage is the development of the press concept, selection of the main components, such as screw size and design, type and size of the compression chamber, materials used, heating systems, filtration systems, etc. [18–20]. The third stage is the manufacturing of detailed models or prototypes to test the performance and efficiency of the press. This stage may include testing prototypes on different types of sunflower seeds, temperature conditions, etc. [21, 22]. In the following stage, there is performed the analysis of the tests and trials results, identifying weaknesses or opportunities for improvement, and modifying the design to achieve better performance and efficiency [23]. After completing the design and refining the press development concept, the next-level prototype or series of presses is manufactured for testing in real production conditions. The sixth stage involves conducting tests on the productivity, performance, and quality of the oil produced, as well as evaluation of costs, extraction ratio, and other factors to assess the efficiency of the press [24, 25]. The last stage of the oil production press is dedicated to the preparation of documentation with a description of the design, technical characteristics, and operating instructions [26, 27].

The present research is devoted to the second and third stages of the screw-type press development. Herewith, the main purpose is to propose a novel design of a press and analyze the stress-strain conditions of its certain components, particularly, connecting shaft and screw. After performing designing operations in the SolidWorks

software, the simulation of the loading conditions taking place during the pressing process is to be conducted in the Flow Simulation application, and the strain-state conditions are to be analyzed in the Simulation application with the help of the finite-element method (FEM). The latter has been effectively implemented in numerous similar investigations, e.g. [28–30].

General Design of the Developed Screw-Type Press

The general design of the developed household (domestic) press for extracting sunflower oil is shown in Figs. 1 and 2. The machine consists of the frame (base) 1, driving electric motor 2, worm-type gearbox 3, safety coupling 4 with rubber-bushed studs (pins), press body (pressing chamber) 5, screw (auger, worm) 6, discharging tray (chute, trough) 7, disc with holes 8 for oilcake pressure regulation, loading (charging, feeding) hopper 9, and intermediate connecting shaft 10. The latter is used to transmit the torque from the gearbox 3 output shaft to coupling 4 with the help of the keyed joints. To prevent breakage of the screw press drive elements under the conditions of sudden overloads exceeding the permissible value, the safety coupling 4 is used to automatically disconnect the output shaft of the gearbox 3 from the shaft 6 of the working member (screw, auger, worm). The proposed safety coupling 4 consists of two half-couplings (driving and driven). The studs (pins) with elastic (rubber) bushings pressed onto them are installed in the flange of the driving half-coupling. The elastic (rubber) bushings are fixed in the corresponding holes of the driven half-coupling during assembling.

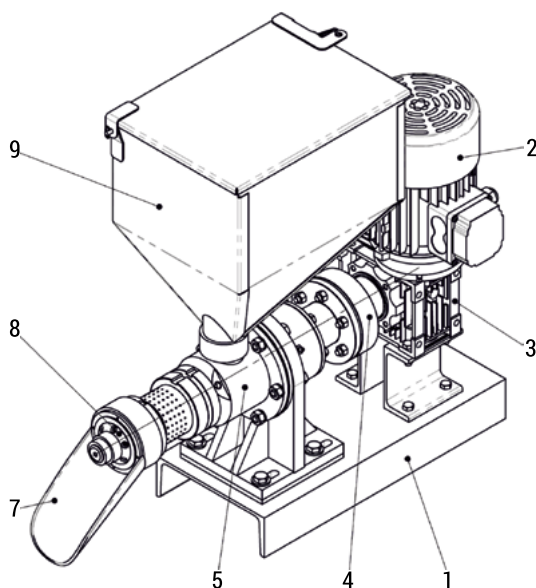


FIG. 1. General design of the developed screw-type press (in the assembled state)

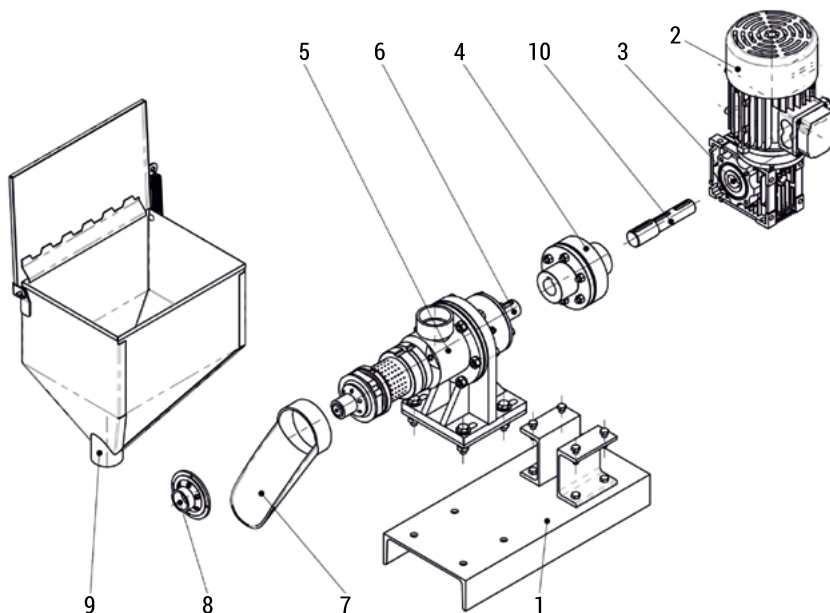


FIG. 2. General design of the developed screw-type press (in the disassembled state)

The proposed press is designed for small and medium-sized craft industries or households. It allows them to work on demand, extracting small batches of oils from different crops. The ideal usage cases can also be farm shops or organic food stores, where oil and other products are made right in front of customers' eyes from raw materials grown by a reliable supplier. This design provides the ability to process not only standard raw materials such as sunflower seeds, sesame seeds, etc. It allows working with more than 100 types of seeds, such as pomegranate, fig, palm, cactus, poppy, caraway, rapeseed, hemp, sea buckthorn, and many others. The nominal output of the proposed press varies in the range of 18...30 kg per hour and can be adjusted by changing the screw speed. The nominal consumed power of the drive is about 1.5 kW. The maximal rotation frequency of the screw does not exceed 60 rpm.

Simulation of the Stress-Strain State of the Press Drive

The screw (auger, worm) is made of AISI 420 (or X40Cr13) alloyed steel (see Figs. 3 and 4). Its maximal rotational speed is 60 rpm and the nominal torque does not exceed 240 N·m, which ensures the highest material pressure in the pressing chamber of about 20 MPa. A finite-element model of the screw was developed in the SolidWorks software using an adaptive (intelligent) mesh to simulate the hardest loading conditions. The following SolidWorks add-ons (applications) are used to perform finite element modeling of the stress-strain state of the screw: Simulation and Flow Simulation. While conducting the computer modeling of the sunflower husk pressing in the Flow Simulation software, there is created a new bulky (loose) material characterized by the corresponding

physical properties: the average width, thickness, length, and unit mass of the sunflower seed are 5.12 mm, 3.27 mm, 9.52 mm, and 0.049 g, respectively; at the moisture level within the range of 4–20% d.b., the bulk density is about 450 kg/m³, porosity is approximately 40%, and terminal velocity – about 6 m /s; the coefficient of friction takes the value of 0.5, and the angle of response is approximately of 38°. The experimental data of the sunflower husk pressing process modeled in the Flow Simulation application are exported to Simulation software.

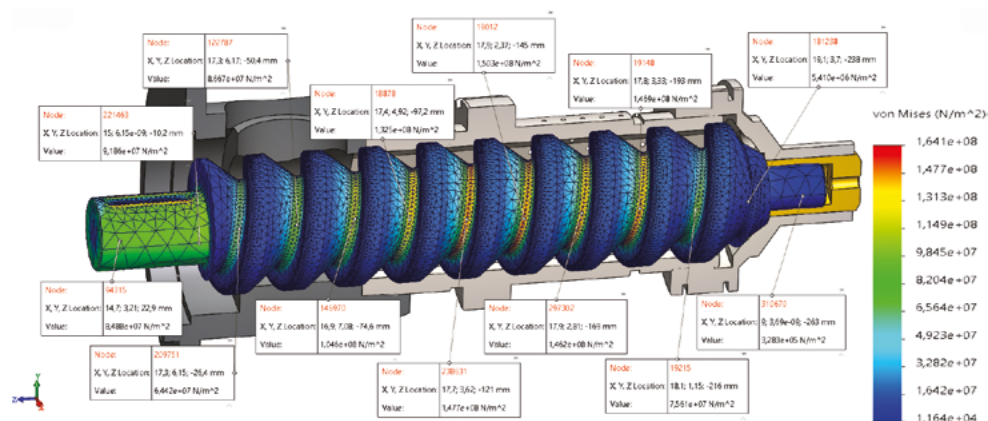


FIG. 3. Simulation of stresses distribution in the screw

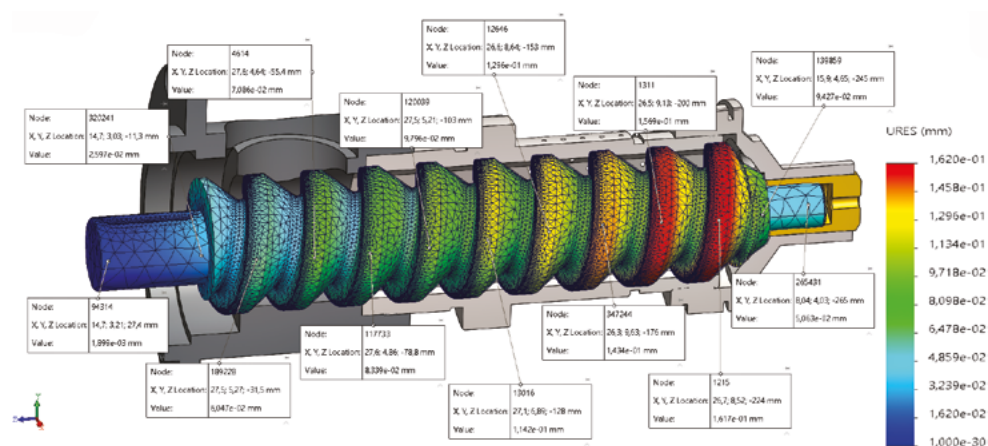


FIG. 4. Simulation of deformations of the screw

Based on the results of computer modeling carried out in the Flow Simulation application, the SolidWorks Simulation software performs the static analysis of the stress-strain state of the screw with the help of the finite-element method with adaptable mesh (see Figs. 3 and 4). The obtained results show that the maximal equivalent stresses are concentrated in the keyway zone, reaching values of more

than 160 MPa. Also, overloading (within 140...160 MPa) occurs in the central zones of the connection of the screw flights with its shaft, i.e., on the surface of the bottom dents of the screw flights. The results of the finite element modeling of the strain state of the pressing screw (Fig. 4) show that the largest deformations of the screw reach 0.16 mm and are observed on its front flights, which are the most loaded during the processes of destruction and compression of the sunflower seeds. The rear end, which is connected to the drive flange, is characterized by the smallest (almost zero) deformations.

The results of the simulation of the stress-strain state of the screw drive shaft, carried out using the finite element method in the SolidWorks software product, are shown in Fig. 5. Having fixed this shaft on the side surface of the internal keyway and applied the rated drive torque in the area of the external keyway, a static analysis of the stress-strain state of the drive shaft was carried out. The largest stress concentrator in this case is the fillet between two stages of the drive shaft, where the stresses of up to 200 MPa are observed. The largest torsional deformations of 0.07 mm occur at one of the shaft ends.

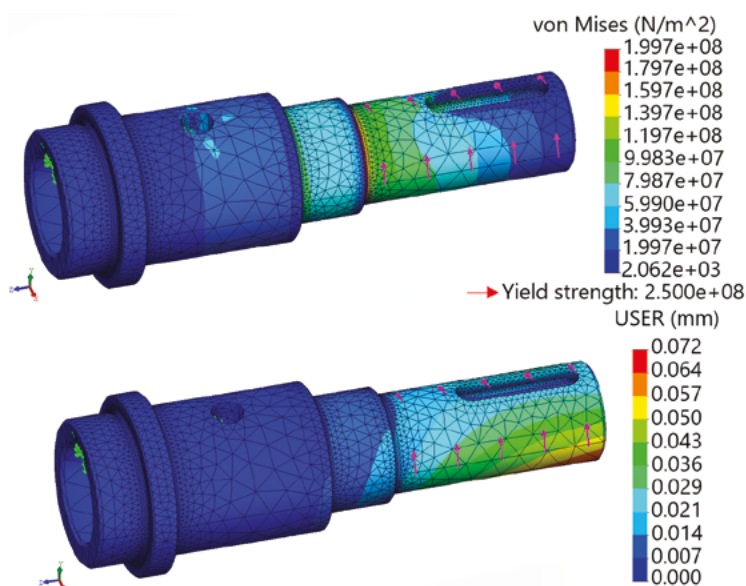


FIG. 5. Simulation of the stress-strain conditions of the screw connecting shaft

Conclusions

The research is focused on the novel design of the screw-type press for sunflower oil extraction. The stress-strain conditions of its components, particularly, connecting shaft and screw, are simulated using the finite element method in SolidWorks software. The maximal deformations and stresses are analyzed. The latter do not exceed

the yield strength of the material used for manufacturing the corresponding parts. Further research may deal with studying the press efficiency and the quality of the oil produced.

References

1. Tonolo F., Coletta S., Fiorese F. et al., 2024, *Sunflower seed-derived bioactive peptides show antioxidant and anti-inflammatory activity: From in silico simulation to the animal model*, Food Chemistry, 439, 138124.
2. Çokay H., Ögütçü M., 2023, *Determining the structure and stability of essential oil-sunflower wax and beeswax oleogels*, Journal of the American Oil Chemists' Society, 100(12), 993–1002.
3. Vujičić N.Š., Sajko J.S., Brkljačić L. et al., 2023, *Self-healing oxalamide organogelators of vegetable oil*, Gels, 9(9), 699.
4. Marriam F., Irshad A., Umer I. et al., 2023, *Vegetable oils as bio-based precursors for epoxies*, Sustainable Chemistry and Pharmacy, 31, 100935.
5. Bashiri S., Ghobadian B., Soufi M.D. et al., 2021, *Chemical modification of sunflower waste cooking oil for biolubricant production through epoxidation reaction*, Materials Science for Energy Technologies, 4, 119–127.
6. Aldamarany W.A.S., Taocui H., Liling D. et al., 2023, *Perilla, sunflower, and tea seed oils as potential dietary supplements with anti-obesity effects by modulating the gut microbiota composition in mice fed a high-fat diet*, European Journal of Nutrition, 62(6), 2509–2525.
7. Roufegarinejad L., Dehghani S., Bakshsi S. et al., 2024, *Oleogelation of sunflower-linseed oils with carnauba wax as an innovative strategy for shortening substitution in cakes*, Food Chemistry, 437, 137745.
8. Vishnual K.S., Ramadesigan V., Seethamraju S., 2024, *Biodiesel synthesis using spent FCC catalyst and CaO from a mixture of sunflower oil and oleic acid*, Bioresource Technology Reports, 25, 101714.
9. Kumar V., Kumar A., Mishra S. et al., 2022, *Effects of emollient therapy with sunflower seed oil on neonatal growth and morbidity in Uttar Pradesh, India: a cluster-randomized, open-label, controlled trial*, The American Journal of Clinical Nutrition, 115(4), 1092–1104.
10. Omrani I., Babanejad N., Shendi H.K. et al., 2017, *Preparation and evaluation of a novel sunflower oil-based waterborne polyurethane nanoparticles for sustained delivery of hydrophobic drug*, European Journal of Lipid Science and Technology, 119(8), 1600283.
11. Metin T.O., Yalcin A., 2023, *Vitamin D: An effective therapy against methotrexate-induced cardiotoxicity*, Tropical Journal of Pharmaceutical Research, 22(9), 1841–1847.
12. Kaur M., Sharma H.K., Kumar N., 2022, *Processing of oilseeds*, in: *Agro-Processing and Food Engineering*, eds. H.K. Sharma, N. Kumar, Springer, Singapore, 483–533.
13. Dotsenko N.A., Gorbenko O.A., Batsurovska I.V., 2023, *Investigation of constructive and technological parameters of an energy-efficient screw oil press*, IOP Conference Series: Earth and Environmental Science, 1254(1), 012135.
14. Gürdil G.A.K., Kabutay A., Selvi K.Ç. et al., 2020, *Investigation of heating and freezing pre-treatments on mechanical, chemical and spectral properties of bulk sunflower seeds and oil*, Processes, 8(4), 411.
15. Romanić R., 2020, *Cold pressed sunflower (Helianthus annuus L.) oil*, in: *Cold Pressed Oils*, ed. M.F. Ramadan, Elsevier, London, 197–218.

16. Demirel C., Herak D., Kabutey A. et al., 2021, *Analysis of oil point threshold indicators of bulk rapeseeds and sunflower seeds under compression loading*, Engineering for Rural Development, 20, 1679–1684.
17. Buffi M., Prussi M., Lotti G. et al., 2017, *Oilseed pressing and vegetable oil properties and upgrading in decentralised small scale plants for biofuel production*, International Journal of Oil, Gas and Coal Technology, 14(1/2), 91.
18. Jain D., Jain S., 2015, *Performance evaluation of screw-press oil expeller using a continuous spiral and decreasing length of pitch of screw*, Agricultural Engineering International: CIGR Journal, 17(1), 213–222.
19. Kabutey A., Herak D., Ambarita H. et al., 2019, *Modeling of linear and non-linear compression processes of sunflower bulk oilseeds*, Energies, 12(15), 2999.
20. Zhang Q., Zhang X., Sun S., 2018, *Simulation study on working performance of pressing cavity of household oil press based on EDEM*, Transactions of the Chinese Society of Agricultural Engineering, 34(24), 283–291.
21. Abdilova G., Sergibayeva Z., Orynbekov D. et al., 2023, *Influence of grinding degree and screw rotation speed on sunflower oil pressing process*, Applied Sciences, 13(17), 9958.
22. Dimić E., Premović T., Takači A., 2012, *Effects of the contents of impurities and seed hulls on the quality of cold-pressed sunflower oil*, Czech Journal of Food Sciences, 30(4), 343–350.
23. Mridula D., Saha D., Gupta R.K. et al., 2019, *Oil expelling of dehulled sunflower: Optimization of screw pressing parameters*, Journal of Food Processing and Preservation, 43(1), e13852.
24. Marušić V., Kljajin M., Marušić S., 2009, *An investigation of the economics of using welded layers for some parts of worm presses for the extraction of oil from sunflower seeds*, Materiali in Tehnologije, 43(2), 103–108.
25. Machate D.J., Melo E.S.P., Oliveira L.C.S. et al., 2022, *Oxidative stability and elemental analysis of sunflower (Helianthus annuus) edible oil produced in Brazil using a domestic extraction machine*, Frontiers in Nutrition, 9, 977813.
26. Shevchuk R., Sukach O., 2020, *Test of the modernized screw oil press*, Bulletin of Lviv National Agrarian University. Agroengineering Research, 24(1), 69–76.
27. Nyoni E., Akinlabi E.T., Madyira D.M., 2018, *Design and performance analysis of vegetable seed oil expellers: A review*, in: *Proceedings of the 11th South African Conference on Computational and Applied Mechanics*, South African Association for Theoretical and Applied Mechanics, Vanderbijlpark, South Africa, 17–19 September 2018, 616–626.
28. Lara-Ojeda L., Bohórquez O., González-Estrada O.A., 2021, *Numerical modeling of a domestic press for vegetable oil extraction using finite element analysis*, Journal of Physics: Conference Series, 2046(1), 012005.
29. Mansor M.N., Salleh S., Fauzi M.R. et al., 2023, *Total lifespan analysis of screw press using static and dynamic simulation*, AIP Conference Proceedings, 2530, 050009.
30. Kachur O., Korendiy V., Havran V., 2023, *Designing and simulation of an enhanced screw-type press for vegetable oil production*, Computer Design Systems. Theory and Practice, 5(1), 128–136.

2.3. Investigation of orthopedic constructions fracture using CAE technologies and the acoustic emission method

Olena Stankevych¹, Andrii Zdobytskyi²

¹*Lviv Polytechnic National University, CAD Department, olena.m.stankevych@lpnu.ua*

²*Lviv Polytechnic National University, CAD Department*

Summary: The use of CAE systems in the known calculations showed the effectiveness and advantages of using endocrown structures for tooth restoration. A methodology for investigating the fracture dynamics of fixed dental orthopedic structures using the acoustic emission method has been developed. Based on the multi-parameter analysis of AE signals and the results of stress distribution modeling of the tooth-endocrown system, it was established that the fracture starts in the tooth root. The metal-ceramic endocrown restoration had the highest fracture resistance.

Keywords: orthopedic dentistry; finite element method; acoustic emission; endocrown; wavelet transform

Introduction

Today, computer-aided design, manufacturing, and engineering (CAD/CAM/CAE) systems are widely used in many areas of dental research (inlays, overlays, veneers, crowns, fixed partial dentures, full reconstruction of the oral cavity, etc.) [1]. If CAD/CAM systems are used for the aided design and manufacture of orthopedic structures using computer technologies, then CAE systems make it possible to study the mechanical behavior of such structures and biological systems under various load conditions.

Endocrown-type restorations are widely used for endodontically treated molar teeth with significant coronal structure loss [2]. The good aesthetics and mechanical performance and good adhesion of such restorations are the main advantages.

To increase the duration of operation of fixed orthopedic structures, it is important not only to ensure the preservation of the structural integrity of the teeth after treatment but also to effectively choose materials for prosthetics, choose the appropriate type of structure, etc.

The literature presents a significant number of studies of fixed orthopedic structures using the finite element method, which is the main tool of CAE systems [3–6]. For example, Lin et al. [4] estimated the risk of fracture for an endodontically treated premolar with MOD preparation and three restoration configurations. Simulations

were performed for three 3D finite elements (FE) models designed with ceramic inlay, endocrown, and conventional crown restorations using the ANSYS application. Dejak and Młotkowski [5] using the ANSYS application have studied the distribution of stresses in tissues and prosthetic restorations (the endocrowns and prosthetic crowns) during masticatory simulation. They established that molars restored with endocrowns are less prone to fracture than those with posts. Riera [6] used the ABACUS application to compare two models of restorations: post-model and endocrown-model. Stress calculation showed that the greatest stress, and therefore the risk of fracture, is at the root (Fig. 1). Moreover, in the post-model the fracture would take place lower in the root than in the endocrown-model.

Thus, the use of CAE systems in the performed calculations showed the effectiveness and advantages of using endocrown structures for tooth restoration. However, the question remains important: which element of the endocrown restoration fractures first due to the long-term effect of the load? Considering Rier's results, it can be assumed that the fracture of a such system starts in the tooth. To test this assumption, it is necessary to conduct experimental studies of structural materials and endocrown systems.

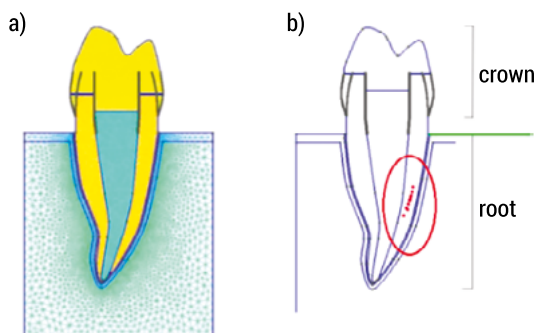


FIG. 1. Mesh of endocrown model (a) and model of the tooth with the center of gravity of the maximum stresses highlighted in red (b)

The Hertz indentation method simulates the loading conditions of dental restorations [7]. Compared to other experimental methods, its advantage in dentistry is that a clinically relevant mechanism of fracture can be determined.

To study the kinetics of the development of fracture in orthopedic structures during mechanical tests, the acoustic emission (AE) method is used, which is based on the generation of elastic waves due to the sudden local restructuring of the material structure [8–11]. The main informative parameters of AE signals in known studies were their amplitude and frequency characteristics. Recently, in the practice of AE signal processing, wavelet transform is widely used, making it possible not only to isolate the signal's frequency components but also to localize them in time. Such local analysis of AE signals can be effective for determining which components of orthopedic structures begin to fracture first.

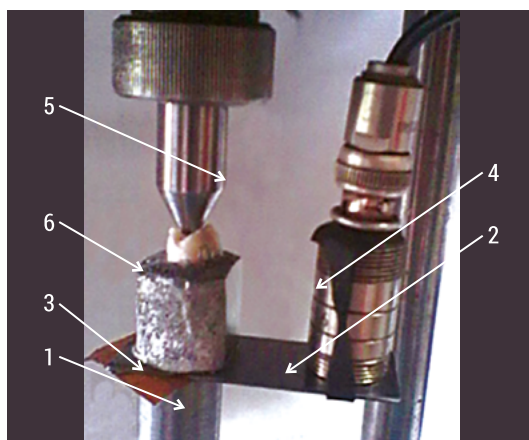


FIG. 2. Experimental setup (6 – the tooth restored by ceramic endocrown)

This study aims to investigate the characteristics of the fracture of fixed orthopedic tooth-endocrown structures during their local loading using the AE method and their comparison with the results of stress distribution modeling of the corresponding biomechanical system.

Materials and Methods

Materials. The main motivation for this study was to compare the endocrowns made of nontraditional (zirconia and metal-ceramics) and conventional materials (ceramics and composite resin) to find some benefits for the patients. The compression testing of materials used in the construction of endocrowns and different types of endocrown restorations was combined with the AE method.

Dental restorative materials used in this study were classified as Type 1: Group *B* – zirconium dioxide, Group *C* – ceramics, Group *D* – metal-ceramics, Group *E* – composite resin, and Group *F* – luting cement. Disc-shaped samples of the restorative materials 13 mm in diameter and 5 mm in thickness were used. Group *A* was the control group, it was teeth without restoration.

Twenty-five human molars were selected. Prepared teeth were used for manufacturing endocrown constructions with nontraditional and conventional materials. The endocrowns were adhesively cemented to teeth using luting cement. The restored and non-restored (Group *A*) molars were fixed in dental low-melting alloy Melot. The endocrown restorations were classified as Type 2: *BE* (with zirconium dioxide endocrowns); *CE* (with ceramic endocrowns); *DE* (with metal-ceramic endocrowns); *EE* (with composite resin endocrowns).

Experimental method. The Hertzian tests were performed at room temperature under a quasistatic compression load. The loading rate was 0.12 mm/min. Fig. 2 shows the scheme of the experimental setup. The sample 6 is mounted on the support 1.

A waveguide 2 and a special anti-friction gasket 3 are used between the sample and the support. An AE sensor 4 is attached to the waveguide with silicone grease. Load is applied to the center of the sample using the indenter 5.

Multiparametric analysis of AE signals. AGU-Vallen Wavelet software (Vallen Systeme) and software modules created in the MathCad were used for the AE signals multiparametric analysis. The continuous wavelet transform (CWT) is used to investigate the AE signals' structural features [13].

The parameters of AE signals, such as the maximum wavelet coefficient WT_{\max} , peak frequency f_{\max} , duration time Δt , bandwidth Δf , and energy E_{WT} were analyzed using the previously developed algorithm (Fig. 3) [14].

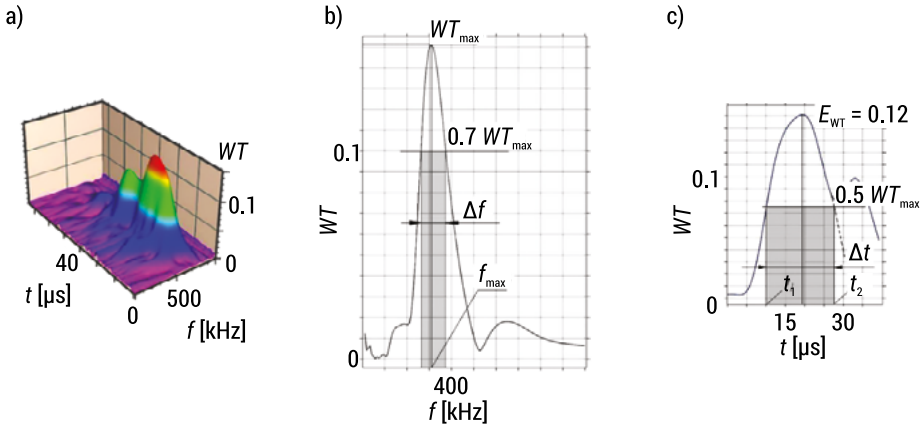


FIG. 3. The parameters of the AE signal local pulse using the CWT: 3D plot of wavelet spectrum intensity (a); 2D frequency (b) and 2D time (c) projections corresponding to the maximum magnitude WT_{\max}

The fracture types were identified by the proposed earlier energy criterion. It makes it possible to identify the AE signal which corresponds to plastic deformation ($E_{WT} \leq 0.01$); microcracking ($0.01 < E_{WT} \leq 0.1$); and macrocrack growth ($E_{WT} > 0.1$) [14].

Means and standard deviations of the number of events corresponding to the different fracture types (%) of samples were computed using the one-way ANOVA.

Results and Discussion

Analysis of the parameters of AE signals during tooth fracture. Fig. 4a shows the typical graph of the load and cumulative AE amplitude on the time. The intensive fracture in the tooth happened in the time interval 45...50 seconds from the start of the test, which the sharp decrease in the load in this time demonstrates. In this time interval, the peak frequency f_{\max} had two main bands: 120–130 kHz and 240–250 kHz (Fig. 4b).

Using the previously proposed algorithm for analyzing the features of AE signals based on the wavelet transform [14], the fracture types were identified.

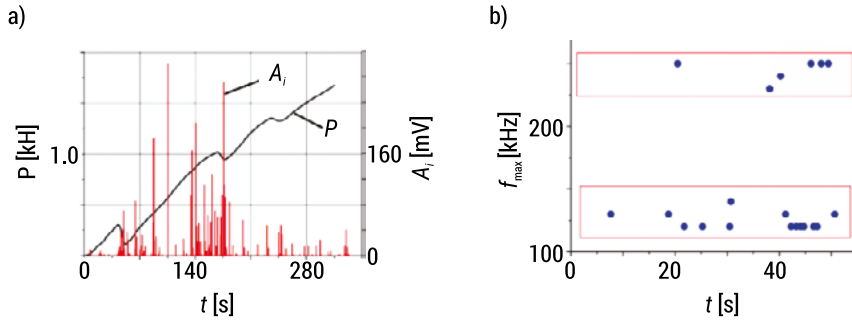


FIG. 4. The typical dependence of the load and cumulative AE amplitude on the time for the tooth specimen fracture (Group A) (a); the distribution of the peak frequencies f_{max} (b)

The investigated materials demonstrated very different acoustic properties. Fig. 5a shows the distribution of different types of failure of materials during compression loading.

A feature of the frequency distribution of AE signals obtained under fracture of the ceramic samples (Group C) is the presence of their two types: I – with one amplitude peak in the frequency band of 135...140 kHz; II – with the distribution of two peaks in the frequency bands of 135...140 and 250...260 kHz. AE signals with a frequency from the band 350...140 kHz had a larger amplitude.

For the metal-ceramic samples (Group D), three types of AE signals are distinguished: I – with one peak in the frequency band of 75...150 kHz; II – with two peaks in the frequency bands of 75...150 and 220...300 kHz; and III – with two peaks in the frequency bands of 75...150 and 450...500 kHz. Since the metal-ceramic sample contains a metal base, elastic deformations can occur in the sample under load action. Therefore, AE signals with higher frequencies (450...500 kHz) were generated under the action of compression load.

The specific feature of the distribution of spectral peaks of AE signals for composite resin samples (Group E) is the presence of two frequency bands of 125...175 (with maximum amplitudes) and 200...250 kHz. The fracture of composite resin samples started immediately after the load application.

For the luting cement samples (Group F), two types of AE signals are distinguished: I – with one amplitude peak in the frequency band of 110...140 kHz; II – with two peaks in the frequency bands of 110...140 and 225...300 kHz. The AE signals with the frequency from the band of 110...140 kHz had the maximum amplitude.

For the number of events corresponding to the brittle fracture (Fig. 5a), the investigated materials can be arranged in this order (from smallest to largest): Group D < Group E < Group A < Group F < Group C.

During the fracture of ceramics, composite resin, and luting cement samples under quasistatic compression loading, the micro- and macrocracking (brittle fracture) alternated. The dominant fracture mechanism for these materials was macrocracking. The spectral characteristics of AE signals detected during the compression test of the metal-ceramic samples were distinguished by the presence of three peak

frequency bands. The main fracture mechanism of metal-ceramic samples was microcracking (Fig. 4a). AE signals were not detected during the test of the zirconium dioxide samples (Group B), and the samples were not fractured.

Features of AE signals during fracture of different endocrown restorations.

Next, the acoustic peculiarities of the endocrown restorations were studied. For all endocrown systems, the AE signals had two peak frequency bands: 240–250 kHz and 400–450 kHz. The AE signals during tooth fracture had the same spectral characteristic. By the criterion of identification of the fracture type of materials [14], micro- and macrocracking with plastic deformation alternate during the fracture of the specimens of Groups BE, CE, and DE. At the same time, the macrocracking was the main fracture mechanism (Fig. 5b). The specimens of Group EE were fractured without plastic deformation, which indicates their highest brittleness.

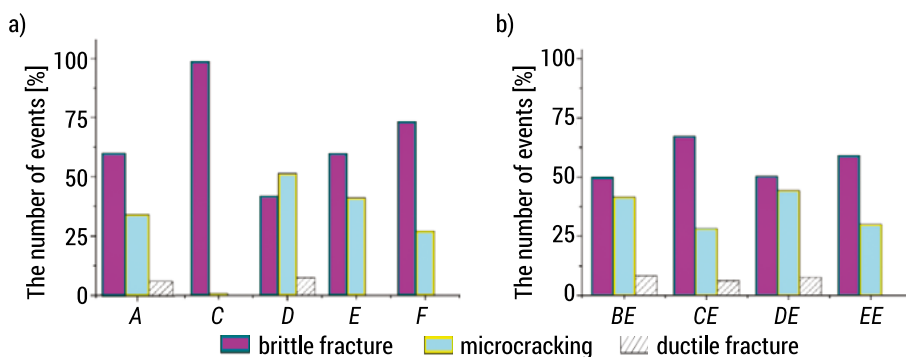


FIG. 5. Distribution of the number of AE events for the different fracture types (%) of Type 1 (a) and Type 2 (b) samples

For the number of events corresponding to the brittle fracture (Fig. 5b), the investigated endocrown systems can be arranged in this order (from smallest to largest): Group DE (50.2%) < Group BE (50.4%) < Group A (59.2%) < Group EE (62%) < Group CE (67%).

Thus, the investigated materials for endocrown restorations had different acoustic properties. At the same time, the acoustic properties and fracture kinetics of the endocrown restorations during compression were similar. Considering the peculiarities of tooth fracture (Group A) it can be assumed that the fracture of all the restoration systems begins with tooth damage. The obtained results confirm known calculations performed using the finite element method of different CAE systems [3-6]. The fractured samples verify this hypothesis. For example, the fracture of the zirconium dioxide samples was not detected. At the same time, the endocrown from zirconium dioxide lost its strong support and cracked under stress due to the crack propagation in the tooth. The metal-ceramic endocrown restoration showed the highest fracture resistance [15].

Conclusions

Multiparametric analysis of AE signals demonstrates the peculiarities of the fracture of the endocrown restorations and their components.

The fracture of endocrown restorations initiates in the tooth. This is agreed upon by the modeling results performed using the CAE system.

The metal-ceramic endocrown restoration demonstrated the highest fracture resistance.

References

1. Constantiniuc M., Manole M., Bacali C. et al., 2021, *Benefits of using CAD/CAM technology in dental prosthetics*, International Journal of Medical Dentistry, 25(1), 124–131.
2. 2. Biacchi G.R., Mello B., Basting R.T., 2013, *The endocrown: an alternative approach for restoring extensively damaged molars*, Journal of Esthetic and Restorative Dentistry, 25(6), 383–390.
3. Hasan I., Frentzen M., Utz K. et al., 2012, *Finite element analysis of adhesive endo-crowns of molars at different height levels of buccally applied load*, Journal of Dental Biomechanics, 3(1), 1758736012455421.
4. Lin C.L., Chang Y.H., Pai C.A., 2011, *Evaluation of failure risks in ceramic restorations for endodontically treated premolar with MOD preparation*, Dental Materials, 27, 431–438.
5. Dejak B., Młotkowski A., 2013, *3D-Finite element analysis of molars restored with endo-crowns and posts during masticatory simulation*, Dental Materials, 29(3), e309.
6. Riera M., 2014, *Study of the risk of fracture and debonding in a tooth restored by a post and a composite core and another by an endocrown methodology using FEA*, Universite Catholique de Louvain.
7. Lawn B.R., Deng Y., Thompson V.P., 2001, *Use of contact testing in the characterization and design of all-ceramic crownlike layer structures: a review*, Journal of Prosthetic Dentistry, 86(5), 495–510.
8. Ereifej N., Silikas N., Watts D.C., 2008, *Initial versus final fracture of metal-free crowns, analyzed via acoustic emission*, Dental Materials, 24, 1289–1295.
9. Lin C.L., Kuo W.C., Yu J.J. et al., 2013, *Examination of ceramic restorative material interfacial debonding using acoustic emission and optical coherence tomography*, Dental Materials, 29, 382–328.
10. Liu X., Fok A., Li H., 2014, *Influence of restorative material and proximal cavity design on the fracture resistance of MOD inlay restoration*, Dental Materials, 30, 327–333.
11. Ortega V.I., Pumarega M.I.L., Nieva N. et al., 2015, *Adhesion study in metal-ceramic systems of dental restoration by acoustic emission*, Procedia Materials Science, 9, 477–483.
12. Karpenko Physico-Mechanical Institute of the NAS of Ukraine. *Acoustic emission system for non-destructive testing SKOP-8M*, https://www.ipm.lviv.ua/our_developments/our_developments_details_id=6.php [accessed: 24.11.2023].
13. Skalsky V.R., Stankevych O.M., Kuz I.S., 2018, *Application of wavelet transforms for the analysis of acoustic-emission signals accompanying fracture processes in materials (A survey)*, Materials Science, 54, 139–153.

14. Stankevych O., Skalsky V., 2016, *Investigation and identification of fracture types of structural materials by means of acoustic emission analysis*, Engineering Fracture Mechanics, 164, 24–34.
15. Skalskyi V., Makeev V., Stankevych O. et al., 2018, *Features of fracture of prosthetic tooth-endocrown constructions by means of acoustic emission analysis*, Dental Materials, 34(3), e46.

2.4. Automated design of fire detection devices body components

Vira Oksentyuk¹, Kostyantyn Kolesnyk², Andrii Kushnir³, Bohdan Kopchak⁴

*Lviv Polytechnic National University, Institute of Computer Science and Information Technologies,
Department of Computer-Aided Design Systems:*

¹vira.oksentyuk@gmail.com, ²kostyantyn.k.kolesnyk@lpnu.ua

*³Lviv State University of Life Safety, Department of Supervision-Preventive Activity and Fire Automatics
andpetkushnir@gmail.com*

*⁴Lviv Polytechnic National University, Institute of Power Engineering and Control Systems,
Department of Electromechatronics and Computerized Electromechanical Systems,
bohdan.i.kopchak@lpnu.ua*

Summary: The master model of fire detector body components was designed and produced using CAX. The 3D model of the fire detector enclosure components was developed and improved by adding fasteners for the Arduino mini board, simulation modeling was carried out, and the lower cover of the fire detector was produced using a 3D printer. This will allow the carrying out of full-scale experiments of the fire detector and system.

Keywords: heat detector, computer added design, microcontroller, 3D-model, 3-D print

Introduction

Application of CAX systems for modeling, research and manufacturing of new body parts of a technical device allows for improvements of its structure and ensures functionality [1]. This approach allows you to develop a master model of the device in 3D and make a 3D print of its body parts [2]. They allow for 3D design of a technical device. However, it is advisable to prepare the model for 3D printing in the systems Ultimaker Cura, PrusaSlicer, Simplify3D, etc., whose software is free and oriented to most modern 3D printers that are in wide use. It is expedient to conduct simulation modeling of the functioning of technical devices in the MATLAB Simulink system, which allows you to develop a structural model and analyze the technical object at the functional-logical level.

Technical devices of intelligent systems in need of improvement include fire detectors (FD), which are part of the fire alarm system (FAS) [3]. One of the most effective methods of fire protection systems is the fire alarm system (FAS). The FAS consists of many components: fire detectors, monitoring and signaling devices, a control panel, an alert system, automatic control devices, backup power, and a monitoring

and control system [3]. FD generally consists of body parts, electronic control board and sensors.[4]. There are list of the FD body examples of optical-electronic smoke FD (Fig. 1).

To improve the functional capabilities of the fire alarm system, it is advisable to use modern algorithms for the hardware component operation of the fire detector [5–8]. Such algorithms of the hardware components operation improve the FD speed operation. Namely, it reduces the time of detection of ignition by thermal fire detectors. In [6], a fuzzy logic block for a multi-sensor fire detector with smoke and heat sensors is proposed and synthesized based on the theory of fuzzy logic with the Mamdani algorithm.

This makes it possible to detect ignition at an early stage and make the right decision on its elimination. In [7], a flame detector with IR and UV sensors was developed using fuzzy logic. A model of this multi-channel flame FD was developed in the MATLAB software.

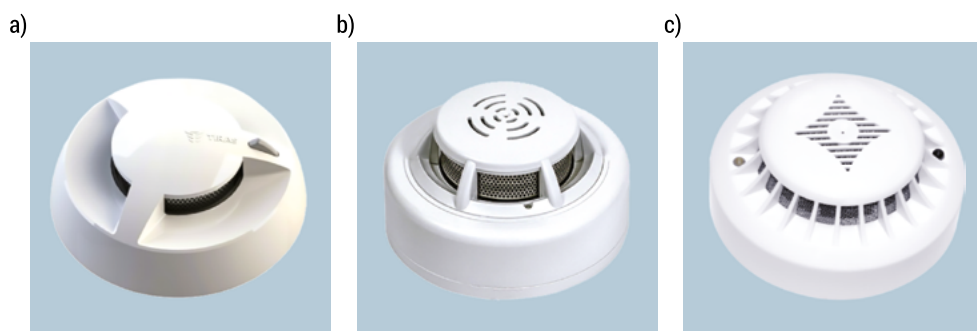


FIG. 1. Fire detectors body examples, a) DETECTO SMK110 – address detector Of the LLC “Tiras-12”, b) SPD2-Tiras is a non-addressable detector of the LLC “Tiras-12”, c) SPD-3 Elite – detector of the “Arton” PE company

The results of simulation studies showed that the fuzzy correction unit recognizes different stages of changes in the wavelength and the frequency of flickering and forms the necessary output signal based on the compiled rule base.

In [8], an improved self-organized radial-basis neural network integrating the fuzzy Takagi-Sugeno model was used to develop a three-channel infrared flame detector. The implementation of the FD algorithms is provided with the help of microprocessor technology. In particular, on the basis of the Arduino microprocessor technology using the C programming language, the hardware implementation of the fuzzy logic of the Sugeno thermal substation was carried out in [9]. For this purpose, a micro-controller based on the Arduino Mega 2560 hardware and computing platform using the C programming language was used.

In [10–13], the authors use an Arduino Uno board with various types of sensors to build intelligent fire detection systems. In [10], the system sends a message about a fire or a malfunction via a GSM modem, turns on the fire extinguishing pumps, gives

alarm signals and turns off the electricity supply to the house. In [11], the proposed system, after exceeding the threshold values of the controlled features, the microcontroller turns on the fan to remove smoke. At the same time, the Arduino sends information about the fire via the ESP8266 Wi-Fi module. In [12, 13], Mamdani's fuzzy logic is implemented on the Arduino Uno board. In work [14], the Arduino Nano board (Italy) was used only to collect information from various sensors and transmit them through the ESP8266 Wi-Fi module to the fuzzy logic controller module implemented on Android.

All these works demonstrate the relevance of improving algorithms for controlling the microprocessor FD component and the need to improve the design of the FD body parts. Therefore, improving the FD efficiency is possible due to the improvement of the algorithm of the FD hardware part and its implementation on the Arduinomini board. For this, it is necessary to improve the design of the FD body parts for the possibility of attaching Arduinomini-type microprocessor boards [9]. The process of modifying the design of the fire detector involves the development of a 3D model of the FD body parts, improvement of the model by adding Arduino board fasteners, simulation modeling and the production of a master model for further full-scale experiments of both the FD body parts and the FD as a whole. The purpose of the research is the 3D design of the FD body parts with the Arduino board and production of these parts using 3D printing technology and master model creation, engineering analysis and optimization of the fire detector design.

Section 1. fuzzy logic algorithm for microcontroller application.

To improve the functionality of the fire detector, it is advisable to use modern algorithms for the fire detector's hardware. For example, algorithm based on a controller with fuzzy logic.

A module based on the Arduino Uno platform was chosen for the study, it has compact dimensions and a low profile. Its basis is the Atmega328 microcontroller, which has the following characteristics: 32 KB of flash memory, 2 KB of RAM, 14 digital inputs/outputs (6 of them can be used as PWM channels), 8 analog inputs and support for popular interfaces and communication connection [9]. Such a hardware control algorithm will improve the fire detector's performance, namely reduce the time it takes to detect ignition by thermal fire detectors.

The mathematical basis of fuzzy logic follow [9]. To explore diverse fuzzy systems within the MATLAB/Simulink software suite, there exists a dedicated toolbox known as the Fuzzy Logic Toolbox. Utilizing this toolbox, fuzzy systems can be effectively represented and simulated through Simulink. This article explores the Sugeno fuzzy inference technique, often referred to as the Sugeno-Kang method, which is a shortened form derived from Takagi-Sugeno-Kang. An illustrative rule in the Sugeno fuzzy model of the first order, specifically when the membership functions of the output data are linear dependencies on two input signals:

IF Input1 = x and Input2 = y, THEN (output will be)

$$z = ax + by + c. \quad (1)$$

where ‘a’ and ‘b’ represent the coefficients of linear dependence on input signals, and ‘c’ is a constant.

In the context of the software implementation of a fuzzy block in the Arduino software environment, optimal outcomes are achieved when utilizing triangular and trapezoidal-shaped membership functions. The triangular curve serves as a membership function and relies on three scalar parameters: a , m , and b , denoted as:

$$\mu_A(x; a, m, b) = \max(\min(\frac{x-a}{m-a}, \frac{b-x}{b-m}), 0). \quad (2)$$

Parameters a and c establish the “legs” of the triangle, and the parameter m denotes the peak.

The trapezoidal curve functions as a membership function and relies on four scalar parameters: a , b , c , and d , as illustrated

$$\mu_A(x; a, b, c, d) = \max(\min(\frac{x-a}{b-a}, 1, \frac{d-x}{d-c}), 0). \quad (3)$$

Parameters a and d establish the location of the “feet” of the trapezoid, while parameters b and c define the “shoulders”.

In [9] our team created a fuzzy Sugeno controller model with two inputs and the determined specifications. The parameters for the membership functions are specified in [9] also.

Based on the previously formulated and tested fuzzy block model in MATLAB/Simulink, it was implemented using the C programming language on the Arduino Mega 2560 board. Arduino software has many advantages, the most important of which is the ability to connect a wide range of modules and sensors to Arduino; the ability to work on different operating systems. The Arduino Mega 2560 board is powered by the Atmel ATmega 2560 microcontroller, operating at a quartz frequency of 16 MHz. In the Arduino software suite, leveraging the established mathematical foundations (1)–(3), we executed the hardware implementation of the proposed zero-order fuzzy Sugeno block with two inputs. Post-Arduino board programming, experimental investigations were conducted by altering the potentiometer voltage input on the board from 0 to 5 V, with the fuzzy block generating a signal.

The Arduino’s calculations yielded an error margin of less than 2.5%. This discrepancy stems from the Arduino’s data bit size, where float variables are utilized alongside an 8-bit digital-to-analog converter. One could augment the bit size by employing a variable of type double float, albeit at the expense of reduced microcontroller speed. The fuzzy block’s complete cycle execution time is 0.004 s, yet operational velocity can

be marginally enhanced through software optimization. Consequently, the implementation of the maximum heat detector's fuzzy logic block with the Arduino board's fuzzy Sugeno block is achieved.

Section 2. Design and Engineering analysis of FD body.

The following software for automated design was used to solve the problem of 3D modeling [15] of FD body parts with an Arduino board. Fusion 360 is a free platform for 3D CAD, modeling, industrial design and mechanical engineering. Blender is a software package for creating 3D computer graphics. Cura is an open source slicing application for 3D printers and 3D printing.

Stages of the design of fire detector body parts, which were performed in this work.

1. 3D modeling of the device in the BLENDER system software and obtaining.stl models for 3D printing in the Cura system.
2. 3D printing of FD body parts using the Cura software and obtaining a master model of the device.
3. Engineering analysis and optimization of FD body parts in the Fusion 360 software system.

In the BLENDER environment, the upper cover and the FD base body were created (Fig. 2). Also, special legs for mounting an Arduino Mini board measuring 33x18 mm were designed and placed on the base. To implement the next stage (obtaining a master model of the device) creation of a master model of the FD body parts using the Cura software environment. The production of the FD body part master model took place on the basis of the equipment of the Department of Automated Design Systems of the "Lviv Polytechnic" National University. In particular, the Ender 3 Max 3D printer was used.

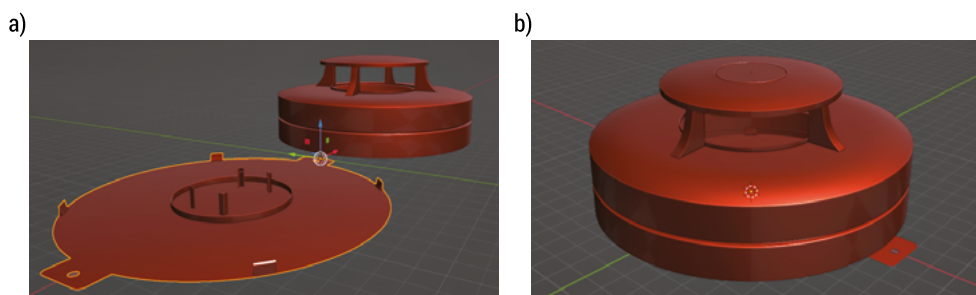


FIG. 2. The body created using the Cura software, a) the body in the disassembled state, b) the case in the assembled state

For the printing process, the CuraSlicer software 'Cura' [15] was successfully applied, which made it possible to prepare and adjust the printing parameters of body part models on a 3D printer, such as speed, layer thickness, filling, etc. After studying

the 3D model of the Fire Alarm, the following modifications were made to the settings of the basic profile of the Ender 3 max printer for PLA plastic. It was the production of the master model of the FD body. In particular, a master model of the F D base with new mounting elements for the Arduino board was 3D printed (fig 3).



FIG. 3. The result of 3D printing of the FD lower cover body with new fastening elements

Post-treatment was carried out using dichloromethane (DCM) solvent for products printed with certain types of plastics such as Acrylonitrile Butadiene Styrene (ABS) or Polycarbonate (PC).

Engineering analysis and optimization of fire detector body parts were carried out in the Fusion 360 software [4] system during these researches. The process included the following stages: 3D construction of Fire Detector parts based on a printed master model (fig 4, a, b, c). Assembly parts of the FD in the Fusion 360. (fig 4, d). Thermal calculation of the fire detector in the temperature range of its operation based on the developed 3D model. Analysis and optimization of the design of the seat place for the Arduino board in the Fire Detector.

The dimensions of 3D models built in Fusion 360 correspond to the actual dimensions of the printed master model. The obtained 3D models allow the carrying out of research of various influences, in particular temperature. This is a significant advantage, as it does not require full-scale tests of a real sample and eliminates the risk of damage to finished master models. The results of modeling before the influence of temperature are taken into account for the correction of production of serial products.

For FD body parts, one of the main parameters of its functioning is the temperature class. Therefore, a study of the body part on the influence of temperature fluctuations of the external environment was carried out. Thermal calculation of the body parts of the fire detector in the temperature range of its operation (50–80°C). The results showed a satisfactory temperature distribution. The fixing elements and the details of the fire detector have been optimized as a result of engineering simulation of the seating position for the Arduino board in the fire detector.

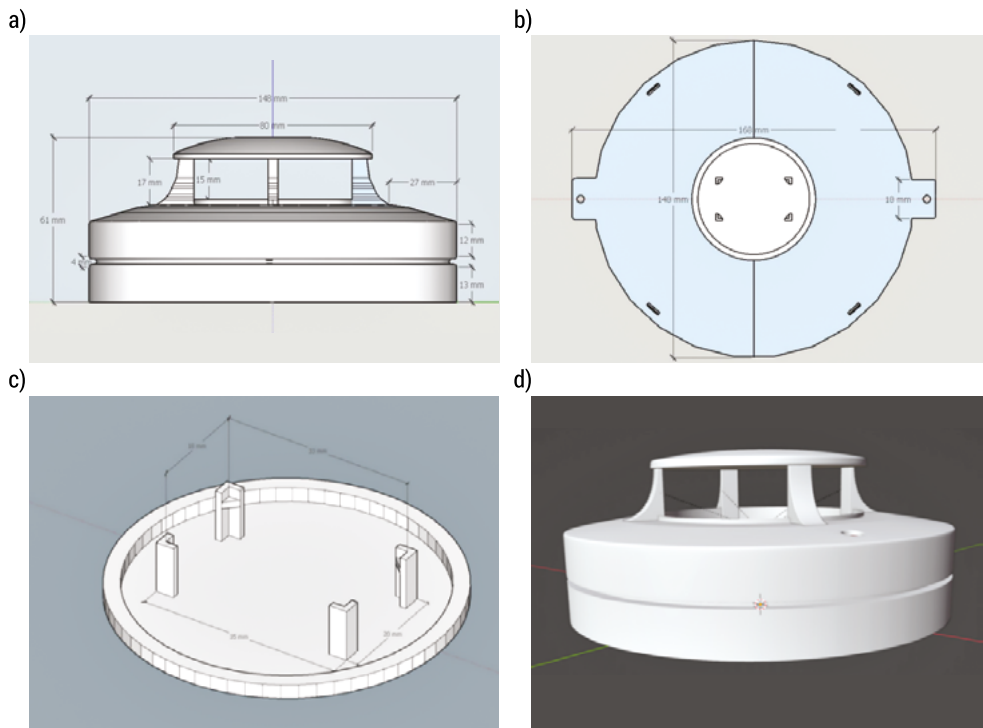


FIG. 4. 3D modeling results in the Fusion 360 system

In general, this paper presents the scientific, applied, and technical-technological results of 3D modeling of body parts of fire detection devices, the selection of modern software for the development and production of the master model. The obtained results will allow to improve the efficiency of the PS and will be useful in the field of 3D modeling and printing.

Conclusions

- The peculiarities of the fire detectors body parts design with the use of microprocessor control based on the Arduinomini board were analyzed.
- The main regularities of the new algorithm for controlling the FD hardware using a controller with fuzzy logic, implemented with the help of Arduinomini microcontroller control, are given
- The design of the FD body parts was improved due to the addition of Arduinomini board fastening elements, and 3D modeling of Fire Detector details was done in Blender software
- 3D printing of Fire Detector details was implemented with the help of Cura software, and its corresponding master model was obtained.

- An engineering analysis and optimization of the fixing elements design in the details of the Fire Detector was carried out with the help of Fusion 360 software.
- The obtained master model will allow for the creation of a Fire Detector with an Arduino board for the implementation of the latest microprocessor control algorithms. It will also improve the performance characteristics of the Fire Detector, in particular the accuracy and speed of operation.

References

1. Nevliudov I., Yevsieiev V., Maksymova S. et al., 2023, *A Small-Sized Robot Prototype Development Using 3D Printing*, in: *XXXI International Conference CAD In Machinery Design Implementation and Educational Issues*, 26–28 October 2023, 12
2. Łukaszewicz A., Skorulski G., Szczebiot R., 2018, *Main aspects of training in the field of computer aided techniques (CAx) in mechanical engineering*, „Proceedings of 17th International Scientific Conference on Engineering for Rural Development”, 865–870.
3. Camba J.D., Contero M., Company P., 2016, *Parametric CAD modeling: An analysis of strategies for design reusability*, *Computer-Aided Design*, 74, 18–31.
4. CEN/TS 54-14:2018, *Fire detection and fire alarm systems – Part 14: Guidelines for planning, design, installation, commissioning, use and maintenance*.
5. Çetin A.E., Merci B., Günay O. et al., 2016, *Infrared Sensor-Based Flame Detection*, in: *Methods and Techniques for Fire Detection. Signal, Image and Video Processing Perspectives*, Academic Press, London, 47–59.
6. Kushnir A., Kopchak B., 2019, *Development of Intelligent Point Multi-Sensor Fire Detector with Fuzzy Correction Block*, in: *IEEE XVth International Conference on the Perspective Technologies and Methods in MEMS Design (MEMSTECH)*, Polyana, Ukraine, 22–26 May 2019, 41–45.
7. Kushnir A., Kopchak B., 2021, *Development of Multiband Flame Detector with Fuzzy Correction Block*, in: *IEEE XVIIth International Conference on the Perspective Technologies and Methods in MEMS Design (MEMSTECH)*, Polyana, Ukraine, 12–16 May 2021, 58–63.
8. Ziteng W., Linbo X., Hongwei F. et al. 2019, *Infrared flame detection based on a self-organizing TS-type fuzzy neural network*, *Neurocomputing*, 337, 67–79.
9. Kushnir A., Kopchak B., Oksentyuk V., 2023, *Development of Heat Detector Based on Fuzzy Logic Using Arduino Board Microcontroller*, in: *IEEE 17th International Conference on the Experience of Designing and Application of CAD Systems (CADSM)*, Jaroslaw, Poland, 22–25 February 2023, 1–5.
10. Okokpuije K., John S.N., Noma-Osaghae E. et al., 2019, *A wireless sensor network based fire protection system with SMS alerts*, *International Journal of Mechanical Engineering and Technology*, 10(02), 44–52.
11. Jeevanandham A.T., Sivamurgan P., 2020, *IoT Based Automatic Fire Alarm System*, *Bulletin of Scientific Research*, 2(1), 29–34.
12. Rehman A., Qureshi M.A., Ali T. et al., 2021, *Smart Fire Detection and Deterrent System for Human Savior by Using Internet of Things (IoT)*, *Energies*, 14.
13. Sarwar B., Sarwar Bajwa I., Ramzan S. et al., 2018, *Design and Application of Fuzzy Logic Based Fire Monitoring and Warning Systems for Smart Buildings*, *Symmetry*, 10(11), 615, 1–24.

14. Umoh U., Inyang U.G., Nyoho E.E., 2019, *Interval Type-2 Fuzzy Logic for Fire Outbreak Detection*, International Journal on Soft Computing, Artificial Intelligence and Applications (IJSCAI), 8(3), 27–46.
15. Manzhilevskiy O., Iskovich-Lototskiy R., 2021, *Modern additive technologies of 3D printing*. Features of practical application, Vinnytsia, 105.

2.5. Recycling product model and its usage in selected aspects of eco-design

Jacek Diakun¹

*¹Poznań University of Technology, Faculty of Mechanical Engineering,
Institute of Material Technology,
jacek.diakun@put.poznan.pl*

Summary: One of the issues that have recently gained importance in the design of products is the consideration of environmental properties. But in the CAD 3D systems one can find a very limited number of tools that are focused on analysis of a product's environmental properties, especially in order to assess the recycling properties of that product. In the paper the Recycling Product Model (RPM) is presented as the reference set of data and modeling mechanisms necessary to deal with recycling properties of the product model. The formal representation of RPM is defined. The functionality of the software for defining the RPM within the CAD 3D environment is presented with examples of demonstration models and case study of real product model. There are also presented potential ways of Recycling Product Model usage during design process.

Keywords: eco-design, design for environment, PLM, Product Lifecycle Management, circular economy

Introduction

Design is a complex process, where various issues are to be taken into account. This multidisciplinary approach is reflected in the term “design for X”. It encompasses a broad range of requirements, such as manufacturability, quality, safety, usability, and also environmental considerations. The latter is reflected by various terms, i.e. Design for Lifecycle, Design for End-of-Life and Design for Disassembly. One of the key issues in Design for Disassembly is modeling the products in order to assess their disassembly properties.

In response to growing concerns about climate change, resource depletion and environmental pollution, the concept of eco-design has become a key approach in the pursuit of sustainable product innovation. The scientific article presents an original approach to this issue, defined as the Recycling Product Model.

Recycling Product model

The Recycling Product Model (RPM) is a defined set of data and modeling mechanisms that enables calculation of the end-of-life quantitative properties of a product within the CAD 3D system [1]. The Recycling Product Model (RPM) consists of the following elements [1]:

- CAD 3D assembly model,
- Extended connection attributes with disassembly attributes (connection constraints),
- Material recycling attributes,
- Product category.

One of the key operations during the recycling of a product is the disassembly of its parts and components. Modeling of this operation within a CAD 3D system requires the exact data on connections used in the product. Because of the geometrical approach used in the CAD 3D systems for the representation of the relationship between parts, the deriving of connections relationship between parts would require drawing up an algorithm that analyses all the potential combinations of geometrical constraints in order to identify the connection type. In order to avoid it another approach has been proposed in the RPM – the connection constraint. The main purpose of connection constraints is the comprehensive and exact representation of connection types in CAD 3D models.

The theoretical model of connection constraint [1] is based on a weighted hypergraph [2]. The hypergraph is a graph where the edge (called hyperedge) joins any number of vertices [2]. In the theoretical model, the vertices of the hypergraph represent connected parts, hyperedges represent connections and connection attributes are represented by hyperedges' weights. The use of the hypergraph allows for a formally simple approach to a situation in which more than two elements of the model are connected. The connections model based on a hypergraph also enables easy implementation using data structures in a computer program.

It was assumed, that the set of all model parts P is the sum of sets M and L :

$$P = M \cup L \cup ML, \quad (1)$$

when: M is the set of connected parts, L is the set of connecting parts, ML is the set of connected and connecting parts.

The connections in the product are defined as hypergraph :

$$G = (K, C, w), \quad (2)$$

when: $K = M \cup ML$, $C = \{C_1, C_2, \dots, C_i\}$ is the set of hyperedges representing connections (1 hyperedge = 1 connection), $w = \{w_1, w_2, \dots, w_i\}$ is the set of hyperedges' weights representing attributes of connection.

The weight w_j is 5-tuple:

$$w_j = (L_j, v, u, r, t), \quad (3)$$

when:, $L_j \in L$, $v \in \{temporary, permanent\}$ is the attribute representing connection nature, u is the set representing connection type, $r \in \{yes, no\}$ is the attribute describing disassembly the connection during recycling process, $t \in R_+$ is the disassembly time in seconds.

The connection types (u set) were defined based on connection types proposed by de Aguiar et al. [3] and are presented in Table 1.

TABLE 1. Connection types and natures defined in Recycling Product Model

Connection type	Connection nature
Free	Temporary
Snap-fitted	
Scotch taped	
Clasped	
Retaining ring	
Threaded	
Magnetical	
Pinned	
Velcroed	
Wired	
Nylon tag fastener	
Nailed	Permanent
Glued	
Riveted	
Welded	
Soldered	

The example connections and their formal representation by connection constraints are presented in three demonstration models.

Demonstration Model 1. Two parts, connected temporary by two bolts and two nuts (Fig. 1).

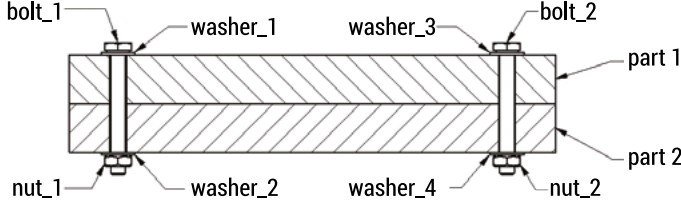


FIG. 1. Demonstration Model 1

The formal representation of the connection constraints of Demonstration Model 1 are as follows:

$M = \{part_1, part_2, washer_1, washer_2, washer_3, washer_4\}$ is the set representing connected parts

$L = \{bolt_1, bolt_2, nut_1, nut_2\}$ is the set representing connecting parts

$C = \{C_1, C_2\}, w = \{w_1, w_2\}$ describes two hyperedges representing two connections

$C_1 = \{part_1, part_2, washer_1, washer_2\}$ is the set representing connected parts in the first connection

$w_1 = \{\{bolt_1, nut_1\}, temporary, threaded, yes, 5\}$ is the weight representing attributes of the first connection

$C_2 = \{part_1, part_2, washer_3, washer_4\}$ is the set representing connected parts in the second connection

$w_2 = \{\{bolt_2, nut_2\}, temporary, threaded, yes, 5\}$ is the weight representing attributes of the second connection

Demonstration Model 2. Two parts, connected temporarily by two snap-fits (Fig. 2).

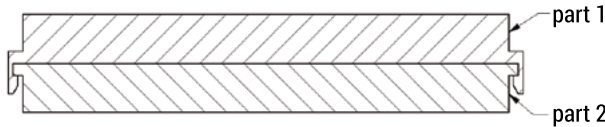


FIG. 2. Demonstration Model 2

The formal representation of connection constraints of Demonstration model 2 are as follows:

$ML = \{part_1, part_2\}$ is the set of connected and connecting parts

$C = \{C_1, C_2\}, w = \{w_1, w_2\}$ describes two hyperedges representing two connections

$C_1 = \{part_1, part_2\}$ is the set representing connected parts in the first connection

$w_1 = \{\{\emptyset\}, temporary, snap - fitted, yes, 1\}$ is the weight representing attributes of the first connection

$w_1 = C_2 = \{part_1, part_2\}$ is the set of connected parts in the second connection

$w_2 = \{\{\emptyset\}, temporary, snap - fitted, yes, 1\}$ is the weight representing attributes of the second connection

Demonstration Model 3. Two parts, connected temporarily by two pins (Fig. 3).

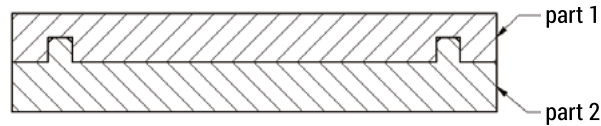


FIG. 3. Demonstration Model 3

The formal representation of connection constraints of Demonstration Model 3 are as follows:

$ML = \{part_1, part_2\}$ is the set to connected and connecting parts

$C = \{C_1, C_2\}, w = \{w_1, w_2\}$ describes two hyperedges representing two connections

$C_1 = \{part_1, part_2\}$ is the set representing connected parts in first connection

$w_1 = \{\{\emptyset\}, temporary, pinned, yes, 0.5\}$ is the weight representing attributes of the first connection

$C_2 = \{part_1, part_2\}$ is the set to connected parts in second connection

$w_2 = \{\{\emptyset\}, temporary, pinned, yes, 0.5\}$ is the weight representing attributes of the second connection

The last two elements of the Recycling Product Model are: material recycling attributes and product category. The material recycling attributes are defined as follows:

- Material recycling profit – the unit profit amount from recycling 1 kg of given material in currency unit (c.u.),
- Material hazardous – the logical attribute that marks the materials hazardous materials used in the product model.

The product category enables classification of a product to one of a group according to the regulations of wastes and recycling. In the Recycling Product Model, the categories are defined based on the Act passed in the Polish Legislature on *electrical waste and electronic equipment* [4].

Computer-Aided RPM modelling

Recycling Product Model Add-in

The practical usage of RPM is possible by using the software aiding creation of the RPM model in CAD 3D system. This software runs within the CAD 3D system Autodesk Inventor as an add-in (Fig. 4) and has the following main functionality:

- Defining connection constraints,
- Defining material recycling attributes,
- Defining product category,
- Calculation of disassembly time, cost and recycling assessment measures.

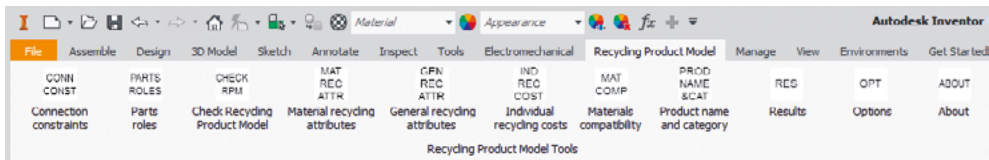


FIG. 4. Recycling Product Model Autodesk Inventor add-in ribbon view

RPM Modelling of Demonstration Models 1–3

The CAD 3D models for Demonstration Models 1–3 with their connection constraints definitions using RPM add-in are presented in Figures 5–7.

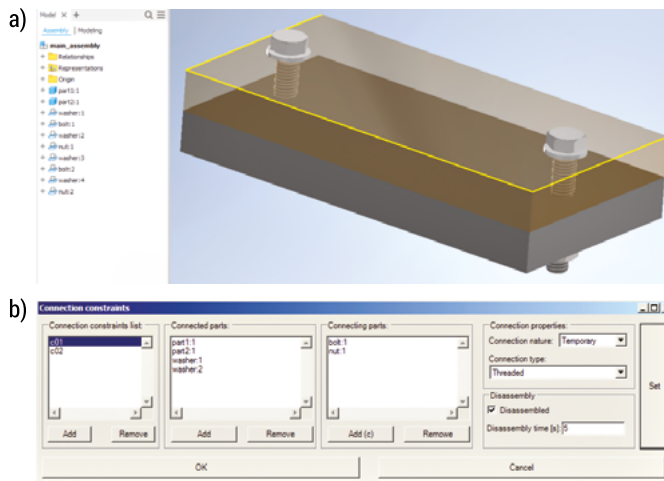


FIG. 5. CAD 3D model (a) and connection constraints definition window (b) using RPM add-in for Demonstration model 1

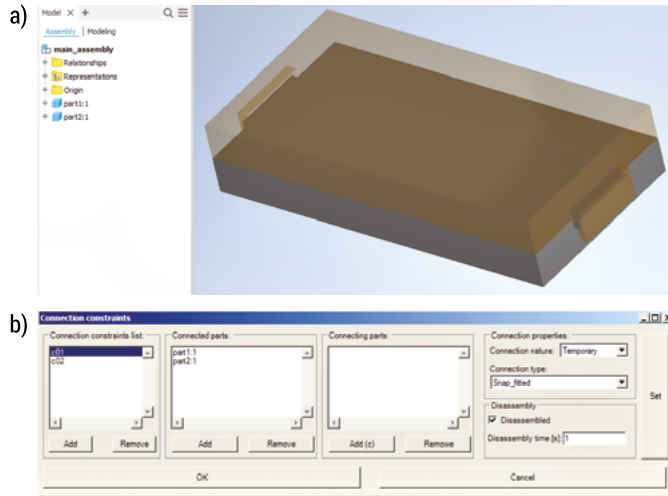


FIG. 6. CAD 3D model (a) and connection constraints definition window (b)using RPM add-in for Demonstration model 2

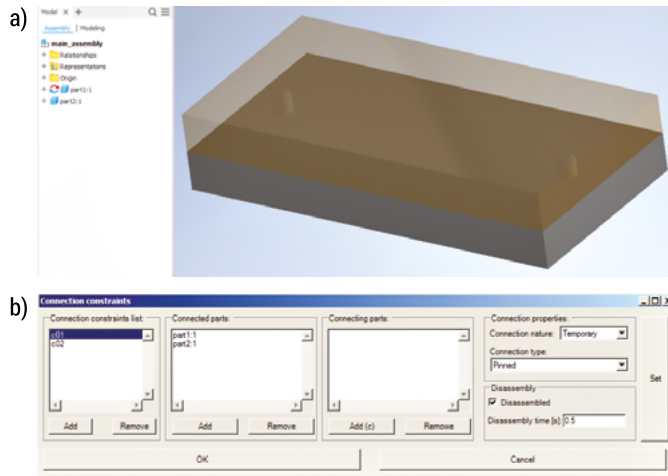


FIG. 7. CAD 3D model (a) and connection constraints definition window (b)using RPM add-in for Demonstration model 3

For the purpose of the RPM creation using the RPM add-in for Demonstration Models 1–3, the material recycling costs (as part of material recycling attributes) was entered (Fig. 8) based on real prices from recycling companies [5–6]. Whenever different kinds of the particular material was in the price list (i.e. single- or multi-color of the plastic), the worst case scenario (lowest price) was used. The usage of polycarbonate (PC) was due to usage of a snap-fit connection [7] in Demonstration

Model 2. For the calculation of product disassembly cost the minimum salary per hour in Poland [8] was assumed. All the monetary amounts are in Polish currency unit (c.u.) – Polish zloty (PLN).

The calculation of total recycling profit in RPM add-in was implemented based on the general equation proposed in [9]:

$$\text{total recycling profit} = \sum \text{recycling profit} - \sum \text{recycling cost}, \quad (4)$$

when: recycling profit – profit from selling components of the product, recycling cost – cost of disassembly of components of the product.

Recycling profit of the part is calculated as:

$$\text{recycling profit} = m_p c_r \quad (5)$$

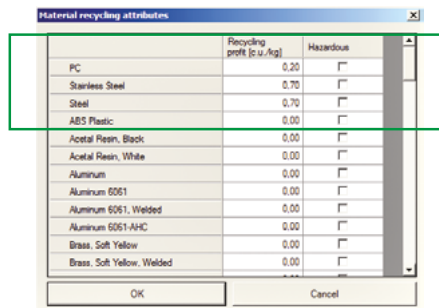
when: m_p is mass of the part [kg], c_r is recycling cost of the part [c.u.].

Recycling cost is calculated as:

$$\text{recycling cost} = t l \quad (6)$$

when: m_p is the disassembly time [s], c_r is labour unit cost [c.u.].

The data from the CAD model are taken using the Autodesk Inventor API (Application Programming Interface). To determine the disassembly times, a collection of measures was performed on original or very similar to original connection types. The disassembly times used in the rest of this are the average of collection of measures for each connection type. The example results of disassembly times and costs, materials recycling profits and total recycling profits calculated by the RPM add-in for Demonstration Model 1 are presented on Figures 9-10. The comparison of total recycling profit is presented in Table 2.



	Recycling profit (c.u./kg)	Hazardous
PC	0.20	<input type="checkbox"/>
Stainless Steel	0.70	<input type="checkbox"/>
Steel	0.70	<input type="checkbox"/>
ABS Plastic	0.00	<input type="checkbox"/>
Acetal Resin, Black	0.00	<input type="checkbox"/>
Acetal Resin, White	0.00	<input type="checkbox"/>
Aluminum	0.00	<input type="checkbox"/>
Aluminum 6061	0.00	<input type="checkbox"/>
Aluminum 6061, Welded	0.00	<input type="checkbox"/>
Aluminum 6061-AHC	0.00	<input type="checkbox"/>
Brass, Soft Yellow	0.00	<input type="checkbox"/>
Brass, Soft Yellow, Welded	0.00	<input type="checkbox"/>

FIG. 8. Material recycling attributes for materials used for Demonstration Models 1-3 defined in the RPM add-in

Results								
Disassembly costs		Materials recycling profits		Total recycling profits				
	Conn. constr. ID	Connected parts	Connecting parts	Connection nature	Connection type	Disassembled	Disassembly time [s]	Disassembly cost [c.u.]
▶	c01	part1:1 part2:1 washer:1 washer:2	bolt:1 nut:1	Temporary	Threaded	Yes	5,0	0,02917
	c02	part1:1 part2:1 washer:3 washer:4	bolt:2 nut:2	Temporary	Threaded	Yes	5,0	0,02917
Total:							10,0	0,05834

FIG. 9. Disassembly costs of Demonstration Model 1 calculated in the RPM add-in

Results						
Disassembly costs		Materials recycling profits		Total recycling profits		
	Material	Part name	Part weight [kg]	Part recycling profit [c.u.]	Material summary weight [kg]	Material summary recycling profit [c.u.]
▶	PC	part1:1	0.05943	0.01189	0.05943	0.01189
		washer:1	0.00045	0.00032		
		bolt:1	0.00617	0.00432		
		washer:2	0.00045	0.00032		
	Stainless Steel	nut:1	0.00150	0.00105	0.01715	0.01201
		washer:3	0.00045	0.00032		
		bolt:2	0.00617	0.00432		
		washer:4	0.00045	0.00032		
		nut:2	0.00150	0.00105		
	Steel	part2:1	0.38877	0.27214	0.38877	0.27214
Total:					0.46535	0.29603

FIG. 9. Material recycling profits of Demonstration Model 1 calculated in the RPM add-in

Results	
Disassembly costs	Materials recycling profits
Total recycling profits	
Value [c.u.]	
▶ Total disassembly cost:	0,05834
Total materials recycling profit:	0,29603
Total recycling profit:	0,23769

FIG. 10. Total recycling profit of Demonstration Model 1 calculated in RPM add-in

TABLE 2. Recycling profits comparison for Examples 1–3

	Demonstration model 1	Demonstration model 2	Demonstration model 3
Total disassembly cost [PLN]	≈0.06	≈0.01	≈0.00
Total materials recycling profit [PLN]	≈0.30	≈0.29	≈0.29
Total recycling profit [PLN]	≈0.24	≈0.28	≈0.29

RPM Modeling of Real Product

The RPM modeling of Demonstration Models 1–3 will be complemented by the real product case study of a portable gas cooker. For the purposes of the recycling profit analysis, the product was modelled in the 3D CAD Inventor system (Fig. 11). Then the necessary RPM elements were defined using the RPM add-in: connection constraints (Fig. 12) and material recycling attributes (Fig. 13). The total recycling profit, calculated in the RPM add-in, is showed in Figure 14.



FIG. 11. Portable gas cooker CAD 3D model

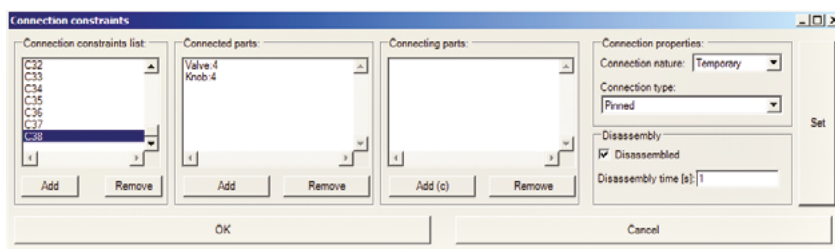


FIG. 12. Connection constraints of portable gas cooker defined in the RPM add-in

Material recycling attributes		
	Recycling profit [c.u./kg]	Hazardous
Aluminum	5.00	<input type="checkbox"/>
Brass, Soft Yellow	17.00	<input type="checkbox"/>
Copper	25.00	<input type="checkbox"/>
Polycarbonate	0.70	<input type="checkbox"/>
Steel	0.70	<input type="checkbox"/>
Steel, Mild	0.70	<input type="checkbox"/>
ABS Plastic	0.00	<input type="checkbox"/>
Acetal Resin, Black	0.00	<input type="checkbox"/>
Acetal Resin, White	0.00	<input type="checkbox"/>
Aluminum 6061	0.00	<input type="checkbox"/>
Aluminum 6061, Welded	0.00	<input type="checkbox"/>
Aluminum 6061-AHC	0.00	<input type="checkbox"/>

FIG. 13. Material recycling attributes for portable gas cooker defined in the RPM add-in

Results		
Disassembly costs	Materials recycling profits	Total recycling profits
	Value [c.u.]	
Total disassembly cost:	-1.35629	
Total materials recycling profit:	17.07905	
Total recycling profit:	15.72276	

FIG. 14. Total recycling profit of portable gas cooker calculated in the RPM add-in

Conclusions

This paper presents the reference set of data and modelling mechanisms necessary to deal with the recycling properties of the product model named the Recycling Product Model (RPM). The practical usage of the RPM is possible using dedicated software that enables estimating the recycling properties of the product during the design stage of the product lifecycle in the one of the most popular CAD 3D systems in the convenient form of an add-in. That way the quick estimation of quantitative assessment measures characterizing the recycling properties of the product can be done directly from the CAD 3D system, supporting the designer with taking into account the end-of-life issues in the design process. The developed RPM add-in can be also implemented in another CAD 3D – that way the same functionality can be available regardless of the CAD 3D system being used.

This paper showed the usage of RPM at the design phase of product lifecycle. But it can also be used at the end of its lifecycle by the recycler in order to compare different recycling strategies connected to the product being withdrawn from exploitation.

The paper focuses on disassembly time and cost during the recycling of the product. Another way of assessment of end-of-life properties of the product relies on quantitative measures of recycling properties of the product. The direct calculation from the RPM will be the next potential way of further research based on this approach.

References

1. Diakun J., 2014, *Recycling product model*, in: *Ecodesign of products in CAD 3D environment with the use of agent technology*, ed. E. Dostatni, PUT Publishing House, Poznań, 57–66.
2. Berge C., 1973, *Graphs and hypergraphs*, North-Holland, Amsterdam.
3. Aguiar J. de, Oliveira, L. de, Silva J.O. da et al., 2017, *A design tool to diagnose product recyclability during product design phase*, Journal of Cleaner Production, 141, 219–229.
4. *Act on electrical waste and electronic equipment*, Dz.U. 2022 poz. 1622. Available online: <https://isap.sejm.gov.pl/isap.nsf/download.xsp/WDU20220001622/T/D20221622L.pdf> [accessed; 23.08.2023].
5. *Plastics recycling price list*. Available online: <https://chemplast.pl/skup-tworzyw-sztucznych-cennik/> [accessed: 23.08.2023].
6. *Materials recycling price list*. Available online: <https://11.ekosylwia.pl/cennik> [accessed: 23.08.2023].
7. *Snap-Fit Joints for Plastics – A Design Guide*, Bayer MaterialScience.
8. *Regulation of the Council of Ministers on the minimal salary in Poland*. Available online: <https://isap.sejm.gov.pl/isap.nsf/download.xsp/WDU20220001952/O/D20221952.pdf> [accessed: 23.08.2023].
9. Karwasz A., 2014, *Recycling costs analysis*, in: *Ecodesign of products in CAD 3D environment with the use of agent technology*, ed. E. Dostatni, PUT Publishing House, Poznań, 94–98.

2.6. Fastening elements by blind rivets – research on the strength aspects

Mikołaj Szyca¹, Robert Kostek², Michał Stopel²

¹PESA Bydgoszcz SA, Technical Department, mikolaj.szyca@pesa.pl

²Bydgoszcz University of Science and Technology, Faculty of Mechanical Engineering

Summary: Blind rivet fasteners are commonly used when access to components is limited, or quick assembly is required. This article presents the experimental results and numerical analyses of riveted fastenings. Simulations were conducted with Ansys Workbench and LS Dyna software. Two steel sheets were riveted together and then subjected to load testing. Finally, the simulation results were compared to the experimental results.

Keywords: blind rivets, strength, fastening

Introduction

Riveted connections have gradually given way to welding in engineering but are still used in machinery and vehicles due to their low cost and ease of use. While considered non-detachable, screw connections are thought to be more advantageous for servicing. Research on breakable rivets, popular since the mid-20th century, is limited, but there are publications discussing their mechanical strength [1–4].

A review of the literature reveals that issues of structural reliability in railway construction often center around the area of connections, as highlighted by the research of Aman et al. [5], Liang et al. [6] and others [7, 8]. Their studies, utilizing finite element analysis and experiments, focused on the impact of residual stresses after riveting on the strength of riveted connections. It is also worth mentioning the investigations by Skorupa et al. [9], which analyzed the influence of various parameters such as the type and material of rivets, pressure riveting force, and secondary bending on the fatigue strength of riveted connections. Modern technologies, including numerical and experimental methods, enable detailed analyses of riveting processes, allowing for the refinement of designs and enhancing the performance of riveted connections in composite materials [10–11]. As this research progresses, we anticipate further innovations that will contribute to developing advanced manufacturing and composite construction technologies. Fatigue testing of breakable rivets can contribute to improving the reliability and safety of public transportation, and the subject matter of these studies is widely addressed by scientists [5, 9, 12–13]. The majority

of research, however, focuses on the use of rivets made from various materials, as well as their application in diverse geometric configurations and fatigue [14–18].

In the face of increasing distances covered by modern trains, the problem of fatigue-related structural damage becomes particularly significant. Research into the influence of factors such as the type of rivets or the pressure riveting force, as described in the work by Yuan et al. [19], or electromagnetic riveting which is described by Cao and Zuo [20–21] provides a fresh perspective on essential aspects of structural durability in railway connections. Predictive maintenance of riveted joints is an approach in maintenance management that relies on forecasting the technical condition and performance of riveted connections before serious issues arise. Utilizing advanced monitoring technologies such as sensors, these systems enable continuous tracking of working conditions and loads on riveted joints. Real-time data analysis allows for the early detection of changes in the structure of the joints, enabling corrective actions to be taken before more significant damage occurs [18, 21].

This article analyses different parameters of the riveting process and their impact on the fatigue strength of railway connections. Utilising the literature mentioned earlier will enable a more comprehensive understanding of this issue and an assessment of the role of individual factors in the context of durability and structural safety in railway engineering.

Material and methods

In the course of this research, a comprehensive set of experimental tests was meticulously conducted on a structural wall to ascertain the classification of the scrutinised rivets. The classification, by the ISO 15977 standard, unequivocally designated the tested rivets as belonging to the “L” category, signifying low strength.

The experimental procedures adhered to the stringent guidelines outlined in the ISO 14589 standard, ensuring a systematic and reliable approach. These tests served as a pivotal step in understanding the mechanical behaviour of the rivets and their suitability for specific applications.

To complement the experimental phase, a sophisticated computational analysis was undertaken using Ansys Workbench software as the preprocessor and LS Dyna as the postprocessor. This analytical approach allowed for a comprehensive exploration of the intricate dynamics involved in the rupture of the rivet core.

The obtained results, derived through the finite element method, provided invaluable insights into the deformations occurring within the rivet core during the rupture process. This analytical depth enhanced the overall understanding of the structural response and failure mechanisms, contributing significantly to the body of knowledge in this field.

Figure 2 in the research findings visually encapsulates samples of the tested material, portraying S235 steel plates with dimensions of approximately $100 \times 30 \times 4$, securely fastened by blind rivet Al-A2 4×12 . The application of force on the specimen

is illustrated in Figure 3 intricately illustrate the geometry of the blind rivet, offering a visual reference to aid in the comprehension of the subsequent analyses.



FIG. 2. S235 steel plates about dimensions 100x30x4 fastened by blind rivet Al-A2 4 × 12

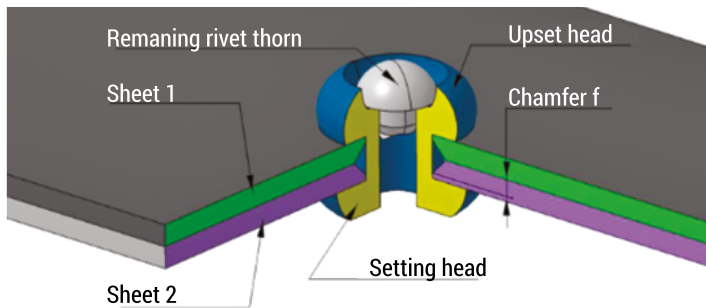


FIG. 3. Geometry of joint [11]

This integrated approach, combining experimental tests with computational simulations, not only ensured a robust evaluation of the rivet's strength classification but also facilitated a nuanced understanding of its structural performance and failure modes. The synergy between empirical observations and computational modeling enriches the validity and applicability of the research findings.

Results and discussion

The results of force measurements conducted during 100 rivet shear tests provided significant insights into the strength of connections. The measured results are presented below in Table 1 and will now be compared with the outcomes obtained from simulations conducted in the LS Dyna software. Figure 4 presents a chart – a histogram based on the research results.

TABLE 1. Basic statistical parameters

Paramter	Value
Average Force	975 N
Median Force (Second Quartile)	975 N
Minimum Force	906 N
First Quartile	959 N
Third Quartile	989 N
Maximum Force	1073 N
Variance	744 N
Standard Deviation	27 N
Mean Deviation	20.7 N
Kurtosis	1.15 N

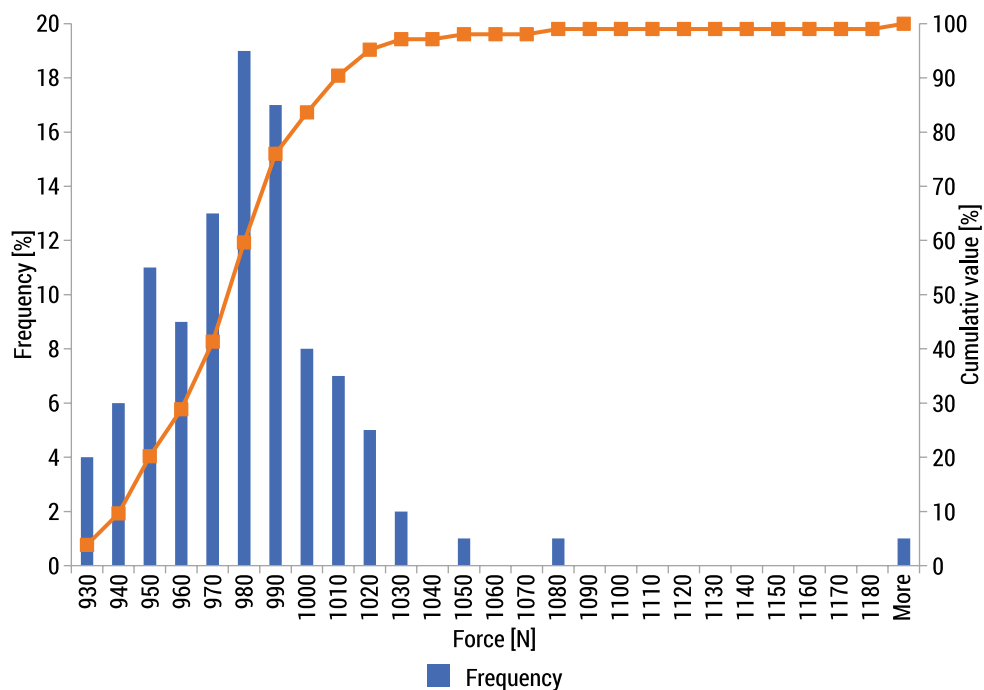


FIG. 4. The histogram based on the research results is presented

Equation (1) describes the method of permissible shear stresses based on experimental test calculation. Equations (2–4) describe the shear stresses on the rivet under the full distribution of forces recorded during the tests.

$$\tau_{sc} = \frac{F}{A} = \frac{F}{\frac{\pi D^2}{4} - \frac{\pi d^2}{4}} = \frac{F}{\frac{\pi (4 \text{ mm})^2}{4} - \frac{\pi (1,9 \text{ mm})^2}{4}} = \frac{F}{12,57 \text{ mm}^2 - 2,83 \text{ mm}^2} = 0,1F \quad (1)$$

where: F – force [N], A – area [mm^2], D -nominal outer rivet diameter [mm], d -nominal inner rivet diameter [mm].

$$F_{\text{MIN}} = 906 \text{ N} \Rightarrow k_{t\text{MIN}} = 90,6 \text{ MPa} \quad (2)$$

$$F_{\text{mean}} = 977 \text{ N} \Rightarrow k_{t\text{mean}} = 97,7 \text{ MPa} \quad (3)$$

$$F_{\text{MAX}} = 1073 \text{ N} \Rightarrow k_{t\text{MAX}} = 107,3 \text{ MPa} \quad (4)$$

where: F_{MIN} – minimal shear force, $k_{t\text{MIN}}$ – minimal shear stress, F_{mean} – shear force, $k_{t\text{mean}}$ – mean shear stress, F_{MAX} – maximal shear force, $k_{t\text{MAX}}$ – maximal shear stress.

In the LS Dyna program, we applied opposing tensile forces to replicate real testing conditions. This approach aimed to simulate the forces experienced during actual experiments. The force value recorded at the point of rupture closely matched the average obtained in our experimental tests described in above calculations (2–4). This alignment indicates a good correlation between the simulated and experimental results.

Figure 6 provides a visual representation of the study conducted within the LS Dyna program. The illustration captures the deformation of the rivet throughout the test. This visual representation is instrumental in understanding how the rivet behaves under simulated conditions and offers valuable insights into its structural response. The close correspondence between simulated and experimental outcomes enhances the reliability and validity of the simulation results (shear force about 900N–1000N), affirming the effectiveness of the LS Dyna program in replicating real-world scenarios.

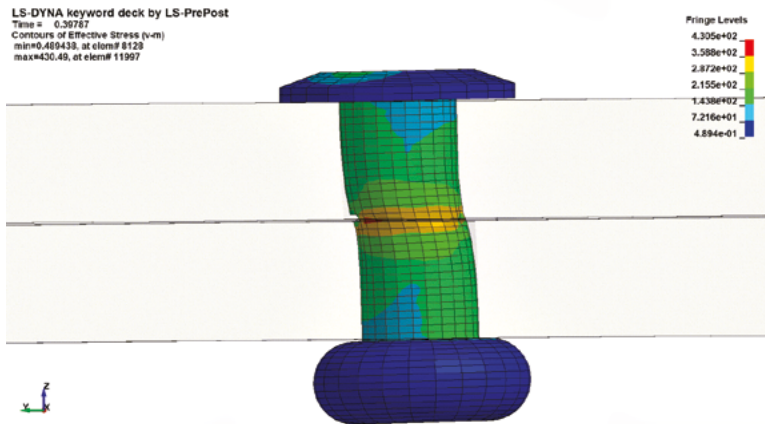


FIG. 6. Simulative study in the LS-Dyna program.

Conclusions

The experimental tests revealed valuable insights into the shearing stresses and deformation of rivets. Despite a substantial spread in applied stresses (275N over 100 trials), it's notable that the distribution wasn't normal. The repeatability of observed deformation suggests potential for future investigations into mechanical strength.

While the tests focused on individual rivets sequentially, expanding the research to walls with multiple rivets simultaneously aims to enhance understanding of complex connections. Observed rivet strength, approximately half of previous tests, emphasizes the importance of considering variables like geometry and material properties in assessing overall strength. This underscores the need for a nuanced approach in designing structures with riveted joints.

In summary, the experimental results not only highlight shearing stresses and deformation but also pave the way for more intricate explorations into the mechanical behavior of riveted connections. These findings carry implications for optimizing design practices in structures with riveted joints.

References

1. Zeng C., Liao W.H., Tian W., 2015, *Influence of initial fit tolerance and squeeze force on the residual stress in a riveted lap joint*, The International Journal of Advanced Manufacturing Technology, 81, 1643–1656, <https://doi.org/10.1007/s00170-015-7235-7>.
2. Zheng B., Yu H., Lai X., 2017, *Assembly deformation prediction of riveted panels by using equivalent mechanical model of riveting process*, The International Journal of Advanced Manufacturing Technology, 92, 1955–1966, <https://doi.org/10.1007/s00170-017-0262-9>.
3. Lubas M., Witek L., 2021, *Influence of Hole Chamfer Size on Strength of Blind Riveted Joints*, Advances in Science and Technology Research Journal, 15(2), 49–56, <https://doi.org/10.12913/22998624/135632>.
4. Haque R., Durandet Y., 2016, *Strength prediction of self-pierce riveted joint in cross-tension and lap-shear*, Materials and Design, 108, 666–678.
5. Aman F., Cheraghi S.H., Krishnan K.K. et al., 2013, *Study of the impact of riveting sequence, rivet pitch, and gap between sheets on the quality of riveted lap joints using finite element method*, The International Journal of Advanced Manufacturing Technology, 67, 545–562, <https://doi.org/10.1007/s00170-012-4504-6>.
6. Liang Q., Zhang T., Zhu C. et al., 2021, *Effect of riveting angle and direction on fatigue performance of riveted lap joints*, Coatings, 11(2), 1–23, 2021, <https://doi.org/10.3390/coatings11020236>.
7. Chang Z., Wang Z., Xie L. et al., 2018, *Prediction of riveting deformation for thin-walled structures using local-global finite element approach*, The International Journal of Advanced Manufacturing Technology, 97(5–8), 2529–2544.
8. Lei C., Bi Y., Li J. et al., 2018, *Experiment and numerical simulations of a slug rivet installation process based on different modeling methods*, The International Journal of Advanced Manufacturing Technology, 97, 1481–1496.
9. Skorupa M., Skorupa A., Machniewicz T. et al., 2010, *Effect of production variables on the fatigue behaviour of riveted lap joints*, International Journal of Fatigue, 32(7), 996–1003, <https://doi.org/10.1016/j.ijfatigue.2009.11.007>.

10. Wu T., Zhang K., Cheng H. et al., 2016, *Analytical modeling for stress distribution around interference fit holes on pinned composite plates under tensile load*, Composites Part B: Engineering, 100, 176–185, <https://doi.org/10.1016/j.compositesb.2016.06.011>.
11. Gray P.J., O'Higgins R.M., McCarthy C.T., 2014, *Effects of laminate thickness, tapering and missing fasteners on the mechanical behaviour of single-lap, multi-bolt, countersunk composite joints*, Composite Structures, 107, 219–230, <https://doi.org/10.1016/j.compstruct.2013.07.017>.
12. Yuan X., Yue Z.F., Yan W.Z. et al., 2013, *Experimental and analytical investigation of fatigue and fracture behaviors for scarfed lap riveted joints with different lap angle*, Engineering Failure Analysis, 33, 505–516, <https://doi.org/10.1016/j.engfailanal.2013.05.019>.
13. Mohammadpour M., Kalajahi M.H., Oskouei R.H. et al., 2014, *Fatigue life estimation of coach peel riveted joints using multi-axial fatigue criteria*, Materials and Design, 62, 327–333, <https://doi.org/10.1016/j.matdes.2014.05.033>.
14. Chen Y., Yang X., Li M. et al., 2019, *Mechanical behavior and progressive failure analysis of riveted, bonded and hybrid joints with CFRP-aluminum dissimilar materials*, Thin-Walled Structures 139, 271–280.
15. Lipski A., Mroziński S., Lis Z., 2011, *Evaluation of the river hole sizing degree effect on the fatigue life*, Journal of Polish CIMAC, 6(3), 119–126.
16. Mucha J., 2017, *Blind Rivet and Plastically Formed Joints Strength Analysis*, Acta Mechanica Slovaca, 21(1), 62–69.
17. Mucha J., Witkowski W., 2015, *The structure of the strength of riveted joints determined in the lap joint tensile shear test*, Acta Mechanica et Automatica, 9(1), 44–49, <https://doi.org/10.1515/ama-2015-0009>.
18. Qasim B.M., Khidir T.C., Incesu A., 2021, *Study Strength of Blind Riveted Lap Joint Structure under Tensile Shear Force*, International Journal of Mechanical Engineering and Robotics Research, 10(7), 363–367, <https://doi.org/10.18178/ijmerr.10.7.363-367>.
19. Yuan X., Yue Z.F., Yan W.Z. et al., 2013, *Experimental and Analytical Investigation of Fatigue and Fracture Behaviors for Scarfed Lap Riveted Joints with Different Lap Angle*, Engineering Failure Analysis, 33, 505–516, <https://doi.org/10.1016/j.engfailanal.2013.05.019>.
20. Cao Z., Zuo Y., 2020, *Electromagnetic riveting technique and its applications*, Chinese Journal of Aeronautics, 33(1), 5–15, <https://doi.org/10.1016/j.cja.2018.12.023>.
21. Zhang X., Yu H.P., Li J. et al., 2015, *Microstructure investigation and mechanical property analysis in electromagnetic riveting*, The International Journal of Advanced Manufacturing Technology, 78(1–4), 613–623.
22. Zhang Y., Bi Q., Yu L. et al., 2018, *Online compensation of force-induced deformation for high-precision riveting machine based on force–displacement data analysis*, The International Journal of Advanced Manufacturing Technology, 94(1–4), 941–956.
23. ISO 15977 – *Open-end blind rivets with break pull mandrel and protruding head AIA/St.*
24. ISO 14589 – *Blind rivets – mechanical testing*.

2.7. Numerical Simulation of the Axial Compression Test of the “Crash-Box” Energy Absorber

*Tomasz Nowak¹, Przemysław Rumianek¹, Jarosław Seńko¹,
Paweł Skoniecki¹, Natalia Wolska¹, Krzysztof Podkowski²*

*¹Warsaw University of Technology,
Faculty of Automotive and Construction Machinery Engineering
qomek@wp.pl, jaroslaw.senko@pw.edu.pl*

²SIMCREATEC

Summary: This paper presents the methodology for numerical simulations of the axial crushing test of collision energy dissipating elements. The results of numerical simulations were obtained using two different numerical methods, Finite Element Analysis (FEM) and Macroelement Method (MM). The need to verify the results of computer simulations using other numerical methods was indicated in the process of selecting parameters and designing the structures of energy-consuming vehicles.

Keywords: energy absorber, crash simulations, finite elements analysis, macroelement method

Introduction

In the automotive industry, thin-walled beams with various cross-sections are commonly used as crash-box elements. In such structures, energy dissipation occurs as a result of irreversible processes of progressive deformation related to local buckling caused by dynamic excitations [1, 2, 3]. Numerical studies of energy dissipation in energy-absorbing structures subjected to axial loads is an important issue in vehicle design.

The presented method of designing energy absorbing structures can be used in the so-called “crash structures” of all types of safety devices and vehicles. In particular, the work highlights issues related to the design of an absorber that meets the regulations specified in the Formula Student regulations.

The presented method of simulation testing of forces and accelerations of the impact energy absorber during crushing has been verified in static and dynamic tests. The comparison of results from the two different simulation methods provides an opportunity to determine whether the simpler and less time-consuming method is sufficient for car crash simulations.

Methods of numerical crash tests

Modeling energy dissipation in energy-absorbing structures subjected to axial loads requires the use of dedicated computer tools, e.g. VisualCrasStudio, Radioss, LS-Dyna. The obtained numerical results depend on the modeling method used. The macroelement method [4, 5] and the finite element method were used to study the parameters of the energy absorber. These are computer tools used in the design of car body structures, especially at the stage of designing structures and optimizing their cross-sections.

The absorber in the FormulaStudent car is a regulatory requirement for competition organizers. The implementing regulations apply restrictions on the dimensions of the absorber and the limit value that may affect the driver during a collision. When testing the absorber of a vehicle with a mass of 300 kg and an initial velocity of 7 m/s, a non-deformable obstacle should be hit. The delay cannot exceed 40 g and 20 g for the average value.

The importance of the basic regulatory solution regarding the crushing force of the absorber and the energy that must be dissipated. Based on the obtained profile values available on the market. To simplify accessibility, the profile must be made of aluminum and the cross-section must be square or flat. computationally for each element of the geometric calculation with the values R_e (yield strength) and R_m (rupture strength). equipped with a plastic moment for a square profile:

$$M_0 = \frac{\sigma_0 \cdot t^2}{4} \quad (1)$$

when: $\sigma_0 = \sqrt{R_e \cdot R_m}$, t - wall thickness.

Having the results for individual cross-sections and thicknesses, it was possible to determine the average crushing force:

$$P_m = M_0 \cdot 52,2 \cdot \sqrt[3]{\frac{C}{t}} \quad (2)$$

The analysis of the results showed that only a few profiles meet these requirements. Their size is so large that when crushed, they would deform sideways so much that they would not fit into the area specified by the regulations. Therefore, attention was focused on round profiles. The full plastic moment was determined from formula (1). The average crushing force [4] was determined from the formula:

$$P_m = M_0 \cdot \frac{25,23 \cdot \sqrt{\frac{2R}{t}} + 15,09}{0,86 - 0,568 \cdot \sqrt{\frac{t}{2R}}} \quad (3)$$

when: M_0 – full plastic moment, R – profile radius.

The selected profiles were numerically tested in Visual Crash Studio. When crushing, a profile without a trigger requires a high force to initiate crushing. The value of the initial force can be lowered by applying a bending, called a trigger. Visual Crash Studio is a program using MM, in which the height, shape and depth to which the trigger had to be pressed were determined.

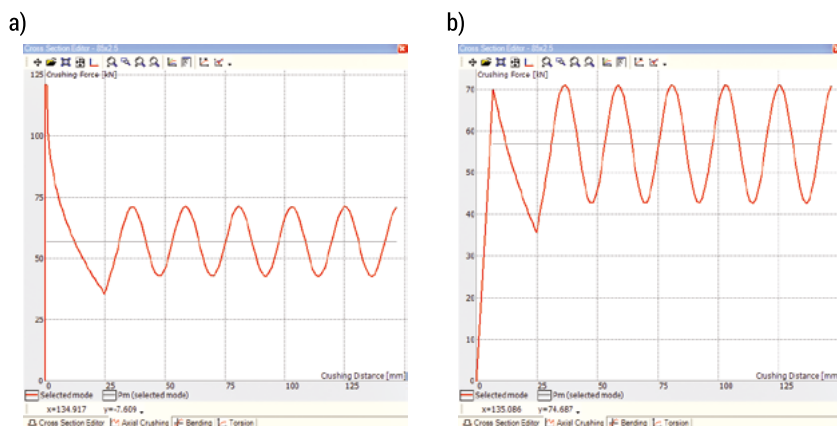


FIG. 1. The value of the force as a function of the crushing distance. a) tube without trigger; b) trigger tube

Place formulas in the text on separate lines. Number the formulas in regular parentheses. Place the descriptions of the symbols used in the formula directly after it, remembering to use *Italic font* for variable symbols. All formulas in the text must be centered. The equation (1) describes the function

$$F(\varphi) = \mu \cdot L(\varphi) + v \cdot S_0(\varphi), \quad (1)$$

when: $L(\varphi)$ is length, $S_0(\varphi)$ is internal area v .

Development of numerical models

In the construction of energy absorbers, the aim is to ensure that the material has high strength while maintaining good ductility [8]. This means that the area under the stress versus strain curve should be as large as possible. This field is a measure of the energy absorbed.

The initiation of progressive deformation and the reduction of the risk of global buckling were solved by the introduction of a crumple initiator (trigger). This name describes the weakening of the structure in the form of embossing. They are performed in the appropriate place on the absorber and at the appropriate depth, depending on the parameters of the energy absorber. The crease initiates the formation of the first plastic fold [6, 7].

The method of modeling the energy absorber in the uniaxial compression test is based on static and dynamic tests performed in laboratory conditions.

Designing new technical solutions requires the use of existing experience and experimental research regarding previous use. Practical numerical solutions presented in the LS-Dyna program, which can be used by selecting design solutions based on the results of experimental tests. Simulation model of the energy absorber with the bumper in the HyperMesh program, followed by simulation crash tests.

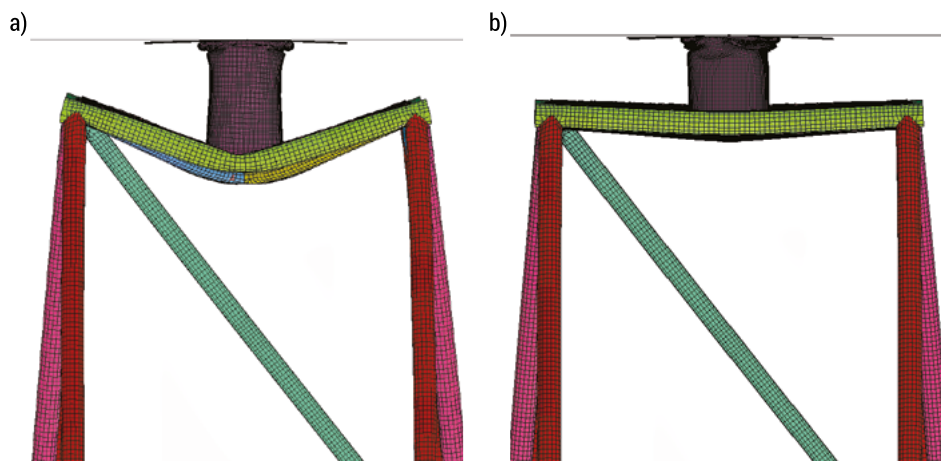


FIG. 2. Deformation of the front frame structure of the Formula Student car in 0.035s; a) without frontal bulkhead reinforcement – test failed; b) with the front bulkhead reinforced with 1.5 mm sheet metal – test passed

Analysis of simulation results

The results of numerical tests were presented as deformation characteristics of the absorbers. The validity of conducting numerical research using various methods was confirmed by comparing the results for the same structures and the same simulation parameters. The macroelement method and the finite element method were used to study the absorber parameters as a computer tool used in the design of car body structures, especially at the stage of designing structures and optimizing their cross-sections. The influence of absorber parameters, such as cross-sectional shape and wall thickness, on its energy dissipation properties was analyzed.

Simulation models were tested for three different diameters: Ø80, 85 and 90mm. 7 different trigger depths were analyzed for each pipe: the basic depth, the so-called nominal, estimated in Visual Crash Studio, and 3 shallower and 3 deeper dents. The effect of trigger crimping height was tested at nominal depth. Basic height, called nominal, estimated in Visual Crash Studio, and 3 additional heights. The constant parameters were the wall thickness of 2.5 mm and the material from which the pipes were made.

Models created in the LS-Dyna pre-processor – LSTC Prepost-processing were used for computer simulation. The model was prepared as follows: a pipe was placed on a plate with “Rigid” properties, without a pressed trigger. 3 cylinders were created,

Rigid properties were assigned to them and movement was given. A plastic material model with piecewise linear reinforcement *MAT_PIECEWISE_LINEAR_PLASTICITY was used. Material properties were determined based on appropriate standards. Finally, a Rigid plate with a mass of 300 kg and an initial velocity of 7 m/s was added.

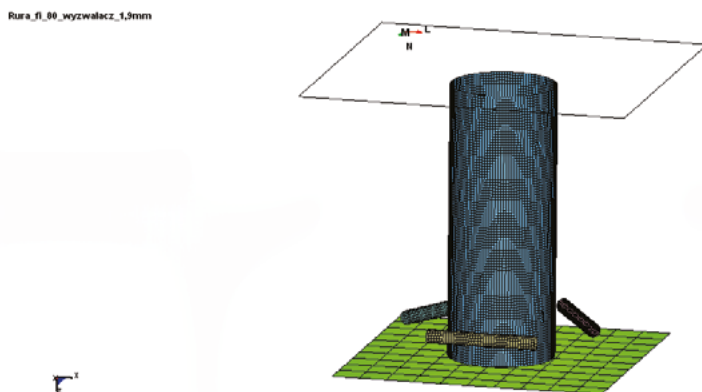


FIG. 3. Numerical model of the impact absorber in the LS-Dyna

The research on the axial absorber design included a total of 33 simulation models, 2 static tests and 1 dynamic test. Based on the conducted research, the influence of the diameter of the absorber tube and the depth of the crush trigger of the deformation process on the crushing characteristics profile of the absorber planned for the Formula Student vehicle was determined.

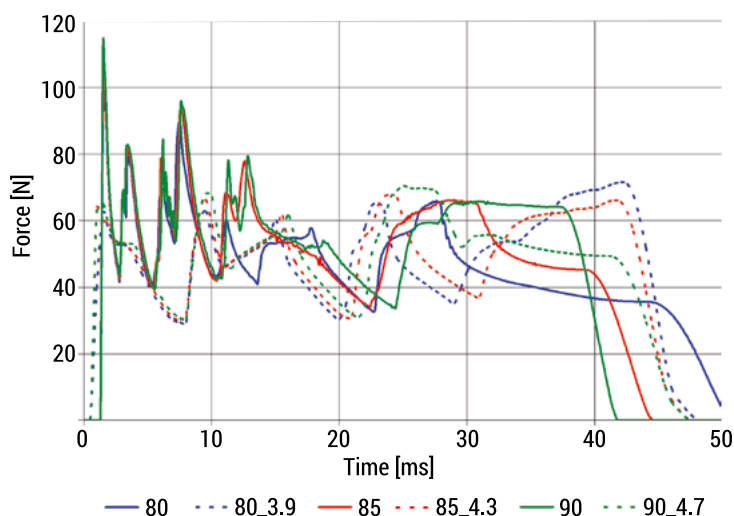


FIG. 4. The force of the absorber as a function of the process duration for circular sections with or without a trigger

The large force impulse in the initial period of pipe crushing is due to the lack of a trigger. The use of a trigger in axial absorbers reduces the force initiating the process by up to 40% in the initial phase of crushing. With the same wall thickness, the pipe with the smallest diameter seems to be the best. The forces acting on it are the smallest, the crushing time is the longest, and, consequently, the acceleration is also the smallest.

Conclusions

In conclusion, the use of CAE tools is standard in vehicle body design. Numerical methods play the crucial role in dynamic tests of vehicle bodies, necessitating ways to assess numerical calculation results. The presented method allows for determining the influence of trigger parameters on the crushing parameters of an axial absorber made of a closed profile.

References

1. Abramowicz W., Jones N., 1986, *Dynamic progressive buckling of circular and square tubes*, International Journal of Impact Engineering, 4(4), 243–270.
2. Alexander J., 1960, *An approximate analysis of the collapse of thin cylindrical shells under axial loading*, The Quarterly Journal of Mechanics and Applied Mathematics, 13(1), 10–15.
3. Kopczyński A., Rusiński E., 2010, *Bezpieczeństwo bierne, pochłanianie energii przez profile cienkościenne*, Oficyna Wydawnicza Politechniki Wrocławskiej, Wrocław.
4. Takada K., Abramowicz W., 2004, *Fast Crash Analysis of 3D Beam Structures Based on Object Oriented formulation*, SAE Technical Paper 2004-01-1728.
5. Tabacu S., 2015, *Axial crushing of circular structures with rectangular multi-cell insert*, Thin-Walled Structures, 95, 297–309.
6. Seńko J., 2019, *Doświadczalne i symulacyjne badania zderzeń pojazdów w kategorii dyssipacji energii*, Sieć Badawcza Łukasiewicz – Instytut Technologii Eksploatacji, Warszawa.
7. Barszcz Z., Podkowski K., Seńko J., 2017, *FEM (Finite Element Method) Numeric Analyses of the Syrenka S201 Car Model*, in: Proceedings of the 13th International Scientific Conference, eds. E. Rusiński, D. Pietrusiak, 415–421.
8. Caban J., Drożdziel P., Seńko J., 2014, *Wybrane materiały konstrukcyjne w budowie pojazdów samochodowych*, Logistyka, 3, 946–953.

2.8. Design and numerical simulations of a modular mine explosion protection vehicle seat

Radosław Nowak¹, Dominik Rodak¹, Jarosław Seńko¹, Katarzyna Stańko-Pająk¹, Karol Sztwiertnia², Tomasz Wróbel¹

¹*Warsaw University of Technology, Faculty of Automotive and Construction Machinery Engineering, jaroslaw.senko@pw.edu.pl*

²*Łukasiewicz Research Network – Warsaw Institute of Technology.*

Summary: This paper presents a proposal for modeling a lightweight seat design for special vehicle crews using the multibody systems method. The explosion-proof seats described, in addition to the function of protecting the crew during the detonation of an explosive charge, also have features allowing ergonomic use and customization for the user. The proposed modular structure of the seats, in addition to the repeatability of the components, reduces production costs and facilitates the configuration of seats with different functions. The structure's modularity also enables a faster process of restoring the chair's functionality in case of damage.

Keywords: explosion-proof seat, explosion energy absorption, multibody simulation

Introduction

The safety of people using means of transport to move is related to the interaction between man and vehicle. The safe interaction between man (driver, passenger) and vehicle usually depends on the interactions resulting from the road on which the object travels or the occurrence of accidental events resulting from vehicle damage [1].

Vehicle safety is defined as active and passive safety. Active safety is the set of factors that reduce the likelihood of an incident or accident occurring on the road and is provided by those elements that enable the driver to reduce the risk of an incident or avoid a hazard [2]. Passive safety is a set of solutions to minimize or reduce the consequences of hazardous events associated with the use of a vehicle. Active safety systems for vehicles include devices that enable the driver to take action to prevent a road incident and the driver's skills and psycho-physical condition. Passive safety refers to vehicle features designed to reduce the consequences of a road incident when the driver is no longer in control. Important elements affecting passive safety in a vehicle are the seats, especially their design and the systems that work with them, e.g., seat belts [2].

Compared to civilian vehicles, the construction of military vehicles is designed for different operating conditions. This is especially true for military special vehicles, where the commonly known active and passive safety systems may not be present, and other vehicle safety solutions are used in parallel [3]. A special vehicle is designed to fulfill a special function, which determines the form of the vehicle body or special equipment [1].

The distinguishing features of special vehicles adapted for passenger transport are a high center of mass, an unladen weight close to the permissible total weight, high moments of inertia of the body, and a small window area [2, 3]. From the point of view of functionality, military special vehicles have the ability to overcome terrain, survive, and continue tasks despite damage to the vehicle [2].

Seats as an element of passive safety

Civilian and military vehicle seats are essential elements of passive safety. The correct shape and firmness of the seat and backrest play a very important role in ensuring comfort while driving and, in the event of a dangerous incident, together with other components such as seat belts, ensure the correct position during impulse overloading. In the event of a road traffic collision, the impulse overload lasts approximately 150 milliseconds from the moment of collision until the vehicle stops. During this time, the driver has no chance to react. Using automotive seat belts results in the body not moving forward and the torso being close to the backrest [3, 4].

The design of safety seats for military special vehicles is additionally adapted to disperse energy in the vertical direction due to the explosion of a charge under the vehicle.

Seats for military special vehicles are designed taking into account the conditions of daily operation of the vehicle and the need to prevent threats from the enemy resulting from damage to the vehicle with an explosive charge.

The seat design of military special vehicles, as in civilian vehicles, should allow comfortable use of the vehicle during transport tasks. Such an effect is achieved by being able to adjust the seat features responsible for adapting to the user's figure and providing the driver or passenger with proper support for body parts in contact with the seat. The individual anthropometric characteristics of the vehicle user, such as height and weight, have a direct impact on the way the anti-sway devices operate. In addition to seat belts and a foot support system, in special vehicle seats, it is important to provide space for arm movement at the top of the seat back [4].

The seat design, which has been developed, ensures that the user's torso, limbs, and head are stabilized and that the silhouette can be adjusted to provide comfortable ergonomic angles for the user.

The standards for vehicle use define the so-called curves of sensitivity of the human body to vertical accelerations resulting from the pressure of the seated person on the seat and the seat back. The normative curves define the exposure time that is comfortable. They are also a guideline for choosing the shape of the seat and the appropriate covering of the seat surfaces due to their hardness; a seat that

is too soft puts strain on the spine; similarly, a lack of thigh support causes fatigue. Setting the correct seating position in the car should be considered as an element of active safety affecting driver fatigue and passive safety affecting musculoskeletal loads during an emergency situation.

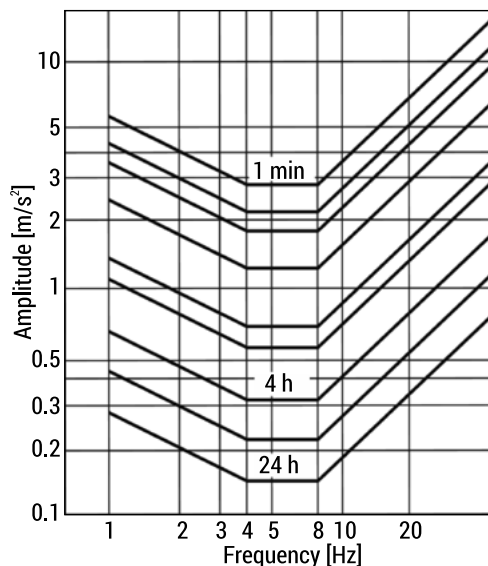


FIG. 1. The acceptable criteria for periodic vibrations for humans [4]

Acceptable periodic vibration criteria for humans are defined as the duration of action with a specific vibration amplitude and frequency in the direction of the forcing causing the greatest injury to the skeletal system – Figure 1.

In special military vehicles, the seats used, in addition to ergonomic requirements, also meet the requirements related to the probability of enemy action, i.e., the use of explosive charges to destroy vehicles.

A typical military special vehicle seat fulfills the task of protecting crew members from force impulses acting on the vehicle in the horizontal and vertical directions resulting from collisions and the action of an explosive charge under and to the side of the vehicle (Table 1).

The modular design of the military special vehicle seat allows its functionality to be tailored to the needs of the driver, commander, or soldiers using it according to the requirements of the position in the vehicle. Seat modules are its constituent parts, which, in addition to the base elements (seat, backrest, headrest, footrest), there are also functional modules that provide the desired kinematics and energy dispersion. Modules are sometimes used in different seat design configurations, whose functions are different due to the function in the vehicle (driver's seat, soldier's seat, system operator's seat), the mounting method (to the wall, to the floor, to the ceiling), the mounting direction (from the side, from behind, from below).

TABLE 1. Comparison of the value of the maximum acceleration and the duration of a frontal car collision at a speed of 30 mph and an explosion under the vehicle [6]

Type of incident	Acceleration (g)	Impulse duration (ms)
Frontal car collision	25 g to 50 g	70 ms to 120 ms
Explosion under the vehicle	100 g to 400 g	3 ms to 30 ms

The specific function of the seats requires additional individual features in their design, e.g., reclining the backrest (in the driver's seat due to the possibility of evacuation), rotating seats (for system operators), folding seats, and backrests (for the soldier).

Modularity, due to the repetitive nature of the components, reduces production costs and facilitates the configuration of seats with different functions; it also contributes, in the event of seat damage, to a faster repair process by replacing the damaged module.

The technology for manufacturing modular structures presents a challenge in terms of the selection of materials for production, where the most desirable feature is the high strength of the materials with low weight and ensuring dimensional and mass stability of the main components. An important issue is the selection of energy dissipation structures and the shaping of the characteristics of the damping element in such a way as to reduce the forces acting on the human body. The location and restraint of the seat should prevent impacts from the side of the vehicle floor from being deformed during the explosion and provide headroom to prevent the occupant from hitting the roof of the vehicle.

Modeling of seat properties in mbs

The vertical displacements of the vehicle seat resulting from the explosion of the explosive result from short-term impacts on the carbody. Mathematical models describing such impacts enable the determination of the dynamic response index (DRIz) introduced by Stech and Payne [2]. In this description, the evaluation of the body response of a vehicle crew member is determined using a simple single-mass model. Using numerical tools, it is possible to perform tests in which the mass of the passenger is separated from the mass of the seat. The multi-mass model allows a simulation study of the effect of seat and seatbelt stiffness on the DRIz coefficient. Using Multibody System (MBS) software, a simulation model can be built to represent the distribution of masses, the kinematics of the system, the design parameters of the springs and dampers used in the seat, and to minimize the acceleration values acting on the occupants [5]. A dynamic model of a seat with seat belts and a mass representing the passenger was developed in MSC.ADAMS/View. The seat model CAD 3D was prepared for numerical calculations – Fig. 2.

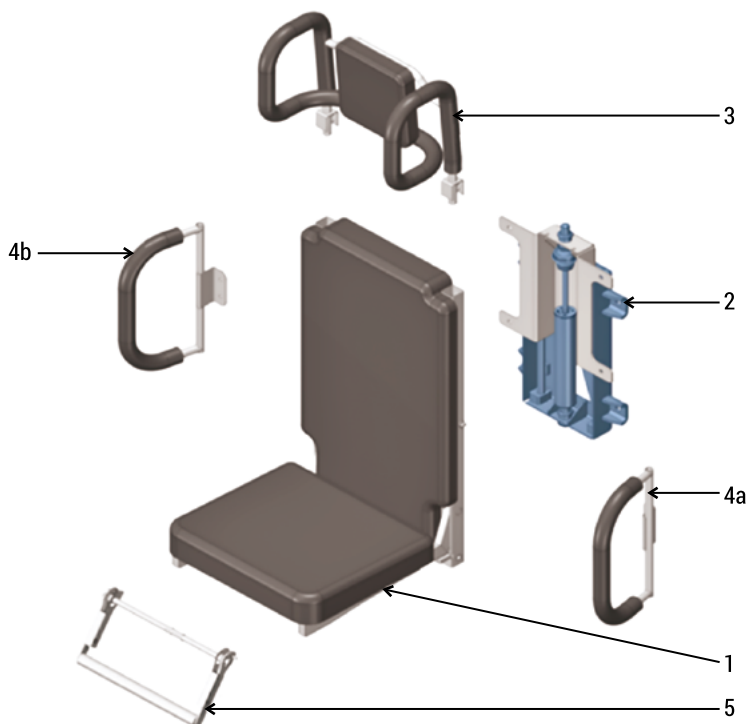


FIG. 2. Model of the modular seat (1 – seat, 2 – absorber module, 3 – headrest module, 4 – side supports, 5 – footrest)

In the model used to determine the dynamic response index (DRIZ) introduced by Stech and Payne [2], the response of the vehicle crew member's body is determined by mass acceleration values. It is assumed that the upper body of mass m rests on top of the lumbar vertebrae. Thus, the spine is represented by a massless spring of constant elasticity k and the soft tissue damping of the body by the damping coefficient c .

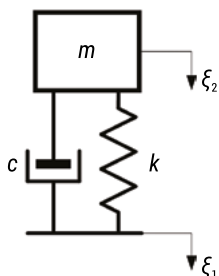


FIG. 3. Model diagram for determining the DRIZ coefficient [2]

The equation of motion for this model is:

$$\ddot{z}(t) = \ddot{\delta} + 2 \cdot \zeta \cdot \omega_n \cdot \dot{\delta} + \omega_n^2 \delta \quad (1)$$

where:

$\ddot{z}(t)$ – is the acceleration in the vertical direction measured at the position of initiation;

δ – is the relative displacement of the system with, , and >0 compression;

ζ – is the damping coefficient with, $\zeta = \frac{c}{2 \cdot m \cdot \omega_n}$;

ω_n – is the natural frequency with, $\omega_n = \sqrt{\frac{k}{m}}$.

The DRIz is calculated by the maximum relative displacement δ_{max} , ω_n and the gravity acceleration g as shown in (2):

$$DRIz = \frac{\omega_n \cdot \delta_{max}}{g} \quad (2)$$

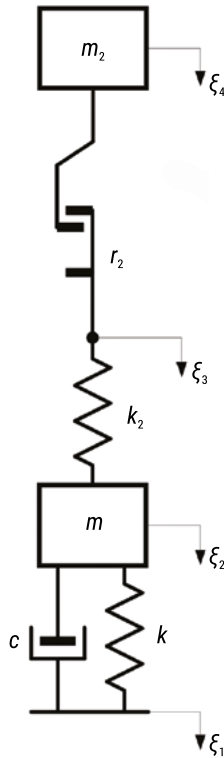


FIG. 4. Model of the seat including seat belts: ξ – displacements of the system's elements, m – seat mass, m_2 – body mass, c – damping coefficient (seat), k – spring constant (seat), r_2 – movement limiter (belts)

The design of seats with impact protection systems is usually supported by simulations in FEM Explicite for observing the deformation of the seat structure. Additional protective mechanisms and structures are taken into account in the design of explosion-proof seats. The design of explosion-proof structures relies on the selection of mechanical parameters through a simulation process. The seat model used to optimize its parameters and characteristics is shown in Figure 4.

The multibody structure of the seat-passenger model was used to determine the DRIz coefficient as a function of the stiffness and damping parameters inherent in seat belts. A dynamic model with a seatbelt occupant was developed in MSC. ADAMS – Figure 5.

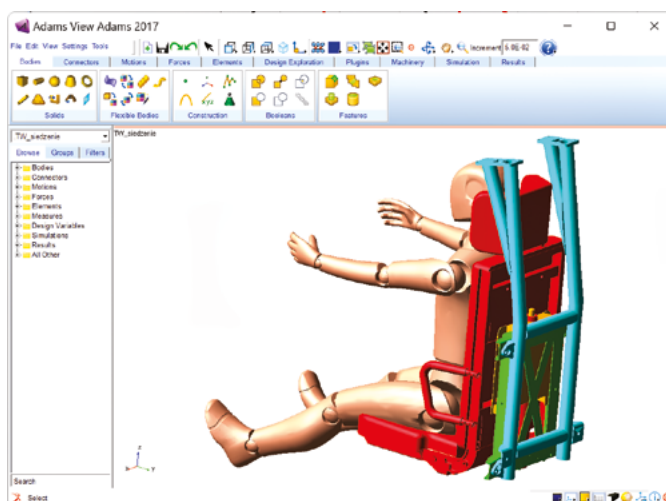


FIG. 5. Parametric simulation model of the seat in MSC.ADAMS

The anti-explosion seat model was developed at MSC.ADAMS is used to optimize the parameters of the anti-explosion mechanism dampers, taking into account backlash and susceptibility in the seat-passenger system. An important element of the non-linear characteristics of the system, controlled and verified during simulation, is the free movement of the passenger relative to the seat.

Some results and analysis

Dynamic simulations of multibody systems have become an essential tool, setting a new standard for improving the design and prototyping of devices and mechanisms.

The use of dynamic simulations of multibody systems has become a tool for obtaining precise numerical results, thus enabling engineers and designers to make informed decisions to optimize structures and improve mechanisms. Using MBS to improve explosion-proof seating, it is possible to select system parameters to minimize acceleration from a cargo explosion.

The numerical data obtained from the dynamic simulations made it possible to analyze the forces and detail the performance of the explosion seat. This information led to modifications to the seat's structure and mechanisms, with the ultimate goal of mitigating accelerations in the vertical plane. In preparing subsequent design variants, engineers conducted research in an iterative manner, assessing the impact of changes to the parameters of the explosion seat structure. Dynamic simulations facilitated the development of the design and reduced the cost and time to improve the proposed technical solutions. Figures 6–9 show examples of the characteristics obtained from the numerical simulations.

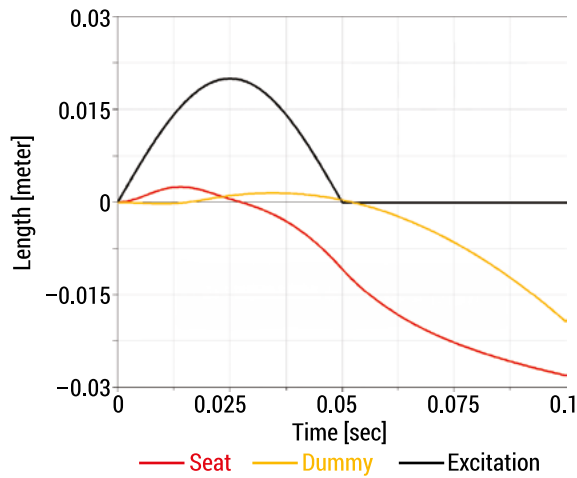


FIG. 6. Length-time graph of a simulation model of the seat in MSC.ADAMS

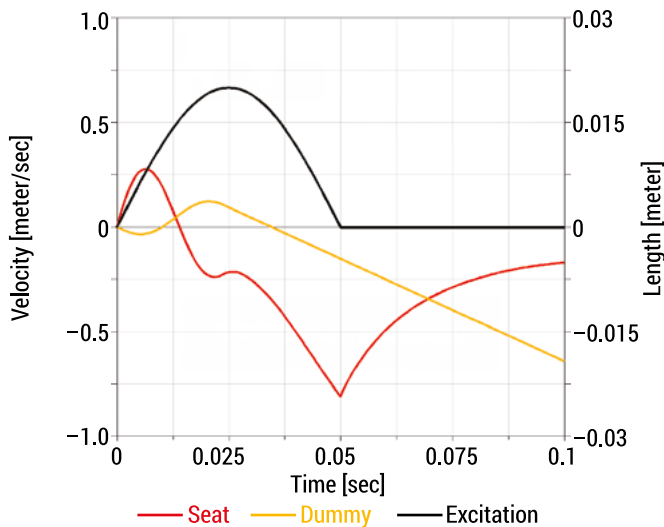


FIG. 7. Velocity-time graph of a simulation model of the seat in MSC.ADAMS

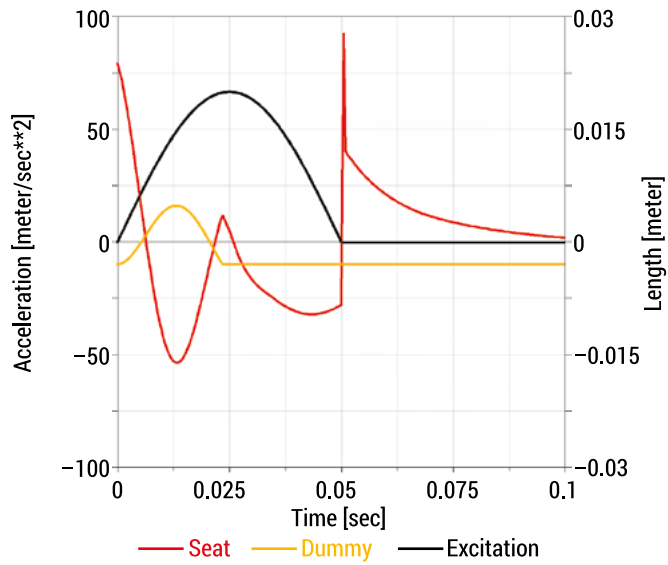


FIG. 8. Acceleration-time graph of a simulation model of the seat in MSC.ADAMS

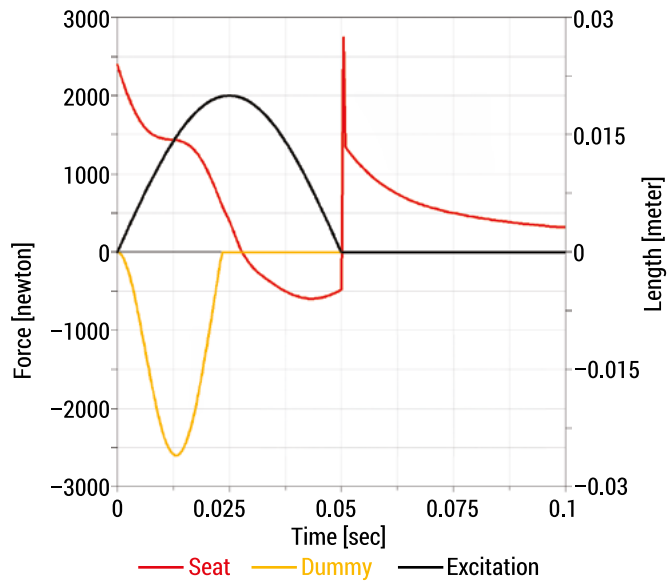


FIG. 9. Force-time graph of a simulation model of the seat in MSC.ADAMS

Conclusions

Due to the current market demand and the modernization plan of the armed forces, there is a need to develop a multifunctional seat to protect the crew members of special military vehicles against the effects of short-term dynamic loads of significant value. None of the manufacturers currently offering mine-blast proofing seats offers such a solution that allows the optimal adjustment of the seat to the requirements of the end user, who must compromise between the level of protection and ergonomics.

In the coming years, in the construction of military combat vehicles, activities aimed at ensuring crew safety will be further developed, e.g., by modernizing or adding new systems.

In the face of escalating global threats and the increasing intensity of warfare, it is imperative to prioritize the development of innovative methods for designing structures that can effectively safeguard the health and lives of military vehicle users. A critical concern is the need for more comprehensive solutions in mine-blast proofing seats currently offered by manufacturers. The absence of a solution that allows for the optimal adjustment of seats to meet the specific requirements of end-users underscores a significant gap in the current market offerings, forcing users to compromise between protection levels and ergonomic considerations. The pressing need for multifunctional seats capable of protecting crew members in special military vehicles against the effects of short-term dynamic loads with substantial magnitudes is evident. The existing market demand, coupled with the ongoing modernization plans of armed forces, presents a unique opportunity to address this gap by developing a product beyond the capabilities of current serial counterparts available in the domestic market. The development of such seats would enhance the safety of military personnel and align with the evolving landscape of modern warfare.

Looking ahead, it is anticipated that the construction of military combat vehicles will witness a surge in activities aimed at ensuring the safety of the crew. This trajectory may involve the integration of advanced technologies, modernization efforts, and the incorporation of new systems that mitigate the impact of short-term dynamic loads on crew members. The trajectory of future developments in military vehicle construction is likely to be driven by a commitment to providing state-of-the-art safety measures without compromising the operational effectiveness and ergonomics of the equipment. In conclusion, the current scenario underscores the critical need for the development of multifunctional seats that strike a balance between optimal protection and ergonomic considerations for military vehicle users. The market demand, coupled with the impending modernization plans of armed forces, presents a compelling opportunity to pioneer innovative solutions that can set new standards in ensuring the safety and well-being of military personnel in the face of evolving global threats.

References

1. Simiński P., 2012, *Bezpieczeństwo pojazdów w badaniach WITPiS*, Nowa Technika Wojskowa, 9.
2. Payne P.R., Stech E.L., 1969, *Dynamic Models of the Human Body*, Wright-Patterson Air Force Base.
3. Research and Technology Organisation of NATO, 2007, *Technical Report TR-HFM-090. Test Methodology for Protection of Vehicle Occupants against Anti-Vehicular Landmine Effects*.
4. NATO Standardization Agency, 2014, *Procedures for Evaluating the Protection Level of Armoured Vehicles – Mine Threat*, AEP-55, vol. 2.
5. Rodak D., Żurawski M., Gmitrzuk M. et al., 2021, *Possibilities of Vacuum Packed Particles application in blast mitigation seat in military armored vehicles*, Bulletin of the Polish Academy of Sciences, Technical Sciences, e138238. DOI: 10.24425/bpasts.2021.138238.

Chapter 3

3.1. Leveraging smart measurement technologies for enhanced food and beverage servicing: a case study of the KYPS system

Andriy Andrushko¹

¹Lviv Polytechnic National University, ICSIT, CAD,
contact author via email for correspondence andrii.m.andrushko@lpnu.ua

Summary: Smart Measurement Technologies (SMT) offer a transformative approach to obtaining accurate and actionable measurements, leading to improved decision-making, operational efficiency, and resource management. The paper aims to shed light on the promising KYPS system that is currently emerging in Ukraine. Utilizing a specific type of ESP32 microcontroller – the ESP32 SX1276 LoRa Development Board – KYPS benefits from its combined capabilities for LoRa-based IoT applications and serves as a notable example of SMT adoption in the food and beverage sector.

Keywords: smart sensor, environment monitoring, microcontroller, low-power, LoRaWAN, ESP32, IoT, hospitality industry, food and beverage sector

Introduction

Smart Measurement Technologies (SMT) refer to a class of advanced systems and devices that leverage sophisticated sensors, data analytics, and connectivity to obtain accurate and real-time measurements; they empower businesses to make informed decisions, improve processes, and achieve sustainable outcomes. Due to their advanced capabilities to support business development, SMT received a lot of attention in the literature both from practitioners [1, 2] and scientific researchers [3, 4, 5]. However, authors are mainly focused on description of SMT application for manufacturing processes [3, 6, 1], electric energy distribution systems [7, 5], or marketing and customer experience [8, 9].

At the same time application of these technologies within service industries is rarely viewed – few studies on IT-enabled services investigate how the technological attributes of smart technology influence service performance in a continuously changing environment [10]. “While smart technologies are more active in some industries, they have not yet been integrated into some sectors” [9].

This article aims to fill this gap and considers the application of SMT within the hospitality industry, focusing on implementation of the technologies in the food

and beverage sector. Specifically, we will consider the KYPs (Keep Your Products Safe) system that is offered by a local Ukrainian company, located in Lviv. The company offers comprehensive services that include environmental control (temperature, humidity), data transmission wireless technologies, user accounts and on-line reporting and analytics, equipment rentals and support. The goal of this paper is to generally present the technology and describe some specifics of its application in the Ukrainian market. Particularly we will focus on the environment monitoring and data collection approaches, as well as on the data transmission wireless technology employed.

Importance of SMT for the food and beverage industry

The food and beverage industry represents a huge sector of services within the hospitality industry that include preparing, presenting, and serving food and beverages to the customers on-premise (at restaurants and hotels) or off-premise (takeaway, restaurant catering service, and food delivery) [11]. Today, many restaurant businesses invest in smart technologies to differentiate from competitors, deliver better service, and provide a good customer experience [9]. Additionally, operation costs are significantly reduced by integrating smart features in operation processes [12, 13].

Smart technology is defined as technology capable of (1) monitoring environments by collecting data through its technology sensors, and (2) analyzing the collected data to provide informational support [14, 15]. The key idea behind the SMT is to leverage advanced sensors, data analytics, and connectivity to obtain accurate and actionable measurements for improved decision-making and operational efficiency. All these factors play a vital role for businesses dealing with food and beverage servicing – hotels, restaurants, SPA resorts, food warehouses, etc. “Instead of relying on periodic testing by quality control personnel within a company or by a governmental organization, companies will be able to use these technologies to identify potential risks and develop science-based measurements to control hazards” [16]. Smart technologies not only improve management capacity and operational efficiency of specific hospitality sectors, but they also enhance service quality and user satisfaction [17].

In the food and beverage sector SMT are employed to monitor and control variables such as temperature, pressure, humidity, and flow rates. The ‘sensing’ concept refers to the capability that a system has to detect events, acquire data, and measure changes that occur in a physical environment [18]. This helps optimize process parameters, improve consistency, and ensure product quality. Automated systems can adjust process conditions in real-time based on sensor measurements, enhancing efficiency and reducing waste.

Additionally, SMT enable real-time monitoring of environmental conditions during transportation and storage. “There is an urgent need to develop efficient technologies to monitor the food supply chain so as to identify and recall unsafe food” [16]. Sensors can track temperature, humidity, and vibration levels to ensure that peris-

hable goods are transported under suitable conditions, preventing spoilage and maintaining product integrity. Temperature indicators still play a critical role in maintaining the safety and quality of perishable and frozen food products because they are eco-friendly and cost-effective [19].

And finally, SMT are irreplaceable when we talk about Data Analytics and Predictive Maintenance. The technologies generate vast amounts of data, which can be analyzed to identify trends, patterns, and potential issues. Data analytics can help optimize operational processes, forecast demand, and enable predictive maintenance of equipment, ensuring minimal downtime and reducing maintenance costs. The 'smart' concept refers to the capability of a system to incorporate actuation and control functions in order to describe and analyze situations and make decisions based on the available data in a predictive or adaptive manner [20].

Implementation of SMT in the food and beverage sector has its specifics, the designer of a system should be able to choose suitable sensors, type of output signals and communication network, as well as put in place some software application to manage the entire measurement process. We continue further with the consideration of the KYPS system and the approaches it employs.

Environment monitoring and data collection

The base chip

The environment monitoring hardware that KYPS uses, is based on the ESP32 low-power System on a Chip (SoC) microcontrollers that include wireless capabilities and a dual-core processor (Fig. 1). ESP32 is a single 2.4 GHz Wi-Fi-and-Bluetooth combo chip designed with the TSMC low-power 40 nm technology. It is designed to achieve the best power and Radio Frequency performance, showing robustness, versatility and reliability in a wide variety of applications and power scenarios [21]. The term "low-power" indicates that the ESP32 chip is optimized for power efficiency. It is designed to consume low power while delivering its functionality, making it suitable for battery-operated or power-constrained devices, these features are very relevant and vital for the Ukrainian market nowadays.

Another very important feature is the Radio Frequency performance. In the context of the ESP32 chip, RF performance refers to how well the chip performs in terms of wireless communication, particularly in the 2.4 GHz Wi-Fi and Bluetooth frequency bands. This includes factors such as signal strength, range, data transmission/reception quality, and interference handling.

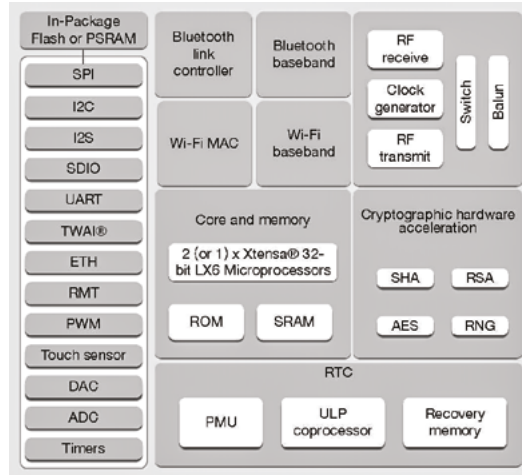


FIG. 1. ESP32 Functional Block Diagram. Source [21]

For its sensors, KYPS uses a particular type of the ESP32 microcontroller, namely the ESP32 SX1276 Lora Development Board (Fig. 2a). This board combines the ESP32 microcontroller and the SX1276 LoRa transceiver module. Each of the components has its specific characteristics that make the board irreplaceable for the goals of SMT:

- The ESP32, a microcontroller designed by Espressif Systems, features a dual-core processor, built-in Wi-Fi and Bluetooth capabilities, a rich set of peripherals, and ample memory. These features make the ESP32 highly versatile and effective for developing IoT applications.
- The SX1276 is a radio frequency transceiver module that operates in the LoRa (Long Range) frequency bands, typically 868 MHz or 915 MHz. It is designed to provide long-range and low-power communication capabilities, making it suitable for applications that require wide-area coverage.

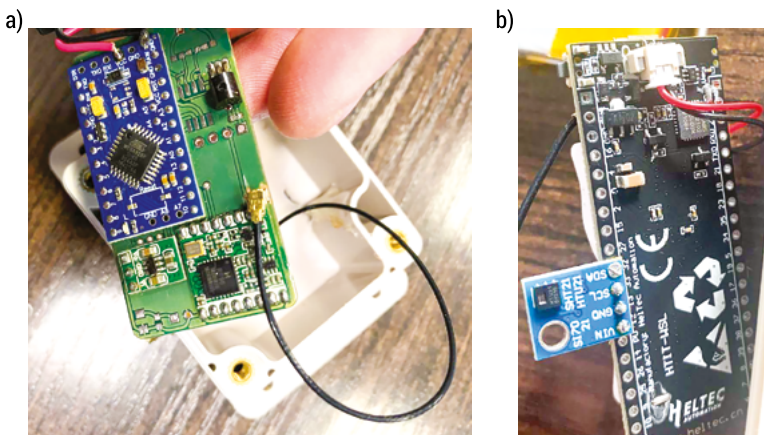


FIG. 2. The ESP32 SX1276 Lora Development Board and the Si7021 sensor

The combination of the ESP32 microcontroller and the SX1276 LoRa transceiver on a single board allows the company’s developers to leverage the capabilities of both components for LoRa-based IoT applications. The board typically includes additional features such as antenna connectors, GPIO pins, and programming interfaces to facilitate development and integration with other hardware components.

The humidity and temperature sensor

To monitor the environmental conditions, the microcontroller is combined with a humidity and temperature sensor. The KYPs technology uses the Si7021 sensor produced by Silicon Laboratories (Fig. 2b). It is a highly accurate and reliable sensor that provides precise measurements of both relative humidity and temperature.

The Si7021 sensor can accurately measure relative humidity (RH) in the range of 0% to 100%. It employs a capacitive humidity sensing element, which measures changes in capacitance due to the absorption or release of moisture by a polymer layer. In addition to humidity, the sensor also provides accurate temperature measurements in the range of -40°C to +125°C. Temperature measurement is performed using an integrated temperature sensor based on a bandgap circuit. The accuracy of both humidity and temperature measurements is very high: ±3% relative humidity and ±0.4°C temperature. Such an accuracy ensures reliable and precise data collection.

The Si7021 sensor is designed to operate with low power consumption, making it suitable for battery-powered or energy-efficient applications. It offers various power-saving modes and has a low standby current, minimizing overall power consumption. It is available in a compact and surface-mount package, making it easy to integrate into electronic designs and sensor modules.

The Si7021 sensor communicates with the ESP32 SX1276 LoRa Development Board using the I2C (Inter-Integrated Circuit) interface. The ESP32 microcontroller, which is part of the development board, has built-in support for I2C communication, allowing it to easily interface with the Si7021 sensor. Table 1 shows the general overview of how the communication between the Si7021 sensor and the ESP32 microcontroller occurs.

TABLE 1. Communication between the Si7021 sensor and the ESP32 microcontroller

Components	Realization
Connection:	The Si7021 sensor is physically connected to the ESP32 development board using two wires: SDA (Serial Data Line) and SCL (Serial Clock Line). These wires carry the data and clock signals for the I2C communication.
I2C Bus Configuration:	The ESP32 microcontroller needs to be configured to use the I2C protocol and communicate with the Si7021 sensor. This involves setting up the I2C bus, specifying the clock frequency, and defining the slave address of the Si7021 sensor.

Components	Realization
Initialization:	In the software code running on the ESP32 microcontroller, the I2C interface is initialized, enabling communication with the Si7021 sensor. This typically involves configuring the necessary I2C pins, setting the clock frequency, and initializing the I2C peripheral.
Sending Commands and Receiving Data:	Once the I2C interface is initialized, the ESP32 microcontroller can send commands to the Si7021 sensor to request humidity and temperature measurements. These commands are typically standardized and defined in the sensor's datasheet or provided in a software library.
Data Acquisition:	Upon receiving the command from the ESP32, the Si7021 sensor performs the requested measurement (humidity or temperature) and sends the corresponding data back to the microcontroller.
Data Processing:	The ESP32 microcontroller receives the data from the Si7021 sensor and can process it as needed. This may involve converting the raw data to meaningful humidity and temperature values, performing calibration, or applying further calculations.
Application Integration:	The humidity and temperature data acquired from the Si7021 sensor can be used within the ESP32 microcontroller's application logic. For example, the data can be displayed on an LCD screen, transmitted over a LoRa network using the SX1276 transceiver, or stored in memory for further analysis.

For the purpose of servicing clients' needs, the environmental data obtained from the sensor is encoded in JSON format and is further transmitted over the local network.

Data transmission network – LoRaWAN

Unlike many SMT devices offered in the western markets [22] which use a standard LAN network, the KYPS system is based on the Long-Range Wide Area Network (LoRaWAN) – a wireless communication protocol specifically designed for long-range, low-power communication between IoT devices and gateways (Fig. 3). It enables devices connection and data exchange over long distances while consuming minimal power. LoRaWAN is a type of Low Power Wide Area Network (LPWAN) that uses open-source technology and transmits over unlicensed frequency bands. Designed for the Internet of Things (IoT), LoRaWAN technology provides a far longer range than WiFi or Bluetooth connections [23].

An end device can connect to a network with LoRaWAN in two ways:

- Over-the-air Activation (OTAA): A device has to establish a network key and an application session key to connect with the network.
- Activation by Personalization (ABP): A device is hardcoded with keys needed to communicate with the network, making for a less secure but easier connection [24].



FIG. 3. The gateway and the sensor

LoRAWAN provides a reliable and cost-efficient solution for connecting and managing IoT devices, and therefore is very valuable for SMT. The following list highlights the key characteristics of the technology:

- *Long Range.* LoRaWAN operates in the sub-GHz frequency bands, typically around 868 MHz or 915 MHz, which allows for long-range communication. Under optimal conditions, LoRaWAN can provide connectivity over several kilometers, making it suitable for applications that require wide-area coverage.
- *Low Power Consumption.* LoRaWAN devices are designed to operate on low power, enabling long battery life. The devices can go into sleep mode and wake up at scheduled intervals to transmit or receive data, conserving energy and extending battery life.
- *Low Data Rates.* LoRaWAN is optimized for applications that transmit small amounts of data at low data rates. It is well-suited for applications where infrequent data updates or sensor readings are sufficient, such as environmental monitoring.
- *Scalability.* LoRaWAN supports a large number of devices connected to a single network. It utilizes a star-of-stars topology, where IoT devices communicate with gateways that serve as intermediaries to forward data to the network server. This allows for efficient management of a large-scale IoT deployment.
- *Security.* LoRaWAN incorporates security measures to protect data transmitted over the network. It includes encryption and authentication mechanisms to ensure the confidentiality and integrity of data exchanged between devices and the network server.

- *Cost-effective*: LoRaWAN offers a cost-effective solution for deploying IoT networks over large areas. The long-range capability reduces the number of gateways required to cover a wide area, leading to lower infrastructure costs compared to traditional cellular networks.

The key features listed above, make the LoRaWAN technology more advantageous compared to standard popular wireless communication protocols such as WiFi or Bluetooth.

Figure 4 illustrates the typical LoRaWAN network architecture, however in real-world deployments, the network can have multiple gateways and devices distributed over a wider area to achieve the desired coverage and capacity:

- the LoRaWAN devices (e.g., sensors, actuators) communicate with the gateways using the LoRaWAN protocol.
- the gateways act as intermediaries between the LoRaWAN devices and the network server. They receive and transmit data between the devices and the network server. Gateways are typically connected to the network server via backhaul connectivity, such as Ethernet, 3G/4G, or Wi-Fi.
- the network server is responsible for managing the LoRaWAN network. It handles device registration, authentication, data routing, and network-wide functions such as security and quality of service.
- the application server interfaces with the network server and processes the data received from the LoRaWAN devices. It typically hosts application-specific logic, data storage, and integration with other systems or services.

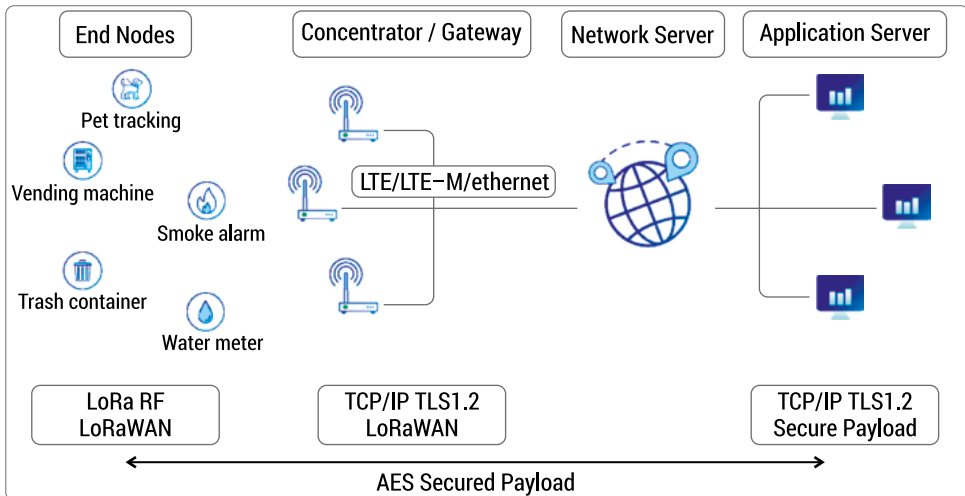


FIG. 4. Typical LoRaWAN network architecture. Source [25]

In addition, the long-range link, base stations, and device battery life are improvements related to a star network architecture. Communications with different data rates do not have interference between 300bps up to 5kbps to 125kHz bandwidth and are distributed in different channels to perform the communication between the connected devices and the gateways [26].

Conclusions

The key idea behind Smart Measurement Technologies is to leverage advanced sensors, data analytics, and connectivity to obtain accurate and actionable measurements, ultimately leading to improved decision-making, enhanced operational efficiency, and better resource management for businesses dealing with food and beverage servicing. Implementation of SMT in the food and beverage sector has its specifics, it is necessary to choose suitable sensors, set up output signals and communication network, as well as software application to manage the entire measurement process. In this article we aimed to present the KYPS system, offered within the food and beverage sector by a local Ukrainian company.

For its sensors, KYPS uses a particular type of ESP32 microcontroller – the ESP32 SX1276 Lora Development Board. This board combines the ESP32 microcontroller and the SX1276 LoRa transceiver module. This combination allows the company to leverage the capabilities of both components for LoRa-based IoT applications. To monitor the environmental conditions, the KYPS technology uses the Si7021 – a highly accurate and reliable sensor that can measure relative humidity in the range of 0% to 100%, and temperature in the range of -40°C to $+125^{\circ}\text{C}$. The Si7021 sensor communicates with the ESP32 SX1276 LoRa Development Board using the I2C interface. The KYPS system is based on the Long Range Wide Area Network (LoRaWAN) which has a lot of advantages compared to popular wireless communication protocols such as WiFi or Bluetooth.

It is worth noting, that the scope of the paper did not allow to elucidate all the aspects of the system, so future studies could delve into the technical characteristics of the appliances, engineering principles of their utilization, and software application for the system management.

References

1. Luis J., 2020, *Industry 4.0: How Measurement Technology Plays a Valuable Role in Smart Manufacturing*, www.ndc.com/blog/posts/2020/01/02/industry-40-how-measurement-technology-plays-a-valuable-role-in-smart-manufacturing [accessed: 5.08.2023].
2. *Optimized usage of the Vaisala viewLinc System – from Room Monitoring to Explosion-proof zones*, www.vaisala.com/sites/default/files/documents/VIM-GLO-EN-CMS-Case-Study-Onopharm_B211779EN.pdf [accessed: 24.07.2023].

3. Schütze A., Helwig N., Schneider T., 2018, *Sensors 4.0 – smart sensors and measurement technology enable Industry 4.0*, Journal of Sensors and Sensor Systems, 7(1), 359–371. DOI: 10.5194/jsss-7-359-2018.
4. Mendez G., Md Yunus M.A., Mukhopadhyay S.C., 2011, *A Wi-Fi Based Smart Wireless Sensor Network for an Agricultural Environment*, in: *Fifth International Conference on Sensing Technology*, Palmerston North, New Zealand, 405–410. DOI:10.1109/ICSensT.2011.6137009
5. Kabalci Y., 2016, *A survey on smart metering and smart grid communication*, Renewable and Sustainable Energy Reviews, 57, 302–318. DOI: 10.1016/j.rser.2015.12.114.
6. Sajjad A., Ahmad W., Hussain S. et al., 2022, *Development of Innovative Operational Flexibility Measurement Model for Smart Systems in Industry 4.0 Paradigm*, IEEE Access, 10, 6760–6774. DOI: 10.1109/ACCESS.2021.3139544.
7. Saldaña-González A.E., Sumper A., Aragües-Peñalba M. et al., 2020, *Advanced Distribution Measurement Technologies and Data Applications for Smart Grids: A Review*, Energies, 13, 3730. DOI:10.3390/en13143730.
8. Han D., Hou H., Wu H. et al., 2021, *Modelling Tourists' Acceptance of Hotel Experience-Enhancement Smart Technologies*, Sustainability, 13, 4462. DOI: 10.3390/su13084462.
9. Tuncer I., 2020, *Customer Experience in the Restaurant Industry: Use of Smart Technologies*, in: *Handbook of Research on Smart Technology Applications in the Tourism Industry*, ed. E. Çeltak, Business Science Reference, Hershey PA. DOI: 10.4018/978-1-7998-1989-9.ch012.
10. Kang L., Jiang Q., Peng C.H. et al., 2020, *Managing Change with the Support of Smart Technology: A Field Investigation of Ride-Hailing Services*, Journal of the Association for Information Systems, 21(6), 1594–1620. DOI: 10.17705/1jais.00647
11. Diaz M., 2019, *Food and beverage in hospitality. Trends in hotel restaurant management*. <https://joinposter.com/en/post/hotel-food-and-beverage> [accessed: 11.07.2023].
12. Hou H., Wu H., 2020, *Tourists' Perceptions of Green Building Design and Their Intention of Staying in Green Hotels*, Tourism and Hospitality Research, 21(1), 115–128. DOI: 10.1177/1467358420963379.
13. Jeremen D.E., Jędrasiak M., Rapacz A., 2016, *The Concept of Smart Hotels as an Innovation on the Hospitality Industry Market – Case Study of Puro Hotel in Wrocław*, Economic Problems of Tourism, 36, 65–75. DOI:10.18276/EPT.2016.4.36-06.
14. Foroudi P., Gupta S., Sivarajah U. et al., 2018, *Investigating the effects of smart technology on customer dynamics and customer experience*, Computers in Human Behavior, 80, 271–282. DOI: 10.1016/j.chb.2017.11.014.
15. Zoughbi S., Al-Nasrawi S., 2015, *Regional development getting smarter with ICT*, in: *Encyclopedia of Information Science and Technology*, ed. M. Khosrow-Pour, IGI Global, Hershey–London, 6525–6533.
16. Yu Z., Jung D., Park S. et al., 2022, *Smart traceability for food safety*, Critical Reviews in Food Science and Nutrition, 62(4), 905–916. DOI:10.1080/10408398.2020.1830262.
17. Lim W.M., Teh P.L., Ahmed P.K. et al., 2018, *Going keyless for a seamless experience: Insights from a unified hotel access control system*, International Journal of Hospitality Management, 75, 105–115. DOI: 10.1016/j.ijhm.2018.03.014.
18. Miranda J., Ponce P., Molina A. et al., 2019, *Sensing, smart and sustainable technologies for Agri-Food 4.0*, Computers in Industry, 108, 21–36. DOI: 10.1016/j.compind.2019.02.002.
19. Zhang C., Yin A.X., Jiang R. et al., 2013, *Time-temperature indicator for perishable products based on kinetically programmable Ag overgrowth on Au nanorods*, ACS Nano, 7(5), 4561–4568. DOI: 10.1021/nn401266u.

20. Nebylov A., Sharan S., Arifuddin F., 2010, *Smart control systems for next-generation autonomous wing-in-ground effect vehicles*, IFAC Proceedings Volumes, 43(15), 112–117. DOI: 10.3182/20100906-5-JP-2022.00020.
21. *ESP32 Series Datasheet, Version 4.3*, www.espressif.com/sites/default/files/documentation/esp32_datasheet_en.pdf [accessed: 27.07.2023].
22. *Mains unit for wireless LAN data logger*, <https://www.testo.com/en/mains-unit-for-wireless-lan-data-logger/p/0572-2020> [accessed: 14.07.2023].
23. Ho N., 2021, *What Is LoRaWAN? Long Range Wide Area Networks Explained*, www.emnify.com/iot-glossary/lorawan [accessed: 15.07.2023].
24. *LoRaWAN*, www.trendmicro.com/vinfo/us/security/definition/lorawan [accessed: 15.07.2023].
25. *LoRaWAN Architecture*, www.thethingsnetwork.org/docs/lorawan/architecture/ [accessed: 12.08.2023].
26. Carvalho Silva J. de, Rodrigues J.J.P.C., Alberti A.M. et al., 2017, *LoRaWAN – A Low Power WAN Protocol for Internet of Things: a Review and Opportunities*, International Multidisciplinary Conference on Computer and Energy Science, Split, Croatia.

3.2. Synthesis of the car speed regulator using the method of pole placement

*Markian Nakonechnyi¹, Orest Ivakhiv², Yuriy Hirniak³,
Oleksandr Viter⁴, Yuriy Nakonechnyi⁵*

¹*Lviv Polytecnic National University, Computer Technology, Automation and Metrology Institute/
Computerized Automatic Systems Department, L'viv, Ukraine, markian.v.nakonechnyi@lpnu.ua*

²*Lviv Polytecnic National University, Computer Technology, Automation and Metrology Institute/
Intelligent Mechatronics and Robotics Department,
contact author via email for correspondence orest.v.ivakhiv@lpnu.ua*

³*Lviv Polytecnic National University, Computer Technology, Automation and Metrology Institute/
Intelligent Mechatronics and Robotics Department, yurii.b.hirniak@lpnu.ua*

⁴*Lviv Polytecnic National University, Computer Technology, Automation and Metrology Institute/
Computerized Automatic Systems Department, L'viv, Ukraine, oleksandr.s.viter@lpnu.ua*

⁵*Lviv Polytecnic National University, Computer Technology, Automation and Metrology Institute/
Information Security Department, L'viv, Ukraine, yurii.m.nakonechnyi@lpnu.ua*

Summary: The state space method was used for the car speed controller design by the pole placement. The simulation was provided in the Simulink environment and allows the proper decision to be taken on the better controller structure. The poles were placed in the proper place as well.

Keywords: PI controller, automatic control, car speed, pole placement, Ackermann formula, Simulink

Introduction

Modern cars are very complicated objects that include both developed software [1] and hardware [2] equipment including contemporary microsystem devices [3]. They ensure reliable autonomy, efficient driver assistance [4], automobile safety [5], including both intelligent tracking [6] and anti-theft [7] systems with GPS capabilities and applications [8], in addition to a new era of electric cars discoveries [9].

Consider a controller synthesis using the state space method for assigning poles [10], [11] which both allows to satisfy all the poles in given positions in contrast to the classical root hodograph method that ensures only two positions, and to simplify this procedure using the Ackerman formula.

Car model creation

The controller satisfied proportional – integral dynamic law is widespread in present day practice, if the object belongs to objects of the 0-th type [9]. A similar approach

can be used in the synthesis of regulators using the method of pole placement. Introducing a *PI* controller into the system increases its order by “one”, so if the object has the n -th order, then the system will have the $(n + 1)$ – th order. So, let us consider the features of the control system synthesis of the car speed that consists of the *PI* controller, the ignition system, the engine and the actual car [9]. More details, the solenoid controls the carburetor throttle position, the engine is represented as an inertial link with a time constant T_e equal to one second, and the vehicle reproduce an inertial link with a time constant T_c equal to three seconds [9]. Using the transducer in the feedback loop, the speed of the car is converted into a value that is compared with the target one. Pressing the accelerator pedal leads to the appearance of an electric current in the winding of the solenoid, which ensures the movement of the throttle, which in turn causes an increase or decrease in the supply of fuel to the combustion chamber of the engine. A change in the fuel supply to the engine combustion chamber is equivalent to a mutation in the force applied to the engine shaft, which in turn causes a change in the engine output torque.

The mathematical model of the internal combustion engine in the first approximation can be represented by a differential equation of the first order [9] in the following form:

$$T_e \frac{dM(t)}{dt} + M(t) = K_e L(t), \quad (1)$$

where $L(t)$ is the linear displacement of the throttle (in centimeters); K_e is the torque transmission coefficient of the engine (N/cm); $M(t)$ is the torque on the engine shaft (N·m); T_e is the engine time constant (seconds).

In our case, the transfer function of the engine from $L(s)$ to $M(s)$ can be given in the following form:

$$W_e(s) = M(s)L(s) = K_e (1 + sT_e) \quad (2)$$

It will obtain the equation of the car motion based on the reasoning that the car moves only in one direction and any other movement is not allowed. The speed of the car is affected only by the action of the torque developed by the engine. The equation of the car motion has the following form:

$$T_c \frac{dV_c(t)}{dt} + V_c(t) = K_c M(t) \quad (3)$$

Applying the Laplace transform to expression (3), the transfer function of the car is obtained from $M(s)$ to $V_c(s)$ as follows:

$$W_c(s) = V_c(s)M(s) = K_c (1 + sT_c) \quad (4)$$

Now, based on expressions (2) and (4), it is possible to write the transfer function of the car from $L(s)$ and $V_c(s)$ in the following form:

$$W_{ec}(s) = W_e(s)W_c(s) \quad (5)$$

and considering the influence of the solenoid (in our case the solenoid is supplied without an inertia link), the coefficient K_d is equal to 0.833 cm/V [9] and the general transmission function has the following form:

$$W(s) = K_d W_e(s)W_c(s) \quad (6)$$

For low power internal combustion engines [9] both values (T_e and K_d) are equal to “ones” (Fig.2). The reaction of a change in the speed of the car to a change in the action of the engine torque occurs with a delay T_e , which, according to the given data, is approximately equal to 3 seconds. As well as the coefficient of the car moment transmission K_c according to the given data [9] is equal to 40 [km/Nm*s] . So, the general transfer function is as follows:

$$W(s) = \frac{33.32}{(3s+1)(s+1)} = K_d \frac{V_c(s)}{L(s)} \quad (7)$$

Using state space variables

It is possible to pass from the equation of the n -th degree to n equations of the first degree, which simplify its solvation using state space variables.

The task of synthesizing the regulator by placing the poles consists in determining the desired position of the roots of the characteristic equation of the system on the complex plane and finding the $\{K_i\}$ coefficients ($i = 1, n$) that ensure their given location on this plane. Let us consider for solving simplicity that the features of the synthesis of a PI controller using the Ackerman formula [12] – [14] for the system of automatic control of the process in the object (Fig.1), which is described by a differential equation of the n -th order. Note that the PI controller transfer function has the following form:

$$\frac{M(s)}{Y(s)} = -\left(K_1 + \frac{K_{n+1}}{s}\right) = -W_{PI}(s) \quad (8)$$

The gain K_1 may be placed both in the feedback link (Fig.1) and in parallel to the integrator with gain K_{n+1} .

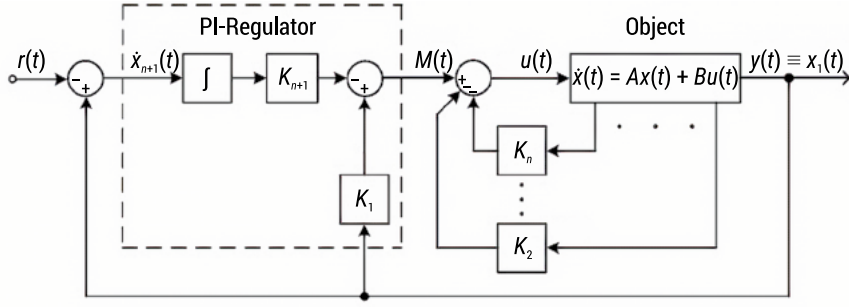


FIG. 1. General structure of object control with PI-regulator using

In general, the state equation of the object (Fig. 1) has the following form:

$$\begin{aligned}\dot{\mathbf{x}}(t) &= \mathbf{A}\mathbf{x}(t) + \mathbf{B}u(t), \\ \mathbf{y}(t) &= \mathbf{C}\mathbf{x}(t) = \begin{bmatrix} 1 & 0 & \dots & 0 \end{bmatrix} \mathbf{x}(t).\end{aligned}\quad (9)$$

The equation of the comparison scheme is as follows:

$$\mathbf{x}_{n+1}(t) = \mathbf{C}\mathbf{x}(t) - \mathbf{r}(t) \quad (10)$$

The object input signal is as follows:

$$\mathbf{u}(t) = -K_1x_1(t) - K_2x_2(t) \dots - K_nx_n(t) - K_{n+1}x_{n+1}(t), \quad (11)$$

where K_1, \dots, K_{n+1} are chosen based on the desired placement of the closed system transfer function poles.

The synthesis procedure is as follows: substituting (11) into (9), we obtain:

$$\dot{\mathbf{x}}(t) = \mathbf{A}\mathbf{x}(t) - \mathbf{B}K_1x_1(t) - \dots - \mathbf{B}K_{n+1}x_{n+1}(t) \quad (12)$$

By combining the variable with the value we obtain the system state vector with feedback. Then, based on the equations (10) – (12), there are as follows:

$$\dot{\mathbf{x}}_f(t) = \begin{bmatrix} \mathbf{A} & \mathbf{0} \\ \mathbf{C} & \mathbf{0} \end{bmatrix} \begin{bmatrix} \mathbf{x}(t) \\ x_{n+1}(t) \end{bmatrix} - \begin{bmatrix} \mathbf{B}\mathbf{K} & \mathbf{B}K_{n+1} \\ \mathbf{0} & \mathbf{0} \end{bmatrix} \begin{bmatrix} \mathbf{x}(t) \\ x_{n+1}(t) \end{bmatrix} + \begin{bmatrix} \mathbf{0} \\ -1 \end{bmatrix} r(t) \quad (13)$$

This equation can be given another form as follows:

$$\dot{\mathbf{x}}_f(t) = \mathbf{A}_a \mathbf{x}_a(t) - \mathbf{B}_a \mathbf{K}_a \mathbf{x}_a(t) + \begin{bmatrix} 0 \\ -1 \end{bmatrix} r(t) \quad (14)$$

where $\mathbf{A}_a = \begin{bmatrix} \mathbf{A} & 0 \\ \mathbf{C} & 0 \end{bmatrix}$, $\mathbf{B}_a = \begin{bmatrix} \mathbf{B} \\ 0 \end{bmatrix}$, $\mathbf{K}_a = \begin{bmatrix} \mathbf{K} & K_{n+1} \end{bmatrix}$.

The characteristic equation corresponding to the expression (10) will be presented in the following $(n+1)$ - th order polynomial form $a_{ca}(s)$

$$a_{ca}(s) = |s\mathbf{I} - \mathbf{A}_a + \mathbf{B}_a \mathbf{K}_a| = s^{n+1} + \alpha_n s^n + \dots + \alpha_1 s + a_0 = 0 \quad (15)$$

In this equation, \mathbf{I} is the unit matrix, the set of $\{\alpha_i\}$ values ($i = \overline{1, (n+1)}$) is known, but there are unknown $(n+1)$ values of gains $\{K_i\}$. To determine them, one can either equate the coefficients with the same degree of s in the left and right parts in equation (11) and thus obtain a system of $(n+1)$ linear equations. Using Ackerman's formula for solving simplicity [12], we write the following form:

$$\mathbf{K}_a = \begin{bmatrix} 0 & 0 \dots & 0 & 1 \end{bmatrix} \begin{bmatrix} \mathbf{B}_a & \mathbf{A}_a \mathbf{B}_a & \dots & \mathbf{A}_a^n \mathbf{B}_a \end{bmatrix}^{-1} a_{ca}(\mathbf{A}_a) \quad (16)$$

To obtain a generalized model of the engine and the car (Fig. 2) in the space of state variables in expressions (2), (4) and (6), we perform the transition from the operator to the time form of the presentation of variables as follows:

$$\dot{V}_c(t) = -\frac{1}{T_c} V_c(t) + K_s \frac{K_c}{T_c} M(t) = -0.33 V_c(t) + 11.1 M(t) \quad (17)$$

$$\dot{M}(t) = -\frac{1}{T_e} M(t) + \frac{K_e}{T_e} L(t) = -M(t) + L(t) \quad (18)$$

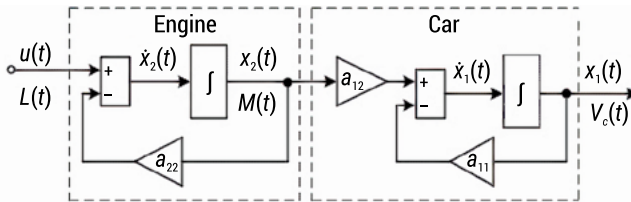


FIG. 2. Generalized structure of the engine and car model

By entering the following notation: $x_1(t) = V_c(t)$, $x_2(t) = M(t)$, $u(t) = L(t)$, let's present a complete model of the engine and the car through the state variables, additionally considering the presence of a transducer in the feedback loop of the system with the transmission coefficient equal to 0.03. The matrixes \mathbf{A} , \mathbf{B} , \mathbf{C} of the equation (5) are modified (the matrix \mathbf{A} is supplied by additional coefficient $a_{31} = 0.03$) as follows:

$$A_f - B_f K_f = \begin{bmatrix} a_{11} & a_{12} & a_{13} \\ a_{21} & a_{22} & a_{23} \\ a_{31} & a_{32} & a_{33} \end{bmatrix} - \begin{bmatrix} K_1 & K_2 & K_3 \end{bmatrix} \quad (19)$$

where $A_f = \begin{bmatrix} -0.33 & 11.1 & 0 \\ 0 & -1 & 0 \\ 0.03 & 0 & 0 \end{bmatrix}$, $B_f = \begin{bmatrix} 0 \\ 1 \\ 0 \end{bmatrix}$, $C_f = \begin{bmatrix} 1 & 0 & 0 \end{bmatrix}$, $a_{11} = 1/T_c = 1/3 = 0.33$,

$a_{12} = (K_d K_c)/T_c = (0.833 \cdot 40)/3 = 11.11$, $a_{11} = K_e/T_e = 1/1 = 1$, $a_{31} = 0.03$,

$a_{13} = a_{23} = a_{32} = a_{33} = 0$.

The controller model structure both with the coefficient K_i in the feedback loop and strait PI line were simulated in in the SIMULINK environment [15] (Fig. 3).

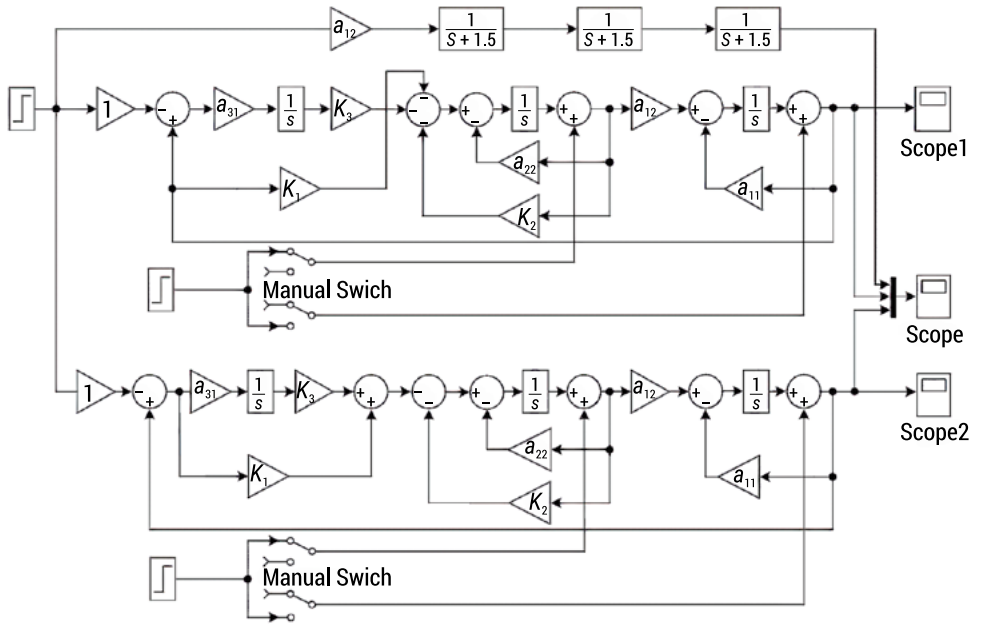


FIG. 3. The controller model in the SIMULINK environment simulation

In the case when the transmission coefficient K_i is introduced into the feedback circuit then its transfer function is as follows:

$$W_1(s) = \frac{V_c(s)}{R(s)} = \frac{K_3 a_{31} a_{12}}{s^3 + s^2(K_2 + a_{11} + a_{22}) + s[a_{11}(K_2 + a_{22}) + K_1 a_{12}] + K_3 a_{31} a_{12}}. \quad (20)$$

If the transmission coefficient K_1 is introduced in parallel to the integrator and the coefficient $K_{n+1}=K_3$ (which will not lead to a change in the characteristic equation of the system), then in this case its transfer function is as follows:

$$W_2(s) = \frac{V_c(s)}{R(s)} = \frac{sK_1a_{12} + K_3a_{31}a_{12}}{s^3 + s^2(K_2 + a_{11} + a_{22}) + s[a_{11}(K_2 + a_{22}) + K_1a_{12}] + K_3a_{31}a_{12}}. \quad (21)$$

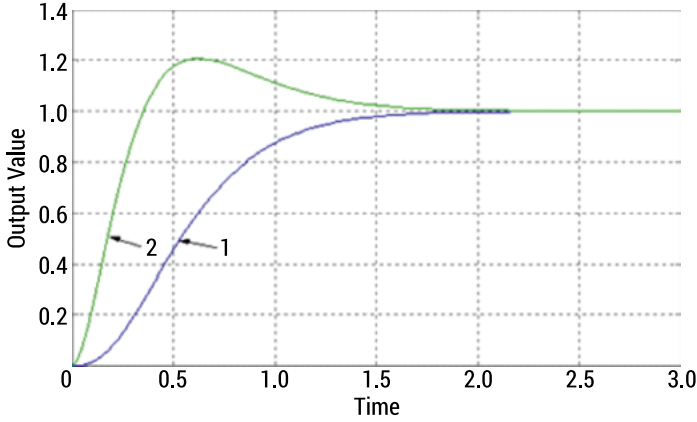


FIG. 4. Transfer characteristics for two implementations of the vehicle speed control system: – curve 1 for the coefficient K_1 in the feedback circuit; $W_1(s)$ – curve 2 for the coefficient K_1 in the forward circuit

In the first case, with the transfer function $W_1(s)$, the jump-like function is integrated, so the rapid movement of the accelerator pedal at the beginning of the process is approximated by a linear function and does not lead to a sharp change in the speed of the car. In the second case, with the transfer function $W_2(s)$, the system response is faster, since a sharp pressing of the accelerator pedal as a jump-like function directly on the channel of direct signal transmission (without delay) affects the supply of fuel to the engine. In practice, both implementations can be used, the first of which can be recommended when it is undesirable to subject the object to a shock from such behavior of the input value influence. The curves at the Figure 4 were obtained using the optimized values of the sought coefficients $K_1 = 0.4841$, $K_2 = 3.1700$, $K_3 = 10.1351$, calculated in the simulation process. Therefore, the transfer functions $W_1(s)$ and $W_2(s)$ are as follows:

$$W_1(s) = \frac{V(s)}{R(s)} = \frac{3.375}{s^3 + 4.5s^2 + 6.75s + 3.375}$$

$$\text{and } W_2(s) = \frac{V(s)}{R(s)} = \frac{5.3739s + 3.375}{s^3 + 4.5s^2 + 6.75s + 3.375} \quad (22)$$

Conclusions

Contrary to the known synthesis methods based on the use of frequency characteristics or root hodograph, Ackermann's formula guarantees obtaining the desired transient function. This method makes it possible to determine the matrix of feedback coefficients by describing the system in the complex space and the desired location of the roots of the characteristic equation. Additionally, due to controller simulation, it is stated that the structure with the gain in the feedback circuit shows the better view of the transient characteristic.

References

1. F. Gustafsson, 2009, *Automotive Safety Systems, Replacing Costly Sensors with Software Algorithms*, IEEE Signal Processing Magazine, 26, 32–47.
2. Ribbens W., 2017, *Understanding Automotive Electronics An Engineering Perspective*, eight edition, Butterworth-Heinemann, Oxford.
3. Swingler J., 2013, *MEMS for Automotive and Aerospace Applications*, eds. M. Kraft, N. White, Woodhead Publishing, Oxford.
4. Gannavaram V T.K., Bejgam R., 2021, *Brief Study and Review on the Next Revolutionary Autonomous Vehicle Technology*, in: *Proceedings of the 2021 International Conference on Advance Computing and Innovative Technologies in Engineering (ICACITE)*, Greater Noida, India, 34–37. DOI: 10.1109/ICACITE51222.2021.9404763.
5. Gannavaram V T.K., Bejgam R., Keshipeddi S.B. et al., 2021, *Study of Automobile Safety Technology Development using Vehicular Safety Device (VSD)*, in: *Proceedings of the 2021 6th International Conference on Inventive Computation Technologies (ICICT)*, Coimbatore, India, 240–244. DOI: 10.1109/ICICT50816.2021.9358670.
6. Hemachandran K., Shubham T., Sai K.G. et al., 2019, *A Technical Paper Review on Vehicle Tracking System*, in: *Proceedings of the 2-nd International Conference on Computer Networks, Big Data and IoT, December 19–20, 2019*, 1–6.
7. Zhengnan S., Haobin J., Shidian M., 2014, *Research of the vehicle anti-theft system based on fingerprint identification technology*, Automobile Parts, 11, 20–22.
8. Tummanapally S.S., Sunkari S., 2021, *Smart Vehicle Tracking System using GPS and GSM Technologies*, <https://ssrn.com/abstract=3884903>. DOI: org/10.2139/ssrn.3884903.
9. Helmers E., Marx P., 2012, *Electric cars: technical characteristics and environmental impacts*, Environmental Sciences Europe, 24(1), 14.
10. Phillips C.L., Harbor R.D., 1996, *Feedback Control Systems*, Upper Saddle River, New Jersey: Prentice Hall.
11. Bishop R.H., Dorf R.C., 2021, *Modern Control Systems*, Prentice Hall PTR.
12. Ackermann J.E., 1972, *Der Entwurf Linearer Regelungssysteme im Zustandsraum*, Regelungstechnik und Prozess-Datenverarbeitung, 20(7), 297–300.
13. Nakonechnyi M., Ivakhiv O., Viter O., 2020, *Synthesis of the Regulator for Robot's Arm Serving by Poles Method Placement Using*, International Journal of Computing, 19(2), 181–189.
14. Nakonechnyi M., Ivakhiv O., Viter O. et al., 2020, *Neurocontrolled Object Parameters Adjustment by Ackermann's Formula Using*, Measuring Equipment and Metrology, 81(1), 22–29.
15. Dabney J.B., Harman T.L., 2001, *Mastering Simulink 4*, Upper Saddle River, New Jersey: Prentice Hall.

3.3. CAD tools for vtol propulsion unit design

Jaroslav Cibulka

¹Czech Technical University In Prague, Faculty Of Mechanical Engineering, jaroslav.cibulka@fs.cvut.cz

Summary: Vertical Take-off and Landing (VTOL) aircraft is a quickly developing mean of personal transport raising completely new challenges for aircraft construction and mainly design of propulsion units. With vertical take-off and landing capabilities, the technology promises fast city centre transportation facing strict noise restrictions together with high performance demands. The aim of this paper is to introduce several strategies used for fast propulsion unit design development based on cooperation with start-up VTOL companies.

Keywords: VTOL; propulsion unit; propeller; blade; parametric CAD model

Introduction

There are 3 main propulsion systems used for VTOL. First one and the easiest to design is *separate propeller units* (Fig.1) for horizontal and vertical flight. This system allows effective design of each horizontal and vertical propellers however creates higher drag forces during horizontal flight and adds weight of non-used system.



FIG. 1. Separate rotors – Zuri VTOL [1]

This problem can be solved by second type which is *tilting rotor system* (Fig. 2).



FIG. 2. Tilting rotors – Jobi VTOL [2]

Here, the transition phase of flight is carried by rotating rotors. The problem of this system is the need to compromise on propeller design for both vertical and horizontal flight propeller efficiency and the technical complexity of the rotating rotor system.

The last system is the *ducted fan configuration* (Fig. 3) where turbofan stator and rotor systems are located inside wings ducts for vertical flight with the benefit of a higher ground effect and other physical phenomena. The ducted fan approach provides better aero-acoustic optimization possibilities while also allowing rotation of the whole unit during the transition phase.

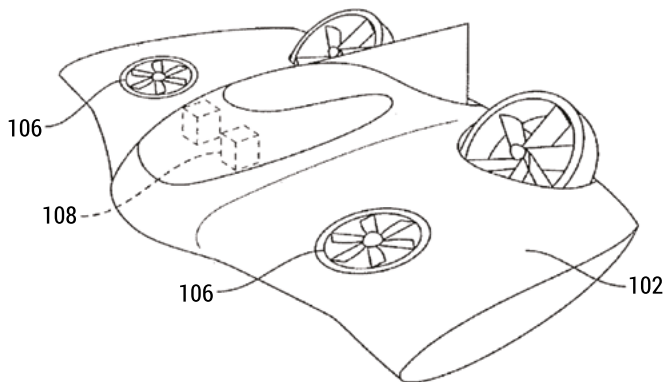


FIG. 3. Ducted fans – P3X VTOL [3]

Propeller design approach

the procedure of every propeller design starts with analytical computation of propeller design parameters based on aircraft performance demands [4]. We compute propeller diameter, propeller revolutions per minute, desired power, and air conditions (pressure and density), main propeller design parameters (angle of attack, angle of incidence, chord length, twist/lean/sweep angles). These parameters give a complete description of propeller design which can then be constructed by one of following approaches. [5]

Design engineer with commercial CAD software

This approach means construction of the whole propeller by the design engineer, starting with propeller profile construction (usually from national advisory committee for aeronautics NACA library), manual positioning of profiles along stacking line and final surface creation with desired surface continuity. The problems with this approach are time consumption, cost (engineer with commercial computer aided design software (CAD) such as CATIA) and complicated possibilities of geometry optimization and modification.

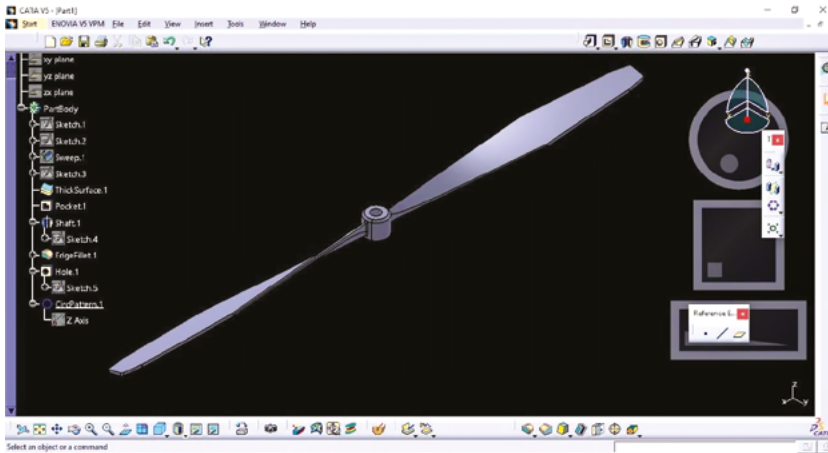


FIG. 4. Catia propeller workflow

Parametric CAD of propulsion unit

parametric CAD tools for propeller/blade design are the best option for fast prototyping. *Qprop* for propeller and *Xrotor* for blade design are opensource tools, constantly being developed by the Massachusetts Institute of Technology. They give complete independent control of parametric design together with low-fidelity aero-acoustic analyses. After mastering the non-intuitive environment, the user is able to generate, quickly analyse and optimize propulsion unit geometry. [6]

Parametric CAD of aircraft

Another parametric CAD tool for description of the whole aircraft is then implemented into the design procedure to give geometric control of the whole aircraft. OpenVSP is a simple .exe opensource software allowing the user to create and parametrically describe the simplified geometry of the whole aircraft with all avionic systems (wings, flaps, propulsion units, landing gear). This geometry is then used for advanced high-fidelity aero-acoustic analyses to give a complete mathematical model of aircraft behaviour. [7]

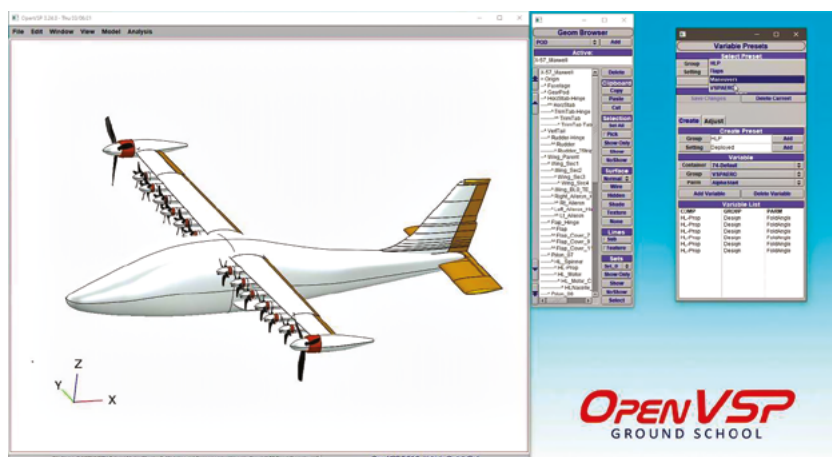


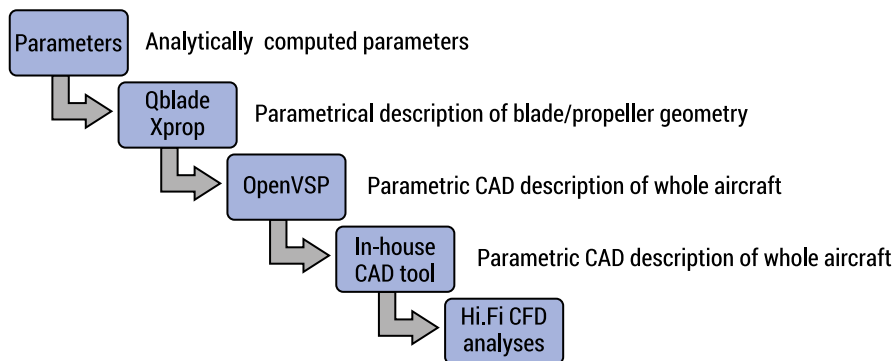
FIG. 5. OpenVSP workflow

In-house parametrical geometry software

For the final stages of blade/propeller design, to capture all details and prepare geometry built specifically for specific aircraft, python/c++ in-house software are used.

Conclusions

This text contains an overview of possible approaches to VTOL propulsion system design. Commercial systems and free-ware CAD software tools were described and compared. The main outcome is a diagram (Diag. 1 VTOL propulsion system strategy) with a simple strategy to create VTOL propulsion systems in a start-up environment.



DIAG. 1. VTOL propulsion system strategy

References

1. <https://transportup.com/zuri-vtol/> [accessed: 20.12.2023].
2. Horne T.A., 2023, *Joby S4: Coming to your airport in 2025? The leader of the eVTOL pack*, <https://www.aopa.org/news-and-media/all-news/2023/april/pilot/joby-s4-coming-to-you-in-2025> [accessed: 20.12.2023].
3. *Porsche Boeing Unnamed (concept design)*, 2019, [https://evtol.news/___media/Aircraft%20Directory%20Images/Porsche%20\(unnamed\)/Porsche-eVTOL-patent-drawing-15-January-2020.jpg](https://evtol.news/___media/Aircraft%20Directory%20Images/Porsche%20(unnamed)/Porsche-eVTOL-patent-drawing-15-January-2020.jpg) [accessed: 20.12.2023].
4. Theodorsen T., 1948, *Theory of Propellers*, McGraw-Hill, New York.
5. Stoll A.M., Stilson E.V., Bevirt J. et al., *Conceptual Design of the Joby S2 Electric VTOL PAV*, in: *14th AIAA Aviation Technology, Integration, and Operations Conference*, 16–20 June, Atlanta. DOI:10.2514/6.2014-2407.
6. Drela M., 2006, *QPROP Formulation*, MIT Aero & Astro, https://web.mit.edu/drela/Public/web/qprop/qprop_theory.pdf [accessed: 17.05.2024].
7. McDonald R.A., Gloudemans J.R., 2022, *Open Vehicle Sketch Pad: An Open Source Parametric Geometry and Analysis Tool for Conceptual Aircraft Design*, AIAA 2022-0004, AIAA SCITECH 2022 Forum.
8. OpenVSP, 2022, *Variable Preset Example: NASA X-57*, <https://www.youtube.com/watch?v=jdm0zL0rcwY> [accessed: 20.12.2023].
9. Cibulka J., 2020, *3D Modelling of Compressor Blades*, master thesis, CTU in Prague.

3.4. Automation of the process of oil pressing using the LabVIEW system

Volodymyr Havran¹, Mykhaylo Lobur¹, Mykhaylo Melnyk¹, Vasyl Tomyuk¹

*¹ Lviv Polytechnic National University, Institute of Computer Science and Information Technologies,
Department of Computer-Aided Design, volodymyr.b.havran@lpnu.ua*

Summary: This article describes the main aspects of the oil pressing process and provides an overview of the National Instruments LabVIEW graphical programming language and its possibilities in terms of utilizing this system in the oil pressing automation process.

Keywords: LabVIEW; oil pressing; process automation; pressure

Introduction

The process of pressing the seeds of oil-bearing crops is quite complicated, because it depends on a great number of technological and structural factors. The main technological factors that affect quantitative and qualitative performance indicators of the screw press are the pressure and temperature. Oil quality in most cases depends on these named parameters. At the industrial level, these problems are solved through complex technological process control systems that are quite costly.

LabVIEW from National Instruments is a graphical programming language that has its roots in automation control and data acquisition. Its graphical representation, similar to a process flow diagram, was created to provide an intuitive programming environment for scientists and engineers. The language has matured over the last 20 years to become a general-purpose programming environment. LabVIEW has several key features which make it a good choice in an automation environment. These include simple network communication, turnkey implementation of common communication protocols (RS232, GPIB, etc.), powerful toolsets for process control and data fitting, fast and easy user interface construction, and an efficient code execution environment [1]. Figure 1 shows an example of a graphical program in the LabVIEW language.

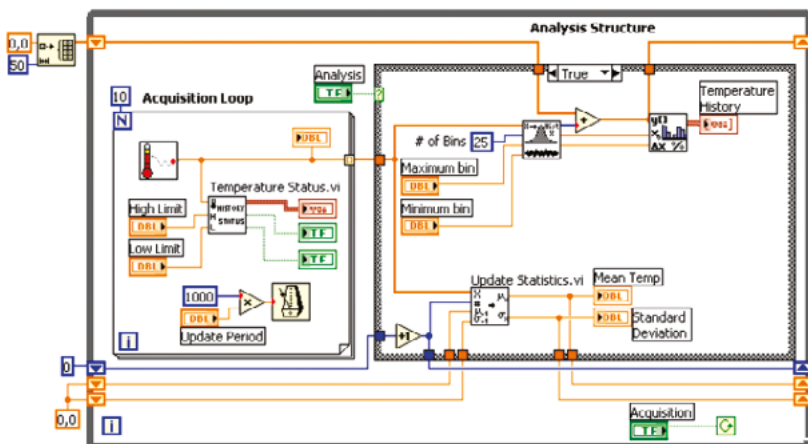


FIG. 1. Graphical program in the LabVIEW language

Overview of the measuring equipment for determining the pressure in the oil press using the LabVIEW system

To determine the pressure in the working zone of the screw press we suggest using the LabVIEW environment. The following parameters should be controlled and managed:

- Pressure in the working chamber,
- Temperatures in different working areas,
- Shaft rotation speed,
- Power of the working engine,
- Vibrations.

In figure 2, we see the developed laboratory-experimental installation with the above mentioned measuring complex.

The electric motor installed on the frame (1) is set in motion through the clutch high-speed shaft of the cylindrical reducer (4). From the low-speed shaft of the reducer through the clutch and torque meter, torque is transmitted to the screw shaft (3). The start and stop of the engine is controlled by using a magnetic starter (5) and the LabVIEW monitoring system. Material seed from the hopper, into which it is put manually, falls into the chamber pressing, where it is pressed in interturn space.

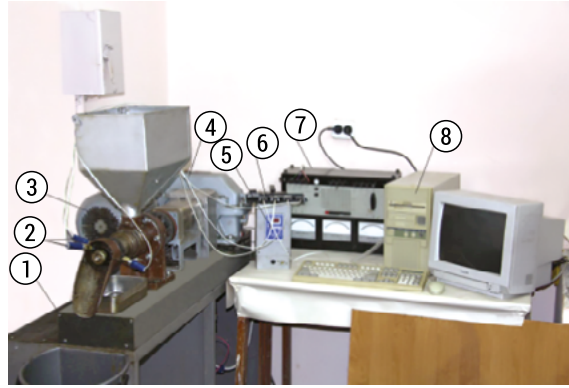


FIG. 2. General view of the measuring equipment for determining the pressure in the pressing chamber of the oil press: 1 – frame; 2 – Keller PA-6T pressure sensors; 3 – screw press; 4 – cylindrical reducer; 5 – frequency converter ATX-3.0; 6 – strain gauge amplifier; 7 – measuring station (KI – 505)

Investigation of connection between productivity and max pressure of automated oil press system

One of the indicators that characterize the process of pressing oilseeds is productivity. The productivity of the screw press can be calculated according to the formula:

$$Q = \rho_r \cdot V_o \cdot \omega, \text{ kg/h} \quad (1)$$

where ρ_r – rapeseed oil volume kg/m^3 ; ω – angular velocity of screw shaft rotation, rad/s ; V_o – the volume of the first turn, m^3 .

Volume V_o is defined:

$$V_o = \frac{kHh}{k+1} \left(\frac{d}{2} + \frac{k+1}{2k+1} H \right) / \cos \alpha \quad (2)$$

where h – step of the screw, $H = \frac{D-d}{2}$ (D and d are outer and inner diameters of screw),

Based on equations (1) and (2), the dependence of press productivity on the rotation frequency of the screw shaft and the pitch of its turns was obtained and represented on Figure 3.

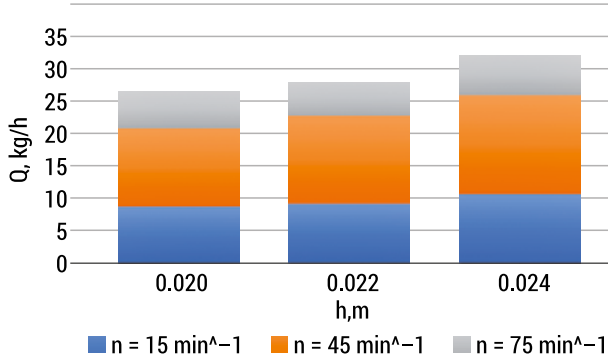


FIG. 3. Press productivity

For the rotation frequency $n = 15 \text{ min}^{-1}$ and the pitch of the screw shaft turns $h = 0.02 \text{ m}$, the productivity will be $Q = 8.50 \text{ kg/h}$, and for the pitch of turns $h = 0.024 \text{ m}$, respectively, $Q = 10 \text{ kg/h}$. The speed of rotation of the screw shaft has a more significant effect on the productivity of the screw press.

Let's find the volume V_1 and V_2 , volume of the oilcake and oil, respectively. Let's write down the following ratios.

$$\begin{cases} \rho_{oc} V_1 + \rho_o V_2 = \rho_{rm} V \\ V_1 + V_2 = \xi V_o \end{cases} \quad (3)$$

where ρ_{oc} – oilcake density, kg/m^3 ; ρ_o – oil density, kg/m^3 ; $\xi \leq 1$ – coefficient of rape-seed volume V_o filling.

Solving the system of equations (3), we obtain:

$$V_1 = \frac{\xi \rho_o - \rho_r}{\rho_o - \rho_{oc}} V_o, V_2 = \frac{\rho_r - \xi \rho_{oc}}{\rho_o - \rho_{oc}} V_o \quad (4)$$

Based on the obtained data (4), we will describe the dependence that characterizes the preservation of mass at the exit of the cake from the pressing chamber:

$$\omega (V_1 + \xi_1 V_2) = v A_{eh} \eta_1 \quad (5)$$

where v – speed of cake exit through exit holes; η_1 – the coefficient that characterizes the uneven use of the area of the outlet holes; A_{eh} – area of exit holes, m^2 ; ξ_1 – coefficient that characterizes the remaining oil in the oilcake.

Speed determination of the cake through the exit holes from the formula (5):

$$v = \frac{\omega (V_1 + \xi_1 V_2)}{A_{eh} \eta_1} \quad (6)$$

To calculate the output of the cake from the exit holes, we will use the theorem on the change in the amount of movement of a mechanical system:

$$\omega(\rho_{oc}V_1 + \xi_1\rho_oV_2)\left(-\frac{\omega(V_1 + \xi_1V_2)}{A_c}v\eta_1\right) = P_cA_{eh}\eta_1 - P_cA_{eh}\eta_1f - P_0A_{eh}\eta_1 \quad (7)$$

where P_c is the pressure in chamber; A_c is the cross-sectional area of the end chamber, m^2 , f is a coefficient that depends on the rotation frequency [2].

$$f = 1 - \left(1 - f_0\right)\left(\frac{\omega}{\omega_{max}}\right)^3 \quad (8)$$

where f_0 is the coefficient of friction during oil separation. From here:

$$P_c = P_0 + \frac{\omega^2}{A_{eh}(1-f)\eta_1}(\rho_{oc}V_1 + \xi_1\rho_oV_2)(V_1 + \xi_1V_2)\left(\frac{1}{A_{eh}\eta_1} - \frac{1}{A_c}\right) \quad (9)$$

If the oil is pressed out completely, then $\xi_1 = 0$. At the same time, it should be noted that $P_0 = 0$ and can be neglected. In this case, we will get:

$$P = \frac{\rho_{oc}V_1^2\omega^2}{A_{eh}(1-f)\eta_1}\left(\frac{1}{A_{eh}\eta_1} - \frac{1}{A_c}\right)_{max} \quad (10)$$

The analysis of formula (10) shows that the value of the maximum pressure is affected by the rotation frequency of the screw shaft, the area of the holes for removing the cake, as well as the volume of turns of the screw shaft.

The calculation of the formula (10) made it possible to obtain the dependence of the maximum pressure on the pitch of the turns and the rotation frequency of the screw shaft, represented on Figure 4.

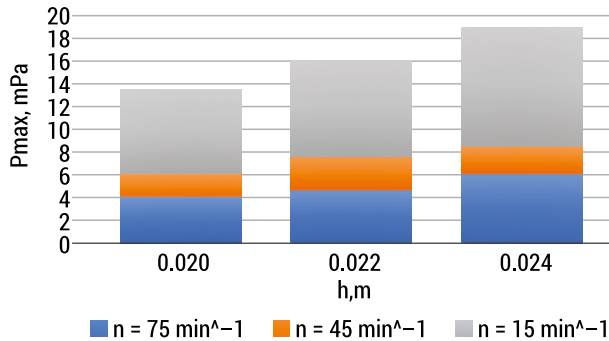


FIG. 4. Dependence of the pressure of the screw press

The analysis of the dependence (Fig. 4) made it possible to conclude that in the range of the studied values of the rotation frequency of the screw shaft and the pitch of the turns, the maximum pressure value $P_{\max} = 19 \text{ mPa}$ is reached at $n = 15 \text{ min}^{-1}$ and the pitch of the turns $h = 0.024 \text{ m}$ and the area of the holes $s = 4,7 \cdot 10^{-4} \text{ m}^2$. [3-6].

If P_{\max} is set in advance, then you can find the total area of the holes for removing the cake A_{eh} from here:

$$A_{eh} = \frac{2A_c}{\sqrt{4 \frac{P_{\max}}{\rho_{oc} V_1^2 \omega^2}} \sqrt{\frac{\rho_{oc} V_1^2 \omega^2}{\eta P_{\max}}}} \quad (11)$$

After calculating equation (11), it was established that for the pressure $P_{\max} = 13,1 \text{ mPa}$, the rotation frequency of the screw shaft $n = 15 \text{ min}^{-1}$ and the pitch of the turns $h = 0.020 \text{ m}$, the area of the holes for removing the cake will be 0.0000769 m^2 .

Benefits of Automating the Oil Pressing Process using LabVIEW:

The automation of the oil pressing process has several benefits, which include:

- **Increased Efficiency:** Automation of the oil pressing process enhances efficiency by reducing the time required to complete the process. The automated system can perform the oil pressing process at a faster rate than the traditional manual method;
- **Improved Accuracy:** The automated system provides a high degree of accuracy in the oil pressing process. The LabVIEW system can monitor and control the various parameters such as temperature and pressure to ensure that the process is carried out with high precision;
- **Consistency:** The automated system provides consistency in the oil pressing process. The LabVIEW system ensures that the process is carried out the same way every time, which eliminates the variability that is associated with the manual method;
- **Reduced Labor Costs:** The automation of the oil pressing process reduces the need for manual labor, which lowers labor costs.

Conclusions:

To conclude, this article described the aspects of the oil pressing process, pressure and rotation specifics, provided an overview of the measuring equipment for determining the pressure in the pressing chamber of the oil press. Considered possibilities of the LabVIEW system in terms of developing and managing an equipment for the oil pressure measuring. Mathematical models play a crucial role in the design of screw presses. By employing mathematical equations and simulations, it is possible to accurately predict the performance, efficiency, and structural integrity of screw presses, thus optimizing their design and operation. These models enable the exploration

of various parameters and configurations, leading to more cost-effective and reliable screw press designs for diverse applications across industries.

The automation of the oil pressing process using the LabVIEW system provides a solution that enables precise monitoring, control, and management of the pressing process, and is a significant improvement over manual processes.

References

1. Elliott C., Vijayakumar V., Zink W. et al., 2007, *National Instruments LabVIEW: A Programming Environment for Laboratory Automation and Measurement*, SLAS Technology, 12(1), 17–24.
2. Kovalyshyn S., Tomyuk V., 2018, *Research on power consumption of screw press for pressing of oil from rape seed*, BIO Web of Conferences, 10, 02011.
3. Toscano G., Pedretti E.F., 2007, *Evaluation of a mathematical model for oil extraction from oleaginous seeds*, Journal of Agricultural Engineering, 2, 11–20.
4. Willems P., Kuipers N., De Haan A.B., 2008, *Hydraulic pressing of oilseeds: experimental determination and modeling of yield and pressing rates*, Journal of Food Engineering, 89, 8–16.
5. Fakayode O.A., Atoó A.E., 2019, *Development, testing and optimization of a screw press oil expeller for moringa (Moringa oleifera) seeds*, Agricultural Research, 8(1), 102–115.
6. Fantino V.M., Bodoira R.M., Penci M.C. et al., 2020, *Effect of screw-press extraction process parameters on the recovery and quality of pistachio oil*, Grasas y Aceites, 71(2), 360.

3.5. CAD modeling and generative manufacturing in orthopedics on the example of a personalized targeter to support osteotomy

Marek Wyleżoł¹, Małgorzata Muzalewska², Jacek Andrzejewski³

¹*Silesian University of Technology, Faculty of Mechanical Engineering,
Department of Fundamentals of Machinery Design, marek.wylezol@polsl.pl*

²*Silesian University of Technology, Faculty of Mechanical Engineering,
Department of Fundamentals of Machinery Design*

³*Poznan University of Technology, Faculty of Mechanical Engineering,
Institute of Materials Technology, Syntplant sp. z o.o.*

Summary: The article describes the process of developing a CAD class model of an individual targeter supporting tibial osteotomy procedures (starting with the creation of a 3D model of the tibia). The virtual model of the targeter was used to produce the targeter as a medical product using 3D printing technology – Digital Light Processing. All targeters were used in procedures that had the status of a medical experiment.

Keywords: tibial osteotomy; CAD systems; voxel modeling; anatomical surfaces, modeling of bone structures

Introduction

Tibial osteotomy [1] is a type of procedure used to correct deviations in the so-called mechanical axis of the limb (Fig. 1), which can result from injuries, diseases, or congenital defects. In the case of the lower limb, the mechanical axis runs through the (Fig. 1b):

- thigh: through two main points: the hip joint (the head of the femur) and the knee joint (the center of the head of the tibia).
- lower leg: through two main points: the knee joint (center of the head of the tibia) and the ankle joint (between the talus and the calcaneus).
- foot: through two main points: the ankle joint (between the ankle bones and the heel bones) and the midpoint between the metatarsal bones.

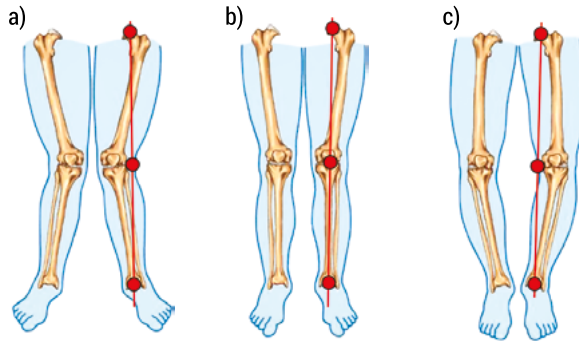


FIG. 1. The position of the mechanical axis of the lower limb, a) valgus, b) correct position, c) varus

This procedure involves cutting and angularly repositioning the tibia bone to correct the anatomical alignment of the mentioned mechanical axis of the lower limb. As a result of this procedure, joint loading returns to a more anatomically even distribution, helping to alleviate pain, restore normal range of motion and prevent further joint damage (Fig. 2).

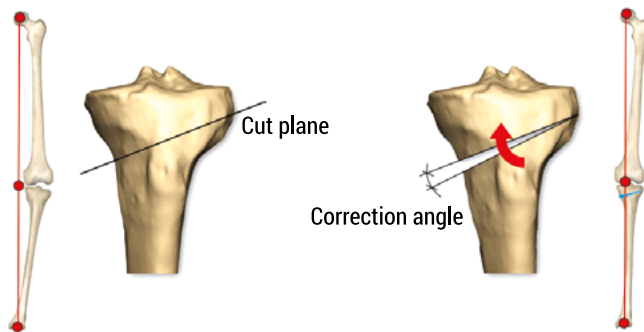


FIG. 2. The Correction of the mechanical axis of the lower limb by angular deviation of the tibia

Chapter 1

The process of cutting the tibia bone involves determining the appropriate geometric parameters and their values. Planning the cutting, as well as the entire procedure, is nowadays facilitated using computer systems based on two-dimensional X-ray images (e.g., PeekMed [2], Fig. 3). A practical challenge is transferring the planning of such a procedure from a computer program environment to a specific patient. Previously, the process of determining the cutting plane relied on the experience of the orthopedic surgeon (often with a certain margin of error) or was aided by targeting devices.

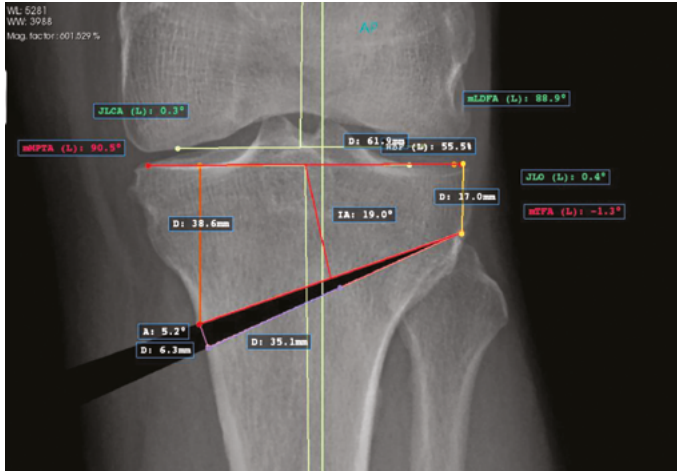


FIG. 3. Planning an example osteotomy with use of the PeekMed [2] system

Targeting devices available on the market typically have a universal nature and require mechanical adjustments for each individual patient, a process that is complex and prone to human errors (for example iBalance® HTO system [3], Fig. 4).

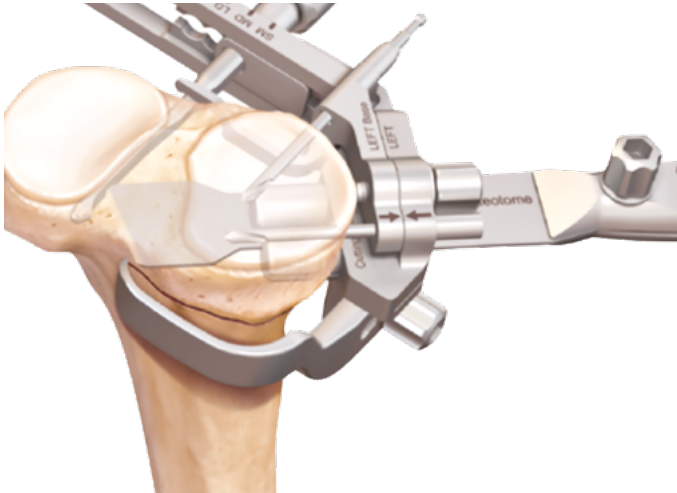


FIG. 4. iBalance® HTO system [3]

Chapter 2

The aim of the proposed personalized targeting device was to enable the precise determination of the cutting plane of the tibia bone for a specific patient, along with guiding the osteotomy during the procedure. The input to making a virtual targeter model is to have a virtual tibia model (Fig. 5). Such a tibia model is generated through

medical imaging (in this case, Computer Tomography) – that is, two-dimensional cross-sectional images of anatomical structures represented in the DICOM format – into a three-dimensional triangular model represented in the STL format.

The process of proper modeling must be preceded by defining a group of auxiliary planes (frontal, articular, cutting and target guide profile) placed in relation to the tibia model (Fig. 5). This process is not clear and requires considerable experience. It is necessary to combine medical knowledge regarding the osteotomy procedure with engineering knowledge.

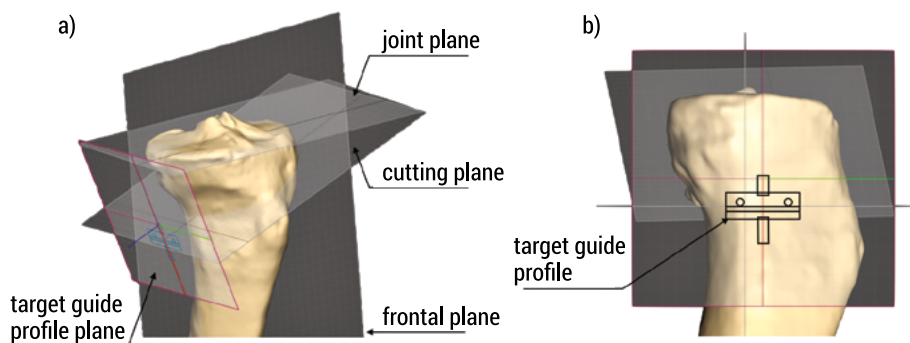


FIG. 5. A group of defined auxiliary planes

The possibility of clearly determining the cutting plane was achieved thanks to the precise adjustment of the contact surface of the target's collar to the curvatures of the surface of a specific patient. The inner surface of the targeting device serves as a geometric representation of the tibia bone's surface at the point of device application, and there is only one such point. A guide with a slot for the osteotome is attached to the collar. Additionally, there are two guides on the collar for fixing the targeter to the bone using Kirschner's wires (Fig. 6).

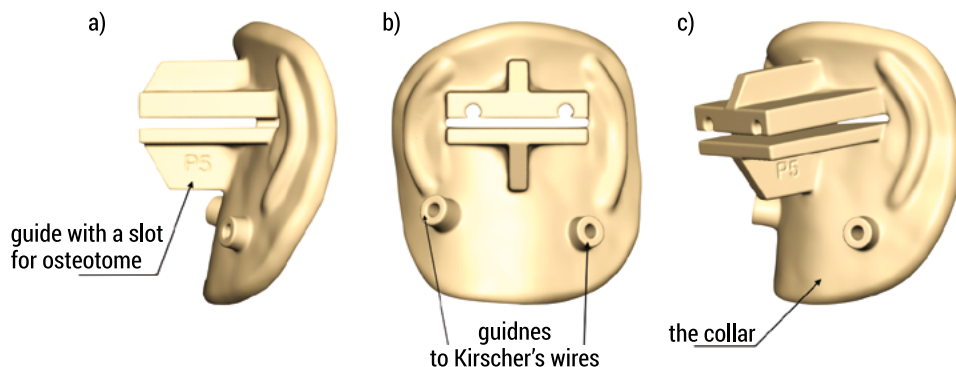


FIG. 6. Some views of the targeter virtual model

This modeling process is carried out within the Freeform Plus [2] system environment, which encompasses various modeling techniques, including voxel-based, surface-based, edge-based, solid-based, and triangular-based approaches. During the designing process of the targeting device, quantitative data from the osteotomy planning system are also utilized. Using the Freeform Plus system, not only a model of the sight was created, but also a simulation of the tibia separation by the value of the osteotomy angle (Fig. 7).

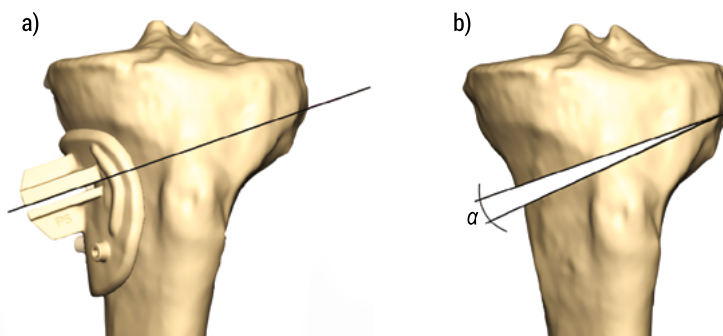


FIG. 7. The targeter on the tibia (a) and the tibia after cutting and tilting by the osteotomy angle

Chapter 3

The targeting device is ultimately manufactured using the DLP technique (Digital Light Processing), which employs UV light technology to harden a polymer resin. In particular case we use the DLP-LCD method since the light source is the LCD screen.

The production device employed for this purpose was Photon Mono X (from Anycubic company). For patient safety, the targeting device is made from Surgical Guide SG01 resin, which complies with ISO 10993 standards (ensuring safe contact with a patient's internal tissues for up to 24 hours). An incidental characteristic of the personalized targeting device is its single-use nature. Given the commonality of using other disposable medical products, this does not pose a problem.

The printing procedure was conducted using the set of parameters suggested by the resin producer, where the layer resolution was 50 μm , and normal layer exposure was 2.5 s. We used 3 bottom layers, where the exposure time was set to 25 s, and all the other machine parameters were set to default values. The slicing software used for the machine code preparation was Photon Workshop V2.1.29RC12 supplied by the printer producer. The supporting structure was generated by the software algorithm; however, some additional support points were added manually (Fig. 8 a, b).

After the printing process, the prepared tools were removed from the printer platform and subjected to cleaning/washing and post-curing procedure, where we used the Wash & Cure device also supplied by the printed producer (Fig. 8 c). The washing step was conducted in isopropanol (IPA) medium, where 3 liters of 99.8 % IPA from WARCHEM company was used. The washing process was conducted for 6 minutes.

After that time, the cleaned parts were cleaned with compressed air and dried in cabinet dryer for 1 hour at 50°C. Before conducting the post-curing process, the supporting structures were removed from the parts. The curing procedure was conducted for 5 minutes on both sides of the printed part. The post-cured parts were then additionally polished using a stainless steel file to smooth out the places where the support structures were removed. To eliminate possible contamination after the polishing process, the final products were cleaned in IPA medium again. The parts were packed into Tyvek bags and sent to the sterilization process.

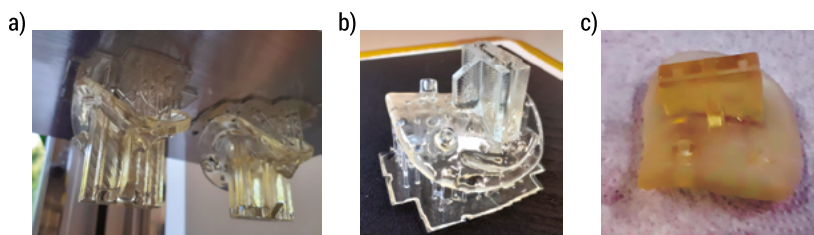


FIG. 8. Targeter during production, a-b) targeter on the printing platform, c) targeter after post-curing procedure

Chapter 4

The use of the targeter was preceded by pre-operative planning. The procedure was simulated using models (tibia and target) printed in FDM technology. However, the osteotome used to make the cut was original. This allowed the surgeon to test the suitability of the sight in simulated conditions (Fig. 9).



FIG. 9. Physical simulation of opening osteotomy, a) physical model of tibia and targeter, b) cutting process, c) tibia after cutting

The previous use of the targeting device in tibial osteotomy procedures has confirmed its effectiveness (Fig. 10). These procedures, totaling five, were conducted at the Galen Ortopedia sp. z o.o. clinic in Bierań (Poland). The doctor Maciej Mierzwiński conducted all procedures. All procedures were successful. The average time of every treatment was about 1.5 hours (taking into account all activities).

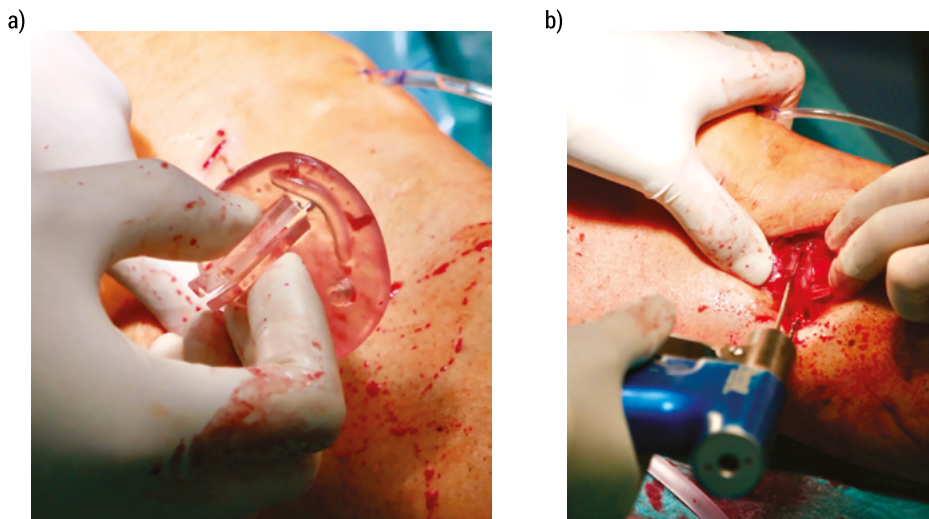


FIG. 10. Use of the targeter during the procedure, a) inserting the targeter, b) cutting tibia

Conclusions

- It is possible to construct a sight with a geometric form that is a hybrid of: a CAD class model and anatomical surfaces.
- To create the targeter 3D model, it is necessary to create a 3D model of the patient's tibia.
- DLP manufacturing technology allows for very accurate production of the targeter (4K HD exposure screen resolution, printing layer thickness 0.05 mm).
- The manufacturing DLP technology used is effective enough.
- The use of the target in the osteotomy procedure confirmed its usefulness (in 5 procedures).
- The design of the targeter was submitted to the Polish Patent Office of Poland (21/04/2023) as an invention and is currently being assessed.

References

1. Menetrey J. (ed.), 2012, *Instructional Course Lecture Book*, ESSKA, Geneva.
2. PeekMed®, *PeekMed*, <https://www.peekmed.com> [accessed: 20.10.2023].
3. Arthrex, *iBalance® HTO*, <https://www.arthrex.com> [accessed: 13.11.2023].
4. Oqton, *Freeform Plus*, <https://www.oqton.com/geomagic-freeform/> [accessed: 13.11.2023].
5. Anycubic, *Anycubic Mono X*, <https://anycubicofficial.pl> [accessed: 14.11.2023].
6. Machines-3D, *Surgical Guide SG01*, <https://www.machines-3d.com> [accessed: 13.11.2023].

3.6. Software and methodological complex for researching the use of graph models

Volodymyr Karkulovskyy¹, Olexandr Markelov¹, Natalia Nestor¹, Oksana Oborska¹

*¹Ukraine, Lviv Polytechnic National University, Department of Computer-Aided Design,
volodymyr.i.karkulovskyy@lpnu.ua*

Summary: The work deals with the development of a software-methodological complex that allows research on the application of graph models on the example of the problem of finding the minimum path in a graph to solve many problems of automated design of complex objects and systems.

Keywords: graph models, algorithms for working with graphs, software-methodological complex, the task of finding the minimum path in a graph

Introduction

The graph [1] is a generalized ordered pair consisting of a set of vertices and a set of edges. Graph models can be used to abstract any type of computer data. Graph theory allows you to model and study the relationship between data and provides answers to a number of questions of location, network configuration, optimization, coordination and a wide range of other practical problems.

Such data structures and their use were first considered by the famous mathematician Leonard Euler, who formulated the basic concepts of graph theory as a branch of mathematics.

Graphs are a method of visual illustration of data and relationships between them. The purpose of graphs is to present too complex data for their further adequate description in text form or algorithms. The clarity and correctness of the data description in the graphs allow for greater efficiency in the use of graphs.

The definition of a graph is so general that this term can be used to describe many events and objects of everyday life. A high level of abstraction and generalization allows you to use typical algorithms of graph theory to solve many apparently dissimilar problems in transport and computer networks, construction design, molecular modeling, etc. Graph theory is also widely used in geographic information systems. Existing or planned houses, structures, blocks are considered as vertices, and roads, engineering networks, power lines connecting them – as edges. The application of various calculations made on such a graph allows, for example, to find the shortest detour or the nearest point where you need to get to, to plan the optimal route. As a special class, you can distinguish optimization tasks on graphs.

Graph models also play a very important role in the automated design of complex objects and systems of various nature. Therefore, the task of developing graph models and algorithms for working with them is a very relevant issue at present.

Search of the shortest path in the graph

One of the important tasks in the design of complex objects and systems is finding the shortest or optimal path between two points of the model. In graph theory, the shortest path problem consists in finding a path between two vertices of the graph so that the sum of the weights of the edges that make up the graph is minimal. Finding the shortest path using graph models has a wide range of applications. This approach can be used not only for laying the optimal route on the map, but also for solving many other problems. For example, the tasks of optimizing both human and financial costs in the field of enterprise management. There are many algorithms for solving the problem of finding the shortest path in a graph. The main ones are:

- **Dijkstra's algorithm** [2] Finds the shortest path from one vertex of a graph to all other vertices. Dijkstra's classical algorithm works only for graphs without edges of negative length.
- **Bellman-Ford algorithm** [3] Searches for the shortest path in a directed graph from one vertex to other vertices.
- **Floyd-Warshell algorithm** [4] Also known as the Floyd algorithm, the Roy-Warshell algorithm, the Roy-Floyd algorithm, or the WFI algorithm is an algorithm for finding shortest paths in a weighted graph with positive or negative edge weights (but no negative cycles). In one execution of the algorithm, the lengths (total weights) of the shortest paths between all pairs of vertices will be found. Although it does not return details of the paths themselves, it is possible to reconstruct the paths with simple modifications to the algorithm.
- **Danzig's algorithm**. [5] Algorithm for finding the shortest paths to all vertices of a planar directed graph. Named after the American mathematician George Danzig. The algorithm is close to Floyd's algorithm, it differs from it only in a different order of performing the same operations.
- **Wave algorithm (Li's algorithm)** [6] Algorithm that allows you to find the minimum path in a graph with edges of unit length. Based on a breadth-first search algorithm. It is used to find the shortest path in a graph, in general it finds only its length.
- **Algorithm A*** [7] finds the optimal path between two vertices in the graph. Depending on the cost function that assigns each edge its "weight", optimality can mean the shortest, fastest or even simplest path. Theoretically, the algorithm can solve all problems that can be presented in the form of the problem of finding the optimal path on a graph.

Each of the above algorithms is effective for solving specific problems.

The main goal of this work is to develop a software system that can provide opportunities to analyze the work of algorithms for finding the shortest path in a graph and choose the most effective of them for the implementation of a specific task of automated design.

Development of the structure of software system

A generalized structure of the software-methodological complex [8] has been developed, which allows the analysis of algorithms for working with graphs (Figure 1).

The main element is the core of the software complex. The core performs the main functions of managing the complex:

- interaction between the user and the software system (interface provision);
- implementation of effective operation of external devices;
- management of the work of subsystems that are responsible for researching the solution of specific practical problems;
- working with the database (saving and using the results of analysis of methods).

At the moment, subsystem 1 is implemented, which is intended for studying algorithms for finding the shortest path in a graph. In the future, it is planned to implement the following subsystems to solve other relevant practical problems. Instructions for the user are provided, which allow you to implement the research methodology.

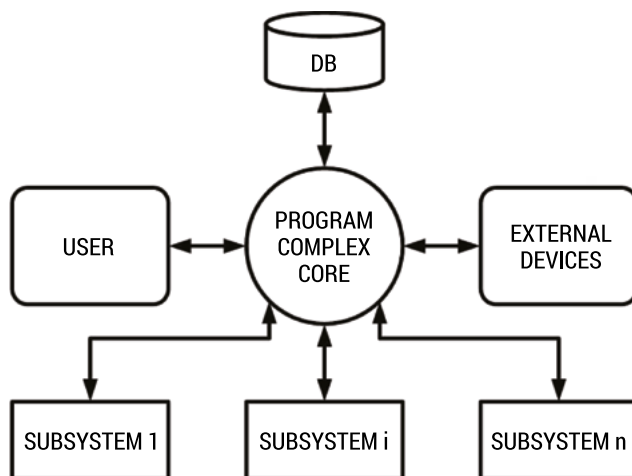


FIG. 1. The structure of the program and methodological complex

Software implementation of the system

Separate methods for solving the problem of finding the shortest path in networks using models based on graph theory have been developed and implemented:

Lee’s algorithm was implemented in [8].

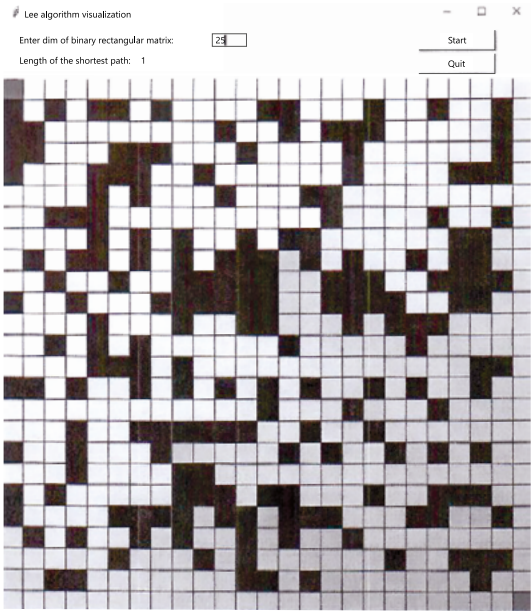


FIG. 2. Software implementation of Lie’s algorithm

Danzig’s algorithm was implemented in [9]

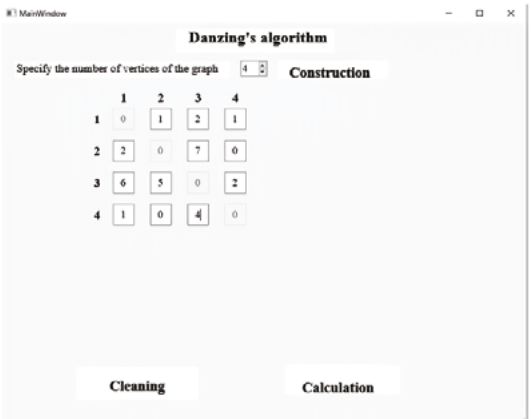


FIG. 3. Software implementation of the Danzig algorithm

Algorithm A* was implemented in [10].

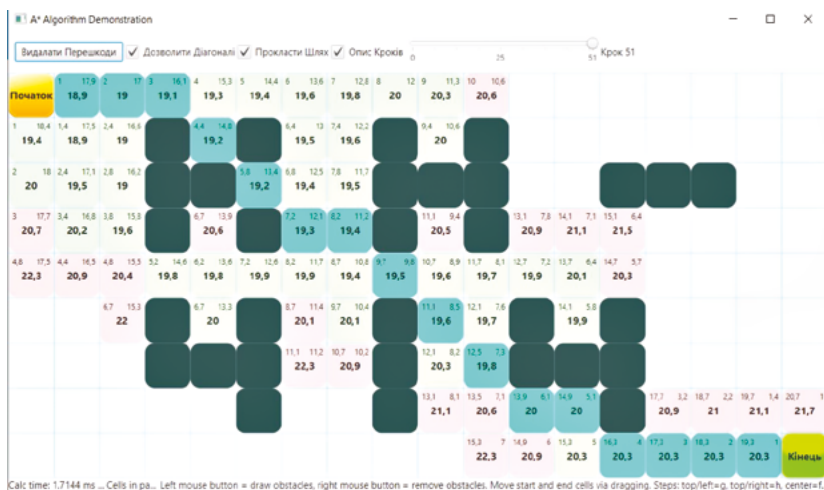


FIG. 4. Software implementation of the A* algorithm

Other algorithms are expected to be implemented.

Conclusions

Graph theory provides an opportunity to solve problems related to solving complex problems of automated design. Of course, at the moment there are many application programs that allow you to simplify this process. But a very important aspect is the process of training specialists who are able to quickly and adequately make important decisions.

References

1. Wilson R.J., 1996, *Introduction to Graph Theory*, Longman, Harlow, <https://www.maths.ed.ac.uk/~v1ranick/papers/wilsongraph.pdf> [accessed: 17.05.2024].
2. <https://www.geeksforgeeks.org/dijkstras-shortest-path-algorithm-greedy-algo-7/>
3. Martens C., Ruchel N., Lang O. et al., 2001, *A FRIEND for assisting handicapped people*, IEEE Robotics & Automation Magazine, 8(1), 57–65, <https://ieeexplore.ieee.org/document/924364> [accessed: 17.05.2024].
4. Hougardy S., 2010, *The Floyd–Warshall algorithm on graphs with negative cycles*, Information Processing Letters, 110(8–9), 279–281. DOI: 10.1016/j.ipl.2010.02.001.
5. Vanderbei R.J., 2008, *Linear Programming: Foundations and Extensions*, 3rd ed., International Series in Operations Research & Management Science, Vol. 114, Springer Verlag.
6. Núñez J., Cruchaga M., Tampier G., 2022, *Wave analysis based on genetic algorithms using data collected from laboratories at different scales*, European Journal of Mechanics – B/Fluids, 95, 231–239, <https://www.sciencedirect.com/science/article/abs/pii/S0997754622000796> [accessed: 17.05.2024].

7. Dechter R., Pearl J., 1985, *Generalized best-first search strategies and the optimality of A^** , Journal of the ACM, 32(3), 505–536.
8. Karkulovskyy V., Kryvyy R., 2023, *A Software Complex for Researching Algorithms for Working with Graphs. The Problem of Finding the Shortest Path. Lie's Algorithm*, in: IV International Scientific and Practical Conference "Actual Problems of Modern Science" (January 31 – February 3, 2023, Boston, USA), 423–427.
9. Karkulovskyy V., Kryvyy R., Jaworskyi N. et al., 2023, *A software complex for researching algorithms for working with graphs*, in: *The experience of designing and application of CAD systems. Proceedings of the 17th IEEE International conference* (Jaroslaw, February 22–25).
10. Karkulovskyy V., Nestor N., Oborska O., 2023, *A software complex for researching algorithms for working with graphs. A^* algorithm*, in: *CAD in machinery design. Implementation and educational issues. Proceedings of the XXXI International conference CADMD 2023* (Supraśl, Poland, 26–28 October).

Chapter 4

4.1. Evaluation of the impact of a three-axis milling plotter accuracy on the surface quality after machining an aluminum alloy

Daria Sałamacha¹, Michał Lelen¹, Jerzy Jóźwik¹, Paweł Pieško¹, Paweł Tomiło²

¹*Lublin University of Technology, 20-618 Lublin, Poland,
Faculty of Mechanical Engineering, Department of Production Engineering,
s97261@pollub.edu.pl*

²*Lublin University of Technology, 20-618 Lublin, Poland, Management Department*

Summary: This paper presents an analysis of the influence of the accuracy of a three-axis milling plotter on the geometric quality of the surface after machining an aluminum alloy during the conventional milling process using the end mill. Milling tests were carried out at five measurement points on an EN AW-7075 T651 aluminum alloy sample using a four-edge end mill with a diameter of 12 mm. The variable technological parameter was a feed rate. The effect of milling conducted using the feed rate v_f range from 1000 to 5000 mm/min was evaluated by analyzing the feed rate impact and sample position in the working space on the average values of the three roughness parameters R_a , R_z and RSm . The results showed that the milling plotter accuracy measured at the selected points in the working space affected the obtained milling accuracy and surface quality.

Keywords: milling plotter accuracy, aluminum alloy, milling, laser interferometry

Introduction

The key aspect in assessing the dimensional and shape accuracy of a part is determining the accuracy of the CNC machine tool. There is an increased demand for high precision machine tools and their assemblies as well as manufactured parts that must meet strict geometrical, kinematic, and quality requirements. In order to achieve and maintain the accuracy of a few micrometres, numerous machine errors affecting the final quality of a product must be controlled and compensated for. These errors may result from irregularities and inaccuracies in the implementation of motion and its trajectory, inaccuracies of displacement, lack of accuracy and repeatability of the CNC axis positioning or the occurrence of backlash in the drive system [1–2, 5].

When assessing the dimensional and shape accuracy of manufactured parts, factors affecting the accuracy of the machine tool and factors related to the correctness of the cutting process should be taken into account. These factors determine the final quality of the parts in the machining process. The dimensional accuracy of parts, evaluated from the perspective of accuracy tests of a technological machine,

depend mainly on the axis accuracy and repeatability of positioning. An inaccuracy in the reproduction of length unit by elements of the machine's actuators, when performing a programmed trajectory of the tool relative to the workpiece, contribute to the dimensional and shape errors of manufactured parts [6].

Whereas, from a technological point of view, there are also other factors that have a significant impact on the quality of the treated surface. The research carried out by the authors of this paper [7] showed that the quality of the machined surface depends on wear, tool and the feed rate v_f . The authors of this paper [8] emphasize that technological parameters such as: feed rate v_f , spindle speed n , workmanship quality, workpiece material's properties and cut depth a_p have the greatest impact on the surface quality. The research [9] showed that the factors that have the greatest impact on the machined surface condition are: the tool type and the amount of vibration damping during a cutting process. Additionally, this paper [10] demonstrates that the surface quality depends primarily on changes in chip thickness due to the rotational tool trajectory. Equally important factors influencing the surface quality are: cooling method [11], tool length [12], milling direction [13] and friction [14].

The most commonly used material in the industry are aluminum alloys. They have a low density, low weight, high corrosion resistance and high current conductivity [15, 16]. These features make these alloys widely used in electrical engineering, aerospace, construction, and shipbuilding industries where the low element weight is important [17]. Requirements set by the industry for manufactured elements are increasing, which is associated with the continuous improvement of machining processes in order to obtain surfaces with increasingly higher accuracy and quality.

The aim of this study is to investigate the influence of the accuracy of a three-axis milling plotter on the surface condition of an aluminum alloy after machining. In addition to the main goal, modeling of the Ra , Rz , RSm roughness parameters can be presented to predict these parameters. Modeling roughness parameters after milling can be the basis for determining the conditions of the machining process in order to obtain the assumed surface roughness. The use of artificial neurons may reduce the experimental trials number performed in the selection and optimization of technological parameters.

Materials and methods

Methodology

The object of the study was an aluminum alloy sample. In order to determine the cause and effect relationships between the milling plotter accuracy and the assessment of the sample surface condition after processing, experimental tests were carried out. The most important research stages included: recording the plotter positioning accuracy values, carrying out the sample cutting process at 5 measurement points and measuring the sample surface roughness. Unidirectional accuracy and repeatability tests of the plotter positioning carried out using two different measurement strategies. The tests were performed with the use of the following: a EN AW-7075

T651 aluminum alloy sample, a laser interferometer LSP 30 Compact and an end mill SGS 44630.

The milling plotter is equipped with the PikoCNC5.0 control system and has the maximum spindle speed of 18000 rpm. The maximum travel of the plotter spindle is 1000 mm for the X axis, 2000 mm for the Y axis and 200 mm for the Z axis. The test stand is shown in Fig. 1.



FIG. 1. Test stand

In the conventional climb milling process, a 44630 cutter of KYOCERA SGS Precision Tools with a diameter of 12 mm and four blades was used (Fig. 2.). The milling cutter made of sintered carbide is dedicated light metal alloys and ensures high precision. The milling cutter is coated with TiB_2 . The technical parameters of the tool were: overall length L – 83 mm, maximum depth of cut l – 30 mm, number of teeth z – 4 [18].

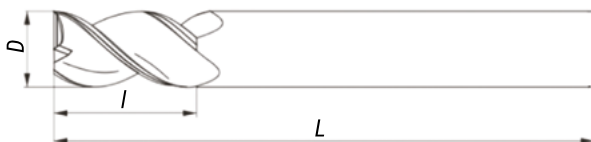


FIG. 2. Drawing of SGS 44630 milling cutter used: D – working part diameter, L – overall length, l – maximum depth of cut [3]

The tested sample was made of a wrought EN AW-7075 T651 aluminum alloy. Due to its mechanical properties, this alloy is used in the aerospace, construction,

and shipbuilding industries for the production of high-loaded parts and structural elements. Table 1 shows the chemical composition of the tested aluminum alloy, while the theoretical mechanical properties are listed in Table 2 [4].

TAB. 1. Chemical composition of EN AW-7075 T651 aluminum alloy [3]

Chemical composition (%)									
Si	Fe	Mg	Cu	Mn	Zn	Ti	Cr	Other	Al
≤0.4	≤0.5	2.5	1.6	≤0.3	5.6	≤0.2	0.23	Zr + Ti ≤0.25	Rest

TAB. 2. Mechanical properties of EN AW-7075 T651 aluminum alloy [3]

Mechanical properties			
Yield Point <i>R_{str}</i> (MPa)	Tensile Strength <i>R_m</i> (MPa)	Elongation (%)	Brinell Hardness (HB)
440	526	11	155

A geometrical view of the sample with the dimensions 190x40x25 mm is shown in Fig. 3. The milling sample was performed in one direction at five selected points in working space. In conventional milling, a two-planes front machining strategy was applied. Each tool pass was conducted for a cut depth of $a_p = 0.5$ mm. The machining process was carried out with the following technological conditions: feed rates $v_f = 1000$ -5000 mm/min, spindle speed $n = 10000$ rpm, dry type of machining.

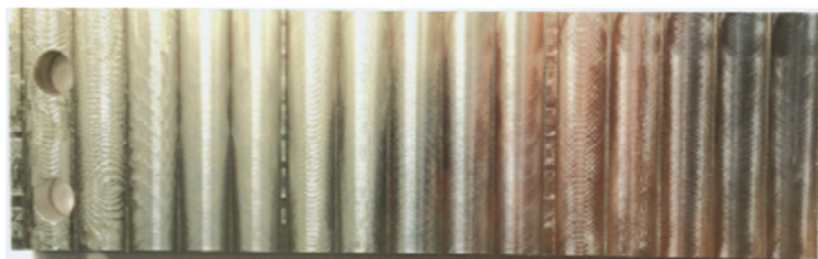


FIG. 3. EN AW-7075 T651 aluminum alloy sample

Results and discussion

Three-axis milling plotter accuracy

The measurements were carried out based on available and known measurement procedures in accordance with the PN-ISO 230-2:2014 Standard for testing machine tools – part 2: Determining the accuracy and repeatability of positioning of numerically controlled axes. The obtained test results allowed the determination of the following

values: unidirectional positioning accuracy (forward A_{\uparrow} , backward A_{\downarrow}) and unidirectional positioning repeatability (forward R_{\uparrow} , backward R_{\downarrow}). Fig. 4 shows the unidirectional positioning accuracy $A_{\uparrow A_{\downarrow}}$ distribution and the unidirectional positioning repeatability $R_{\uparrow R_{\downarrow}}$ distribution on the table working space obtained according to the linear and the ‘pilgrim’ strategies.

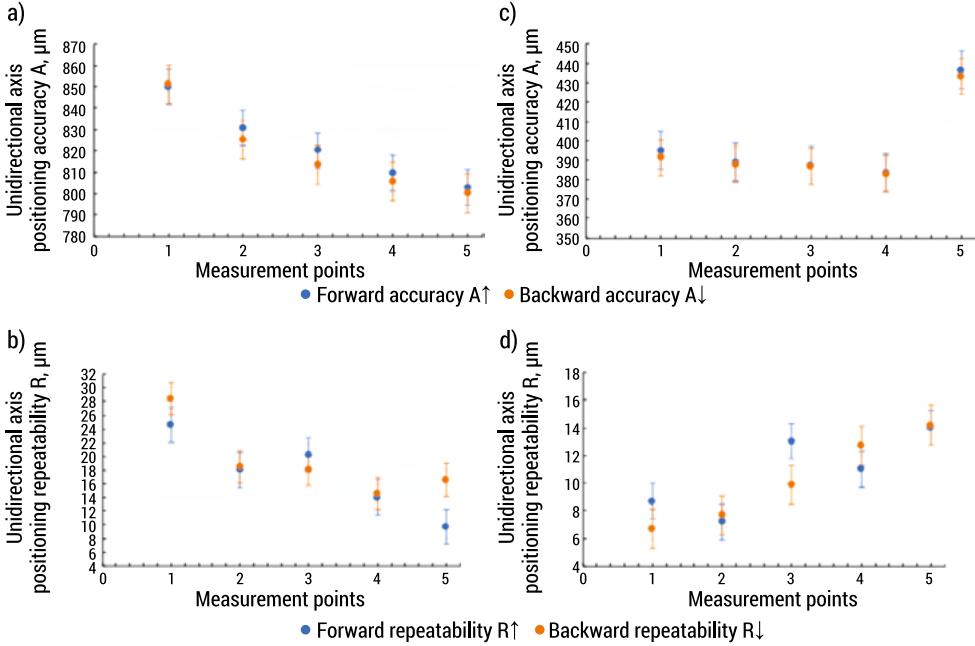


FIG. 4. Accuracy and repeatability distribution of the milling plotter: a) forward and backward accuracy A_{\uparrow} for the linear strategy, b) forward and backward repeatability R_{\downarrow} for the linear strategy, c) forward and backward accuracy A_{\downarrow} for the ‘pilgrim’ strategy, d) forward and backward repeatability R_{\downarrow} for the ‘pilgrim’ strategy

It can be seen that, in the linear strategy, the further away from the origin of the plotter coordinate system the machining location is, values for the positioning accuracy $A_{\uparrow A_{\downarrow}}$ and the positioning repeatability $R_{\uparrow R_{\downarrow}}$ have a smaller error. In a linear strategy, the smallest error value for the $A_{\uparrow A_{\downarrow}}$ and the $R_{\uparrow R_{\downarrow}}$ parameter was recorded for a measurement point P_5 . The highest value of the error was recorded for measurement point P_1 which was the closest point to the origin of the plotter’s coordinate system. Whereas, in the ‘pilgrim’ strategy, the further away from the origin of the plotter the machining location is, the higher values for the positioning accuracy $A_{\uparrow A_{\downarrow}}$ and the positioning repeatability $R_{\uparrow R_{\downarrow}}$ are. The highest error value for the $A_{\uparrow A_{\downarrow}}$ and the $R_{\uparrow R_{\downarrow}}$ parameters was recorded for the measurement point P_5 . The smallest error value for the $A_{\uparrow A_{\downarrow}}$ parameter was recorded for point P_4 and the $R_{\uparrow R_{\downarrow}}$ parameter was recorded for point P_1 .

Additionally, according to the machine manufacturer, the tolerance limit for the $A\uparrow A\downarrow$ parameter was 10 μm and for the $R\uparrow R\downarrow$ parameter 12 μm . It can clearly be observed that the $A\uparrow A\downarrow$ value parameter exceeded the permissible tolerance limit values for two strategies. In the linear positioning strategy, the $R\uparrow R\downarrow$ parameter values were exceeded for the point from P_1 to P_4 . At point P_5 , the tolerance limit was exceeded by the unidirectional backward repeatability parameter $R\downarrow$. On the other hand, the tolerance limit was not exceeded by the unidirectional forward repeatability parameter $R\uparrow$ at P_5 . In the 'pilgrim' strategy, the values of the $R\uparrow R\downarrow$ parameter were exceeded for the P_5 point. At the point P_3 , the tolerance limit has been exceeded for the $R\uparrow$ parameter and for the P_4 point the tolerance limit was exceeded for the $R\downarrow$ parameter. The $R\uparrow R\downarrow$ parameter values were within the tolerance limit for the P_1 and P_2 points. The $R\downarrow$ parameter value which is within the given tolerance range was recorded at point P_3 . The $R\uparrow$ parameter value which is within the given tolerance range was recorded at point P_4 . Exceeding the tolerance limit follows that the laser head did not move along the defined trajectory, but rather along a path deviating from a straight line over the defined measuring length.

Statistical analysis

In order to evaluate the surface quality of the sample after the milling process, the surface roughness measurements were carried out at 5 measuring points. The mean Ra , Rz and RSm parameters values were determined. Each roughness measurement was repeated five times for each feed rate v_f and measurement point. Next, the average values of the Ra , Rz , RSm parameters were determined. Fig. 5 shows bar graphs illustrating accuracy and repeatability influence of the milling plotter on the analyzed surface roughness parameters.

It can be seen from Fig. 5 that a decrease in positioning accuracy values and an increase in positioning repeatability values of the milling plotter resulted in an increase of the average surface roughness sample values. The maximum average Ra , Rz and RSm parameters values were recorded for the smallest parameter $A\uparrow A\downarrow = 500 \mu\text{m}$. Whereas, the smallest average Ra , Rz and RSm parameters values were recorded for the highest parameter $A\uparrow A\downarrow = 551.2 \mu\text{m}$. The maximum average Ra , Rz and RSm parameters values were also recorded for the highest positioning repeatability $R\uparrow R\downarrow = 16.6 \mu\text{m}$. In turn, the smallest average surface roughness parameters values were recorded for the parameter $R\uparrow R\downarrow = 11.4 \mu\text{m}$. It is worth noting that the farther away points were from the coordinate system origin, the increase of the Ra , Rz and RSm average parameters values was observed. This increase was also due to increase in feed rates v_f . For the maximum feed rate $v_{fmax} = 5000 \text{ mm/min}$, the highest average roughness parameters values were recorded: $Ra_{av} = 3.43 \mu\text{m}$, $Rz_{av} = 11.41 \mu\text{m}$ and $RSm_{av} = 0.5 \mu\text{m}$. Whereas, for the minimum speed rate $v_{fmin} = 1000 \text{ mm/min}$, the lowest average roughness parameters values were recorded: $Ra_{av} = 0.75 \mu\text{m}$, $Rz_{av} = 4.01 \mu\text{m}$ and $RSm_{av} = 0.12 \mu\text{m}$.

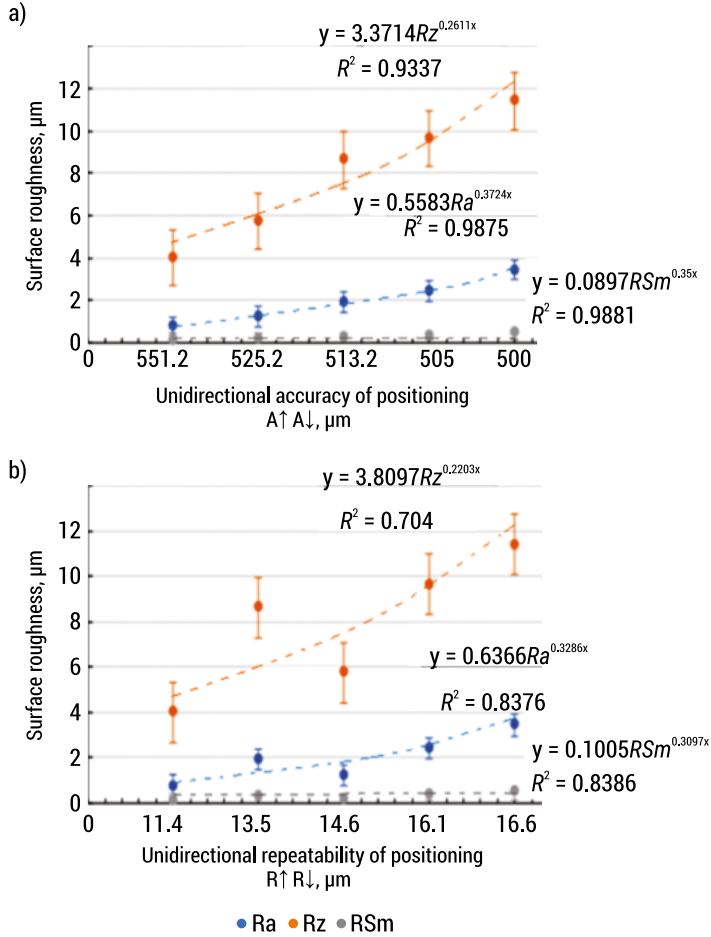


FIG. 5. The surface roughness parameters in relation to the unidirectional positioning accuracy and repeatability of the milling plotter in milling process: a) positioning accuracy $A \uparrow A \downarrow$, b) positioning repeatability $R \uparrow R \downarrow$

Sample surface quality

Simulations were carried out for an EN AW-7075 T651 aluminum alloy sample using machine learning algorithms. The predictive model consisted of two input quantities (the $A \uparrow A \downarrow$, $R \uparrow R \downarrow$ parameters) and the three output quantities Ra , Rz and RSm parameters. There were 5 measurements of three surface roughness parameters per input value. Due to the nature of the data, it was decided to use a regression model to average the data from measurements for each of the roughness parameters. For this purpose, the model with the best metrics (R^2 SCORE, Mean Absolute Error (MAE) and Root Mean Square Error (RMSE)) was selected from among the following models: Random Forest Regressor, Linear Regression, Gradient Boosting Regressor, XGBRF Regressor. The Gradient Boosting Regressor model had the best metrics which achieved the highest metrics for all roughness parameters. This means that GBR had seen

the best improvement in previous errors. Fig. 6 presents the roughness values fitted by the model for each parameter.

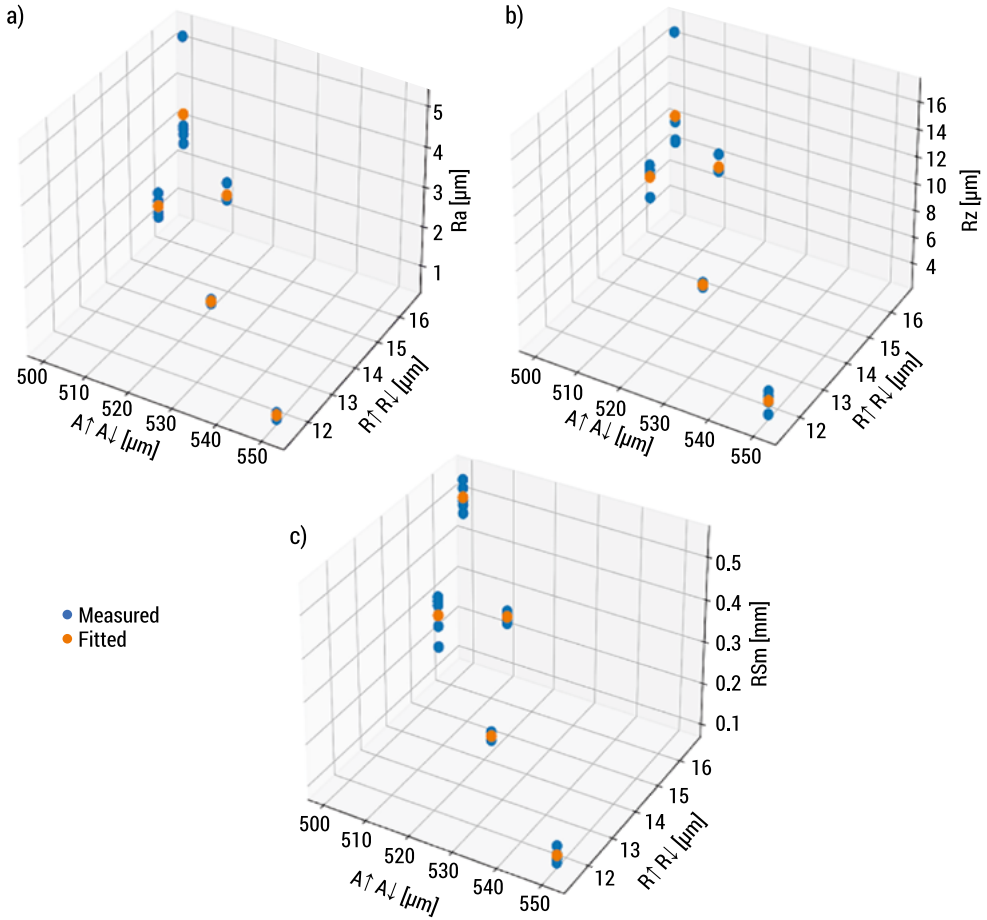


FIG. 6. Values measured and fitted for the parameters: a) Ra , b) Rz , c) RSm

Fig. 6 shows the roughness values fitted by the model for each of the parameters. Due to the nature of the input data for the positioning accuracy and repeatability parameters and the output data for the roughness parameters, a predictive model was selected that best matched the optimal single value for each of the 3 samples. In order to check the relationship between the $A\uparrow A\downarrow$ and $R\uparrow R\downarrow$ parameters and the Ra , Rz , RSm parameters, a test was conducted to check a correlation between the data. The Pearson's correlation coefficient was used in the test. Similarly, correlation between the $A\uparrow A\downarrow$, $R\uparrow R\downarrow$ parameters and the Rz , RSm parameters was determined. The results of checking linear correlation between the plotter accuracy parameters and the sample roughness parameters are shown in Fig. 7.



FIG. 7. Correlation matrix

The matrix is symmetric. Each pair has a correlation coefficient ranging from -1 to 1, which means that there is a significant negative correlation between the $A\uparrow A\downarrow$ parameter and all roughness parameters. The $R\uparrow R\downarrow$ parameter shows a positive correlation with the roughness parameters. A complete linear correlation between the Ra and RSm parameters is also noticeable.

The relationship between roughness parameters and the plotter positioning accuracy and repeatability parameters varies for different parameters. While the $A\uparrow A\downarrow$ parameter increase, the average values of the Ra , Rz and RSm parameters decrease. However, when the $R\uparrow R\downarrow$ parameter values increase, the Ra , Rz and RSm parameters increase. This may have an impact in production applications where the surface roughness needs to be controlled or predicted based on the accuracy and repeatability results of a milling plotters positioning.

Conclusions

The results of this study have led to the following conclusions:

- the results obtained with the linear strategy are burdened with grave errors, which significantly reduces their accuracy. Therefore, the ‘pilgrim’ measurement strategy is more reliable and accurate. This is due to the fact that in the linear measurement strategy, the head is approached and the position value is read at a given measurement point only once. However, in the ‘pilgrim’ strategy, the probe moves to a given measurement point and reads the value four times, which significantly increases the accuracy of the measurement,
- slight changes in the plotter positioning accuracy and repeatability can lead to significant difference in the average values of the surface roughness parameters. Decreasing the plotter positioning accuracy values and increasing the positioning

repeatability values resulted in an increase in the average values of the sample surface roughness,

- the farther away the points from the plotter's origin, the increase in the average values of the Ra , Rz and RSm parameters was recorded. This increase resulted also from increasing the feed rates v_f . Performing the milling process at the furthest point from the origin coordinate system resulted in exceeding the plotter accuracy tolerance limit for the unidirectional backward repeatability R_{\downarrow} . This resulted in a measurement error that affected the recording of the maximum average surface roughness parameters value, thereby deteriorating test sample quality.

Among the selected models, the Gradient Boosting Regressor model had the best fit to the data. This model achieved the highest values for the R^2 SCORE, MAE, and RMSE metrics, which were, respectively, 0.781, 0.719 and 0.965. The XGBRF Regressor model was also characterized by a high level of fit, as its R^2 SCORE was at the same level as the Gradient Boosting Regressor model, but the other metrics were worse. The Random Forest Regressor model was characterized by the smallest fit.

The conducted studies provide valuable cognitive conclusions, allowing for the assessment of cause-and-effect relationships between the accuracy parameters and the surface roughness parameters of the aluminum alloy sample. This information is needed to optimize measurement processes and can help to improve machine performance and machining quality. By understanding how different the machine accuracy parameters affect the surface roughness parameters of manufactured parts, manufacturers can make decisions to enhance the overall efficiency of the milling process.

References

1. Honczarenko J., 2009, *Numerically controlled machine tools*, WNT 2009 (in Polish).
2. Adamczyk S., 2008, *Measurements of geometric surfaces. Outlines of shape, waviness and roughness*, WNT 2008 (in Polish).
3. Zawada-Michałowska M., 2022, *High-Performance Milling Techniques of Thin-Walled Elements*, Advances in Science and Technology. Research Journal, 16(3), 98–110.
4. Kulisz M., Zagórski I., Jóźwik J. et al., 2022, *Research, Modelling and Prediction of the Influence of Technological Parameters on the Selected 3D Roughness Parameters, as Well as Temperature, Shape and Geometry of Chips in Milling AZ91D Alloy*, Materials, 15(12), 4277.
5. Korpysa J., Kuczmazewski J., Zagórski I., 2021, *Dimensional Accuracy and Surface Quality of AZ91D Magnesium Alloy Components after Precision Milling*, Materials, 14(21), 6446.
6. Zhang X., Yu T., Zhao J., 2020, *Surface generation modeling of micro milling process with stochastic tool wear*, Precision Engineering, 61, 170–181.
7. Yao Y., Zhu H., Huang C. et al., 2019, *Investigation on chip formation and surface integrity in micro end milling of maraging steel*, International Journal of Advanced Manufacturing Technology, 102, 1973–1984.
8. Gao Q., Li W., Chen X., 2019, *Surface quality and tool wear in micro-milling of single-crystal aluminum*, Proceedings of the Institution of Mechanical Engineers, Part C, 233, 5597–5609.

9. Zhang J., Feng C., Wang H. et al., 2019, *Analytical Investigation of the Micro Groove Surface Topography by Micro-Milling*, Micromachines, 10, 582.
10. Wojciechowski S., 2018, *Zagadnienia mechaniki precyzyjnego frezowania narzędziami monolitycznymi*, Wydawnictwo Politechniki Poznańskiej, Poznań, 13–15.
11. Sun Z., To S., Zhang S. et al., 2018, *Theoretical and experimental investigation into non-uniformity of surface generation in micro-milling*, International Journal of Mechanical Sciences, 140, 313–325.
12. Wojciechowski S., Maruda R.W., Królczyk G.M. et al., 2018, *Application of signal to noise ratio and grey relational analysis to minimize forces and vibrations during precise ball end milling*, Precision Engineering, 51, 582–596.
13. Pieśko P., 2014, *Research on the influence of static stiffness of shank cutters on the geometrical accuracy of objects made of aluminum alloys*, Wydawnictwo Politechniki Lubelskiej, Lublin 25–30 (in Polish).
14. Lianos I., Agirre A., Urreta H. et al., 2014, *Micromilling high aspect ratio features using tungsten carbide tools*, Proceedings of the Institution of Mechanical Engineers, Part B, 228, 1345–1360.
15. Kuram E., Ozcelik B., 2013, *Multi-objective optimization using Taguchi based grey relational analysis for micro-milling of Al 7075 material with ball nose end mill*, Measurement, 46, 848–865.
16. Miko E., Maj P., 2013, *Examination of positioning accuracy and diagnostics of CNC lathes*, PAK, 596), 558–561.
17. Jurczak W., 2010, *Problems and perspectives of aluminum alloys in marine structures*, Zeszyty Naukowe Akademii Marynarki Wojennej, 51(4), 89–106 (in Polish).
18. Allindustrial, *Frez kwadratowy SGS44630*, <https://allindustrial.com/kyocera-sgs-precision-tools/> [accessed: 10.08.2023].

4.2. Design and material selection optimization for additively manufactured modular components of a bioprosthetic hand

Łukasz Gałęczka¹, Małgorzata Muzalewska¹, Marek Wyleżoł¹

*¹Silesian University of Technology, Mechanical Engineering,
Department of Fundamentals of Machine Design,
marek.wylezol@polsl.pl, malgorzata.muzalewska@polsl.pl, lukasz.galeczka@polsl.pl*

Summary: This article explores the optimization of design and material selection for modular components of a bioprosthetic hand using additive manufacturing. Focusing on system requirements, it explores CAD optimization techniques and material choices, evaluating new polymers. The study aims to improve the functionality and accessibility of bioprosthetic hands, offering insights into future research and development.

Keywords: Hand bioprosthesis, 3D printing, foaming filaments, additive manufacturing

Introduction

The oncoming of 3D printing has ushered in a transformative era in the field of prosthetics. This technology, characterized by its additive manufacturing process, allows production of prosthetic components with a high level of customization. Unlike traditional manufacturing techniques, 3D printing is not limited by subtractive processes. Instead, it enables the fabrication of complex structures, which would have been either impossible or expensive to produce using traditional methods.

The notable change in 3D printing's application to prosthetics lies in its ability to customize products to the unique anatomical features of individual users. Prosthetic devices, particularly hands, require a high degree of personalization to ensure not only proper fit but also optimal functionality. With 3D scanning technologies, precise digital models of a user's residual limb can be created, forming the basis for a prosthetic design that aligns perfectly with their physiology. This personalization extends beyond mere sizing; it allows for the adjustment of grip strength, finger articulation, and even the weight distribution of the prosthetic hand, thereby serving the specific lifestyle and needs of the user.

Traditional manufacturing methods for prosthetics are typically labor-intensive and time-consuming, often resulting in products that are generic and require further modifications for a proper fit. These methods, while reliable, offer limited flexibility

in terms of design innovation. They often rely on standard molds and pre-set sizes, which can be hard fitting and uncomfortable for the end-user. However, traditional techniques tend to be pricy when it comes to bespoke solutions, rendering personalized prosthetics inaccessible to many.

In contrast, additive manufacturing, with its layer-by-layer construction approach, excels in producing complex prosthetic components at a fraction of the time and cost. This efficiency is a significant advantage, especially in developing countries or for individuals who lack access to specialized prosthetic services. Furthermore, 3D printing enables the use of a diverse range of materials, including lightweight and durable polymers, which can be optimized for specific properties such as flexibility, strength, or even aesthetic appeal. The ability to experiment with varied materials opens new avenues for enhancing the comfort and functionality of prosthetic hands, making them more adaptable to various daily activities.

Bioprosthesis requirements and modular components

The functional requirements of a bioprosthetic hand are multifaceted, encompassing a range of mechanical capabilities that are essential for replicating the complex movements of a natural hand. One of the primary considerations is grip strength, which is important for performing everyday tasks such as holding objects, opening doors, or using tools. The bioprosthetic hand must be able to withstand sufficient force to grip objects securely, yet also be delicate enough to manage fragile items without dealing damage to the object [1, 2].

Another crucial aspect is the range of motion. A bioprosthetic hand should ideally mimic the natural movement of a human hand, which includes not just the flexion and extension of fingers but also more complex motions like rotation and abduction. This requires a sophisticated design that can replicate the intricate joint mechanisms of a biological hand. Fine motor skills are also paramount. For a user to perform tasks requiring precision, such as typing or threading a needle, the bioprosthetic fingers need to have a high degree of dexterity. This involves not only the accurate replication of finger movements but also the ability to provide sensory feedback, which can be a significant challenge in prosthetic design [2, 3].

Ergonomics plays a crucial role in the design of bioprosthetic hands. A prosthetic that is uncomfortable to wear, regardless of its functionality, is less likely to be used effectively. The design must therefore consider factors such as weight distribution, pressure points, and overall fit. Modular components in bioprosthetics offer a solution to this challenge. By designing the hand in segments – fingers, palm, wrist – each part can be tailored to fit the user's residual limb comfortably. This modularity also facilitates adjustments and replacements, ensuring the prosthetic remains comfortable over time, even as the user's needs or body conditions change. The interface between the prosthetic and the residual limb is particularly critical. It must be designed to minimize friction and pressure, preventing discomfort or injury to the user. Advanced

materials that are soft yet durable, such as silicone or thermoplastic elastomers, are often used in these contact areas to enhance comfort [4, 5].

The aesthetic aspect of a bioprosthetic hand is more than just a matter of appearance; it has a profound psychological impact on the user. A prosthetic that closely resembles a natural hand can significantly boost the user's confidence and self-esteem, facilitating social interactions and reducing the stigma often associated with limb loss. The modularity of bioprosthetic components also plays a role in aesthetics. Modular design allows for the customization of the prosthetic's appearance, including skin tone, nail detail, and even the shape and size of the hand, to match the user's natural limb as closely as possible. This customization can be crucial for the emotional and psychological well-being of the user, aiding in their social reintegration and personal acceptance of the prosthetic limb [6].

CAD optimization and material selection for 3D printing

Balancing Form and Function

In the design of bioprosthetic hands, the use of Computer-Aided Design (CAD) is critical for achieving a harmonious balance between aesthetic appeal and functional efficacy. CAD enables designers to experiment with various shapes and structures, allowing them to create prosthetic components that are not only effective in performing their intended functions but also visually pleasing. This balance is crucial, as a prosthetic hand must be more than just a functional tool; it should also be an extension of the user's body image [4].

Through CAD, designers can meticulously modify each aspect of the prosthetic hand, from the curvature of the fingers to the contours of the palm. This level of detail is essential for ensuring that the prosthetic is comfortable to wear and performs as closely as possible to a natural hand. Furthermore, CAD software allows for rapid prototyping, enabling designers to quickly produce and test models, refining the design iteratively until the optimal balance between form and function is achieved.

Optimization of Printing Parameters

The optimization of 3D printing parameters is another area where slicers prove indispensable. Key printing parameters, such as layer height, infill density, and printing speed, have a profound impact on the strength, resolution, and overall quality of the printed prosthetic parts (Fig. 1). The foaming parameters depend on the temperature. The added foaming agent expands under temperature and aerates the currently fused filament. The filament itself can be printed between 190°C and 240°C, as the temperature increases the hardness of the filament decreases in the Shore 92A to 55A range. However, when adjusting the print, it is important to control the flow rate, which should decrease as the temperature increases, as the filament itself can extend the line thickness 60%. An overlap of about 5% in the filament can assist in the stability of the print, however, anything beyond this has a negative impact on quality. Through slicer, these parameters can be precisely adjusted to suit the specific

requirements of each component of the prosthetic hand. For example, a higher layer resolution might be used for areas requiring finer detail, like the fingertips, while a lower resolution could be sufficient for less intricate parts. Similarly, the infill density can be varied to balance the strength and weight of the components, ensuring that the prosthetic is both durable and comfortable to wear [7].

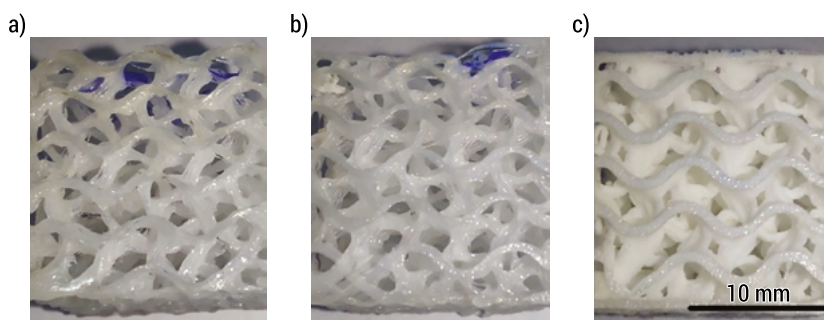


FIG. 1. The impact of temperature and flowrate on print quality: a) 190°C, fl = 0.8, b) 210°C, fl=0.5, c) 240°C, fl=0.3

Characteristics of Foaming Filaments

In the context of bioprosthetic hands, the choice of material plays a pivotal role in the overall performance and user experience of the prosthetic. Foaming filaments represent a significant advancement in this area, offering unique properties that are highly beneficial for prosthetic use. These filaments are known for their lightweight nature, which is crucial in reducing the overall weight of the prosthetic. A lighter prosthetic is easier to maneuver and reduces the strain on the user's residual limb, enhancing comfort during prolonged use [7].

Durability is another key characteristic of foaming filaments. Prosthetic hands are subject to various stresses and strains in daily use, and the material must be able to withstand these without degrading. Foaming filaments offer this resilience, maintaining their structural integrity over time. Additionally, these materials can provide a degree of cushioning and shock absorption, which is beneficial in protecting the delicate components of the prosthetic hand from impact or stress [8].

The porous structure of foaming filaments (Fig. 2) also contributes to their suitability for prosthetics. This type of structure can be selected to the user's preference, depending on whether he or she wears a fabric liner, the perspiration of the skin and the ease with which this type of sockets rubs the skin. The overall structure can be a kind of set of values that modify the parameters of the filament, which will change the temperature at a particular location to obtain a particular softness or increase the % flowrate to create a rougher surface. Additionally, in the case of a particular component configuration, it is possible to produce a component whose outer surface will be hard and smooth while, the infill will be printed at a high temperature of 240°C and a flowrate of 0.8 creating a soft, yet bonded infill [4].

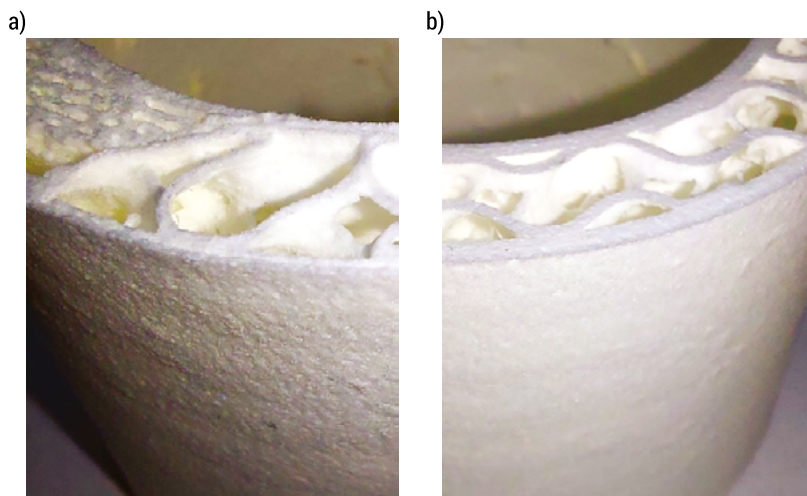


FIG. 2. Prosthetic socket made with foamed filament technology a) randomized settings b) settings selected by trial and error

Additive manufacturing processes fdm vs. Sla

When it comes to additive manufacturing processes for bioprosthetic hands, two of the most prominent techniques are Fused Deposition Modeling (FDM) and Stereolithography (SLA). Each of these methods has its own set of advantages and is suited to different components of the prosthetic based on the requirements of strength, precision, and material biocompatibility.

FDM technology is extensively utilized in the production of prosthetic hands due to its versatility, cost-effectiveness, and compatibility with a wide range of thermoplastic materials. This method is particularly advantageous for constructing the larger, less intricate parts of the prosthetic hand, such as the palm and the forearm section. The reasons for this preference include the ability of FDM to fabricate robust and durable parts efficiently, making it a cost-effective solution for these less detailed sections. Furthermore, the availability of materials suitable for prosthetic use, such as ABS and PLA, which are known for their strength and lightweight properties, adds to the appeal of FDM for these prosthetic components [6].

SLA is recognized for its exceptional resolution and precision, attributable to its use of a laser to polymerize liquid resin layer by layer. This method is especially beneficial for producing the smaller, more detailed parts of the prosthetic hand, such as the fingertips, intricate joint mechanisms, and the internal gearing or linkage systems. The high resolution of SLA allows for the creation of parts with complex geometries and fine details that are crucial for the functional and aesthetic requirements of these components. Additionally, the smooth surface finish provided by SLA improves the appearance of the prosthetic hand, particularly for the parts that are visible, contributing to a more natural and appealing look. However, it is important

to note that while SLA offers superior detail and finish, it generally comes at a higher cost compared to FDM, and the range of materials suitable for SLA is more limited, which may restrict its application depending on the specific requirements of the prosthetic hand [6].

Conclusions



FIG. 3. Transition from a CAD model with parametric elements to a slicer with added settings for the density of individual objects, along with examples of application in hand bioprosthetics and prosthetic socket

Picking out the update systems to optimize the prosthesis manufacturing process is difficult. However, proper optimization in terms of parameterization in CAD allows for much greater possibilities of change within individual systems, and thus the possibility of iteration at a lower cost.

In addition, using foamed filament technology, we can obtain a larger field of possibilities for the parameterization of a given device as well as reduce costs (Fig. 3). Due to the foaming of the material, we can overcome many of the disadvantages of printing in standard TPU. We can manipulate the roughness, softness, as well as the entire cross-sectional structure just by manipulating the temperature and flow of the filament. And these properties the filament itself has, when added to the right type of printer, optimize the component itself in terms of print technology. After considering such things as the material, the manufacturing technology, and the specific modelling properties, we have a simple path in which we adapt the entire manufacturing process to the specific component in the prosthesis and its application and needs.

References

1. Silva B.B. da, Hellmeister L.A.V., Porsani R.N. et al., 2020, *Design and Development of a Myoelectric Upper Limb Prosthesis with 3D Printing: A Low-Cost Alternative*, in: *Advances in Additive Manufacturing, Modeling Systems and 3D Prototyping*, eds. M. Di Nicolantonio, E. Rossi, T. Alexander, Springer, Cham, 318–327.
2. Fajardo J., Ferman V., Cardona J.D. et al., 2020, *Galileo hand: An anthropomorphic and affordable upper-limb prosthesis*, *IEEE Access*, 1, 1–13.
3. Vujaklija I., Farina D., 2018, *3D printed upper limb prosthetics*, *Expert Review of Medical Devices*, 15(7), 505–512.
4. Gałęczka Ł., Muzalewska M., 2023, *Modyfikacja struktury protezy ręki za pomocą druku 3D*, in: *Metody komputerowe – 2023. Studencka konferencja naukowa*, Gliwice, czerwiec, ed. P. Fedeliński, G. Działkiewicz, J. Ptaszny, Politechnika Śląska, Gliwice, 25–28.
5. Smail L.C., Wilkins C., Neal C. et al., 2020, *Comfort and function remain key factors in upper limb prosthetic abandonment: findings of a scoping review*, *Disability and Rehabilitation. Assistive technology*, 16(8), 1–10.
6. Górski F., Wichniarek R., Kuczko W. et al., 2022, *Automated design and rapid manufacturing of low-cost customized upper limb prostheses*, *Journal of Physics Conference Series*, 2198(1), 012040.
7. Iacob M.C., Popescu D., Marinescu R. et al., 2023, *Assessment of the Flexural Fatigue Performance of 3D-Printed Foot Orthoses Made from Different Thermoplastic Polyurethanes*, *Applied Sciences*, 13(22), 12149
8. Gałęczka Ł., 2023, *Hand bioprosthesis prototype*, master thesis, Gliwice.

4.3. The role and development of CAx methods and tools in reverse engineering

*Andrzej Łukaszewicz¹, Andriy Kernytskyi², Mykhaylo Melnyk³,
Andriy Holovatyy⁴, Grzegorz Skorulski⁵*

*¹Bialystok University of Technology, Faculty of Mechanical Engineering,
Department of Machine Design and Exploitation, a.lukaszewicz@pb.edu.pl*

*²Lviv Polytechnic National University, Institute of Computer Science and Information Technologies,
Department of Computer Aided-Design: andriy.b.kernytskyi@lpnu.ua,*

³mykhaylo.r.melnyk@lpnu.ua, ⁴andrii.i.holovatyi@lpnu.ua

*⁵Bialystok University of Technology, Faculty of Mechanical Engineering,
Department of Materials and Production Engineering, g.skorulski@pb.edu.pl*

Summary: This article explores the diverse reverse engineering methods utilized in industries for the reconstruction of 3D objects. It discusses the different stages of the process, examining the integration of modern technologies in reverse engineering, including 3D scanning, CAx systems, and artificial intelligence. The study underscores the importance of reverse engineering in product development and its potential future implications.

Keywords: reverse engineering, CAx, 3D scanning, 3D modelling

Introduction

In today's fiercely competitive global market, manufacturing companies continually seek innovative methods to reduce the time required to develop new products that will meet the demands and expectations of consumers [1].

In contemporary mechanical engineering, any given product is viewed as an information-bearing entity. At all stages of its lifecycle, models reflecting the product's geometric shape, precision, manufacturing methods, etc., are utilized [2]. The most common method involves creating a model based on drawings in a computer-aided design (CAD) system. However, in certain cases it proves beneficial to use an existing physical sample to accelerate the development of new products or the analysis of existing products [3, 4]. Using reverse engineering methods and tools, you can quickly obtain a suitable 3D model or product with modified shape and dimensions [5]. Fig.1 presents an example of product development cycle [6].

Additionally, reverse engineering is extremely important in areas like repair of unique equipment, recovery of lost technical documentation, restoration work,

restoration of rare equipment, among others. In these sectors, traditional design and restoration methods might not be effective or even entirely absent, making the application of reverse engineering essential [7].

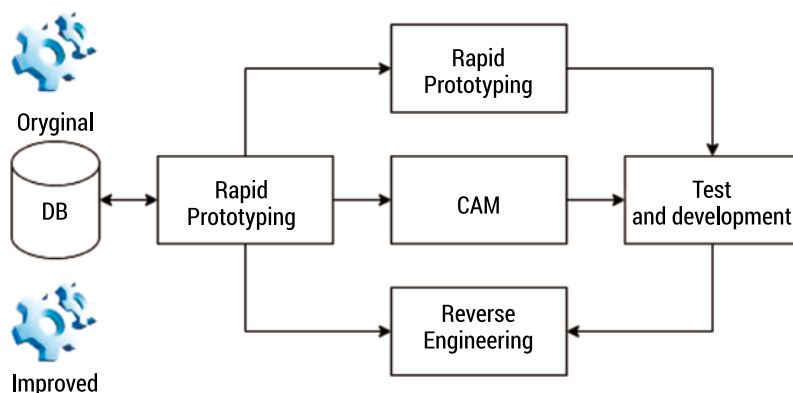


FIG. 1. Product development cycle

Reverse Engineering Process

Based on the discussion of studies [1–6], the general process of reverse engineering includes the following stages:

- get a product/object for which reverse engineering must be carried out,
- disassembling the product into individual components,
- each part is carefully analysed to understand its function and construction,
- use of a 3D scanner to digitize the product,
- reconstruction is carried out using CAD systems that create 3D models of the product,
- when the 3D model is developed, it is documented with detailed drawings, specifications, and other relevant information,
- 3D model can be modified and improved using CAD systems,
- the 3D model can also be selected to reproduce the product using different manufacturing methods such as 3D printing, injection molding or CNC machining.

Approaches to Reverse Engineering

Certain manufacturing requirements, such as rapid prototyping or working with specific CAX systems, do not require solid geometric models but rather involve working directly with a virtual product model in the form of a 3D point cloud. Nevertheless, the number of these problems is relatively smaller compared to those requiring solid-state or surface models [7–9]. The reverse engineering of product geometry includes the construction of solid-state models based on 3D scanning of the product. As most 3D modelling systems do not support the creation of solid models based on triangular

surfaces, the development of specialized tools has been necessary to convert scanned data into surfaces compatible with CAD systems [10–14].

Within modelling systems such as SolidWorks and CATIA, special modules have been created to work with complex scanned surfaces and develop corresponding CAD models through a 4-step meshing process to go from sketches to surfaces and finally to bodies. Specialized systems for reverse engineering 3D geometry also exist. Simultaneously, based on product complexity, three distinct reverse engineering approaches can be utilized [4, 15, 16]:

- 3D scanning as a basis for step-by-step geometry learning,
- 3D modelling considering a set of geometric primitives,
- creating a solid geometry from individual parts that reproduce a 3D scan.

The first approach typically requires the use of additional modules, which allows bypassing the built-in functionality of CAD. This approach is commonly used for high-precision products featuring curved elements. In this method, 3D scanning serves as the foundation for creating marks (points, lines, planes), building a basic coordinate system, and determining dimensions. The 3D scan is then utilized purely for comparison with the created model and visual inspection. A prime example of the application of this approach is a flat blade developed based on a series of intersecting planes (Fig. 2 and Fig. 3).

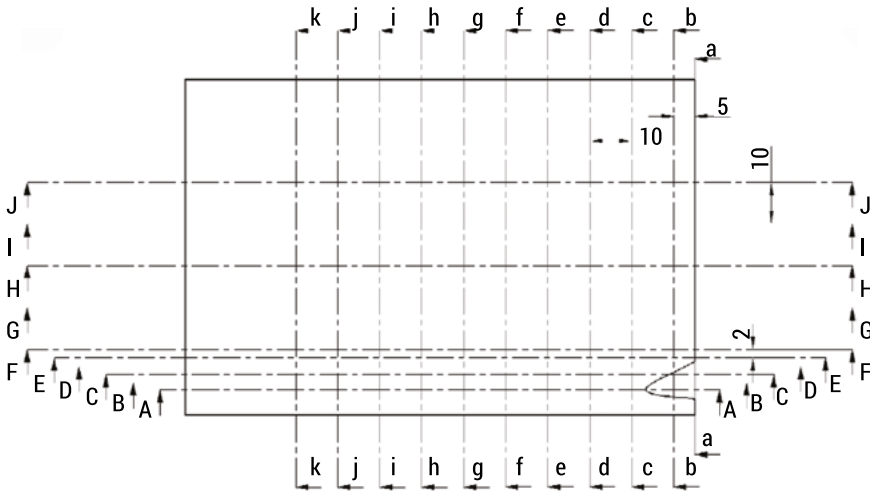


FIG. 2. Orientation of cutting planes [8]

The second approach is used for a variety of products and, depending on their complexity, can be used to create a complete model or an assembly of key elements that will subsequently be connected to free-form surfaces. Primitives can be designed

in specialized reverse engineering software, maximizing automation of the process, or measured in 3D scanner-compatible software, followed by development in a CAD system. The latter option is the most versatile but requires additional capital investments.

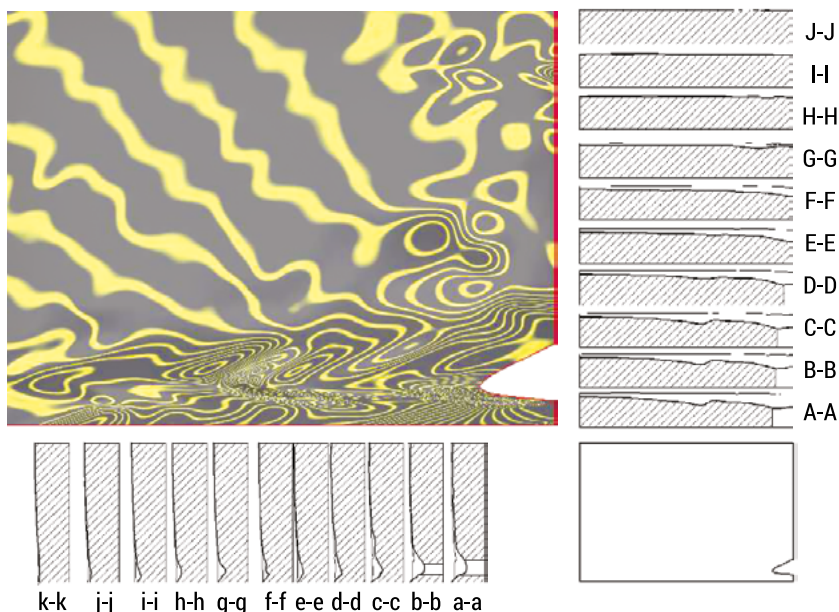


FIG. 3. Blade sections in shear planes and top view with the “zebra” option [8]

Primitives can be transferred to the CAD system through standard interfaces (for example, STEP or IGES) or measured for subsequent development. After import into the CAD system, the 3D model is gradually reproduced and optimized (Fig. 4).

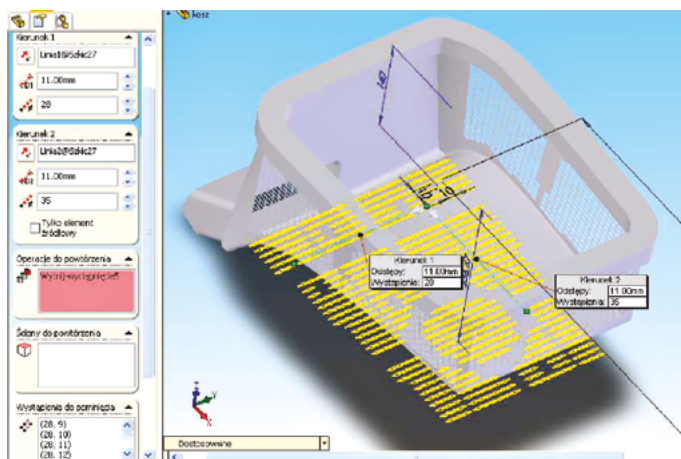


FIG. 4. Step-by-step restoration of the three-dimensional model [9]

The third approach is used to create models of complex shapes that often cannot be defined by regular geometries such as planes, cylinders, or spheres. This method yields a model with less accuracy compared to the first two approaches. However, its construction speed is significantly faster, and, in some cases, the process can be entirely automated. The main challenge with this transformation is that the triangulation model consists of triangles that do not lie on the same plane. Therefore, it becomes necessary to “stitch” all parts together to form a single surface. A construction method based on sequentially filling the surface with the aid of its curvature sections (Fig. 5 and Fig. 6) is, however, gaining increased popularity.



FIG. 5. Measuring points imported into the CAD system [10]



FIG. 6. View of the upper surface stretched on previously generated 3D curves [10]

Development of Reverse Engineering Methods

Advancements in reverse engineering within mechanics and automotive engineering, put forth through computer programs and CAD systems, have significantly enhanced the efficiency and precision of mechanical object analysis. Let's examine the primary evolutions in reverse engineering methods of mechanical objects fostered by the employment of computer programs and CAD systems [3, 4, 6, 19]:

- 3D modelling and digital prototyping (80s and 90s). With the development of computer technologies, architectures and 3D graphics tools, the modelling and visualization of components, assemblies and systems have become an integral part of reverse engineering. This made it possible to reproduce accurate models of mechanical objects considering their functionality, configuration, and ergonomics with higher accuracy indicators,
- the use of 3D scanning (1990s – present). Implementing 3D scanners to reproduce the geometry of physical objects greatly simplifies the reverse engineering process. Developers can now receive precise digital models they can then edit and modify in CAD prior to prototyping or manufacturing,
- reverse engineering software (2000s – present). The emergence of dedicated reverse engineering software (e.g., Siemens NX, CATIA, Autodesk Inventor, SolidWorks) permits the analysis of components, connections and systems considering mass, aerodynamics, construction, and other characteristics of the object,
- increasing the level of design automation (2010s – present). The integration of reverse engineering with other engineering processes, such as computer simulation, verification, validation, and optimization, makes the design process more efficient and automated.

In conclusion, the introduction of computer programs and automated design systems in the reverse engineering of mechanical objects has increased the methods of analysis, the accuracy of the reproduced results, and the process's overall efficiency.

Current State of Reverse Engineering Tools

The current state of reverse engineering methods in mechanics is characterized using the latest technologies, hardware, and software, which allow fast and accurate analysis and reproduction of mechanical objects. Modern methods of reverse engineering in mechanics include:

- the use of 3D scanners allows to significantly speed up the process of reverse engineering, reproducing accurate three-dimensional models of mechanical objects. Modern 3D scanners can work with very large, large, medium, and small objects [7, 10, 14],
- the use of CAD, such as SolidWorks, CATIA, Autodesk Inventor, Siemens NX, allows for conducting a more accurate and detailed analysis of mechanical objects, simulating their operation, and carrying out the necessary optimizations [14-20],

- photogrammetry allows for the reproduction of mechanical parts and components using images from multiple angles. This method has become an affordable reverse engineering technique thanks to the combination of modern high-resolution cameras and advanced image processing software [21].

Development of Reverse Engineering Methods

In the mechanical, automotive, and aerospace sectors, reverse engineering continues to evolve with new technologies and approaches. Some of the key trends in the development of reverse engineering methods:

- the integration of cloud technologies allows reverse engineering of mechanical objects with remote collaboration between different team members, which facilitates the analysis and optimization of projects simultaneously and remotely [22],
- the implementation of machine learning algorithms and artificial intelligence in the process of reverse engineering offers the possibility of automating certain stages of analysis, comparing similar projects, and determining optimal solutions [23],
- 3D printing technologies, especially with the use of production materials and metals, allow you to quickly create prototypes and check the reproduced objects at the stage of reverse engineering, ensuring the speed of implementation of solutions and the efficiency of the process [14, 19],
- integration of reverse engineering with augmented and virtual reality technologies can simplify the process of analysis, design and optimization of mechanical components considering their location, interaction, and real conditions of use of systems [24],
- using Internet of Things (IoT) technologies, reverse engineering can use data streams from real equipment and objects to accurately analyse and reproduce the functionality of mechanical systems [25].

Based on these trends, reverse engineering techniques in mechanical, automotive, and aerospace industries will become even more accurate, faster, and more efficient, considering more aspects of the actual functioning of mechanical objects.

Conclusions

Inverse projection methods are employed in various fields where there is a need to gather data on uncertain 3D surfaces. Measurement data can be utilized to create a CAD model of a real object and then, for instance, be used to discern changes in the shape of the processed object or create a processing program permitting CNC to duplicate or create a specific geometric element.

Moreover, reverse engineering will continue to propel technological advancements. With the progression of 3D printing, reverse engineering can formulate digital models suitable for 3D printing. Such innovation will aid in reducing costs and production time, as well as enhance the precision of the final product.

Overall, reverse engineering will persist as a crucial instrument in product development and innovation. Its ability to analyse and improve existing products will facilitate technological advancement, leading to more sophisticated and advanced products in the future.

References

1. Ulrich K.T., Eppinger S.D., Yang M.C., 2020, *Product Design and Development*, 7th ed., McGraw Hill Education.
2. Huang G.Q., Mak K.L., 1999, *Current practices of engineering change management in UK manufacturing industries*, International Journal of Operations & Production Management, 19(1), 21–37.
3. Várady R.R., Martin R.R., Cox M.J., 1997, *Reverse engineering of geometric models – an introduction*, Computer-Aided Design, 29(4), 255–268.
4. Geng Z., Bidanda B., 2017, *Review of reverse engineering systems – current state of the art*, Virtual and Physical Prototyping, 12(2), 161–172.
5. Fan L., Wang J., Xu Z. et al., 2022, *A Reverse Modeling Method Based on CAD Model Prior and Surface Modeling*, Machines, 10(10), 905.
6. Raja V., Fernandes K.J., 2008, *Reverse Engineering: An Industrial Perspective*, Springer Science & Business Media, London.
7. Gao J., Chen X., Zheng D. et al., 2006, *Adaptive restoration of complex geometry parts through reverse engineering application*, Advances in Engineering Software, 37, 592–600.
8. Łukaszewicz A., Miatluk K., 2007, *The practical application of reverse engineering for object with free-form surfaces*, Machine Dynamics Problems, 31(3), 51–57.
9. Matyjasek M., Łukaszewicz A., 2007, *Metody generowania i analizy wirtualnego modelu kosiarki poduszkowej w środowisku SolidWorks*, in: *Komputerowe Wspomaganie Nauki i Techniki CAX'2007. IV warsztaty naukowe*, Bydgoszcz–Duszniki-Zdrój, 25–28.
10. Karpiński R., Łukaszewicz A., 2006, *Projektowanie form elementów o powierzchniach krzywoliniowych z wykorzystaniem technik inżynierii odwrotnej*, in: *Inżynierowie nowej ery a zagadnienia technologii wytwarzania i materiałów*, ed. L. Gardyński, Liber Duo, Lublin, 37–42.
11. Łukaszewicz A., 2008, *CAX education as an inseparable part of integrated product development*, in: *Design methods for industrial practice*, ed. R. Rochatyński, Oficyna Wydawnicza Uniwersytetu Zielonogórskiego, 313–320.
12. Łukaszewicz A., 2008, *Method for propeller reconstruction using reverse engineering*, Scientific proceedings of Riga Technical University, Series 6: Transport and Engineering. Transport. Aviation transport, 27, 149–155.
13. Łukaszewicz A., Miatluk K., 2009, *Reverse Engineering Approach for Object with Free-Form Surfaces Using Standard Surface-Solid Parametric CAD System*, Solid State Phenomena, 147–149, 706–711.
14. Łukaszewicz A., Kernysky A., 2011, *Rapid prototyping in UAV applications on the example of 3D printing technique*, CADMD'2011, 29–30.

15. Page D., Koschan A., Abidi M., *Methodologies and Techniques for Reverse Engineering – The Potential for Automation with 3-D Laser Scanners*, in: *Reverse Engineering. An Industrial Perspective*, eds. V. Raja, K.J. Fernandes, Springer, London, 11–32.
16. Lindskog E., Berglund J., Vallhagen J. et al., 2016, *Layout planning and geometry analysis using 3D laser scanning in production system redesign*, *Procedia CIRP*, 44, 126–131.
17. Xinchang Z., Cui W., Li W. et al., 2019, *A Hybrid Process Integrating Reverse Engineering, Pre-Repair Processing, Additive Manufacturing, and Material Testing for Component Remanufacturing*, *Materials*, 12(12), 1961.
18. Li L., Li C., Tang Y. et al., 2017, *An integrated approach of reverse engineering aided remanufacturing process for worn components*, *Robotics and Computer-Integrated Manufacturing*, 48, 39–50.
19. Buonamici F., Carfagni M., Furferi R. et al., 2018, *Reverse engineering modeling methods and tools: a survey*, *Computer-Aided Design & Application*, 15(3), 443–464.
20. Tao F., Qi Q., Liu A. et al., 2018, *Data-Driven Smart Manufacturing*, *Journal of Manufacturing Systems*, 48, 157–166.
21. Zhao L., Zhang H., Mbachu J., 2023, *Multi-Sensor Data Fusion for 3D Reconstruction of Complex Structures: A Case Study on a Real High Formwork Project*, *Remote Sensing*, 15(5), 1264.
22. Wang H., Yin F., Tay Y. et al., 2019, *Cloud-based design and manufacturing through process-validation-oriented intelligent application*, *Journal of Ambient Intelligence and Humanized Computing*, 10(6), 2393–2405.
23. Jayakiran R.E., Sridhar C.N.V., Rangadu V.P., 2015, *Knowledge Based Engineering: Notion, Approaches and Future Trends*, *American Journal of Intelligent Systems*, 5(1), 1–17.
24. Jovanovikj I., Yigitbas E., Sauer S. et al., 2020, *Augmented and Virtual Reality Object Repository for Rapid Prototyping*, in: *8th International Conference on Human-Centred Software Engineering (HCSE)*, Eindhoven, Netherlands, 216–224.
25. Shwartz O., Mathov Y., Bohadana Y. et al., 2018, *Reverse Engineering IoT Devices: Effective Techniques and Methods*, *IEEE Internet of Things Journal*, 5(6), 4965–4976.

4.4. Applying software development black-box, grey-box and white box reverse engineering frameworks to the mechanical industry

Oleh Kernyskyy¹, Andriy Kernyskyy², Mykhaylo Melnyk³,
Andrzej Łukaszewicz⁴, Krzysztof Pytel⁵, Marian Banas⁶

¹Lviv Polytechnic National University, Institute of Computer Science and Information Technologies,
Department of Automated Control Systems, oleh.b.kernyskyy@lpnu.ua

²Lviv Polytechnic National University, Institute of Computer Science and Information Technologies,
Department of Computer Aided-Design, andriy.b.kernyskyy@lpnu.ua, ³mykhaylo.r.melnyk@lpnu.ua

⁴Bialystok University of Technology, Faculty of Mechanical Engineering, Department of Machine Design
and Exploitation, a.lukaszewicz@pb.edu.pl

⁵AGH University of Science and Technology, Faculty of Mechanical Engineering and Robotics, Department
of Power Systems and Environmental Protection Facilities: kpytel@agh.edu.pl, ⁶mbanas@agh.edu.pl

Summary: This study aims to develop a reverse engineering framework for mechanical components, adapting existing IT reverse engineering approaches (Black-box, Grey-box, and White-box) to meet the specific needs of the mechanical industry. The implementation of this framework has the potential to expedite the analysis, optimization, and rebuilding of mechanical systems through enhanced automation, offering significant advantages in various fields, including automotive, aerospace, medical, and construction sectors.

Keywords: reverse engineering, information technology, Black-box, Grey-box, and White-box methods, framework

Introduction

The traditional methods of reverse engineering mechanical parts typically require significant time and resources, as they necessitate physical disassembly and analysis of system components [1]. By adapting information technology (IT) reverse engineering techniques such as Black-box, Grey-box, and White-box, it becomes possible to offer new methodologies, enhance design comprehension, optimize processes, and reduce costs for the analysis and modernization of mechanical components.

The objective of this study is to devise a reverse engineering framework for mechanical parts, utilizing adapted IT reverse engineering methods. This model will account for the specifics of mechanical components, offering the flexibility to employ varying methods as required.

The escalating complexity of mechanical systems, coupled with the constant demands for their improvement and development, fosters the need for innovative, efficient reverse engineering methods. The successful implementation of such a reverse engineering framework could have a significant impact on multiple industries, including the automotive, aerospace, medical, robotics, and construction sectors [2].

The adoption of IT reverse engineering techniques applied to mechanical parts can deliver several advantages, thus underscoring their feasibility:

- utilizing IT methodologies makes it possible to automate the processes of data collection and modelling, as they are founded on software and computer algorithms. This can significantly expedite the analysis of mechanical components and lower the cost of reverse engineering,
- IT reverse engineering approaches (Black-box, Grey-box, and White-box) are already successfully employed for the analysis of software, hardware, and system components [3–4]. Hence, there is already an established basis for broadening their application in various sectors, including mechanical components,
- the implementation of IT reverse engineering approaches allows for precise tracing of problem sources and can improve the design processes of mechanical parts to ensure appropriate quality, wear resistance, and efficiency,
- the employment of Black-box, Grey-box, and White-box reverse engineering methods for mechanical parts can enhance the efficiency and adaptability of the process, as these approaches can be selected based on available information and specific analysis requirements,
- the adaptation of IT methodologies will encourage the exchange of knowledge and skills between different engineering fields, thereby contributing to innovative development and new discoveries.

Literature Review

Reverse engineering in IT employs three primary methods: Black-box, Grey-box, and White-box. Each of these methods offers specific applications, advantages, and limitations:

- Black-box reverse engineering is used to analyse the external behaviour of the system and its results without accessing the internal structure or code of the program. It is applicable to software testing, analysis of web applications, databases, network equipment, and security audits. The simplicity of the process and lower resource consumption due to a focus on the system's external behaviour are amongst its advantages. However, it has limitations such as a lack of insight into the internal code which can potentially lead to incomplete or inaccurate analysis, an inability to assess code security and efficiency, and it being less suitable for detailed analysis [5–7],
- Grey-box reverse engineering is a hybrid approach that combines elements of Black-box and White-box methods. It provides limited access to the internal specifics of a system, offering a deeper understanding of its operation compared

to Black-box, yet with less complexity compared to the White-box method. This strategy is used mainly in software testing, development of patches, and optimization of program performance. An important advantage is that it allows identification of potential issues without the need for intense code intervention. However, the limited access to the system's internal components could result in an incomplete or inaccurate analysis, dependent on the interaction with the system's users [5, 8],

- White-box reverse engineering provides comprehensive or maximum feasible access to internal systems. It requires a detailed analysis of components such as the program code, algorithms, and design. This method is primarily used in application code analysis and enhancement, performance optimization, patch development, and understanding algorithms and system architecture. Its primary advantage is the opportunity to conduct a thorough analysis of the system. This allows for identifying problem causes, modelling and predicting future failures, and developing protection methods against hacking. Yet, it also has its limitations. White-box reverse engineering is resource-intensive, demands significant time, and presents challenges in code analysis and interpretation. It requires a deep understanding of the programming language and the system's architecture [6, 9].

Methods of mechanical systems reverse engineering are often used for analysis, modelling, and optimization of the design and construction of mechanical components. The main methods employed in this field include [10–15]:

- the 3D scanning method involves the creation of precise three-dimensional models of mechanical components based on their physical blueprints. This allows the production of detailed duplicates of original solutions or the reproduction of missing parts,
- the computer modelling method utilizes specialized programs for modelling mechanical systems and analysing their operation. This might include an analysis of stress, heat loss, and the performance of mechanical operations,
- the disassembly and analysis method involves examining individual components of the mechanical system, their design, materials, and assembly. This approach allows the identification of weaknesses and potential improvements to the structure.

The problems that can be addressed through the adaptation of IT reverse engineering methods include:

- IT reverse engineering methods can hasten the process of analysing mechanical systems by automating certain processes that traditionally demand significant effort and time from specialists,
- adapted IT reverse engineering techniques can assist in the process of analysing the internal structures of mechanical systems, identifying design characteristics and key design elements,

- the application of adapted IT reverse engineering techniques will enable testing and validation of the design of mechanical parts, pinpointing their weaknesses and areas for improvement,
- adapting IT reverse engineering techniques can aid in integrating mechanical systems with contemporary technologies such as the Internet of Things (IoT), artificial intelligence (AI), and augmented reality (AR), enhancing overall efficiency and functionality.

Adapting IT reverse engineering techniques to mechanical systems can provide significant benefits such as improved productivity, reduced development time, and improved product quality through new approaches to design analysis and structural optimization.

Although the adaptation of IT reverse engineering methods for mechanical parts is a relatively new direction, some examples of successful use of this approach can be found in various industries [16–18]:

- in the aviation industry, the reverse engineering approach allows analysing the structure of engines and aerodynamic parts, comparing different designs and implementing improvements. Besides, the use of 3D scanning to create exact copies of aviation components and restoration of historical aircrafts solve problems with production and replacement of old units and components in the aircraft fleet,
- in the automobile industry, reverse engineering is used to analyse competing products, improve engine cooling systems, optimize aerodynamic drag, and modernize drive equipment. Usage of 3D scanning and computer modelling speeds up the design and prototyping process of new cars, including transmission parts, bodywork, and more,
- in biomedical engineering, reverse engineering allows for the analysis and improvement of the design of medical devices, such as prostheses, needles, fuses, surgical instruments, etc. Use of 3D scanning and computer modelling foster the development of individual prostheses or implants according to the size of the patient, and the creation of bionic devices,
- in technical support of the sports and entertainment industry, reverse engineering helps to analyse and optimize ergonomics, wear resistance and materials together with 3D scanning and computer modelling to customize sports equipment. Reverse engineering helps in restoration of antique artifacts and cultural heritage items, using 3D scanning and computer modelling to reconstruct details.

Adaptation of reverse engineering methods in IT to mechanical parts and development of reverse engineering framework based on adapted methods

It is possible to create a framework for reverse engineering of mechanical parts by adapting Black-box, Grey-box, and White-box methods of reverse engineering of IT systems. Here we propose a possible framework with the following adaptations:

- Black-box reverse engineering for mechanical parts: this method consists of analysis by observing the external behaviour, characteristics, and properties of mechanical parts without accessing the internal details of the structure or materials. It is possible to test mechanical parts under different conditions, examining their respective results at different stages of loading and wear,
- Grey-box reverse engineering for mechanical parts: this approach combines elements of black-box and white-box methods, performing analysis with limited access to internal details of a system or component, such as some aspects of construction or materials. This provides a better understanding of how the system works, based on both experimental data and existing information about its design and fabrication.
- White-box reverse engineering for mechanical parts: this method provides access to all internal details of a system or component, such as construction, materials, and design parameters. The analysis is carried out with a complete understanding of the mechanical system, including geometry, materials, connection methods, etc. 3D scanning, photogrammetry or CMM techniques can be used to create detailed models of mechanical components.

The framework includes the following stages:

- determination of the goals and scope of reverse engineering,
- collection of information and data about mechanical parts,
- selection of reverse engineering methods and tools based on available information (Black-box, Gray-box, or White-box),
- conducting research, analysis, and modelling,
- obtaining results, interpretation, and validation,
- implementation of results for the improvement, modification, or creation of new mechanical parts.

Considering the framework of reverse engineering of mechanical parts, adapted from the methods of reverse engineering in IT (Black-box, Gray-box, and White-box), the main processes include data collection, analysis stages, modelling, and validation of results:

1. Data collection. At this stage, information is collected about a mechanical part or system. Depending on the selected reverse engineering method (Black-box, Gray-box, White-box), information on external characteristics, partial access to internal parts or full access to all components of the system can be collected.

2. Stages of analysis:
 - Black-box stage. Analysis of external behaviour of a mechanical part, study of its characteristics, ergonomics, and resistance to various influences, without access to detailed information about design and materials,
 - Grey-box stage. Analysis of the finer characteristics of a system in which internal and external aspects of mechanical parts are combined. It helps to learn more about the design, materials, manufacturing, and installation of the system,
 - White-box stage. Deep analysis of a mechanical system considering all components, such as construction, materials, connecting elements and algorithms of system operation.
3. Modelling: at this stage, algorithms and software are used to model the mechanical system. This process may include the generation of 3D models, stress calculations, heat transfer analysis, kinematics studies, etc.
4. Validation of results: the processed data and obtained models are subjected to validation to verify the correctness of the obtained results and to correct possible inaccuracies. This may include comparison with real properties of mechanical parts, control of dimensions, materials, compliance with technical standards, or comprehensive testing of model operation in real conditions.

Thus, the framework of reverse engineering of mechanical parts, adapted from the methods of reverse engineering in IT, provides a sequence of advanced methods and approaches, which makes it possible to analyse mechanical systems in different degrees of detail, to conduct modelling and validation of results considering the needs and available information about mechanical parts.

Results and Discussion

The mechanical parts reverse engineering framework, adapted from IT, can be applied in a variety of practical scenarios. These include:

- recreating lost or damaged components when original blueprints are unavailable,
- analysing competitor designs to understand their design methods, materials, and to identify strengths and weaknesses, aiming for self-improvement,
- creating product prototypes for testing and quality assurance before mass production,
- developing specialized equipment and tools based on existing ones for specific projects,
- identifying problems in the operation of mechanical parts and suggesting improvements for efficiency and reliability,
- use in academia and research for understanding fundamental principles and inspiring new ideas in design and manufacturing.

These practical scenarios demonstrate the broad spectrum of possibilities for the use of the reverse engineering framework for mechanical parts, adapted from IT reverse engineering methods. It assists manufacturers, engineers, and scientists in gaining a deeper understanding of how mechanical systems operate, leading to the development of efficient, reliable, and innovative products and solutions.

However, the usage of this framework does come with limitations that need to be addressed. These include:

- the lack of sufficient or high-quality source data can pose significant challenges. Efforts to recreate a mechanical part or system can prove burdensome if the necessary source data is inadequate,
- resource intensity is another hurdle. Not all reverse engineering methods are quick or efficient. System modelling or analysis can require substantial resources for research, analysis, and model formation,
- intellectual property issues can arise when reverse engineering someone else's mechanical parts. It's crucial to consider the potential patent or copyright issues, especially in a commercial context,
- finally, questions of accuracy can emerge. The precision of models derived from reverse engineering largely depends on the quality of the initial data and methods used in the analysis and modelling process. Low data quality or high representativeness can lead to potentially inaccurate or erroneous results, posing another challenge.

Conclusions

The adaptation of IT reverse engineering techniques to mechanical components can spur innovation across various industries. Black-box, Grey-box, and White-box methods can be utilized to analyse, model, and validate complex mechanical systems, potentially benefiting sectors like aerospace, automotive, and medical industries. These techniques offer varying levels of access to internal components, leading to improvements and optimization in design while contributing to increased efficiency.

The implementation of automated tools paves the way for the development of advanced methods of analysis, modelling, and validation. However, it's important to acknowledge the limitations and recognize the need for continuous improvement.

Research and applications can extend to new experimental methods, integration with other technological innovations such as augmented reality and thermography, and the exchange of knowledge among professionals. More effective validation methods and educational programs can contribute to an enhanced understanding and progression of mechanical design and manufacturing. These avenues have the potential to increase the efficiency of solutions across multiple fields and inspire novel ideas.

References

1. Várady T., Martin R.R., Cox J., 1997, *Reverse engineering of geometric models – an introduction*, Computer-Aided Design, 29(4), 255–268.
2. Raja V., Fernandes K.J., 2008, *Reverse Engineering: An Industrial Perspective*, Springer Science & Business Media, London.
3. Luna-Herrera Y.A., Pérez-Arriaga J.C., Ocharán-Hernández J.O. et al., 2023, *Comprehension of Computer Programs Through Reverse Engineering Approaches and Techniques: A Systematic Mapping Study*, in: *New Perspectives in Software Engineering. Proceedings of the 11th International Conference on Software Process Improvement CIMPS 2022*, eds. J. Mejia, M. Muñoz, A. Rocha et al., vol 576, Springer, Cham, 126–140.
4. Petrenko A., Schlingloff H., Ulrich A., 2005, *Black-box testing of communicating systems*, in: *5th International Conference on Application of Concurrency to System Design, St. Malo, France*, 164–173.
5. Constantinides C., Müller S., Wassermann B., 2019, *Hardware reverse engineering: Overview and open challenges*, in: *Proceedings of the ACM on International Symposium on Physical Design*, New York: ACM, 7–14.
6. Bertolino A., 2007, *Software Testing Research: Achievements, Challenges, Dreams*, in: *Proceedings of Future of Software Engineering (FOSE 07)*, Minneapolis, 23–25 May, 85–103.
7. Beizer B., 1995, *Black-Box Testing: Techniques for Functional Testing of Software and Systems*, John Wiley & Sons, Inc., Hoboken.
8. Cornélissen B., Zaidman A., van Deursen A., 2008, *A Controlled Experiment for Program Comprehension through Trace Visualization*, IEEE Transactions on Software Engineering, 34(3), 341–355.
9. Jhala R., Majumdar R., 2009, *Software model checking*, ACM Computing Surveys 41(4), Article 21, 1–54.
10. Beyer D., Podelski A., 2022, *Software Model Checking: 20 Years and Beyond*, in: *Principles of Systems Design. Essays Dedicated to Thomas A. Henzinger on the Occasion of His 60th Birthday*, eds. J.F. Raskin, K. Chatterjee, L. Doyen et al., Springer, Cham, 554–582.
11. Łukaszewicz A., Miatluk K., 2007, *The practical application of reverse engineering for object with free-form surfaces*, Machine Dynamics Problems, 31(3), 51–57.
12. Łukaszewicz A., Kernysky A., 2011, *Rapid prototyping in UAV applications on the example of 3D printing technique*, in: *XIX Polish-Ukrainian Conference on CAD in Machinery Design. Implementation and Educational Problems: CADMD'2011*, 29–30.
13. Helle R.H., Lemu H.G., 2021, *A case study on use of 3D scanning for reverse engineering and quality control*, Materials Today, 45(6), 5255–5262.
14. Givi M., Cournoyer L., Reain G. et al., 2019, *Performance evaluation of a portable 3D imaging system*, Precision Engineering, 59, 156–165.
15. Kartnik T.R.V., Reddy C.R., Yadiki G.K., 2016, *Design Analysis and Optimization of Disc Brake (Two Wheeler)*, International Journal of Advanced Technology and Innovative Research, 8(22), 4321–4328.
16. Wilkinson C., 2015, *Obsolescence and Life Cycle Management for Avionics*, U.S. Department of Transportation, Federal Aviation Administration, Washington, <https://www.tc.faa.gov/its/worldpac/techrpt/tc15-33.pdf> [accessed: 17.05.2024].
17. Rozesara M., Ghazinoori S., Manteghi M. et al., 2013, *A reverse engineering-based model for innovation process in complex product systems: Multiple case studies in the aviation industry*, Journal of Engineering and Technology Management, 69, 101765.
18. Fu P., 2008, *Reverse Engineering in the Automotive Industry*, in: *Reverse Engineering. Springer Series in Advanced Manufacturing*, eds. V. Raja, K. Fernandes, Springer, London, 141–155.

4.5. The use of artificial intelligence in teaching and learning CAx: perspectives and approaches

*Andriy Kernytsky¹, Anastasiia Kernytska², Uliana Marikutsa³,
Grzegorz Skorulski⁴, Myroslava Vovk⁵*

¹*Lviv Polytechnic National University, Institute of Computer Science and Information Technologies,
Department of Computer Aided-Design, andriy.b.kernytsky@lpnu.ua*

²*Lviv Polytechnic National University, Institute of Computer Science and Information Technologies,
Department of Information Systems and Networks, anastasiia.kernytska.sa.2022@lpnu.ua*

³*Lviv Polytechnic National University, Institute of Computer Science and Information Technologies,
Department of Computer Aided-Design, ulyana.b.marikutsa@lpnu.ua*

⁴*Bialystok University of Technology, Faculty of Mechanical Engineering,
Department of Materials and Production Engineering, g.skorulski@pb.edu.pl*

⁵*Lviv Polytechnic National University, Institute of Applied Mathematics and Fundamental Sciences,
Department of Mathematics, myroslava.i.vovk@lpnu.ua, a.lukaszewicz@pb.edu.pl*

Summary: In this article, the authors, who have among others extensive experience as educators in technical universities, explore the potential of applying Artificial Intelligence (AI), namely ChatGPT, in teaching and learning Automated Design Systems (CAx). The need to introduce AI into the learning process, as well as technologies that are already in use, has been identified and analysed. Various approaches to integrating AI into learning processes are discussed, along with challenges faced during this integration. The authors provide practical example and results demonstrating the success of AI implementation and an interesting application of integrating ChatGPT with PlantUML.

Keywords: AI, Education, CAx, CAD, ChatGPT, PlantUML

Introduction

In today's world, AI is increasingly influencing various aspects of life. One of the directions in which AI is actively used is CAx [1–3]. Given the complexity, interdisciplinary nature, and dynamics of the development of this field, traditional teaching methods may not meet the growing demands of the market and technological progress [4]. When studying CAx in technical universities, students and instructors are forced to spend a significant amount of time searching for the necessary information and do not always get the desired result. Therefore, there is a need to automate information collection processes and provide convenient access to information for users. Considering the huge volumes of data that are processed in information systems, the achievement of such goals is possible only with the use of AI technologies [5].

However, in the field of education, AI is in the initial stages of development. Therefore, it is important to consider the possibilities of integrating AI with the educational process of students' development to improve the quality of education, promote innovative solutions and better understand the problems and trends of the development of the industry [6].

The use of AI within the walls of technical universities opens many other new possibilities for improving the teaching and learning process based on the individual needs of each student. However, along with these opportunities come challenges that require attention and informed decisions. It is also important to understand that artificial intelligence cannot completely replace the teacher, but it can become a powerful tool for improving the quality of education and the development of learners [7].

Literature Review

The study [8] examined approaches to the use of artificial intelligence in virtual classrooms, as well as their advantages for improving the understanding of course participants. The study [5] evaluates the hypotheses of how students perceive the use of artificial intelligence programs in education, as well as how educational institutions are prepared for this and how society in general will react to the widespread introduction of artificial intelligence in education. It was shown [9, 10] that most artificial intelligence tools in education are dominated by chatbots. Artificial intelligence has the potential to be used for personalized, scalable, and affordable learning. The results [11] confirm the positive impact of artificial intelligence and computer science on the success of students, an increase in motivation to study was found. The diversity of the work of artificial intelligence and scientists who work directly on the problems of introducing artificial intelligence into various areas of society, as well as proposals for a wider practice of openness to the space of artificial intelligence, are explored in works [12–17].

Much of the potential of AI is revealed in the implementation of intelligent tutoring systems [18]. These systems support learning by focusing on individualized student training.

As for CAx, they are key to modelling various systems and devices [19, 20]. The use of AI opens new opportunities for optimizing design processes [1–3].

Instruction in CAx proves to be demanding, given that it frequently obliges students to comprehend intricate software interfaces and design methods. Notable hurdles encompass:

- maintaining student involvement,
- accommodating varying skill levels, and
- guaranteeing students comprehend the key principles before advancing to complex subjects.

Despite the great potential of using AI in the educational process, it is important to consider some limitations and possible risks. In particular, AI cannot completely replace traditional methods of learning and teaching, but only supplement and optimize them [8].

The following three key AI methodologies that are used for training at technical universities can be distinguished [4, 5]:

- intelligent tutoring systems using AI to support the learning process. They adapt to the needs and learning style of the student, providing personalized learning based on feedback and progress tracking,
- reinforcement learning has been used in simulators to teach students to work with complex hardware and software,
- using machine learning algorithms to analyse data about students and their performance can help identify weaknesses, suggest recommendations for improvement, or even single out groups of students for special support.

AI has already significantly influenced the teaching methodology in technical universities and continues to gain momentum. It is important to understand that the success of using AI depends on combining technologies with effective pedagogical strategies [8].

The results of studies [3–6, 11, 12] show that the use of artificial intelligence in education can be beneficial, but it is worth carefully examining its impact on learning and considering the risks and challenges it can create:

- lack of independence in the performance of work by students of education. AI makes it difficult for the teacher to understand whether the student himself wrote this work or AI,
- reducing the need for effort. For example, automatically checking the correctness of answers can reduce the need for the student to independently check tasks. In addition, artificial intelligence can provide students with recommendations and hints as they complete tasks, which can reduce their need to exert effort to solve problems,
- AI can lead to a change in communication between teachers and students, as well as between students. This can affect social interaction and the development of communication skills,
- the use of artificial intelligence can lead to dependence on technology and the loss of skills that can be useful in real life,
- GPT's chatbot models may provide incorrect or incorrect answers to questions, including those related to social issues or stereotypes.

Practical Examples and Results

Today, the most advanced chatbot with artificial intelligence developed by OpenAI is ChatGPT. It quickly gained the attention of a mass audience for its detailed and well-formed answers, although their factual accuracy was subject to considerable criticism.

Communication between a machine and a person using chat turned out to be convenient. Such a model allows us to explain to the machine what is required of it [9, 15].

The integration of ChatGPT as the most prominent AI tool in the educational sector marks a significant turning point. As this tool possesses the capability to grasp, generate, and efficiently communicate in human language, this allows it to undertake roles like a digital mentor, a teaching aide, a proofreader, and much more, which makes its applications and advantages limitless.

There are calculus examples of attempts to use ChatGPT with specific CAx systems. For example, ChatGPT is actively used for 3D Modelling using SketchUp systems. ChatGPT helps to solve problems, be a tutor and provide tips, validate design, suggest material and texture.

It can be also used with AutoCAD in several ways, such as design optimization, generative design, pattern recognition, automated drafting, quality control.

We want to provide practical examples and results demonstrating the success of AI implementation, such as intelligent tutoring systems, data analysis for feedback provision, and an interesting application of integrating ChatGPT with PlantUML.

The ChatGPT can be used by both instructors and students. Instructors can exploit these resources to conceptualize lesson plans, assignments, and projects that correspond with set learning objectives and curriculum norms. Furthermore, they can apply ChatGPT to create, and compile personalized educational content, including presentations, quizzes, worksheets, and several other resources custom-made to cater to their students' needs (Fig. 1).

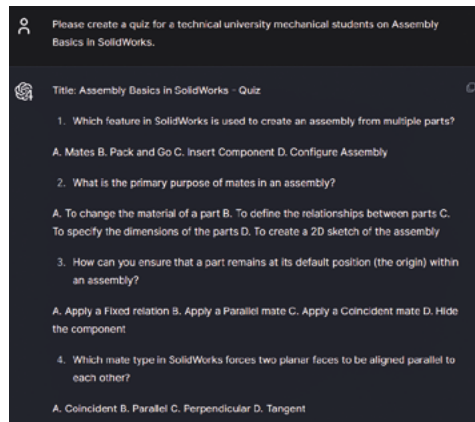


FIG. 1. For instructors – content creation

Instructors can also utilize ChatGPT by tapping into the AI's ability to aid in the formation, coordination, and structuring of course material in a sequential and effective way. ChatGPT can be instrumental in setting up course targets and goals, creating subject matter, structuring lessons, identifying and amassing relevant course resources and materials.

ChatGPT can enable students to retrieve precise and to-the-point data. For example, a Google search can yield countless results, making it a challenge for students to narrow down the focus of their original information requirements (Fig. 2).

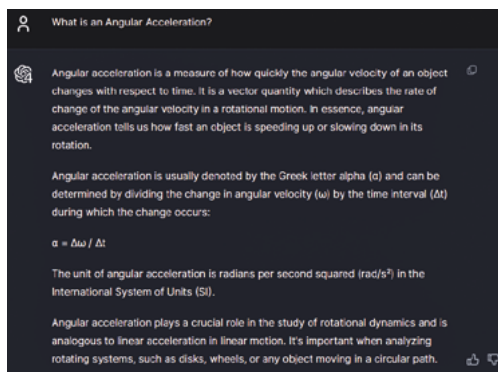


FIG. 2. For students – Google or Wikipedia Alternative

With ChatGPT, the feedback is perceptive and pointed, solving the minor hurdles that could impede learning progression. ChatGPT can aid students with homework, assignments, and learning struggles. Nevertheless, to tackle plagiarism and authenticity concerns, appropriate rules and strategies need to be set in place.

Incorporating ChatGPT for self-examination introduces a versatile, engaging, and personalized learning method (Fig. 3 and Fig. 4). This can supplement traditional teaching practices and enrich the overall learning experience. It offers active recollection, instant feedback, boosted engagement, enhanced confidence.

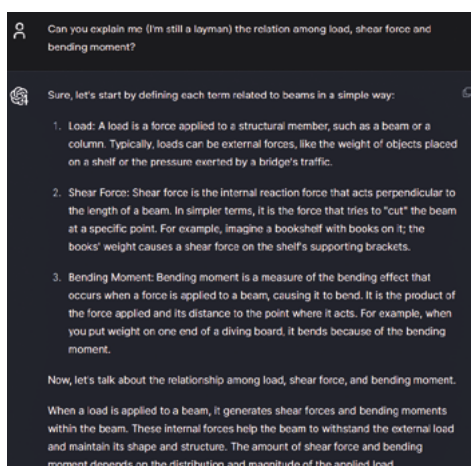


FIG. 3. For Students – Learning Companion

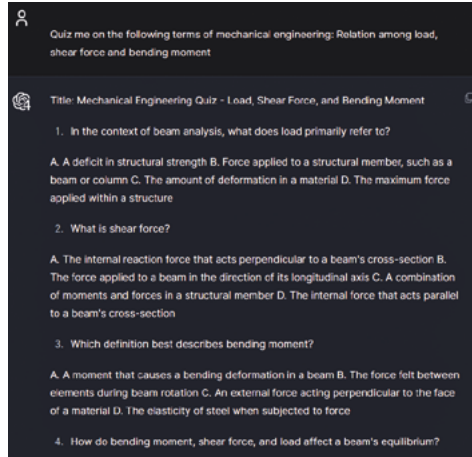


FIG. 4. For Students – Check the progress

ChatGPT can augment and fine-tune the method of research across a spectrum of academic initiatives, tasks, or personal ventures. It can lend a helping hand at various stages of research such as:

- selecting a subject,
- acquiring foundational knowledge on a topic,
- finding relevant resources,
- orchestrating the research,
- assisting in citing references.

However, ChatGPT may at times, offer incorrect or insufficient data, leading to potential misinterpretations or confusions among students and educators.

PlantUML is an open-source tool used to create UML (Unified Modeling Language) diagrams and has many benefits for CAX students. Here are some key benefits:

- PlantUML supports several types of UML diagrams, making it convenient to represent different aspects of a system. Class diagrams, sequence diagrams, activity diagrams, object diagrams, and component diagrams, all of these diagrams allow students to better understand and connect the different components of a CAX system,
- thanks to its simple textual description syntax, PlantUML makes creating UML diagrams simple, which makes learning easier,
- PlantUML can be easily integrated with many popular development platforms, making it easier to use in larger projects,
- thanks to the speed and ease of diagramming in PlantUML, students can increase their productivity by focusing on the main design issues rather than the time-consuming details of diagramming.

The Fig. 5. And Fig. 6 show the process of creating an activity diagram of the quadcopter reengineering process. ChatGPT is given a process description and asked to generate code to build a diagram in the PlantUML system.

```

1. Set up the 3D scanner.
2. Disassemble the quadcopter (if necessary) to scan individual parts.
3. Mount the disassembled parts to prepare for scanning.
4. Calibrate the 3D scanner.
5. If the scanner calibration is successful, proceed to the following steps.
   - While there are more parts to scan,
     - Scan one part and capture point cloud data.
     - If all required surfaces have been scanned, process the point cloud data.
     - Otherwise, adjust the scanner or part position and go back to scanning the part.
   - Align the scans.
   - Merge the scans.
     - If the scan quality is acceptable, save the resulting 3D model.
     - Otherwise, adjust the scanner settings, rescan the part, and go back to aligning and merging the scans.
   - Verify that all parts have been scanned.
   - Export the scanned data as a 3D model.
   - Import the 3D model into the computer-aided design (CAD) software.
6. If the scanner calibration is not successful, troubleshoot and recalibrate the scanner; then go back to the calibration step.

```

FIG. 5. Providing ChatGPT with the quadcopter reengineering process to generate the code for PlantUML

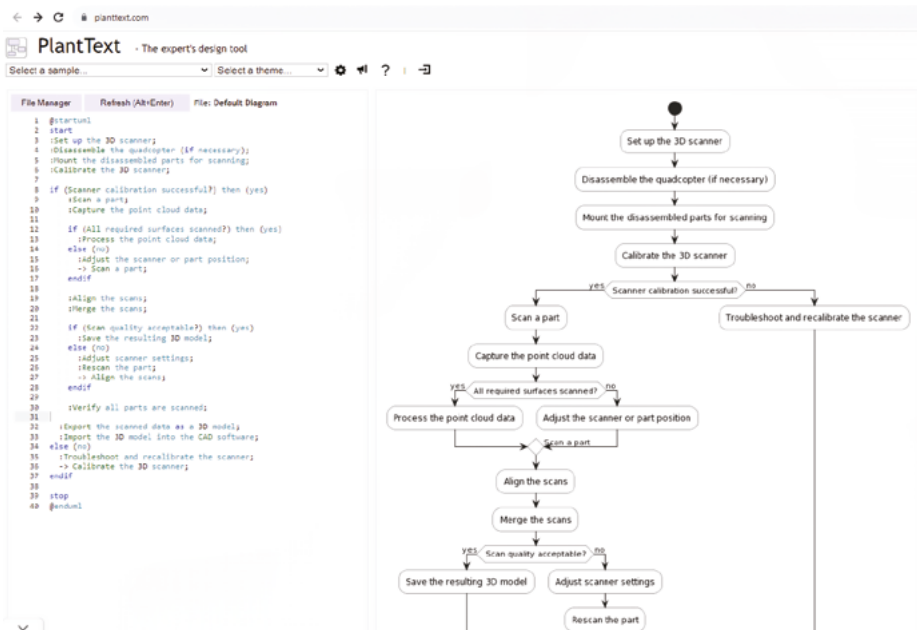


FIG. 6. Resulted diagram based on the code generated by ChatGPT

Instructors should utilize ChatGPT as a supplementary tool, not as a substitute for their professional expertise. Despite its high level of advancement, ChatGPT comes with its own limitations and was not explicitly designed for pedagogical purposes.

To extract maximum benefits from this tool, it's critical that both instructors and students be trained on its proper usage. While ChatGPT is straightforward to begin using, its comprehensive capabilities warrant additional training.

A known limitation of ChatGPT is its occasional propagation of erroneous information. Remembering that the tool is not flawless, it becomes key to ensure that all facts and data are duly double-checked.

To curb misuse, a firm code of conduct governing AI usage in the classroom should be laid out. These rules should be equally applicable to both students and teachers. And akin to any other technology, the process should be consistently monitored and fine-tuned, especially when working with a tool like ChatGPT, which offers countless ways to accomplish a task.

Conclusions and Perspectives

It is necessary to continue research in the field of application of artificial intelligence in education to find new opportunities for improving the educational process and increasing the effectiveness of learning. It is necessary to develop technologies that allow interaction with artificial intelligence in an intuitive and accessible way. For the successful implementation of artificial intelligence technologies in the educational environment, it is necessary to ensure interaction between technology developers, instructors, and students, as well as involve experts from various fields in this process, from CAX.

References

1. Hunde B.R., Woldeyohannes A.D., 2022, *Future prospects of computer-aided design (CAD) – A review from the perspective of artificial intelligence (AI), extended reality, and 3D printing*, Results in Engineering, 14, 100478.
2. Pokojski J., Szustakiewicz K., Woźnicki Ł. et al., 2022, *Industrial application of knowledge-based engineering in commercial CAD / CAE systems*, Journal of Industrial Information Integration, 25, 100255.
3. Madan A.K., Kharbanda P., Yadav P. et al., 2023, *AI and Machine Learning Uses in CAD/CAM*, International Journal of Research Publication and Reviews, 4(4), 4397–4401.
4. Holmes W., Bialik M., Fadel C., 2019, *Artificial Intelligence in Education. Promise and Implications for Teaching and Learning*, Center for Curriculum Redesign, Boston.
5. Alhumaid K., Naqbi S., ElSORI D. et al., 2023, *The adoption of artificial intelligence applications in education*, International Journal of Data and Network Science, 7(1), 457–466.
6. David R.S., 2023, *The convergence of AI, design-based research, and the learning sciences: A potential journey marking AI's integration into the academy*, i-manager's Journal of Educational Technology, 20(3), 1.
7. Ruiz-Rojas L.I., Acosta-Vargas P., De-Moreta-Llovet J. et al., 2023, *Empowering Education with Generative Artificial Intelligence Tools: Approach with an Instructional Design Matrix*, Sustainability, 15(15), 11524.

8. Khan M., Lulwani M., 2023, *Inspiration of Artificial Intelligence in Adult Education: A Narrative Overview*, OSF Preprints.
9. Hwang G.J., Chang C.I., 2023, *A review of opportunities and challenges of chatbots in education*, *Interactive Learning Environments*, 31(7), 4099–4112.
10. Georgescu A.A., 2018, *Chatbots for Education – Trends, Benefits and Challenges*, Conference proceedings of eLearning and Software for Education (eLSE), 2, 195–200.
11. García-Martínez I., Fernández-Batanero J.M., Fernández-Cerero J. et al., 2023, *Analysing the Impact of Artificial Intelligence and Computational Sciences on Student Performance: Systematic Review and Meta-analysis*, *Journal of New Approaches in Educational Research*, 12(1), 171–197.
12. Kikerpill K., Siibak A., 2023, *AI in schools and universities: mapping central debates through enthusiasms and concerns*, in: *Research Handbook on Artificial Intelligence and Communication*, ed. N. Seungahn, Edward Elgar Publishing, 94–107.
13. Piercey D., 2023, *50 Strategies for Integrating AI into the Classroom ebook*, Shell Education.
14. Tadesse A., 2023, *AI for Teachers: An Educator's Guide to Using Artificial Intelligence in 2024*.
15. NeoMind Ascend, 2023, *ChatGPT Revolutionary Teacher: The Ultimate Guide for Fast, AI-Powered Learning*.
16. Baker R., Siemens G., 2014, *Educational data mining and learning analytics*, in: *The Cambridge Handbook of the Learning Sciences*, ed. R.K. Sawyer, Cambridge University Press, 253–272.
17. Sabourin J.L., Shores L.R., Mott B.W. et al., 2013, *Understanding and Predicting Student Self-Regulated Learning Strategies in Game-Based Learning Environments*, *International Journal of Artificial Intelligence in Education*, 23, 94–114.
18. Aleven V., Roll I., McLaren B.M. et al., 2016, *Help helps, but only so much: Research on help seeking with intelligent tutoring systems*, *International Journal of Artificial Intelligence in Education* 26(1), 1–19.
19. Ullman D.G., 2017, *The Mechanical Design Process*, David Ullman LLC.
20. Ulrich K.T., Eppinger S.D., Yang M.C., 2020, *Product Design and Development*, 7th ed., McGraw Hill Education.

4.6. Application of 3-D simulation in the educational process for designing the manipulator of a robotic mobile platform

Vitaliy Mazur¹, Kostyantyn Kolesnyk², Sofia Panchak²

¹*Lviv Polytechnic National University, CAD Department, Vitaliy.V.Mazur@lpnu.ua*

²*Lviv Polytechnic National University, CAD Department*

Summary: The experience of using computer-aided design and 3-D simulation tools in the development of a manipulator for a robotic mobile platform in the educational process is presented. Using Autodesk Inventor, design documentation was prepared and a G-code file was created for the manufacture of manipulator details on a 3-D printer. To reproduce the dynamics of the manipulator's functioning, a 3-D simulation was carried out using Matlab Simulink. Simplified models for conducting preliminary engineering calculations of the manipulator construction are proposed.

Keywords: robotic mobile platform; manipulator; computer-aided design; 3-D simulation; educational process

Introduction

Today, robotic mobile platforms (RMP) are widely used to automate the processes of moving cargos in industrial systems and in warehouses. For the unification of loading/unloading operations of small parts, bulk materials and liquids, it is advisable to use standardized containers. For this, RMPs must be equipped with a manipulator and a working surface for placing these containers during their movement. As a result of previous studies, an experimental model of RMP was developed for movement along orthogonal routes [1].

In modern robotics, the use of universal rather than specialized manipulators for equipping robotic mobile platforms is often practiced [2]. This can lead to an increase in the dimensions, weight and energy consumption of the RMP [3, 4]. In addition, the use of manipulators with a large number of freedom degrees to perform primitive operations of loading/unloading containers complicates the control system and increases its cost [5, 6]. The insufficient area of the working surface of the RMP limits the number of containers that can be moved by the mobile platform at the same time [7, 8]. The asymmetric placement of the manipulator relative to the center of the working surface of the RMP [9] does not ensure unification

of container loading/unloading operations for the four sides of the platform, which is necessary when the platform moves along orthogonal routes. The use of two lanes for the simultaneous movement of several mobile platforms with non-orthogonal routes leads to an increase in the area of warehouse space and its inefficient use. All this determines the need to develop a specialized cylindrical manipulator to minimize the area when it is placed in the center of the working surface and ensure symmetrical access for all sides of the RMP during loading/unloading operations. The need to improve the skills of practical application of automated design and 3-D simulation in the educational process also determines the relevance of this work.

The purpose of the work is to develop the construction of the manipulator for the RMP with the use of automated design and 3-D simulation tools for the preparation of technical documentation and verification of the correctness of the adopted design decisions.

Manipulator Design Using the Autodesk Inventor System

The developed original construction of the cylindrical manipulator [10] is presented in Fig. 1. The central axis of the manipulator with the help of an azimuth stepper motor (ASM) provides rotation of the horizontal traverse within $\pm 180^\circ$ with an accuracy of 0.9° . A stepper motor on the traverse with the help of a worm gear and a retractable part changes the length of the traverse within $8\div 17$ cm from the central axis. A vertical rod at the end of the retractable part of the traverse is moved up and down by a servo motor (SM) and provides movement of an electromagnet (EM) to capture/release containers that are in nests on the working space of the manipulator. Based on the known coordinates of the nests centers, the number of stepper motors steps is determined to establish the necessary angle of rotation of the traverse and its length in polar coordinates.

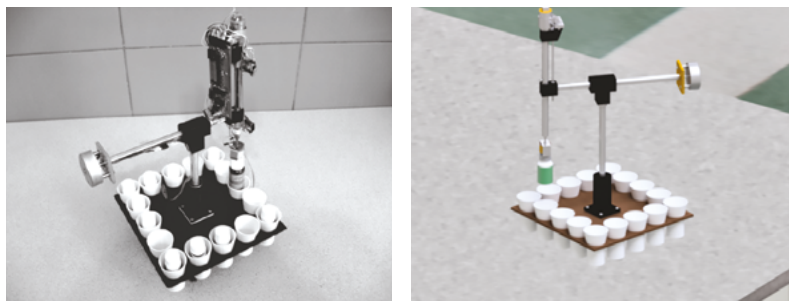


FIG. 1. The photo of the manipulator and its realistic image built in Autodesk Inventor

A computer model of the manipulator was developed in the Autodesk Inventor system. To simplify the model, the small components of the manipulator were combined into single bodies-parts, which formed the Assemble unit. The construction tree of the assembly unit is shown in Fig. 2.

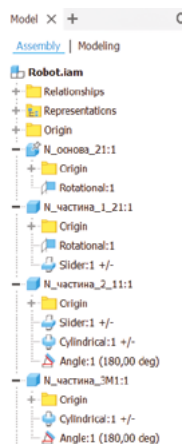


FIG. 2. Construction tree of the manipulator assembly unit

As shown in the construction tree, connections and dependencies have been established between all parts of the assembly unit. The following types of connections are used: rotary, cylindrical, sliding. Each type of connection completely determines the location and nature of movement of the selected components.

On the basis of the built model, design documentation was developed using Autodesk Inventor tools – drawings of individual parts and assembly drawings (Fig. 3).

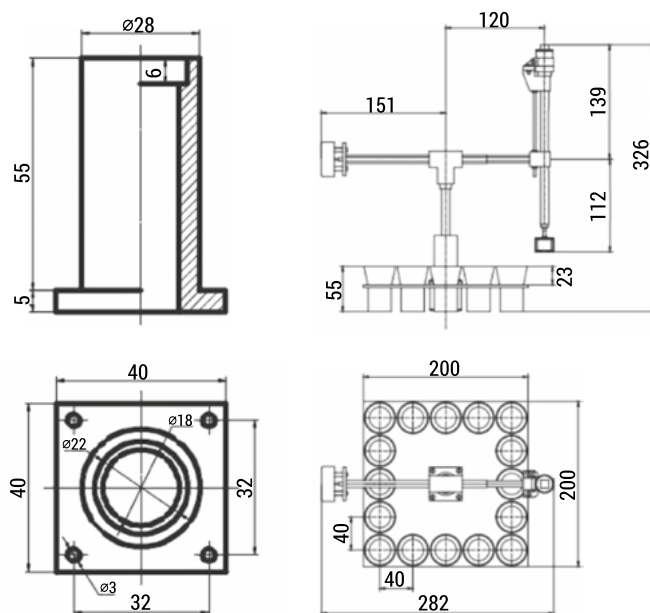


FIG. 3. Flange drawing and assembly drawing of the manipulator

To build a realistic image, the model of the manipulator was supplemented with models of containers and their nests. The resulting realistic image of the manipulator after rendering is presented in Fig. 1.

Drawings and 3-D models of manipulator parts were obtained using Autodesk Inventor tools. To manufacture these parts on a 3-D printer, the control files with G-code were obtained using the FlashPrint program. The drawing and a fragment of the G-code for the manufacture of the container nest are presented in Fig. 4.

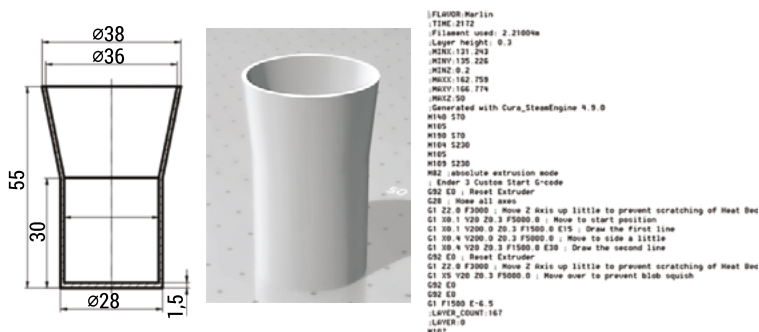


FIG. 4. Drawing and fragment of the G-code for the manufacture of a container nest on a 3-D printer

3-D Simulation Using Matlab Simulink

For exporting assembly models to Simscape Multibody, a special Simscape Multibody Link plugin was used, which was installed in the Autodesk Inventor system. This plugin presents an assembly model in Autodesk Inventor as an XML file and body geometry files that can later be converted to Simscape Multibody models using the smimport function. At the same time, the XML file is converted to a MATLAB Simulink file with the slx extension.

The graphic representation of the exported manipulator model in the MATLAB Simulink environment is shown in Fig. 5.

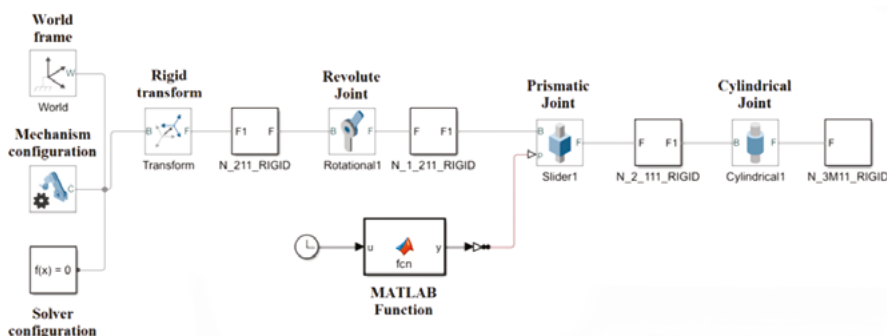


FIG. 6. Manipulator model in the MATLAB Simulink environment

The manipulator model in the MATLAB Simulink environment consists of the following blocks:

- World frame – provides access to the world or terrestrial coordinate system, as a unique fixed orthogonal coordinate system predefined in any mechanical model.
- Mechanism configuration – specifies the gravity and simulation parameters of the mechanism to which the block connects.
- Solver configuration – defines the parameters of the solver for use in modeling.
- Rigid transform – defines a fixed 3-D rigid transformation between two blocks. The two components independently determine the translational and rotational parts of the transformation.

The connection block models and their properties in the MATLAB Simulink are shown in Fig. 7.



FIG. 7. Description of connection block models and their properties in the MATLAB Simulink

- Revolution Joint – a rotary joint acting between two blocks. This joint has one rotational degree of freedom, represented by one rotary element.
- Prismatic Joint – a prismatic joint between two blocks. This joint has one translational degree of freedom represented by one prismatic element.
- Cylindrical Joint – a cylindrical connection of two blocks. This joint has one translational and one rotational degree of freedom, represented by one rotary element and one prismatic element, coinciding along one axis.

The model presents four subsystems with blocks of outputs and connections, which correspond to four separated parts of the manipulator (Fig. 8).

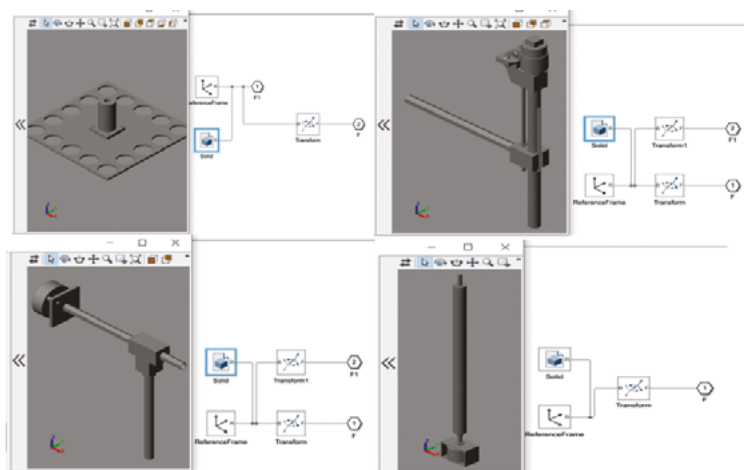


FIG. 8. Subsystems of separated parts of the manipulator

To simulate the dynamics of the manipulator's functioning, a clock block and a MATLAB block are added, which describes the function with an equation according to which the movement is carried out.

For the built model, simulation of the manipulator functioning in dynamics was carried out. The simulation results are presented in the form of a 9-second video (Fig. 9).

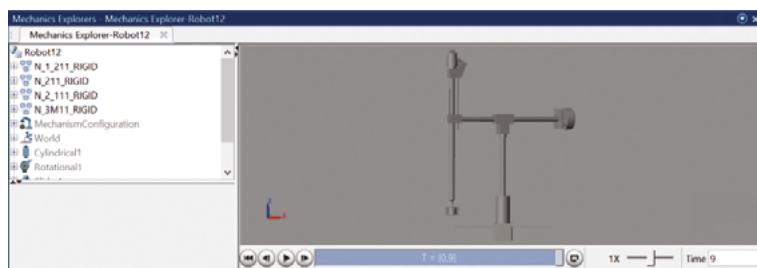


FIG. 9. The result of the simulation of the manipulator functioning in dynamics

The paper proposes simplified manipulator models for preliminary engineering calculations. These models do not take into account the mass of the thin-walled tubes of the traverse and its moving part, as well as the geometric dimensions of the stepper motor on the traverse and the vertical rod with servo drive, electromagnet and container, which are presented by the point masses. Such simplifications are permissible, taking into account the purpose of the specified models.

Since the rod with the container can extend beyond the perimeter of the platform (Fig. 10), the resistance of the mobile platform to overturning under the weight of the container is determined by the following ratios

$$m_2 = m_c + m_s \quad (1)$$

$$F = g \cdot (m_2 \cdot L_2 - m_1 \cdot L_1) / L_2 \quad (2)$$

$$P \cdot L > F \cdot (L_2 - L) \quad (3)$$

Where: m_1 is the mass of a stepper motor on the traverse; m_c is the mass of the container; m_s is the total mass of the rod with a servo motor and an electromagnet; L_1 is the distance from the vertical axis of rotation to the center of mass of the stepper motor on the traverse; L_2 is the distance from the vertical axis of rotation to the point of attachment of the vertical rod (8 L2 17 cm); L is the distance from the vertical axis of rotation to the support point Q, which located on the perimeter connecting the wheels of the mobile platform; F is the reduced overturning force; P is the total weight of the mobile platform with the manipulator.

With a limited value of L_2 and a significantly greater total weight P compared to the weight of the rod with the container, the stability of the mobile platform is ensured.

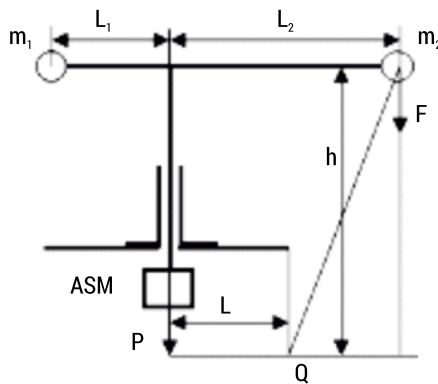


FIG. 10. A model for determining the stability of the RMP with a manipulator against overturning

The following model provides the determining of the allowable angular acceleration to avoid skipping the steps of the azimuth stepper motor (Fig. 11).

The permissible angular acceleration a of the azimuth stepper motor with a given moment M_m is determined as follows

$$a \cdot M_m / (m_1 L_1^2 + m_2 L_2^2) \quad (4)$$

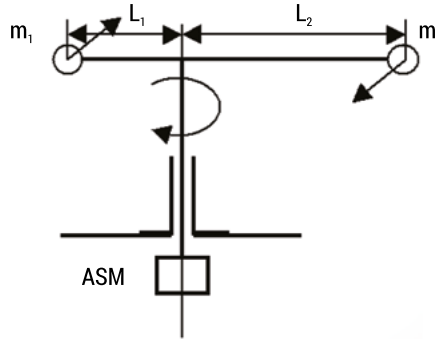


FIG. 11. A model for determining the permissible angular acceleration of ASM

Limitation of the angular acceleration value is ensured by a smooth change in the speed of the stepper motor. To increase the value of M_m , it is advisable to use a stepper motor with a worm gear.

In order to avoid the displacement of the container C from the poles of the electromagnet EM (Fig. 12) due to the action of the centrifugal force F_c at the attraction force of the electromagnet F_a and at angular speed of rotation of the traverse w , such condition must be fulfilled

$$m_c L_2 w^2 < (F_a - m_c g) k \quad (5)$$

Where: k is the coefficient of rest friction for an iron/iron couple.

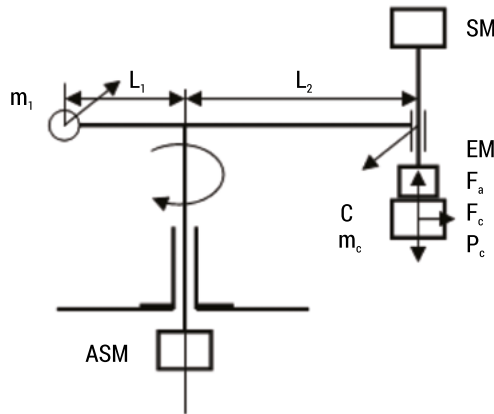


FIG. 12. Displacement of the container from the poles of the electromagnet due to centrifugal force

Conclusions

The following scientific and practical results were obtained in the work:

1. The construction of a cylindrical manipulator for a robotic mobile platform has been developed that ensures accurate positioning and loading/unloading of standardized containers during their movement in the storage system.
2. The integrated use of automated design tools, 3-D simulation and 3-D printing for the preparation of construction documentation and the manufacturing of manipulator details ensures students' practical mastery of CAD/CAM systems in the educational process.
3. The simplified models for engineering calculations of the manipulator construction are proposed.

References

1. Mazur V., Panchak S., 2021, *Experimental model of a mobile platform for moving on orthogonal routes*, CAD in Machinery Design: Implementation and Educational Issues (CADMD 2020), IOP Conf. Series: Materials Science and Engineering, 1016, 012011, 1–8. DOI: 10.1088/1757-899X/1016/1/ 012011, <https://iopscience.iop.org/article/10.1088/1757-899X/1016/1/012011/pdf>.
2. KUKA Arc Welding Robots, <https://www.kuka.com/en-us/industries/metal-industry/arc-welding/kuka-arc-welding-robots/> [accessed: 17.05.2024].
3. AgileX Bundle Mobile Manipulator + Bunker Chassis, <https://www.ground.ghostysky.com/en/product/agile%C2%B7x-mobile-manipulator/> [accessed: 17.05.2024].
4. KMR iiwa, <https://www.kuka.com/en-us/products/mobility/mobile-robot-systems/kmr-iiwa> [accessed: 17.05.2024].
5. ER-FLEX Mobile Cobot, <https://www.rarukautomation.com/mobile-robots/er-flex/> [accessed: 17.05.2024].
6. Waypoint Robotics partners with Productive Robotics to build mobile manipulation robot, <https://roboticsandautomationnews.com/2021/04/22/waypoint-robotics-partners-with-productive-robotics-to-build-mobile-manipulation-robot/42622> [accessed: 17.05.2024].
7. RB-VOGUI+, <https://robotnik.eu/products/mobile-robots/rb-vogui-en/#more-versions> [accessed: 17.05.2024].
8. Mobile Manipulator MMO-500, <https://www.neobotix-robots.com/products/mobile-manipulators/mobile-manipulator-mmo-500> [accessed: 17.05.2024].
9. Mobile Collaborative Robot, <https://www.desmasa.com/en/mobile-collaborative-robot/> [accessed: 17.05.2024].
10. Mazur V., Panchak S., 2023, *Control System of Mobile Platform Manipulator*, 17th International Conference on the Experience of Designing and Application of CAD Systems, IEEE, 1–4. DOI: 10.1109/CADSM58174.2023, <https://ieeexplore.ieee.org/xpl/conhome/10076488/proceeding>.

4.7. Educational aspects of designing a low-energy electromagnetic field generating system

Krzysztof Pytel¹, Wiktor Hudy², Andriy Zdobytskyi³, Henryk Noga²

¹*AGH University of Science and Technology,*

Faculty of Mechanical Engineering and Robotics, krzysztof.pytel@agh.edu.pl

²*University of the National Education Commission, Institute of Technical Science*

³*Lviv Polytechnic National University, Department of Computer Design Systems*

Summary: The contemporary development of electronic technologies presents us with ever-increasing challenges in the field of electronic system design and construction. One of the areas that is gaining importance is the creation of systems that generate low-energy electromagnetic fields. Such systems find applications in various fields, from industry to medicine, and serve as a crucial educational tool for future engineers and scientists. This publication focuses on the educational aspects of designing and building such systems while emphasizing the need for further research into their effectiveness and the impact of modifications on performance and safety. This publication serves as an introduction to the topic of designing low-energy electromagnetic systems, and the educational aspects of this subject are significant in the context of modern technology development. The final assessment of the effectiveness and safety of such systems remains open to further research and experiments that can contribute to further progress in this field.

Keywords: Engineering Education, Electromagnetic Field, Arduino

Introduction

In the face of dynamic technological advancements, education has become a crucial area of research. Electromagnetism, one of the fundamental branches of physics, deals with the study of the relationship between electric fields and magnetic fields, as well as their mutual interactions. In education, understanding the theoretical foundations of electromagnetism is essential to develop the scientific and technical competencies of students [1].

The theoretical foundations of electromagnetism, necessary for understanding the processes of generating electromagnetic fields, encompass basic laws and relationships related to electricity and magnetism. Important topics include the laws of Ampère, Faraday, Lenz, Gauss, Coulomb, and Biot-Savart. Understanding these laws and relationships allows for the analysis and design of electromagnetic systems,

including low-energy electromagnetic systems. The practical application of these theoretical principles is crucial for electrical engineers, physicists, and designers from other fields collaborating on diverse electrical and electronic systems [2].

The implementation of the project required familiarizing the student with concepts and phenomena that have a decisive impact on the functioning of the designed system to generate low-energy electromagnetic fields. It is essential to introduce concepts and phenomena relevant to the project, namely: electromagnetic induction, resistance, Gauss law, and methods for measuring kinetic energy. In the educational project, which involves generating a low-energy electromagnetic field, moving ferromagnetic sleeves are used. These sleeves are made of materials with strong magnetic properties such as nickel, iron, and cobalt. The measurement of the energy of the moving element in the electromagnetic field will involve determining the amount of energy that the object carries when connected to the power supply. LEDs can be used for measurement; they will measure the time it takes for the moving object to pass between two sensors. On the basis of this time and the mass of the object, its velocity and kinetic energy can be calculated. It was assumed that the designed electromagnetic system, serving as an educational model, will have a kinetic energy below 17J for safety reasons [3].

The publication focused on the educational aspects of designing low-energy electromagnetic field generation systems, as the topic is crucial in the context of educating future engineers who will be working on various projects, including electromagnetic technologies. The publication presented the design and implementation of a low-energy electromagnetic field generation system in the context of educational applications, aiming to identify issues related to the design of such systems and to present practical applications in the teaching process.

Possibilities of using low-energy electromagnetic field generation systems in educational experiments

Contemporary methods of generating low-energy electromagnetic fields, such as electromagnetic induction, thermoelectromagnetic generation, and thermoelectric semiconductors, are analyzed for their advantages and limitations. Educational efforts require various approaches, including content personalization, interactive laboratories, and adjusting the pace of learning to effectively transfer knowledge from teachers to students. Low-energy electromagnetic field generation systems find practical applications in electromagnetism experiments, in analyzing the efficiency of wireless energy transfer, and as alternative power sources for electronic devices, enabling a practical understanding of electromagnetic concepts in a scientific educational context. These methods not only engage students but also support the development of their technical and scientific skills [4].

The selection of educational projects is a crucial element in today's education landscape, where technologies are becoming increasingly prevalent. Selection aims to ensure effective learning and engaging teaching processes. It is important to implement practical projects in a way that allows adaptation to individual student needs.

This may involve content personalization, adjusting the pace of learning, and accommodating different learning styles. Educational projects allow students to experiment and apply knowledge in a controlled environment. This can include virtual experiments, simulations, and real-life experiments. The educational initiatives aim to help students in developing technical skills and problem solving abilities. Laboratories equipped with real-world elements for learning technologies enable students to acquire practical technical skills [5].

Adapting educational projects to students' needs and modern technology is possible thanks to digital technologies, access to software, and computer hardware. The practical aspects of designing educational systems require an integrated approach that takes into account both the students' pedagogical needs and the available technologies and students' knowledge. As technologies and tools for learning become more advanced and accessible, they enable the transformation of standard lessons into effective educational environments that facilitate essential teaching activities not only efficiently but also in a way that enhances skills, enriches knowledge, and nurtures students' interests. These environments provide solid foundations for their future professional development [6].

Low-energy electromagnetic field generation systems can be applied in education. They find practical use in teaching, experiments, and projects because projects related to the utilization of electromagnetism involve designing and conducting experiments. In these applications, small devices that generate low-energy electromagnetic fields are used. The impact of changes in the coil winding count on electromotive force can be studied using a simple design with low-voltage sources. Practical experiments with these systems enable understanding the relationship between technical parameters and the performance of electromagnetic systems. Other experiments in the field of electrical engineering can explore the application of low-energy electromagnetic fields to analyze various methods of enhancing energy transmission efficiency through electromagnetic fields, applicable in wireless energy transmission. Experiments may include projects of low-energy electromagnetic field generation systems serving as alternative power sources for small electronic devices such as sensors, microcontrollers, or small sensors. Such systems can be used in environmental monitoring systems or in smart homes. Educational projects related to electromagnetism involve participants in practical experiences. Low-energy generation systems allow safe experimentation to comprehend abstract electromagnetic concepts in practice. Practical applications of low-energy electromagnetic field generation systems not only engage, but also aid in developing technical and scientific skills [5].

Educational project allowing exploration of low-energy electromagnetic field generation systems applications

In today's dynamic technological environment, there is a growing demand for designing and building various electronic systems. In response to these needs, an educational project has been prepared. The goal of this project is to design and build a launcher

capable of generating an electromagnetic field that gives moving objects the appropriate speed of motion. Starting from the concept through the design and construction of the electromagnetic system, all the way to measuring the speed of moving objects, this educational project sheds light on the complexity and possibilities of such technology. The final results and conclusions from this analysis contribute to deepening the student's knowledge of electromagnetism and open new avenues for application in future engineering projects. Executing such an educational project transcends theoretical boundaries, becoming a practical tool for experiments and demonstrations in the realm of electromagnetism [5].

The fundamental components of the designed system include the launch tube, coils, capacitors, and other elements. During the experiments, a specially designed electromagnetic system with four prepared coils will be employed. The tube moving the object passes through the center of these coils and acts as an insulator, as it lacks magnetic properties. The diameter of our tube is marginally larger than the diameter of the moving object we used in the experiments. The number of turns on these coils, along with other parameters like coil thickness and length, will influence the initial speed of the moving object. This project not only helped us grasp the concept of electromagnetism, but also opened avenues for the student to explore in this field. It aligns with the evolution of technical education and shows how deeply theoretical knowledge can be applied in practice. The noteworthy aspect of the experiment was the determination of the time impulses considering the distance between individual coils. Under the influence of the current flowing through the coils, a magnetic flux was induced in them, causing the coils to behave like magnets. When a ferromagnetic or metal object was placed near a coil through which an electric current was passing, it was attracted by the coil. When the power supply was connected, the metal core of the propelled object accelerated towards the center of the coil. However, when it reached the center of the coil, its movement stopped. The inertia of the propelled object led to an attempt to push it out, but the magnetic field created inside the coil prevented it from leaving the coil area. As a result, the propelled object began to oscillate, as if it were attached to a spring, until it finally came to a stop inside the coil. This phenomenon is significant from the perspective of magnetism and kinematics physics, and its application can be diverse in various fields of science and technology, such as electromagnetic particle accelerators or unmanned aerial vehicle systems [3].

The experiment involved designing and building an electromagnetic launcher with a maximum energy of 17 kJ for educational purposes. The primary goal of the project was to develop a system with suitable equipment and software that would enable the device to operate in a manner to verify whether the propelled object would achieve maximum momentum and leave the launcher [4].

The first issue was to analyze the impact of various factors on the magnetic gap between the coil and the propelled object. The size of this gap was determined by several components, such as the thickness of the accelerating tube's wall, the loose placement of the coil within the tube, the thickness of the coil's spool (the coil's structural element), and the required distance between the propelled object and the internal

diameter of the accelerating tube, enabling the propelled object to pass through freely. The second important aspect was the use of a tool to monitor the movement of the object through successive coils. Inductive sensors were employed, which, due to their construction, had some delay in their operation. An alternative could have been the use of phototransistors, characterized by their quick reaction time, eliminating delays. The third aspect involved the selection of capacitors for the circuit. The capacitors used needed to have a high capacity to store electrical charge. Connecting capacitors in series could lead to increased voltage, while connecting them in parallel could increase capacitance and the duration of the pulse. Properly matching the capacitor connection was crucial in providing the appropriate electromagnetic impulse [2].

The designed system consists of several components necessary for conducting the experiment. The following elements will be required to build the electromagnetic launcher:

- coil (total length: 25 mm, inner hole diameter: 11 mm, wound with six layers of copper wire with a diameter of 0.4 mm in 54 turns per layer, resulting in approximately 324 turns per coil),
- resistor (passive element of an electrical circuit used to limit the current flowing through it). It is a linear element: the voltage drop across it is directly proportional to the current flowing through the resistor. When current flows through it, it converts electrical energy into heat.),
- accelerating object (neodymium magnet with dimensions: 20 mm length, 6.0 mm diameter, and a mass of 4.0 g, characterized by a strong magnetic field relative to its size and mass, as well as being durable and corrosion-resistant),
- capacitor (capacity: 470 μ F, storing the energy necessary to accelerate the object),
- accelerating object sleeve (made of nonmagnetic material – acrylic sheet with internal diameter of 7.00 mm and external diameter of 10.00 mm, nonconductive material, made of plastic to prevent energy loss in eddy currents during the activation of the magnetic field. The sleeve wall is thin, allowing minimal distance between the internal diameter of the coil and the external diameter of the accelerated object),
- universal board serving as a base, on which control and power elements are mounted. It includes a NANO V3 16MHz USB Type-C module – ATmega328P – CH340, which is responsible for controlling the operation of the entire system. The power and control circuits are also located on the board,
- semiconductor driver or another type of switch that triggers the discharge of the capacitor through the coil and accelerates the object.

The electromechanical system characterized by low energy demands necessitates a meticulously engineered coil (Figure 1) designed to generate a suitable magnetic field conducive to the acceleration of the object. The coil has been meticulously fabricated from wound copper wire upon a custom spool, fashioned through additive manufacturing with a 3D printer. The configuration comprises four spools, each having

an inner hole diameter of 11 mm and a length of 25 mm, thereby ensuring the requisite quantity of wire turns with the appropriate thickness. The additive manufacturing process has produced components of exceptional precision crucial to the success of the project [1].

The manufactured coils were connected in series and the power supply to the system is provided by a 9 V battery. A key component in the designed electromagnetic device is the universal board that facilitates the easy connection of various elements, including modules, sensors, and controllers. This board allows for the creation of personalized electronic circuits. The Hall sensor module (KY-003) has been employed for magnetic field detection. The Hall sensor operates on the Hall effect, where a magnetic field applied to a semiconductor causes the deflection of electrons under the influence of electromagnetic forces. This phenomenon leads to the creation of a potential difference in the semiconductor, which can be measured and utilized for magnetic field detection [2].

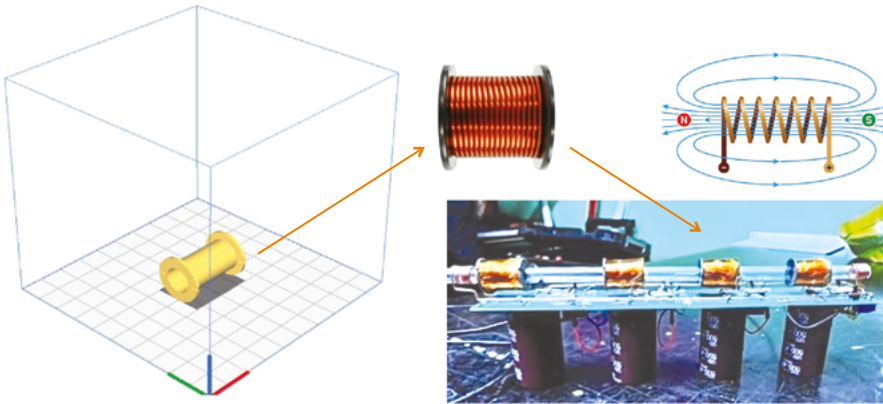


FIG. 1. The 3D printing project, wound coil, and system to generate a low-power electromagnetic field

In the electromagnetic system, the Hall sensor module is utilized to detect the passage of an object moving at a certain speed through the electromagnetic coil. When the neodymium magnet moves through the coil, it generates a magnetic field detected by the Hall sensor. Subsequently, this signal is transmitted to the microcontroller, which deactivates the electromagnetic coil, ensuring the proper functioning of the device. The Hall sensor module is connected to the microcontroller using three pins: power, ground, and output signal. The output signal from the Hall sensor changes its logical state upon detection of the magnetic field. This is a switching signal that can be read by the microcontroller as a digital signal. The application of the Hall sensor module in the electromagnetic system allows for the precise detection of the passage of a moving object through the electromagnetic coil, enabling the measurement of its energy [1].

The operation principle of the system involves generating a homogeneous magnetic field inside the coil, with field lines curving at the ends of the coil, resembling the shape of magnetic field lines around a permanent magnet. This generated magnetic field accelerates a mass, for example, 5.0 g, bringing it to a specific velocity. Applying a direct current voltage to the electromagnetic coil windings causes an object made of ferromagnetic material, placed on one side of the coil, to be attracted into the coil's interior through magnetic induction. The force acting on the projectile is proportional to the change in coil inductance and always acts in the direction of increasing the coil inductance [6].

The acceleration of the accelerated object can be increased by sequentially activating multiple coils, which is one way to enhance the system's efficiency, especially by modulating their actions. In a multi-coil electromagnetic system, the sequential activation of these coils depends on the position and instantaneous velocity of the accelerated object. Therefore, each coil has a different operating time. The coil stores electrical energy, which is then transformed into magnetic energy. The resulting magnetic field causes the accelerated object to rapidly be drawn into the coil area, where it accelerates sharply.

In an case of the electromagnetic system, the applied neodymium magnet moves inside a tube under the influence of the magnetic field. Utilizing the strong magnetic field of the magnet enables the necessary force and velocity for the accelerated object, which is the main goal of the project. Analyzing the phenomenon using basic equations of classical mechanics allows obtaining theoretical values based on experimental results.

As part of the project, an Arduino NANO module was employed, serving as a baseboard with the ATmega328 microcontroller. This board is equipped with 14 digital inputs/outputs and features a mini USB connector and a power socket. The Arduino module, which functions as the microcontroller, was utilized for precise control of the current flowing through the coils. These coils were tasked with generating an appropriate magnetic field to accelerate the moving object. In the experiment conducted, an electromagnetic system was constructed using four coils. A tube passing through the center of these coils was made from a nonmagnetic material, serving as an insulator. The diameter of the tube was slightly larger than the diameter of the moving object used for testing.

Parameters such as the number of coils wound around the barrel, the number of turns, the thickness, and the length of the coils significantly influence the initial velocity of the projectile. It is also crucial to consider the temporal impulses related to the distance between individual coils. Under the influence of the current flowing through the coil, a magnetic flux was induced and the coil behaved like a magnet. When a ferromagnetic element or a metal object is applied, it is attracted by the coil through which the current flows.

Within the project, a dedicated software was developed, written using the Arduino IDE environment, which calculates the speed and energy of the moving object. This intricate process illustrates the complex interactions between the magnetic field and the motion of the ferroelectric material inside the electromagnetic coil.

Conclusions

The process of creating the system necessitated the design of the system component in a CAD environment, the fabrication of the component using a 3D printer, the construction of the coil, the production of the sleeve for accelerating the ferromagnetic object, the preparation of the accelerated object, the development of the microprocessor system, and the programming of it to control the coils, as well as to calculate the speed and energy of the moving object. Another integral aspect of the project is predicting its evolution.

The potential educational applications of low-energy electromagnetic field-generating systems and the challenges that may arise in future research make the implementation of an educational project look different in each instance. Experiments play a crucial role in the teaching process for various reasons. They allow the practical application of theory, aiding students in comprehending abstract concepts. Furthermore, experiments enable learning through personal experience, contributing to a deeper understanding of the material. Experiments also require various practical skills, such as observation, measurement, data analysis, and problem solving, which are significant both in learning and later in professional life. Engaging experiments enhance students' interest in science, motivating them to further their learning. Through analysis of results, pattern identification, and drawing conclusions, students develop critical thinking and problem solving skills. Experiments also allow for the practical application of acquired knowledge in real situations, helping to understand why that knowledge is essential and how it can be useful in practice.

Many experiments span multiple scientific fields, helping students understand the connections between different areas of knowledge. Additionally, experiments allow students to explore areas of science that fascinate them, potentially leading to the development of passions and interests that have the potential to transform into future professional careers.

References

1. Lobur M., Salo Y., Farmaha I. et al., 2021, *Automated ARM CPU-Based Cloud System for the Industrial Internet of Things*, in: *2021 IEEE XVIIth International Conference on the Perspective Technologies and Methods in MEMS Design (MEMSTECH)*, Polyana (Zakarpattya), Ukraine, IEEE, 25–28.
2. Quarta D., Pogliani M., Polino M. et al., 2017, *An Experimental Security Analysis of an Industrial Robot Controller*, in: *2017 IEEE Symposium on Security and Privacy (SP)*, San Jose, CA, USA, IEEE, 268–286.

3. Durelli G.C., Pogliani M., Miele A. et al., 2014, *Runtime Resource Management in Heterogeneous System Architectures: The SAVE Approach*, in: *2014 IEEE International Symposium on Parallel and Distributed Processing with Applications*, Milan, Italy, 142–149.
4. Karp M., Podobas A., Jansson N. et al., 2021, *High-Performance Spectral Element Methods on Field-Programmable Gate Arrays: Implementation, Evaluation, and Future Projection*, in: *2021 IEEE International Parallel and Distributed Processing Symposium (IPDPS)*, Portland, OR, USA, 1077–1086.
5. Ao H., Yan H., Zhang H. et al., 2022, *Teaching Reform and Practice of Strengthening Engineering Education in Mechanical Engineering Specialty*, in: *2022 International Conference on Engineering Education and Information Technology (EEIT)*, Nanjing, China, 45–48.
6. Koishi T., Matsumoto R., Fujimoto H., 2022, *Estimation and Positioning Control of Lateral Displacement Using Coil Current in Dynamic Wireless Power Transfer with Rectangular Coil on Dynamic Bench*, in: *The Wireless Power Week (WPW)*, Bordeaux, France, 322–326.

List of Tables

1.7. Study of the technical characteristics of modern LED lamps	67
Table 1. Characteristics of the lamps	68
Table 2. Measurement results of the “IEK” 11 watt	69
Table 3. Measurement results of the “Etron” 10 watt	69
Table 4. Measurement results of the “Ledstar” 10 watt	70
Table 5. Measurement results of the “Lightmaster” 11 watt	70
Table 6. Measurement results of the “Feron” 10 watt	71
Table 7. Measurement results of the “Electro house” 10 watt	71
Table 8. Measurement results of the “Kodak” 10 watt	72
Table 9. Measurement results of the “Luxray” 11 Watt	72
Table 10. Measurement results of the “Jazzwau” 11 watt	73
Table 11. Measurement results of the “Neo Max” 10 watt	73
2.5. Recycling product model and its usage in selected aspects of eco-design	125
Table 1. Connection types and natures defined in Recycling Product Model	127
Table 2. Recycling profits comparison for Examples 1–3	133
2.6. Fastening elements by blind rivets – research on the strength aspects	136
Table 1. Basic statistical parameters	139
2.8. Design and numerical simulations of a modular mine explosion protection vehicle seat	149
Table 1. Comparison of the value of the maximum acceleration and the duration of a frontal car collision at a speed of 30 mph and an explosion under the vehicle [6]	152
3.1. Leveraging smart measurement technologies for enhanced food and beverage servicing: a case study of the kyp system	161
Table 1. Communication between the Si7021 sensor and the ESP32 microcontroller	165
4.1. Evaluation of the impact of a three-axis milling plotter accuracy on the surface quality after machining an aluminum alloy	206
Tab. 1. Chemical composition of EN AW-7075 T651 aluminum alloy [3]	209
Tab. 2. Mechanical properties of EN AW-7075 T651 aluminum alloy [3]	209

List of Figures

1.1. MEASUREMENT OF EM FIELD CHARACTERISTICS IN LABORATORY BUILDINGS.....	12
Fig. 1. Cylindrical model of the human body and a vertically polarized plane wave.....	14
Fig. 2. The receiving-transmitting antenna with the generator SA6.....	17
Fig. 3. The setup for measurement of the spectral EM field characteristics.....	17
1.2. DEVELOPMENT OF HDL MODELS OF HETEROGENEOUS MICROSYSTEMS FOR BEHAVIORAL LEVEL OF COMPUTER-AIDED DESIGN	20
Fig. 1. Sensitive element of MEMS comb-drive capacitive accelerometer (a) and MEMS piezoresistive accelerometer (b). Piezoresistors are connected to the Wheatstone bridge to measure acceleration	21
Fig. 2. Verilog-AMS behavioral model of the MEMS crab-leg resonator	22
Fig. 3. Verilog-AMS behavioral model of the sensitive element of the comb-drive microaccelerometer	23
Fig. 4. VHDL-AMS behavioral model of MEMS piezoresistive acceleration sensor (accelerometer)	24
Fig. 5. VHDL-AMS model of the integrated microaccelerometer with sigma-delta control..	26
Fig. 6. Change in the output voltages on the plates of the upper capacitor C1 and the lower capacitor C2.....	27
Fig. 7. External acceleration change a_{ext}	27
Fig. 8. Output voltage change V_{out}	27
Fig. 9. Simulation results of microaccelerometer with sigma-delta control	28
1.3. BEHAVIORAL MODELLING AND SIMULATION OF MICROELECTROMECHANICAL GYROSCOPES	30
Fig. 1. Different constructions of MEMS gyroscopes	31
Fig. 2. Schematic view of the model “sensitive element-spring-damper” (where c_x, c_z – damping coefficients, k_x, k_z – spring constants of the spring elements on x - and z -direction respectively).....	32
Fig. 3. Differential capacitor formed by the electrodes deposited on the mechanical sensitive element (rotor), substrate and cover (stators) of the sensor.....	32
Fig. 4. CAD models of MEMS tuning fork (a) and comb-drive (b) gyroscopes.....	33
Fig. 5. VHDL-AMS model of microelectromechanical tuning fork gyroscope.....	34
Fig. 6. VHDL-AMS model of microelectromechanical comb-drive gyroscope	37

Fig. 7. Drive and sense oscillations of the sensitive element of MEMS tuning fork gyroscope caused by Coriolis force at $\Omega = 1$ °/c.	37
Fig. 8. Capacitance change at an angular velocity oscillations of 1°/s and frequency of 100 Hz.....	38
Fig. 9. Drive oscillations on x-direction and sense oscillations on z-direction of the sensitive element.....	38
Fig. 10. Capacitance changes C_1 and C_2	39

1.4. HARDWARE AND SOFTWARE DEVELOPMENT FOR VIBRATION MONITORING SYSTEM	40
Fig. 1. Structure of the system for monitoring the vibration acceleration spectrum	42
Fig. 2. Typical I ² C connection diagram of the ADXL345 accelerometer to the Raspberry Pi mini-computer	43
Fig. 3. Structural software diagram of the system for vibration acceleration spectrum monitoring	45
Fig. 4. Changing the output signals of the accelerometer acceleration along the Z axis and all three axes.....	46
Fig. 5. Spectrum of the vibration acceleration signal along the Z-axis and all three axes	46
Fig. 6. Change in the output signals of the vibration acceleration along the X-axis and all three axes during impact	46

1.5. MATHEMATICAL MODELLING OF THE ROOT CROPS SEPARATION AND CLEANING MACHINE'S PARAMETERS INFLUENCE ON THE INTENSITY OF ITS FUNCTIONING	49
Fig. 1. Schematic of a machine for separation and cleaning root crops from contamination using a dry method.....	52
Fig. 2. Dependence of the amplitude of oscillations of the working container of the ma- chine for cleaning and separating root crops from contamination by a dry method on the oscillating mass at the angular speed of rotation of unbalanced masses $\omega_1 = \omega_2 = 140\text{s}^{-1}$: 1 – stiffness of the work container attachment springs 12kN/m; 2 – 15kN/m; 3 – 18kN/m.....	55
Fig. 3. Dependence of the amplitude of oscillations of the working container of the machine for cleaning root crops from contamination by the dry method on the oscillating mass at the angular speed of rotation of unbalanced masses $\omega_1 = \omega_2 = 110\text{s}^{-1}$: 1 – stiffness of the work container attachment springs 12kN/m; 2 – 15kN/m; 3 – 18kN/m.....	56

1.6. AXISYMMETRIC CONTACT PROBLEM FOR A SPACE WITH A SPHERICAL CAVITY.....	58
Fig. 1. Pressing an axisymmetric stamp in a half-space with a spherical cavity.....	59
Fig. 2. Relative contact pressure at $\nu = 0.3$, $\delta = 0.001R$, $a = 0$, $b = 0.08$	63
Fig. 3. Relative contact pressure at $\nu = 0.3$, $\delta = 0.0001R$, $a = 0$, $b = 0.03$	63
Fig. 4. Relative contact pressure at $\nu = 0.3$, $\delta = 0.00001R$, $\beta = 1$, $\alpha = 0.7; 0.8, 0.9$	64
Fig. 5. Relative contact pressure at $\nu = 0.3$, $\delta = 0.0001R$, $\beta = 0.8$, $\alpha = 0.9; 0.8, 0.7$	64

1.7. STUDY OF THE TECHNICAL CHARACTERISTICS	
OF MODERN LED LAMPS	67
Fig. 1. LED lamps under investigation	68
Fig. 2. LED lamp “IEK” 11 Watt	69
Fig. 3. LED lamp “Etron” 10 Watt	69
Fig. 4. LED lamp “Ledstar” 10 Watt	70
Fig. 5. LED lamp “Lightmaster” 11 Watt	70
Fig. 6. LED lamp “Feron” 10 Watt	71
Fig. 7. LED lamp “Electro House” 10 Watt	71
Fig. 8. LED lamp “KODAK” 10 Watt	72
Fig. 9. LED lamp “Luxray” 11 Watt	72
Fig. 10. LED lamp “Jazzwau” 11 Watt	73
Fig. 11. LED lamp “Neo Max” 10 Watt	73
Fig. 12. Generalized research characteristics of modern lamps. Graphical dependence of light emission on the voltage of light sources of the brands “IEK”, “Etron”, “Ledstar”, “Lightmaster”, “Feron”, “Electro House”, “KODAK”, “Luxray”, “Jazzwau”, “Neo Max”	74
Fig. 13. Graphic dependences of light output on the voltage of light sources of the brands “IEK”, “Etron”, “Ledstar”, “Lightmaster”, “Feron”, “Electro House”, “KODAK”, “Luxray”, “Jazzwau”, “Neo Max”	74
Fig. 14. Graphical dependences of the lamp heating temperature on the voltage of light sources of the brands “IEK”, “Etron”, “Ledstar”, “Lightmaster”, “Feron”, “Electro House”, “KODAK”, “Luxray”, “Jazzwau”, “Neo Max”	75
1.8. MODELING AND OPTIMIZATION OF 3D OBJECT RECOGNITION	
USING NEURAL NETWORKS	78
Fig. 1. Satellite image of the Tu-95 bomber at the Engels-2 air base	79
Fig. 2. Satellite image of the Tu-95 bomber decoy copies at the Engels-2 air base	79
Fig. 3. Typical PointNet architecture	81
Fig. 4. 3D Object used in research	81
Fig. 5. Visualization of point cloud obtained using Polycam software	82
Fig. 6. Visualization of point cloud obtained using Autodesk ReCap Photo software	82
Fig. 7. Visualization of point cloud obtained using EinScan-SE scanner	82
Fig. 8. Dependence of the number of points to scanning environment	83
Fig. 9. Dependence of the number of points to model quality criteria	83
Fig. 10. Training of the neural network	84
Fig. 11. Dependence of the data loss to neural network learning epoch	84
Fig. 12. Dependence of the recognition accuracy to neural network learning epoch	85
Fig. 13. Point cloud before optimization	85
Fig. 14. Point cloud after optimization	85
Fig. 15. Result of 3D objects shape recognition	86

2.1. MODELLING MULTI-BOLTED CONNECTIONS	
AT THE PRELOADING STATE IN A SYSTEMIC APPROACH	89
Fig. 1. Multi-bolted system and its subsystems.....	91
Fig. 2. Hybrid model of a single bolt connector.....	92
Fig. 3. Multi-bolted connection analysed as an example: a) solid model, b) discrete model ..	94
Fig. 4. Component joint investigation on the testing machine.....	95
Fig. 5. Normal characteristic of a contact joint between the connected components.....	95
Fig. 6. Selected calculation results: a) reduced stress map in the components of the multi-bolted connection, b) final distribution of forces in the bolts.....	96
2.2. DESIGNING AND STRENGTH ANALYSIS OF A SCREW-TYPE PRESS	
FOR SUNFLOWER OIL PRODUCTION	100
Fig. 1. General design of the developed screw-type press (in the assembled state).....	102
Fig. 2. General design of the developed screw-type press (in the disassembled state)	103
Fig. 3. Simulation of stresses distribution in the screw.....	104
Fig. 4. Simulation of deformations of the screw	104
Fig. 5. Simulation of the stress-strain conditions of the screw connecting shaft	105
2.3. INVESTIGATION OF ORTHOPEDIC CONSTRUCTIONS FRACTURE	
USING CAE TECHNOLOGIES AND THE ACOUSTIC EMISSION METHOD	108
Fig. 1. Mesh of endocrown model (a) and model of the tooth with the center of gravity of the maximum stresses highlighted in red (b)	109
Fig. 2. Experimental setup (6 – the tooth restored by ceramic endocrown)	110
Fig. 3. The parameters of the AE signal local pulse using the CWT: 3D plot of wavelet spectrum intensity (a); 2D frequency (b) and 2D time (c) projections corresponding to the maximum magnitude WT_{\max}	111
Fig. 4. The typical dependence of the load and cumulative AE amplitude on the time for the tooth specimen fracture (Group A) (a); the distribution of the peak frequencies f_{\max} (b).....	112
Fig. 5. Distribution of the number of AE events for the different fracture types (%) of Type 1 (a) and Type 2 (b) samples	113
2.4. AUTOMATED DESIGN OF FIRE DETECTION DEVICES	
BODY COMPONENTS	116
Fig. 1. Fire detectors body examples, a) DETECTO SMK110 – address detector Of the LLC “Tiras-12”, b) SPD2-Tiras is a non-addressable detector of the LLC “Tiras-12”, c) SPD-3 Elite – detector of the “Arton” PE company.....	117
Fig. 2. The body created using the Cura software, a) the body in the disassembled state, b) the case in the assembled state.....	120
Fig. 3. The result of 3D printing of the FD lower cover body with new fastening elements	121
Fig. 4. 3D modeling results in the Fusion 360 system.....	122

2.5. RECYCLING PRODUCT MODEL AND ITS USAGE IN SELECTED ASPECTS OF ECO-DESIGN	125
Fig. 1. Demonstration Model 1	128
Fig. 2. Demonstration Model 2	128
Fig. 3. Demonstration Model 3	129
Fig. 4. Recycling Product Model Autodesk Inventor add-in ribbon view	130
Fig. 5. CAD 3D model (a) and connection constraints definition window (b)using RPM add-in for Demonstration model 1	130
Fig. 6. CAD 3D model (a) and connection constraints definition window (b)using RPM add-in for Demonstration model 2	131
Fig. 7. CAD 3D model (a) and connection constraints definition window (b)using RPM add-in for Demonstration model 3	131
Fig. 8. Material recycling attributes for materials used for Demonstration Models 1-3 defined in the RPM add-in	132
Fig. 9. Disassembly costs of Demonstration Model 1 calculated in the RPM add-in	133
Fig. 9. Material recycling profits of Demonstration Model 1 calculated in the RPM add-in	133
Fig. 10. Total recycling profit of Demonstration Model 1 calculated in RPM add-in	133
Fig. 11. Portable gas cooker CAD 3D model	134
Fig. 12. Connection constraints of portable gas cooker defined in the RPM add-in	134
Fig. 13. Material recycling attributes for portable gas cooker defined in the RPM add-in	134
Fig. 14. Total recycling profit of portable gas cooker calculated in the RPM add-in	134
2.6. FASTENING ELEMENTS BY BLIND RIVETS – RESEARCH ON THE STRENGTH ASPECTS	136
Fig. 2. S235 steel plates about dimensions 100x30x4 fastened by blind rivet Al-A2 4 × 12	138
Fig. 3. Geometry of joint [11]	138
Fig. 4. The histogram based on the research results is presented	139
Fig. 6. Simulative study in the LS-Dyna program.	140
2.7. NUMERICAL SIMULATION OF THE AXIAL COMPRESSION TEST OF THE “CRASH-BOX” ENERGY ABSORBER	143
Fig. 1. The value of the force as a function of the crushing distance. a) tube without trigger; b) trigger tube	145
Fig. 2. Deformation of the front frame structure of the Formula Student car in 0.035s; a) without frontal bulkhead reinforcement – test failed; b) with the front bulkhead reinforced with 1.5 mm sheet metal – test passed	146
Fig. 3. Numerical model of the impact absorber in the LS-Dyna	147
Fig. 4. The force of the absorber as a function of the process duration for circular sections with or without a trigger	147

2.8. DESIGN AND NUMERICAL SIMULATIONS OF A MODULAR MINE	
EXPLOSION PROTECTION VEHICLE SEAT	149
Fig. 1. The acceptable criteria for periodic vibrations for humans [4]	151
Fig. 2. Model of the modular seat (1 – seat, 2 – absorber module, 3 – headrest module, 4 – side supports, 5 – footrest)	153
Fig. 3. Model diagram for determining the DRIZ coefficient [2]	153
Fig. 4. Model of the seat including seat belts: – displacements of the system's elements, m – seat mass, m_2 – body mass, c – damping coefficient (seat), k – spring constant (seat), r_2 – movement limiter (belts)	154
Fig. 5. Parametric simulation model of the seat in MSC.ADAMS	155
Fig. 6. Length-time graph of a simulation model of the seat in MSC.ADAMS	156
Fig. 7. Velocity-time graph of a simulation model of the seat in MSC.ADAMS	156
Fig. 8. Acceleration-time graph of a simulation model of the seat in MSC.ADAMS	157
Fig. 9. Force–time graph of a simulation model of the seat in MSC.ADAMS	157
3.1. LEVERAGING SMART MEASUREMENT TECHNOLOGIES	
FOR ENHANCED FOOD AND BEVERAGE SERVICING:	
A CASE STUDY OF THE KYPS SYSTEM	161
Fig. 1. ESP32 Functional Block Diagram. Source [21]	164
Fig. 2. The ESP32 SX1276 Lora Development Board and the Si7021 sensor	164
Fig. 3. The gateway and the sensor	167
Fig. 4. Typical LoRaWAN network architecture. Source [25]	168
3.2. SYNTHESIS OF THE CAR SPEED REGULATOR USING	
THE METHOD OF POLE PLACEMENT	172
Fig. 1. General structure of object control with PI-regulator using	175
Fig. 2. Generalized structure of the engine and car model	176
Fig. 3. The controller model in the SIMULINK environment simulation	177
Fig. 4. Transfer characteristics for two implementations of the vehicle speed control system: – curve 1 for the coefficient K_1 in the feedback circuit; $W_1(s)$ – curve 2 for the coefficient K_1 in the forward circuit	178
3.3. CAD TOOLS FOR VTOL PROPULSION UNIT DESIGN	180
Fig. 1. Separate rotors – Zuri VTOL [1]	180
Fig. 2. Tilting rotors – Jobi VTOL [2]	181
Fig. 3. Ducted fans – P3X VTOL [3]	181
Fig. 4. Catia propeller workflow	182
Fig. 5. OpenVSP workflow	183
Diag. 1. VTOL propulsion system strategy	184
3.4. AUTOMATION OF THE PROCESS	
OF OIL PRESSING USING THE LABVIEW SYSTEM	185
Fig. 1. Graphical program in the LabVIEW language	186

Fig. 2. General view of the measuring equipment for determining the pressure in the pressing chamber of the oil press: 1 – frame; 2 – Keller PA-6T pressure sensors; 3 – screw press; 4 – cylindrical reducer; 5 – frequency converter ATX-3.0; 6 – strain gauge amplifier; 7 – measuring station (KI – 505)	187
Fig. 3. Press productivity	188
Fig. 4. Dependence of the pressure of the screw press	189
3.5. CAD MODELING AND GENERATIVE MANUFACTURING	
IN ORTHOPEDICS ON THE EXAMPLE	
OF A PERSONALIZED TARGETER TO SUPPORT OSTEOTOMY	192
Fig. 1. The position of the mechanical axis of the lower limb, a) valgus, b) correct position, c) varus	193
Fig. 2. The Correction of the mechanical axis of the lower limb by angular deviation of the tibia	193
Fig. 3. Planning an example osteotomy with use of the PeekMed [2] system	194
Fig. 4. iBalance® HTO system [3]	194
Fig. 5. A group of defined auxiliary planes	195
Fig. 6. Some views of the targeter virtual model	195
Fig. 7. The targeter on the tibia (a) and the tibia after cutting and tilting by the osteotomy angle	196
Fig. 8. Targeter during production, a-b) targeter on the printing platform, c) targeter after post-curing procedure	197
Fig. 9. Physical simulation of opening osteotomy, a) physical model of tibia and targeter, b) cutting process, c) tibia after cutting	197
Fig. 10. Use of the targeter during the procedure, a) inserting the targeter, b) cutting tibia	198
3.6. SOFTWARE AND METHODOLOGICAL COMPLEX FOR RESEARCHING	
THE USE OF GRAPH MODELS	199
Fig. 1. The structure of the program and methodological complex	201
Fig. 2. Software implementation of Lie's algorithm	202
Fig. 3. Software implementation of the Danzig algorithm	202
Fig. 4. Software implementation of the A* algorithm	203
4.1. EVALUATION OF THE IMPACT OF A THREE-AXIS MILLING PLOTTER	
ACCURACY ON THE SURFACE QUALITY AFTER MACHINING AN	
ALUMINUM ALLOY	206
Fig. 1. Test stand	208
Fig. 2. Drawing of SGS 44630 milling cutter used: D – working part diameter, L – overall length, l – maximum depth of cut [3]	208
Fig. 3. EN AW-7075 T651 aluminum alloy sample	209
Fig. 4. Accuracy and repeatability distribution of the milling plotter: a) forward and backward accuracy $A\uparrow$ for the linear strategy, b) forward and backward repeatability $R\downarrow$ for the linear strategy,	

c) forward and backward accuracy $A \uparrow$ for the ‘pilgrim’ strategy,	
d) forward and backward repeatability $R \downarrow$ for the ‘pilgrim’ strategy	210
Fig. 5. The surface roughness parameters in relation to the unidirectional positioning accuracy and repeatability of the milling plotter in milling process:	
a) positioning accuracy $A \uparrow A \downarrow$, b) positioning repeatability $R \uparrow R \downarrow$	212
Fig. 6. Values measured and fitted for the parameters: a) R_a , b) R_z , c) R_{Sm}	213
Fig. 7. Correlation matrix.....	214
 4.2. DESIGN AND MATERIAL SELECTION OPTIMIZATION FOR ADDITIVELY MANUFACTURED MODULAR COMPONENTS OF A BIOPROSTHETIC HAND.....	217
Fig. 1. The impact of temperature and flowrate on print quality:	
a) 190°C, $fl = 0.8$, b) 210°C, $fl=0.5$, c) 240°C, $fl=0.3$	220
Fig. 2. Prosthetic socket made with foamed filament technology	
a) randomized settings b) settings selected by trial and error	221
Fig. 3. Transition from a CAD model with parametric elements to a slicer with added settings for the density of individual objects, along with examples of application in hand bioprosthetics and prosthetic socket	222
 4.3. THE ROLE AND DEVELOPMENT OF CAX METHODS AND TOOLS IN REVERSE ENGINEERING.....	224
Fig. 1. Product development cycle.....	225
Fig. 2. Orientation of cutting planes [8].....	226
Fig. 3. Blade sections in shear planes and top view with the “zebra” option [8]	227
Fig. 4. Step-by-step restoration of the three-dimensional model [9].....	227
Fig. 5. Measuring points imported into the CAD system [10]	228
Fig. 6. View of the upper surface stretched on previously generated 3D curves [10]	228
 4.5. THE USE OF ARTIFICIAL INTELLIGENCE IN TEACHING AND LEARNING CAX: PERSPECTIVES AND APPROACHES.....	241
Fig. 1. For instructors – content creation.....	244
Fig. 2. For students – Google or Wikipedia Alternative	245
Fig. 3. For Students – Learning Companion	245
Fig. 4. For Students – Check the progress.....	246
Fig. 5. Providing ChatGPT with the quadcopter reengineering process to generate the code for PlantUML	247
Fig. 6. Resulted diagram based on the code generated by ChatGPT	247
 4.6. APPLICATION OF 3-D SIMULATION IN THE EDUCATIONAL PROCESS FOR DESIGNING THE MANIPULATOR OF A ROBOTIC MOBILE PLATFORM	250
Fig. 1. The photo of the manipulator and its realistic image built in Autodesk Inventor	251
Fig. 2. Construction tree of the manipulator assembly unit	252

Fig. 3. Flange drawing and assembly drawing of the manipulator.....	252
Fig. 4. Drawing and fragment of the G-code for the manufacture of a container nest on a 3-D printer.....	253
Fig. 6. Manipulator model in the MATLAB Simulink environment	253
Fig. 7. Description of connection block models and their properties in the MATLAB Simulink	254
Fig. 8. Subsystems of separated parts of the manipulator	255
Fig. 9. The result of the simulation of the manipulator functioning in dynamics	255
Fig. 10. A model for determining the stability of the RMP with a manipulator against overturning.....	256
Fig. 11. A model for determining the permissible angular acceleration of ASM.....	257
Fig. 12. Displacement of the container from the poles of the electromagnet due to centrifugal force.....	257
4.7. EDUCATIONAL ASPECTS OF DESIGNING A LOW-ENERGY ELECTROMAGNETIC FIELD GENERATING SYSTEM.....	
Fig. 1. The 3D printing project, wound coil, and system to generate a low-power electromagnetic field	264

